

In Situ X-ray Investigation of Nanostructures During Growth and Processing

Habilitationsschrift

zur Erlangung der Lehrbefugnis
für das Fach Experimentalphysik
an der Technisch-Naturwissenschaftlichen Fakultät
der Johannes Kepler Universität Linz

eingereicht von

Dr. Tobias Schülli
Beamline Gruppenleiter an der
European Synchrotron Radiation Facility (ESRF)
in Grenoble

Preface

The present work supplies an overview on the in situ works during growth or processing of nanostructures, mainly semiconductors, as realized over the last 6 years on the Beamline BM32 at the ESRF in Grenoble. It has required the close collaboration with a variety of colleagues who are authors or co-authors of the publications that make up this work. They have in common that a vast part of the experiments were carried out on BM32 if not stated otherwise. Scientific work in general and synchrotron experiments in particular strongly depend on exchange and collaboration. I am thus deeply indebted to Gilles Renaud, Beamline responsible on BM32, with whom I enjoyed many years of collaboration. My thanks go as well to the beamline personnel and colleagues Marie-Ingrid Richard, Marion Ducruet, Olivier Geaymond, Olivier Ullrich and Remi Daudin, with whom most of the present works have been carried out. In particular I would like to acknowledge Günther Bauer for his commitment and enthusiasm that always were a driving source of motivation in developing collaborations and when facing the sometimes complex experimental difficulties.

Grenoble, March 2011

Tobias Schüllli

And further, by these, my son, be admonished:
of making many books there is no end; and much
study is a weariness of the flesh.
Ecclesiastes 12:12

To Charlotte, Marion, Antoine and Arthur

Contents

Preface	iii
1 Introduction	1
1.1 In situ X-ray scattering applied to growth of semiconductors	1
1.2 <i>In situ</i> x-ray scattering on synchrotron sources	1
1.3 Examples of <i>in situ</i> growth presented in this work	2
1.3.1 The growth chamber on BM32 at the ESRF	2
1.3.2 Epitaxial growth of Ge on Si(001)	2
1.3.3 Role of metallic nanostructures in semiconductor growth and catalysis . .	4
2 Ge on Si(001) <i>in situ</i> growth	7
2.1 X-ray <i>in situ</i> methods applied to Ge on Si(001)	7
2.1.1 <i>X-ray in situ observation of semiconductor heteroepitaxy: from surface reconstruction to island growth</i> Semiconductor Science and Technology 26, 064003(2011)(invited review article)	7
2.2 The 2xN reconstruction on the Ge wettinglayer	22
2.2.1 <i>In-depth atomic structure and composition of the 2 times N reconstruction of the initial growth stages of the Ge wetting layer on Si(001) by surface x-ray diffraction</i> Physical Review B 83, 195426 (2011).	22
2.3 <i>In situ</i> monitoring of Ge-island growth on Si(001)	38
2.3.1 <i>In situ investigation of the island nucleation of Ge on Si(001) using x-ray scattering methods</i> Applied Physics Letters 89, 143114 (2006)	38
2.4 Evolution of Ge-domes on Si(001) during growth	42

2.4.1	<i>In situ x-ray scattering study on the evolution of Ge island morphology and relaxation for low growth rate: Advanced transition to superdomes</i> Physical Review B 80, 045313 (2009)	42
2.4.2	<i>In situ x-ray study of the formation of defects in Ge islands on Si(001)</i> submitted to Applied Physics Letters (2011)	52
3	Ge-growth on prepatterned substrates	57
3.1	SiGe islands on nominal and prepatterned Si(001)	57
3.1.1	<i>Enhanced Relaxation and Intermixing in Ge Islands Grown on Pit-Patterned Si(001) Substrates</i> Physical Review Letters 102, 025502 (2009).	57
4	Atomic ordering in SiGe islands	63
4.1	Atomic ordering in MBE grown SiGe islands	63
4.1.1	<i>X-ray study of atomic ordering in self-assembled Ge islands grown on Si(001)</i> Physical Review B 72, 165315 (2005).	63
4.2	Growth dependence of atomic ordering in SiGe islands	73
4.2.1	<i>Atomic ordering dependence on growth method in Ge:Si(001) islands: Influence of surface kinetic and thermodynamic interdiffusion mechanisms</i> Physical Review B 82, 035307 (2010).	73
5	Solid-liquid-gas interaction during growth	83
5.1	Complex faceting and strain in nanowires	83
5.1.1	<i>Structural investigation of silicon nanowires using GIXD and GISAXS: Evidence of complex saw-tooth faceting</i> Surface Science 602, 2675 (2008).	83
5.2	Liquid AuSi droplets below the eutectic temperature	91
5.2.1	<i>Substrate-enhanced supercooling in AuSi eutectic droplets: a way to even lower growth temperatures and an insight into the fundamental structure of liquids</i> Nature 464, 1174 (2010).	92
5.3	Gas environment and catalytic nanostructures	110
5.3.1	<i>Shape Changes of Supported Rh Nanoparticles During Oxidation and Reduction Cycles</i> Science 321, 1654 (2008).	110
6	Outlook on the growth of complex systems	117

7 Appendix	121
Literature	129
Zusammenfassung	131

Chapter 1

Introduction

1.1 In situ X-ray scattering applied to growth of semiconductors

The growth of crystals and in particular of epitaxial layers and nanostructures is of importance in nowadays semiconductor technology. Nanostructures are furthermore at the heart of research on novel devices and materials ranging from ultrafast transistor architectures in nanoelectronics to functional materials based on *e.g.* improved catalytic behaviour of nanostructures. In the case of semiconductors, the crystal quality and eventual effects as strain and composition are of particular importance in order to design and understand their electronic properties in detail. As x-ray diffraction can be used as a direct probe for strain, it has gained significant importance as a characterization tool in semiconductor industry and research using compact laboratory x-ray sources or synchrotron radiation. The tool of x-ray diffraction accesses lattice parameters in an ensemble average at highest precision and supplies complementary information to most microscopy methods. For the *in situ* study of growth processes, the potential of x-rays stands on a unique basis. The absence of specific requirements for sample preparation, as well as the tolerance of x-rays to high temperatures or complex sample environments clearly make them an intriguing instrument to be applied during growth. The monitoring by x-rays of i.e. film thicknesses [1], internal structure of crystals as strain fields and dislocations [2] has since many decades shown the potential of this techniques for the study of nanostructures in general. However to probe such small amounts of matter with x-ray beams, highly brilliant synchrotron radiation is a prerequisite. It's advent and progressing availability has since the late 1990's led to new field of structural investigations using x-rays. Numerous investigations were published on the study of homogeneous ensembles of nanostructures with the aim of spatially resolving the internal structure of such islands. Particular efforts were undertaken to trace a 3D image of the strain fields and the composition distribution in such islands [3, 4].

1.2 *In situ* x-ray scattering on synchrotron sources

X-rays have often been applied as an *in situ* characterization tool during processes or phase transitions for their weak interaction with the sample but as well because of their transmission

of materials and their compatibility with sample environments and extreme conditions in terms of temperature and pressure. Classical topics addressed *in situ* with x-rays are bulk phase transitions as order-disorder behaviour in alloys [5], change of the melting point under confined conditions [6,7], as well as the modification of bulk behaviour by the presence of interfaces [8]. The advent of modern synchrotrons as highly brilliant x-ray sources enabled more and more surface sensitive studies, leading to the development of dedicated instruments for surface diffraction (see refs. [9–11] as reviews on this topic). Although *in situ* growth of thin films is generally possible on laboratory sources, details on modification of reconstructions that may represent the growth front remain reserved to synchrotron sources which can offer up to 8 orders of magnitude higher brilliance. Instruments built for the investigation of surfaces are intrinsically valid for the *in situ* observation of nanostructure growth under ultra-high-vacuum (UHV) conditions if the sample environment can supply the conditions in terms of deposition sources and control of the sample temperature.

1.3 Examples of *in situ* growth presented in this work

1.3.1 The growth chamber on BM32 at the ESRF

The majority of experiments presented in this work are published results essentially dealing with the preparation and growth on Si surfaces, a topic developed in the *in situ* growth chamber on BM32 at the European Synchrotron Radiation Facility (ESRF) in the years 2003 until 2009. This chamber was designed originally for the study of reconstructions of surfaces and later developed to a molecular beam epitaxy (MBE) system, mainly used for the study of metal deposition on oxides [12]. As a user facility, it can be equipped with up to six sources, Knudsen cells or electron beam evaporators. Base pressures of several 10^{-11} mbar can be reached, the residual gas can be analyzed by a mass spectrometer. The heating stage allows working temperatures up to 1500°C, the temperature being controlled by a pyrometer, calibrated at several melting points throughout the concerned temperature regime. A rectangular beryllium window allows for the x-ray beam to enter, a cylindrical beryllium window allows to detect an angular range up to 110° scattering angle in the vertical plane and up to 45° in the horizontal plane. The instruments z-axis geometry is ideally suited for surface diffraction and thus the *in situ* analysis of growth phenomena. Besides x-ray scattering, Reflection High Energy Electron Diffraction (RHEED) and Auger Electron Spectroscopy (AES) can be performed on the sample during growth. Figure 1.1 presents a sketch and a photo of the MBE system as present on Beamline BM32.

1.3.2 Epitaxial growth of Ge on Si(001)

Chapter 2 introduces the basics of the x-ray scattering methods generally referred to as Grazing Incidence Diffraction (GID) and Grazing Incidence Small Angle X-ray Scattering (GISAXS) and uses the example of Stranski-Krastanov (SK) growth of Ge on Si(001) to present an overview on the various parameters accessible by these *in situ* techniques. Section 2.1 draws a comparison

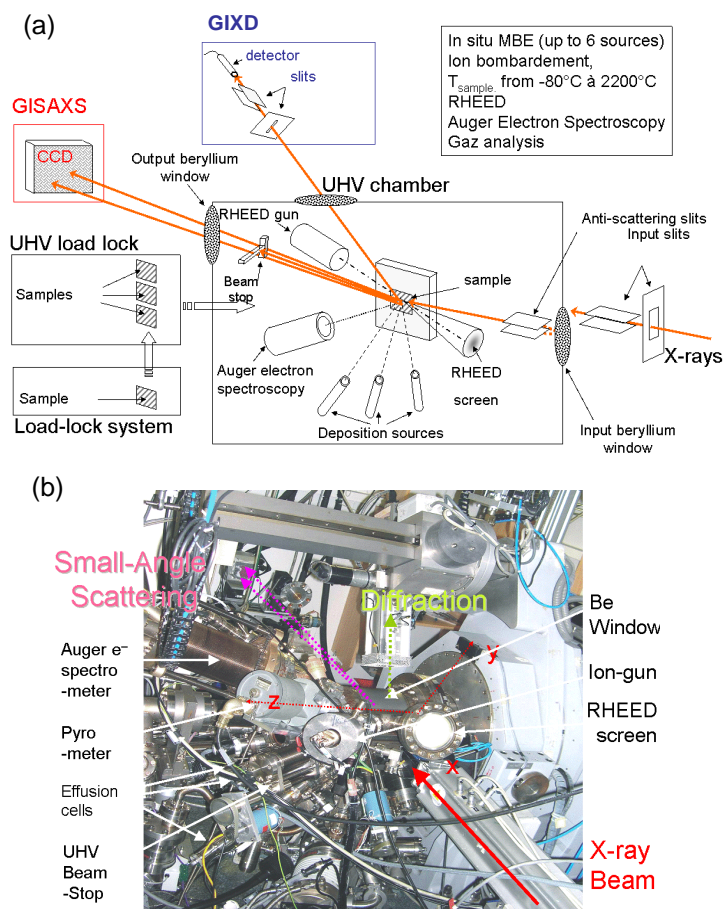


Figure 1.1: Presentation of the surface diffraction instrument on BM32(a): Sketch of the multi-chamber system and the various deposition sources and *in situ* characterization tools. (b) Photo of the main chamber. The beam trajectories for forward scattering (Grazing incidence small angle X-ray scattering, GISAXS) and grazing incidence X-ray diffraction (GIXD) are indicated.

also to competing or complementary techniques applicable during MBE growth, such as electron diffraction or electron microscopy. Accessing the parameters strain, shape and composition during growth allows to trace an image of their interdependence as influenced by thermodynamics and growth kinetics. Following this short review of techniques and results obtained during SK-growth of Ge on Si(001), details on the very early stages are presented in section 2.2. In the very early phase of Ge deposition on Si(001), a layer-by-layer type of growth is observed up to very few deposited atomic thicknesses. During this stage (called wetting layer growth) the surface atoms change their arrangement at every deposited atomic layer. This can be followed with x-rays, and one particular of these reconstructions is analyzed in detail. A modification of

the crystal lattice in all three dimensions is found, not solely affecting the surface layer of atoms but extending into a depth of about 1 nm (corresponding to ~ 8 atomic layers). For deposits higher than 4 atomic monolayers (ML) of Ge, the nucleation of coherent dislocation free islands sets in. These coherent island nucleate in the form of a first family which is flat, mainly $\{105\}$ faceted and highly strained. All these attributes can be identified with the *in situ* x-ray scattering methods as shown in section 2.3. Following the transitional stage of $\{105\}$ truncated pyramids, "dome" shaped islands evolve in order to allow a higher degree of relaxation. These represent higher indexed and steeper facets, the dominating ones being $\{113\}$ and $\{15\ 3\ 23\}$. During the transition from pyramid to dome growth, a material transport is taking place, leading to a partial mobilization of the previously deposited wetting layer, presumably in the close environment of the islands. After this stage, the onset of dislocation marks the growth of an island type generally referred to as "superdome": The facets are essentially the same as for domes, however an almost complete relaxation of the lattice is observed. This growth regime is recorded and described in terms of the evolution of the island's shape, volume and lattice relaxation in detail in section 2.4. Subsection 2.4.2 focuses on the observation of defects and the evolution of these during the superdome growth. In chapter 3, the parameters of external shape, strain and composition are compared between islands grown on flat Si(001) and on prepatterned Si substrates. This procures on the one hand information on the progress that can be obtained by new growth methods in terms of lattice relaxation without defect formation. On the other hand, the direct comparison between two samples, simultaneously grown on a patterned and non-patterned part of a Si(001) substrate, combined with a complex inverse Monte Carlo fitting process allows for 3D modeling of the internal distribution of strain and chemical composition. These two parameters define the local elastic energy and thus permit to conclude on fundamental issues of the growth process and the thermodynamic stability of the grown islands. Another property of SiGe islands or layers grown on Si(001) is the phenomenon of forming ordered SiGe alloys. As no such ordering has been obtained in bulk alloys it is not considered to be a thermodynamically stable state but is rather attributed to a certain growth kinetics depending on growth mode and temperature. The detection of ordered domains in SiGe islands grown by MBE on Si(001) allow thus to trace *a posteriori* kinetic effects which are too fast to detect with state of the art *in situ* methods. An investigation of this atomic ordering and its dependence on different growth modes, offering substantially different kinetics at comparable growth temperatures is presented in chapter 4.

1.3.3 Role of metallic nanostructures in semiconductor growth and catalysis

The motivation to deal with metallic nanostructures in the framework of semiconductor growth comes clearly with the growing interest in the study and the understanding of nanowire growth. These highly promising structures can be grown epitaxially onto Si(111), using a metal "catalyst" that can form a low-temperature eutectic with the semiconductor. Using a chemical vapour deposition (CVD) process, above the eutectic point, these catalysts crack the gas molecules and form a liquid metal-semiconductor alloy. Upon saturation, the semiconductor precipitates trigger a selective growth of a pillar at the position of the liquid droplet. The latter remains at the tip of the growing wire. Compared to solid source MBE, this fairly complex growth process

necessitates profound experimental work in order to be understood. Chapter 5 introduces in section 5.1 a characterization study of the faceting of the sidewalls of hexagonal silicon nanowires grown by the described procedure, using gold as catalyst. The wires growing along the [111] direction, a saw tooth like faceting allows high density, low indexed {111} and {113} facets. Furthermore a compression of the crystal lattice inside the wires is observed. The complexity of the vapour-liquid-solid (VLS) process that is forming the wires, called for *in situ* studies during growth. In first publications *in situ* SEM or TEM was used, leading to speculations on the consumption of the catalyst during growth [13]. Further studies revealed that the catalyst was found to be liquid or solid at the same temperature, depending on thermal history [14]. These observation on liquid-solid transitions were the basis for a profound study of the interaction of liquid AuSi droplets with a Si(111) surface using x-ray diffraction. It is found that for the solidification of the eutectic liquid, the interface between the droplets and the substrates plays a particular role. Fivefold structures present in the form of a particular surface reconstruction stabilize the liquid phase which can be significantly supercooled. This may on the one hand enable a lowering of the growth temperatures, on the other hand it is a direct observation of the influence of five fold symmetry on the stability of liquids. These findings are presented in detail in section 5.2. Due to the fundamental consequences that can be drawn from this study on solid-liquid interactions and the internal structure of liquids, an article explaining the phenomenon of supercooling is added in the appendix 7. It has been published in a magazine distributed at European high schools. The potential of x-rays as *in situ* tool for the study of growing nanowires lies in their compatibility with gas atmospheres and thus CVD growth environment. While such an extension to the instrument on beamline BM32 has been planned over the last years and is currently in the commissioning phase, experiments using gases at very low pressures have been performed in order to observe metallic nanostructures during catalytic reactions. While in the case of nanowires, such metal catalysts act as "solvents" when forming a liquid eutectic with the semiconductor, other gas reactions take solely place at the surface of the nanoparticles. An investigation presented in section 5.3.1 gives an example of an *in situ* observation of a catalytic reaction involving cyclic shape changes of epitaxial Rh nanoparticles.

Chapter 2

In-situ growth of Ge on Si(001)

2.1 X-ray *in situ* methods applied to Ge on Si(001)

The following pages shall give a review on the tools supplied by an *in situ* MBE system coupled to a synchrotron beamline. The comparison with electron scattering methods shows that the weak interaction with the sample and the ease of quantitative data treatment are the decisive arguments for the use of x-rays. This technique of *in situ* x-ray measurements has been developed mainly for the study of surfaces and their reconstructions on only a handful of specialized synchrotron beamlines in the early 1990's. Twenty years later, the increase in availability of synchrotrons has led to the use of highly brilliant x-rays by an increasing number of scientific communities. In this section, an example of highly specific use of synchrotron radiation to semiconductor growth is given by the detailed studies on the various stages of SK-growth of Ge on Si(001). In this highly studied system, x-rays still can reveal profound understanding of phenomena and the evolution of structural parameters as strain, interdiffusion and faceting that are generally observed in *post mortem* approaches with growth termination at different stages. Using Bragg diffraction, the principle probe is the lattice parameter, but a detailed analysis of the diffraction patterns allows further conclusions on interdiffusion, formation of defects and the sizes and shapes of the growing islands. In parallel to Bragg diffraction, the technique of GISAXS can be used with essentially the same instrumentation. It allows a fast and more straightforward analysis of the parameters shape and size of growing islands without carrying information about the crystal lattice inside.

2.1.1 *X-ray in situ observation of semiconductor heteroepitaxy: from surface reconstruction to island growth*

T. U. Schülli

Semicond. Sci. Technol. 26, 064003(2011) (invited review article)

X-ray *in situ* observation of semiconductor heteroepitaxy: from surface reconstruction to island growth

T U Schülli

CEA, Institut Nanoscience et Cryogenie, SP2M, F-38054 Grenoble, France and ESRF Grenoble, BP 220, 38043 Grenoble, France

E-mail: schulli@esrf.fr

Received 16 November 2010, in final form 13 February 2011

Published 29 March 2011

Online at stacks.iop.org/SST/26/064003

Abstract

The structural *in situ* characterization of heteroepitaxial growth with x-rays has proven to be able to track details and quantify parameters generally inaccessible to other non-destructive methods applied during growth. The important increase in the availability of synchrotron radiation over the last 10 years has led to a variety of instrumental developments allowing for optimum growth conditions during x-ray scattering experiments. As one of the most studied systems, Ge on Si(001) serves as an excellent example for an in-depth analysis of the complete epitaxial process. The different growth phases as seen with x-rays are presented, and a quantification of a variety of parameters is explained.

(Some figures in this article are in colour only in the electronic version)

1. Introduction: x-ray diffraction from surfaces and nanostructures

1.1. Scattering methods as tools for structural analysis

X-ray diffraction as a structural characterization tool for condensed matter, crystalline, amorphous or liquid has proven its usefulness since the first sources became available with the arrival of x-ray tubes in the early 20th century. It was at the forefront of understanding the atomistic structure of crystals and liquids [1]. During the second half of the last century, various microscopy methods have proven to be able to directly image length scales far below the wavelength of visible light and down to atomic length scales. Major developments in electron optics and sample preparation led transmission electron microscopy (TEM) to achieve atomic resolution by imaging atomic columns in crystals. For surface studies and thus as well for investigations of semiconductor nanostructures, the development of scanning probe microscopy (SPM) was beneficial [2]. The most convenient probes for the study of semiconductor surfaces are the tunneling current (STM), atomic force (AFM) or focused electron beams (SEM). As far as shading effects by the probe can be avoided, these methods can also be used during

deposition [3, 4]. In particular, STM has been used at high resolution during the growth of Ge on Si [3].

Scattering methods in general offer almost completely complementary information as compared to the aforementioned imaging tools: for a scattering method, the derived structural parameters represent generally a spatial average, whereas methods such as electron microscopy visualize individual atomic columns to image a crystal. Among the scattering methods, the access to x-rays in the form of synchrotron radiation is more difficult than to electron diffraction, available as standard equipment in ultrahigh vacuum (UHV) chambers used in molecular beam epitaxy (MBE). Reflection high energy electron diffraction (RHEED) is often used to accompany MBE growth. Its strong points are the ease of alignment and high surface sensitivity. These enable a quantitative interpretation of the scattering pattern in terms of surface orientation and the size of the surface unit cell. Furthermore, RHEED patterns yield an identification of simple growth characteristics as layer-by-layer or island growth. Low-energy electron diffraction (LEED) is also widely used in the community of surface physics. It uses electrons with a kinetic energy typically up to a few hundred eV. This kinetic energy is about two orders of magnitude lower than in RHEED, leading to high scattering angles and a two-dimensional (2D) symmetric spot

	XRD	LEED	RHEED	He-Atoms	neutrons
Surface sensitivity	+++ Tuneable	+++	+++	+++ Only topmost layer	++ Working at grazing incidence leads to loss of useful flux
Quantitative data treatment	+++ Easy, mostly kinematic	+	+	+++ kinematic	+++ kinematic
3D resolution	+++	++ SPA-LEED (2D) I-V LEED (3D)	-	-	+++
Availability	++ Synchrotrons required	+++	+++	++	- Insufficient brilliance for <i>in situ</i>
Resolution (Coherence length)	+++ (>1000 nm, up to tens of μm)	++ (10-100 nm)	+	+	+
Tolerance of sample environment	+++ Vacuum, Gas Liquid	+	++	+	+++

Figure 1. Comparison between scattering methods that can be applied to study *in situ* the growth of semiconductor nanostructures. The evaluations range from +++ (well adapted) to + (poorly adapted) or - (inappropriate). For more details, see the text.

pattern recorded in backscattering geometry. From the spot distances and geometry, the surface unit cell size and orientation can be extracted. A spot profile analysis (SPA-LEED) can even yield information about sizes of reconstruction domains, islands and facet orientation [5]. Furthermore, when tuning the electrons' kinetic energy V , the spot intensities I vary as a function of acceleration V and these $I(V)$ curves carry information about the internal structure of the unit cell. This technique called I-V LEED requires a treatment respecting dynamic scattering processes [6]. The strong interaction between electrons and condensed matter allows amplification free detection of electron scattering patterns on fluorescent screens [7]. The weaker scattering power of x-rays *versus* electrons at comparable wavelengths presents a drawback as well as an invaluable advantage: current electron scattering systems produce diffraction patterns that allow a real-time monitoring of the growth. The interpretation of the scattering pattern remains mostly qualitative; however, the shape of the diffraction spots allows us for example to detect the formation of epitaxial islands on a surface. However, due to space charge density the beam parallelism remains low and hence limits the resolution for the determination of strain distribution or the precise atomic positions inside the surface unit cell. Even while eventually taking into account resolution functions, a quantitative exploitation of a recorded intensity pattern remains difficult due to the strong electron (beam)–electron (sample) interaction: the scattering path for a fixed point \mathbf{p} on the screen cannot be determined as a unique function of p_x , p_y (coordinates on the screen). The structure determination depends strongly on the correct modeling of the sample and the dynamic nature of multiple scattering effects [6].

The kinematic interpretation of the scattering pattern together with the high resolution that can be achieved is thus often the decisive argument for the use of x-rays. A drawback of grazing incidence diffraction (GID) applied to surfaces and epitaxial nanostructures is that the use of synchrotron radiation is almost indispensable. Besides the discussed x-ray and electron scattering techniques, other methods of potential interest are He-atom scattering or neutron scattering. He atoms can be used as lab size equipment; they supply a purely surface sensitive technique without any possibility of 3D resolution. Neutrons are only poorly available and even large scale facilities cannot supply beam conditions that would allow for detailed *in situ* growth studies. Figure 1 presents an overview over various scattering methods. Note that high angular resolution and the spectral bandwidth of the applied beams result in the coherence length of the experiment [8]. The latter sets the limit of spatial resolution of the atomic positions inside a unit cell: when probing periodic long-range ordered objects as crystals in a diffraction experiment, the resolution Δr of the real space positions of atoms in one unit cell scales inversely with the coherence length ℓ as $\Delta r \propto \frac{1}{\ell}$.

1.2. History of x-ray scattering as an *in situ* tool for semiconductor growth

The intrinsic advantages of scattering methods as *in situ* tools for structural characterization are their flexible probe-to-sample distance and the fact that they work in almost any temperature regime. For x-rays, additional advantages lie in the weak interaction with the sample and thus the

absence of any influence on the growth, as well as in their compatibility with all variants of sample environments necessary for growth. These can range from UHV to gas atmospheres or even liquid environments [9–11]. In addition to these environmental advantages, radiation damage caused by x-rays remains limited and even organic semiconductor monolayers have proven to be stable on synchrotron sources for more than 24 h in the beam [12]. With the advent of synchrotrons as dedicated x-ray sources in the early 1980s, the first *in situ* growth experiments on semiconductors were performed on instruments that were able to supply UHV conditions and that were originally designed for surface preparation and analysis. Reconstructions on the surfaces of metals and semiconductors [13] had been discovered before, and even *in situ* studies of their evolution during growth have been performed using LEED and RHEED. The use of highly brilliant x-rays on synchrotron sources enabled one to resolve their three-dimensional atomic structure in great detail due to the possibility of a straightforward quantitative data treatment as explained in section 1.3 [13–15]. This overcomes the problem of pure surface sensitivity as supplied by RHEED as well as the problem of multiple scattering effects as present in I-V LEED analysis. Furthermore, even very complex structures on oxides could be analyzed, as x-rays, unlike electrons, do not suffer from the insulating character of such surfaces [16]. On these instruments, originally designed for surface diffraction, the first experiments of *in situ* observation of semiconductor growth were performed [17, 18]. At the same time, chemical vapor deposition (CVD) growth was also followed *in situ* using synchrotron light [19].

With the arrival of the third generation synchrotron sources in the mid-1990s, the possibility of following the growth of semiconductor heterostructures *in situ* appeared to be extremely valuable and beyond pure feasibility studies. Today, almost 20 years later, an analysis of all relevant growth stages is accessible on a few state-of-the-art MBE or CVD systems, rapidly growing in number and complexity (see e.g. [20–23]). Among the roughly 50 synchrotrons working now worldwide (each operating between 10 and 50 beamlines), many instruments have been added or have been refurbished over the last 10 years. Together with the amount of planned further projects, dedicated instruments for *in situ* growth become more and more available, mitigating the historical drawback of limited access to synchrotron radiation.

1.3. The kinematic approach—interpretation of reciprocal space

The use of x-rays in a scattering experiment benefits from their weak interaction (relative to electrons) with matter. In most applications, the kinematic scattering theory can be applied [24], or at least relatively simple approximations for multiple scattering processes can describe the scattered intensity distribution [25–28]. Figure 2 sketches the situation for an incoming plane wave $\psi = A e^{i(-\mathbf{k}_i \cdot \mathbf{r} + \omega t)}$ with wave vector \mathbf{k}_i and frequency ω that is scattered by point scatterers at locations \mathbf{r}_j . To evaluate the scattered intensity at a given point \mathbf{p} on the screen, we have to sum up all scattered contributions,

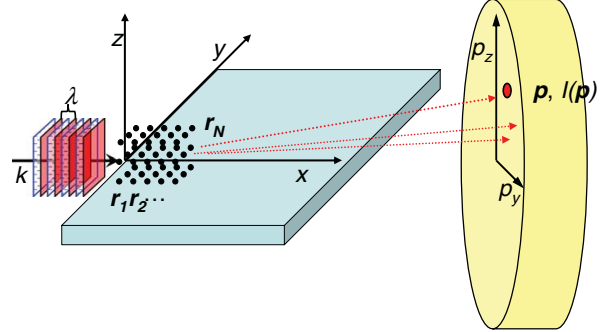


Figure 2. A plane wave which is scattered by point scatterers \mathbf{r}_j , here in periodic arrangement. On the detection screen, the scattered intensity is recorded as a function of the scattering angle.

while respecting the phase difference for the incoming wave described by \mathbf{k}_i and the scattered wave described by \mathbf{k}_f . If we consider the amplitude of the incident wave to be unity, the scattered intensity can be written as

$$\begin{aligned} \langle I_t \rangle_t &= I = \left\langle \left| \sum_{j=1}^N \hat{A}_j e^{i(\mathbf{k}_f - \mathbf{k}_i) \cdot \mathbf{r}_j} e^{i\omega t} \right|^2 \right\rangle_t \\ &= \left| \int \rho(\mathbf{r}) e^{i\mathbf{Q} \cdot \mathbf{r}} \cdot d\mathbf{r} \right|^2. \end{aligned} \quad (1a)$$

In the last step, we simply admit that we can only measure the time-averaged intensity $\langle I_t \rangle_t$ and that we write our scattering density $\rho(\mathbf{r})$ as a series of delta functions at the locations of the point scatterers located at \mathbf{r}_j as $\rho(\mathbf{r}) = \sum_{j=1}^N \hat{A}_j \delta(\mathbf{r}_j)$. In this form, the scattered intensity I describes the square of the Fourier transform (FT) from the scattering density $\rho(\mathbf{r})$ in real space to the space of momentum transfer $\mathbf{Q} = \mathbf{k}_i - \mathbf{k}_f$. It is thus practical for their interpretation to describe x-ray diffraction patterns in *reciprocal space* defined by \mathbf{Q} .

It should be recalled here that this simple interpretation of Fourier space is only valid for weakly scattering objects. This is often fulfilled for x-rays and thus the basis of quantitative analysis of x-ray diffraction. For the case of nanostructures as weak scatterers, the kinematic scattering theory or simple approximations can be applied [26].

1.3.1. Basic considerations for x-ray scattering from growing nanostructures. In semiconductor heteroepitaxy, the objects of interests to be studied during the growth are typically surface reconstructions, thin films (in Stranski Krastanov (SK) growth mode generally referred to as wetting layers (WL) [29]), and finally three-dimensional (3D) islands. The internal structure of all these objects is crystalline and thus periodic; their scattered intensity distribution can be referred to as a discrete sum over all atoms of the structure:

$$I = f_{\text{at}}(\mathbf{Q}) \sum_{j=1}^N e^{i\mathbf{Q} \cdot \mathbf{r}_j}, \quad (2)$$

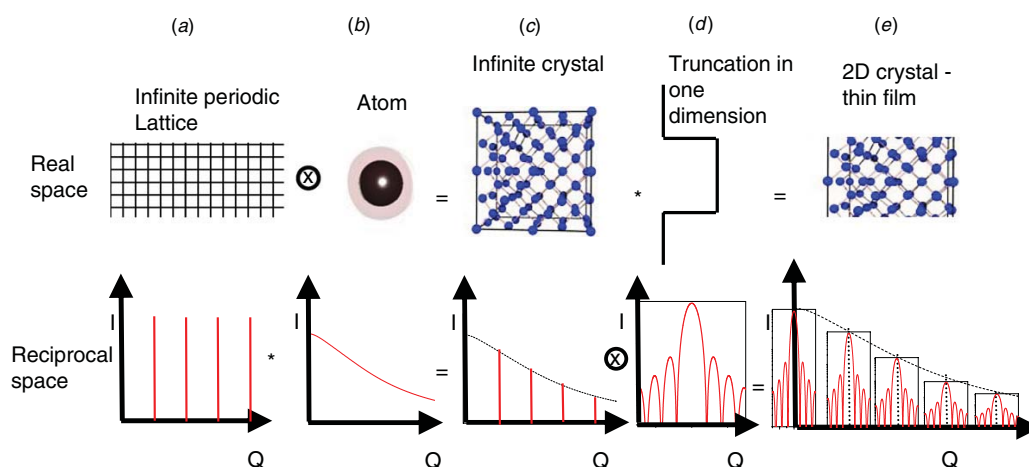


Figure 3. Graphical representation of the construction of a thin crystalline film in real and reciprocal (Fourier) space. Making use of equations (3a) and (3b), the problem is split into several objects with well-known FT. For details, see the text.

where f_{at} is the FT of one atom constituting the crystal. This expression already makes use of the (easy to prove) convolution theorem, stating that the FT of a convolution is the product of the corresponding FTs (equation (3a)) and the FT of a product is the convolution of the FTs of the factors (equation (3b)):

$$FT(f \otimes g) = FT(f) \cdot FT(g) \quad (3a)$$

$$FT(f \cdot g) = FT(f) \otimes FT(g). \quad (3b)$$

When treating crystalline structures, this proves to be very useful: an elemental crystal can be easily imagined to be built by a convolution of a discrete lattice and the atom existing on every lattice site. The FT of this crystal can thus be written as in equation (2). In the case of a unit cell containing more than one atom, f_{at} in equation (2) has to be replaced by the FT of the unit cell of the crystal. Periodic lattices in real space lead to a series of discrete peaks in reciprocal space, referred to in the following as reciprocal lattice points. Figures 3(a)–(c) show this step by step in real and reciprocal space: the intensity of these peaks follows the envelope given by $f_{\text{at}}(Q)$, a monotonic decrease toward higher values of Q . In the case of a more complex unit cell taking into account several atoms, this envelope function is called the structure factor $F(Q)$. As $F(Q)$ is only of importance at the reciprocal lattice points, it is generally given as an indexed value F_{hkl} at every position with the reciprocal coordinates carrying the Miller indexes h , k and l . As in the case of ‘small crystals’ or a thin film in the example in figure 3, the finite nature of the sum in equation (2) could be produced by suggesting an infinite sum multiplied by a shape function $\Omega(\mathbf{r})$ being unity inside the small crystal and zero outside (figure 3(d)). The FT of such a construct is thus simply the FT of the shape function convoluted with the series of discrete peaks. Hence, the FT of the shape function is reproduced at every reciprocal lattice point (figure 3(e)).

For growing epitaxial semiconductor nanostructures or thin films, the detailed observation of the evolution of only a few reciprocal lattice points representing Bragg reflections

of the growing crystals is thus sufficient to obtain information about the 3D islands as a whole. This holds even for the (000) indexed point, which describes the scattering region for very low momentum transfer Q or, equivalently, very low scattering angles. When observing growing nanostructures on a surface, x-rays are usually applied under grazing incidence, and thus the signal recorded close to the forward direction is referred to as grazing incidence small angle x-ray scattering (GISAXS).

Here, the positive interference between all scattering atoms of the structure is independent of their mutual distance and thus no information about the atomic structure can be found. However, the high intensity in this region makes it most suitable to follow evolving growth morphologies in real time [27, 30]. Furthermore, it is in the forward scattering region, where 2D intensity maps are most easily detected with 2D detectors, without moving any diffraction angle. This presents another decisive advantage when real-time recording is requested. In the small-angle-scattering regime, one speaks typically about scattering angles 2θ between 0.01 and 1° , corresponding to a momentum transfer $Q = \frac{4\pi \sin\theta}{\lambda}$ of about $0.01 \dots 1 \text{ nm}^{-1}$ for an x-ray wavelength of typically 0.1 nm. In this regime, scattering from objects of sizes of 5–500 nm can be recorded, a region of interest when observing growing SK islands. For the observation of the internal structure of these, diffraction as a probe of interatomic distances is the method of choice. As surface sensitivity is in the focus of interest, GID is usually applied. The instrumentation for such experiments consists in most cases of a UHV chamber coupled to a z -axis diffractometer [31]. This geometry allows for a constant angle of incidence, typically close to the critical angle of total external reflection, when exploring reciprocal space. The critical angle in the x-ray regime generally exploited lies between 0.05 and 0.4° , depending on the x-ray energy and the electron density of the material. For Bragg peaks requiring momentum transfers Q that lie in the surface plane, highest surface sensitivity is obtained as both incident and exit beams are in the regime for total external reflection. This situation is sketched in figure 4. To obtain information about lattice

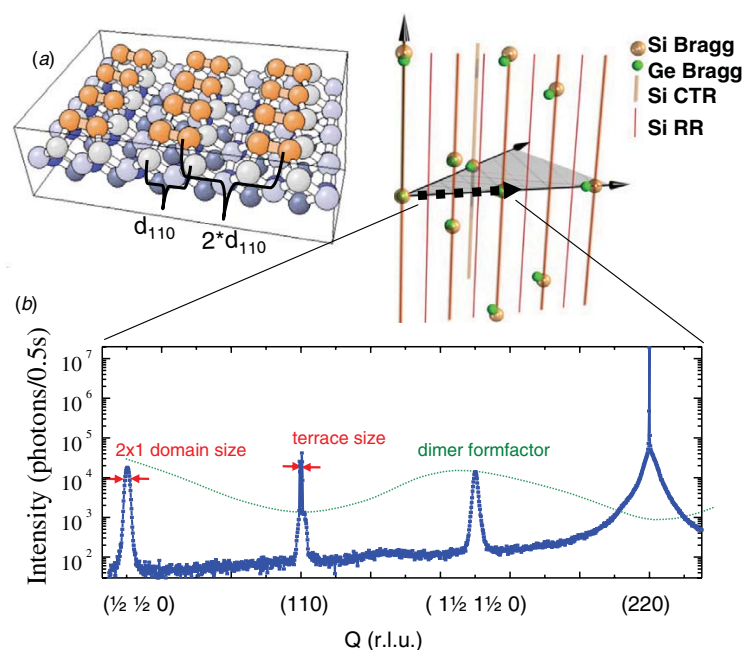


Figure 6. (a) Sketch of the dimerized 2×1 reconstructed Si(001) surface, leading to a doubling of the spatial periodicity along the $[110]$ direction. In (b) an x-ray diffraction scan along $[110]$ is shown. The fractional order peaks are attributed to the (2×1) reconstruction, on the (110) and (220) positions they are superimposed by the CTR and the bulk Bragg peak. The variation in the intensity of the reconstruction peaks is due to the structure factor of (2×1) unit cell indicated as a dotted line.

conditions at the CEA-LETI facilities in Grenoble. All wafers were covered with a 0.8–0.1 nm thin surface oxide and presented a miscut $\leq 0.1^\circ$. Prior to the *in situ* growth, the samples were placed in a separate UHV chamber for outgassing at 200–250 °C during 24 h in order to remove organic contaminations. After transfer to the growth chamber at a base pressure of 10^{-10} mbar, the sample temperature was ramped up with 1–2 h stops at 400 and 600 °C. The temperature control was assured by a IRCON pyrometer observing the sample surface through a sapphire viewport. Thermal oxide desorption was obtained by annealing for 20 min at 900 °C or at 850 °C with a supporting Si-flux of about 0.03 nm min^{-1} . On a Si(001) surface this leads to the formation of a (2×1) reconstruction due to dimerization along the $[110]$ direction [42]. This stage was followed *in situ* by RHEED and x-ray diffraction following the appearance of the (2×1) reconstruction peaks. The resulting surface unit cell is twice as big as the bulk unit cell. In reciprocal space this leads to peaks at fractional order positions. Although locally this (2×1) structure is of twofold symmetry, the domain structure present on the reconstructed surface leads to a preservation of the fourfold symmetry as present in the scattering pattern from the bulk. In a surface diffraction experiment all four $\langle 110 \rangle$ directions are thus indistinguishable.

In the case of monoatomic steps on the surface, a step presents at the same time a 90° rotation of the dimer rows [3, 32]. For surfaces with very low miscut the terrace sizes become very large and thus several reconstruction domains can coexist within one terrace. In an x-ray diffraction experiment,

the domain size and the terrace size can be determined during the surface preparation. In figure 6(b) a radial or $\theta-2\theta$ scan (see [1]) along the $[110]$ in-plane direction of a Si(001) surface is presented, together with a sketch of real and reciprocal space in (a). The intensity distribution as a function of reciprocal lattice units (r.l.u.) shows several discrete peaks. The lowest index allowed Bragg reflection along this axis is the Si(220) one. At the (110) position, as indicated in the sketch in (b), the CTR interconnecting the Si(111) and Si(11 $\bar{1}$) reflections is visible. Its intensity and width are correlated to the surface roughness and the terrace size [15, 38, 39] and its sharpening and increase can serve as a direct measure of surface quality during preparation. Furthermore, on all fractional positions $(\frac{n}{2} \frac{n}{2} 0)$, one observes peaks stemming from the inter-row distance of the (2×1) dimer rows. Their half width is correlated to the average (2×1) domain size. The half width for all three reconstruction peaks in figure 6(b) is of the order of 0.006 r.l.u. corresponding to a domain size of about 30 nm. The variation of the intensity between these three (2×1) peaks can be attributed to the structure factor and thus the internal atomic arrangement of the (2×1) unit cell. In the measured $[110]$ direction, this roughly represents the formfactor of one dimer in the plane. A thorough analysis of multiple peaks from this reconstruction and the intensity distribution along the (2×1) rods (see figure 5) yield a 3D determination of this specific reconstruction [37].

While the unit cell sizes and thus the nomenclature $(2 \times 1, 7 \times 7, \text{etc})$ were generally first determined by electron scattering techniques [42], the internal structure of the surface unit cell is better determined with x-rays if more than the topmost

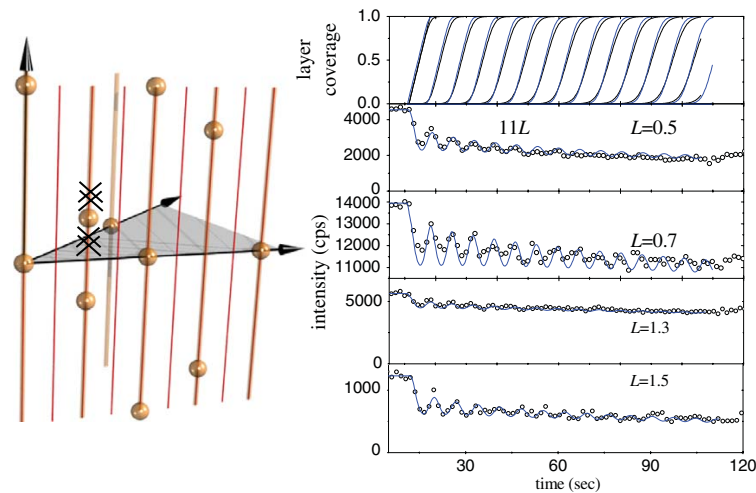


Figure 7. Homoepitaxial growth of GaAs(001). Oscillations on various positions L on the 11 L CTR (indicated by crosses in the scheme on the left) witness the layer-by-layer growth. The successive layer completion as a function of deposition time is plotted in the uppermost graph (from [44]).

atomic layer has to be taken into account, x-rays can even be considered as the unique method for 3D surface structure resolution [38, 43].

Further important information that can be extracted from the scan in figure 6(b) is the size of the terraces at the surface. The CTR at the (110) position has a width of 0.003 r.l.u., reflecting a terrace size of about 60 nm. As its intensity is related to the flatness of the surface, one generally observes growth oscillations during layer-by-layer growth on high-quality semiconductor surfaces.

An example of such growth oscillations for homoepitaxial growth of GaAs on GaAs is shown for different L -positions on the [11 L] truncation rod in figure 7. Simultaneous fitting of the damped oscillations on all positions on the CTR renders this method sensitive to the starting of a new layer before 100% completion of the topmost one. The layer completion as a function of deposit can be extracted from the simultaneous fitting of the data and is shown in the topmost graph [44]. An extension of this numerical modeling and fitting to the evolution of the surface reconstruction domain sizes is presented in [45].

2.2. Formation of the Ge WL

The surface quality in terms of roughness may evolve during epitaxial deposition. During heteroepitaxy, particular attention may be paid to changes in the surface reconstruction. For systems presenting a Stranski Krastanov (SK) growth mode one generally distinguishes a first phase of the deposition where only a WL, pseudomorphically strained to the substrate, is formed. The 4.2% lattice mismatch between Ge and Si causes compressive strain in the Ge WL. This leads to a modification of the (2 \times 1) reconstruction of the surface as soon as Ge is deposited. In order to allow for a lateral relaxation of the last atomic layer (i.e. the reconstructed layer), it becomes favorable to form vacancies of complete dimers in

the dimer rows. An optimization of elastic energy then leads to a periodic arrangement of the missing dimers in order to form dimer vacancy lines [46]. For every N th dimer line missing (figure 8(d)), a new periodicity is built up along the dimer lines and the original (2 \times 1) reconstruction is converted into a (2 \times N) reconstruction. As some Si-Ge intermixing takes place due to surface diffusion processes, the driving force to form dimer vacancies is minimal in the beginning of the Ge-deposition and grows until the WL has obtained its critical thickness of about 3–4 ML. As a consequence, N starts at high numbers and decreases as more dimers are missing and thus the distance between two dimer vacancy lines decreases [3]. Figure 8(a) shows a radial scan along the [110] direction as indicated in the sketch of figure 8(e) by the black arrow for Ge deposits of 1–5 ML. The satellite peaks appearing to the left of the (110) and (220) positions can be attributed to this modified (2 \times N) reconstruction. The distance to the (110) and (220) positions corresponds directly to the reciprocal distance of the average dimer vacancy periodicity. N is thus easily determined from graph 8(b) and is about 12 for 1 ML, 9 for 2 ML and 8 for 3 ML. The intensity decreases already at this value, which marks also the minimum for N in this study. This decrease in intensity is due to a beginning roughening of the surface, a precursor to SK island formation. Furthermore, the increase in width in this peak proves a poor definition of the N periodicity. For 4 ML the signal further decreases and the (2 \times N) peaks broaden due to strong local variations of N and hence a weaker definition of this reconstruction. At a deposit of 5 ML, a shoulder appears to the left of the Si(220) Bragg peak indicating a partial lattice relaxation due to island formation (figure 8(c)). At the same time, N increases again. The tendency of the formation of an increasing number of missing dimers in one row, i.e. a decrease in N for the early stages of WL growth, is an indication for elastic energy as driving force for this vacancy formation. With the onset of surface roughening and island formation, this tendency can be

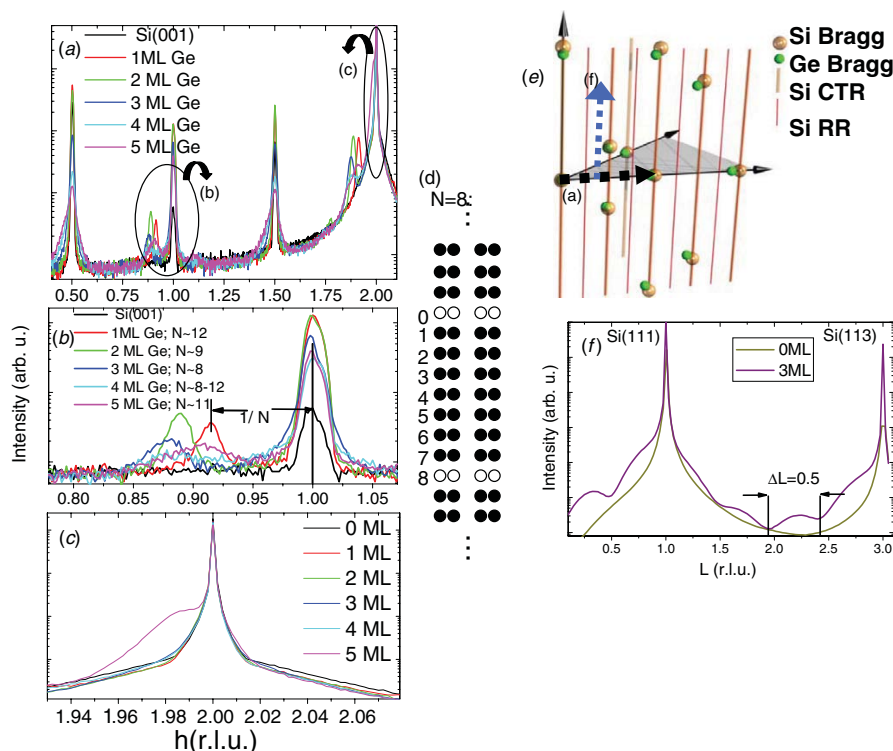


Figure 8. Evolution of the Si(001)-(2 \times 1) reconstruction during Ge deposition. (a) The radial scan along [1 1 0] shows peaks of the (2 \times 1) reconstruction, the Si(220) Bragg peak and the appearing signals of the (2 \times N) reconstruction on the Ge WL. The zoom in (b) shows the evolution of one of the (2 \times N) peaks and thus the distance N between two missing dimers as a function of Ge deposit. (c) From 1–4 deposited MLs no lattice relaxation is visible around the Si(220) Bragg peak, until island nucleation sets in at 5 ML. (d) Real space representation of the (2 \times N) reconstruction for $N=8$: every eighth dimer in a row is missing (indicated in white). (e) sketch representing the scans in (a) (black arrow) and (f) (vertical blue arrow). (f) Scan along the [1 1 L] truncation rod for Si(001) before and after deposition of 3 ML of Ge.

reversed. With the high elastic distortion of the WL, it is clear that the crystal structure below this reconstructed surface layer might be modified as well. Information about this subsurface region can be gained by studying the intensity evolution along a CTR. The presence of the latter is attributed to the semi-infinity of the crystal and the finite penetration depth of the x-ray wave. This still covers a few thousand atomic layers that scatter coherently along these CTRs, i.e. with a well-defined phase between each atomic layer. If one considers a few top-layers that suffer from a phase shift due to atomic displacements caused by surface reconstruction and relaxation effects, the waves scattered from these will cause interference effects modulating the intensity distribution along the CTR. These interference effects can probe the depths down to which the surface effects range into the crystal: figure 8(f) shows the intensity distribution along the (1 1 L) rod for bare Si(001) and after deposition of 3 ML of Ge. The oscillations along the scan witness a period of 0.5 r.l.u. and correspond thus to a thickness of 2 unit cells, i.e. about 1 nm in real space. Recording the interference effects on several CTRs, one obtains holographic information about the 3D structure of the disturbed surface layer (for an introduction to CTR analysis, see e.g. [15, 39]). The influence of this specific (2 \times N) reconstruction on the precise atomic arrangement and the chemical composition of

the upper layers of the substrate is the subject of current studies using *in situ* surface diffraction [47].

2.3. Nucleation of coherent islands

The second phase of SK growth of Ge on Si(001) is the nucleation of coherent, i.e. dislocation free islands [48]. The transition from a pseudomorphic WL to partially relaxed islands is inherently the one which is most easily detectable with x-rays, as demonstrated in figure 8 for Ge on Si(001) and in [49] for InAs on GaAs(001). Early studies on second-generation synchrotron sources have investigated the strain relaxation in SiGe islands on Si(001) [17]. In these studies, the first level of relaxation remained unobserved: the formation of flat highly strained pyramids as reported in [50]. The {105} faceted low aspect ratio pyramids or huts have been reported to nucleate for Ge deposits higher than 4.0 ML for deposition temperatures between 450 and 650 °C [51]. Their x-ray diffraction signal is in close vicinity to the Si-Bragg peak and thus difficult to resolve. However, a combination of GISAXS and diffraction can clearly reveal the pyramidal shape with {105} facets and correlate it to the diffraction signal. In this example, the complementarity of *in situ* x-ray diffraction to *in situ* microscopy becomes clear: the strain relaxation and eventually the composition of growing

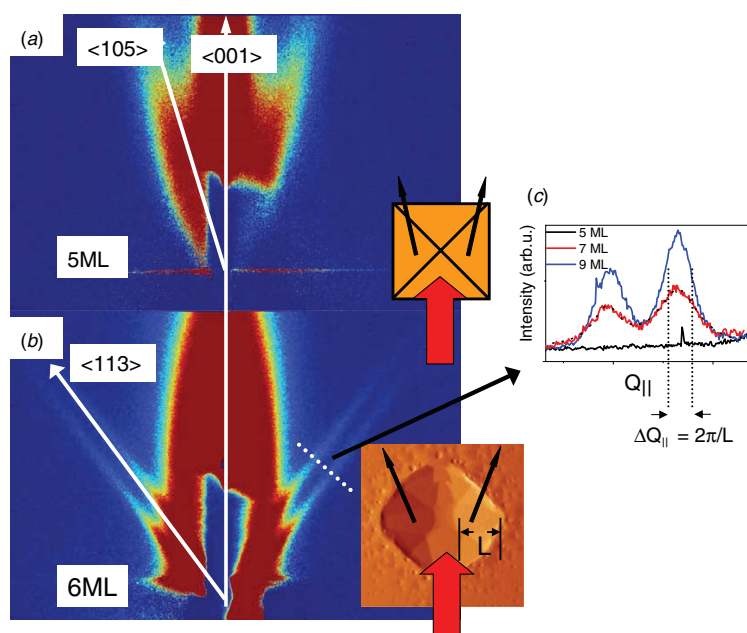


Figure 9. (a) GISAXS image cutting through the truncation streaks of a $\{105\}$ faceted pyramid (sketched in the inset on the lower right) obtained by a deposition of 5 ML of Ge on Si(001) at a growth temperature of 600 °C. (b) For a deposit of 6 ML domes are formed, yielding streaks from $\{113\}$ facets. An AFM image of such a dome is presented in the inset. From the width of these streaks, the size of the domes can be extracted as shown in (c). (c) Cut through truncation streaks from a $\{113\}$ facet. The FWHM $\Delta Q_{||}$ allows for a straightforward determination of the facet size. From references [54, 55].

islands can well be determined with x-rays, whereas the morphological parameters are easily accessible with methods as *in situ* STM as well as low energy electron microscopy (LEEM) or more generally SEM. Their capacity as *in situ* tools has been demonstrated in [4] for SEM and notably with great detail on Ge/Si(001) in [3] with STM. As these microscopy methods however are somewhat blind for the internal structure, they are entirely complementary to x-ray diffraction. A combination of both would supply the most complete *in situ* tool. For these reasons, the exploration of x-ray scattering signals near the origin of reciprocal space becomes of interest: whereas diffraction explores the wide angle region (typically between scattering angles of 10 and 100°) in order to explore atomic distances with high resolution, scattering at small angles corresponds to signals stemming from ‘big’ structures in real space. During an *in situ* experiment with x-rays, GISAXS can thus supply the shape information in a relatively straightforward way, playing the role of the *in situ* microscope. In order to resolve such structures, the beam divergence has to be low, and the beam has to be small, in order to detect small angle scattering signals very close to the forward direction. A complete review of this technique has been published recently [52]. Recording the region in the vicinity of the origin of reciprocal space is generally done with a 2D detector. In this case only the sample orientation has to be chosen in an appropriate way in order to follow the growth of islands. The FT of nanoscaled objects becomes particularly simple to interpret if well-defined facets truncate the objects: these two-dimensional truncations lead to one-dimensional streaks in reciprocal space, similar to the CTRs discussed above.

Figure 9(a) shows a GISAXS image for the appearance of $\{105\}$ faceted pyramids for 5 ML of Ge deposited at 600 °C on Si(001). The angle between the surface normal and the facet streak allows a simple indexation of its orientation, as long as the crystallographic coordinate system is known from diffraction. For deposits of Ge on Si(001) higher than 5 ML, the growing islands change in shape and continue to grow as ‘domes’. These are truncated by $\{113\}$ and $\{15323\}$ facets [53], which can as well be detected by GISAXS and are shown in figure 9(b). The splitting of the streaks is caused by interference effects between waves scattered by the islands before and after reflection at the free surface: when scattering from islands on a flat surface is observed under total external reflection conditions, the purely kinematic treatment of the scattered intensity is no longer valid and multiple scattering events must be considered. In the distorted wave Born approximation (DWBA), four scattering processes can be identified to add up coherently [25–27]:

- (1) the kinematic scattering, i.e. the wave is only scattered by the island;
- (2) the wave is reflected at the surface *before* being scattered by the island;
- (3) the wave is reflected at the surface *after* being scattered by the island;
- (4) the wave is reflected *before and after* being scattered by the island.

The interferences between these contributions is of importance when the angle of incidence of the x-rays α_i is in the vicinity or below the critical angle of total external

reflection α_c . It is important to remark here that these multiple scattering effects are all in between a relatively simple object (a flat surface) and the structure to be investigated (a faceted island). In our case this leads e.g. to the splitting of the streaks without modifying their full width at half maximum (FWHM) value. Multiple scattering effects inside the island can be neglected. The FWHM of the streaks in figure 9(b) can be exploited to determine the facets' size L :

$$L = \frac{2\pi}{\Delta Q_{\parallel}}. \quad (4)$$

Performing a rotation around the surface normal of the sample all facets which are present can be detected and their size determined. It is thus possible to determine shape and size of a faceted object in a very straightforward way, as shown in figure 9(c), and to follow these parameters during growth [54].

Whether the pyramid to dome transition depends solely on the deposited amount of Ge or whether pyramids can exist as a metastable state during several minutes has been the object of discussions [50]. Several studies aiming at a strain analysis combined with a compositional analysis underline the importance of elastic relaxation to accommodate the higher Ge content with the formation of higher aspect ratio islands without introduction of dislocations. Mainly based on a post growth chemical analysis by selective etching, these are able to quantify differences in the Ge content in pyramids and domes, without explaining the driving forces of Si interdiffusion [56, 57]. For the pyramids, formed initially on top of the WL, the composition of the latter seems to be of key importance in view that the material forming the pyramids is collected by surface diffusion processes, including atomic exchange from the topmost layers. This underlines the importance and potential of x-ray *in situ* methods applied to the complete growth process, including the formation of the WL. The diffraction methods presented in this paper can be backed up by x-ray photo emission electron microscopy [58].

2.4. Chemical composition of epitaxial islands

Definitely one of the most critical points that can be addressed in an x-ray diffraction experiment is the chemical composition. This can be done either by a correlation between lattice parameter and composition [59, 60], in case the elastic properties of the alloys in question are known, or by using anomalous diffraction as a method that determines directly the chemical composition in reciprocal space [61, 62]. A third method may be used for composition analysis in compound semiconductor islands: it is based on a comparison of intensities between Bragg peaks with different structure factors. This has been demonstrated in a very elegant way by Kegel *et al* [26] for the case of $\text{In}_x\text{Ga}_{1-x}\text{As}$ islands obtained by InAs deposition on a GaAs substrate. For the zincblende structure, the structure factors for the (200) and (400) Bragg reflections read $F_{200} = (f_{\text{Ga}} - f_{\text{As}})$ and $F_{400} = (f_{\text{Ga}} + f_{\text{As}})$, respectively. As the atomic numbers of Ga (31) and As (33) are fairly similar, we obtain a very high intensity ratio $\frac{I_{400}}{I_{200}} = \frac{(f_{\text{Ga}} + f_{\text{As}})^2}{(f_{\text{Ga}} - f_{\text{As}})^2}$ between these two reflections. For InAs, this ratio is much lower and for an $\text{In}_x\text{Ga}_{1-x}\text{As}$ alloy, the ratio lies somewhere in between. In this way the ratio

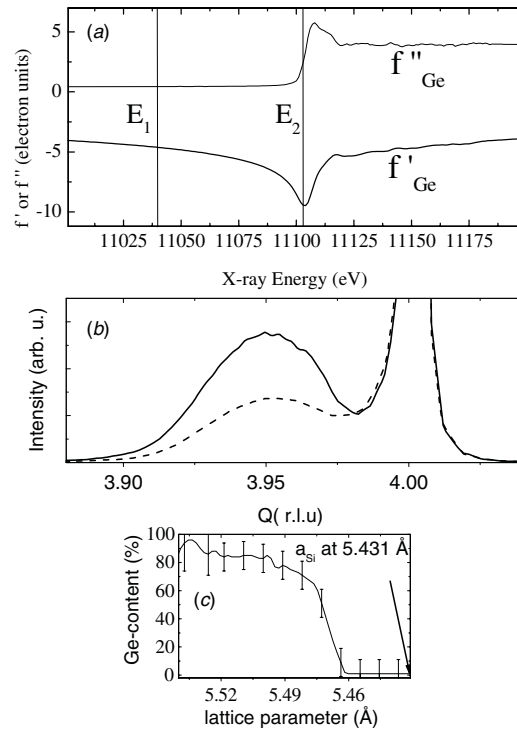


Figure 10. (a) Energy dependence of the resonant corrections f' and f'' for Ge in the vicinity of the Ge K-edge. (b) Radial scan across the (400) reflection of SiGe islands on Si(001) for two different x-ray energies E_1 and E_2 indicated in (a). (c) Result from (b); the Ge content can be determined as a function of lattice parameter. Note that for lattice parameters ≤ 5.46 Å the Ge content is 0; thus, all scattered intensity stems from strained Si. From [62].

between two intensities from two Bragg peaks (400) and (200) corresponds to a well-defined In content x inside the $\text{In}_x\text{Ga}_{1-x}\text{As}$ islands.

In SiGe no such differences in the structure factors for different Bragg peaks exist and thus the composition analysis of SiGe alloys has to be done in a different way. In this case, the x-ray energy dependence of the atomic scattering factor of one element is exploited. The goal is again to evaluate an intensity ratio but this time of only one Bragg reflection measured at different x-ray energies. Anomalous diffraction makes use of the energy dependence of the atomic scattering factor close to the absorption edge of a specific element. The complex atomic scattering factor is generally written as $f(Q, E) = f_0(Q) + f'(E) + i f''(E)$ where $f_0(Q)$ describes the momentum-dependent or non-resonant part and $f'(E)$ and $f''(E)$ stand for the energy-dependent correction terms. These terms are only important close to an absorption edge. Figure 10(a) shows the correction terms for Ge in the vicinity of the Ge K-edge at 11.103 KeV and two typical energies E_1 and E_2 where the experiment may be performed are indicated. Varying the x-ray energy between E_1 and E_2 will thus modify the scattering contribution of Ge in the spectra and the change in intensity can then be attributed to a certain Ge-content x of an alloy $\text{Ge}_x\text{Si}_{1-x}$. The graph in figure 10(b) shows a radial scan across the (400) reflection of SiGe islands

on Si(001) for two energies E_2 right at the Ge K-edge and E_1 60 eV below. With the scattered intensity $I \propto |f|^2$, the ratio between both intensities can be written as

$$\frac{I_{E_1}}{I_{E_2}} = \frac{\left| x(f_{0\text{Ge}}(Q) + f'_{\text{Ge}_{E_1}} + i f''_{\text{Ge}_{E_1}}) + (1-x)(f_{0\text{Si}}(Q) + f'_{\text{Si}} + i f''_{\text{Si}}) \right|^2}{\left| x(f_{0\text{Ge}}(Q) + f'_{\text{Ge}_{E_2}} + i f''_{\text{Ge}_{E_2}}) + (1-x)(f_{0\text{Si}}(Q) + f'_{\text{Si}} + i f''_{\text{Si}}) \right|^2} \quad (5)$$

Thus, once the atomic scattering factors at both energies are known, the concentration can be determined in reciprocal space, i.e. as a function of lattice parameter. The result is plotted in figure 10(c). It becomes clear that even for lattice parameters that are about 0.6% bigger than Si, no Ge is found. The signal corresponding to these lattice parameters is thus attributed to the strained region in the substrate underneath the islands. Due to the rather complex procedure, requiring a change of x-ray energy and sufficient calibration of the latter, this method so far has been mainly applied *ex situ*, where the measurement time is less restrictive than during growth. Beyond the *in situ* growth of Ge on Si [55], it has proven its usefulness during *in situ* measurements by simply enhancing the contrast and thus the visibility of growing GaN quantum dots in an AlN matrix [63].

2.4.1. Chemical composition and elastic energy. The access to the chemical composition of growing islands is of interest in order to track influences of kinetics and equilibrium thermodynamics at different growth temperatures and stages of the growth. Producing sample series for different growth stages and analyzing them *ex situ* by selective etching [56, 57] or energy filtering TEM [64] have shed light on basic processes of intermixing. Besides being potentially applicable *in situ*, during growth, the composition determination with x-rays presents another extremely intriguing advantage: as the composition is determined as a function of lattice parameter, the result directly delivers the elastic energy and the compressive or tensile forces which the material is locally exposed to. The equilibrium lattice parameters as well as the elastic constants for $\text{Si}_{1-x}\text{Ge}_x$ alloys are known in great detail [65, 66]. Thus measuring the Ge concentration x at a given lattice parameter a and supposing that the equilibrium lattice parameter a_x is known, the elastic strain ϵ can be calculated as

$$\epsilon = \frac{a - a_x}{a_x} \quad (6)$$

The volumetric elastic energy then results from Hookes' law:

$$E_v = 2\mu \frac{1+\nu}{1-\nu} \epsilon^2 \quad (7)$$

Here, μ and ν are the material parameters known as shear modulus and Poisson ratio. The point-by-point evaluation of elastic energy in reciprocal space allows for the estimation of strain gradients, but also for the integration and averaging of the elastic energy per atom over a complete island. The

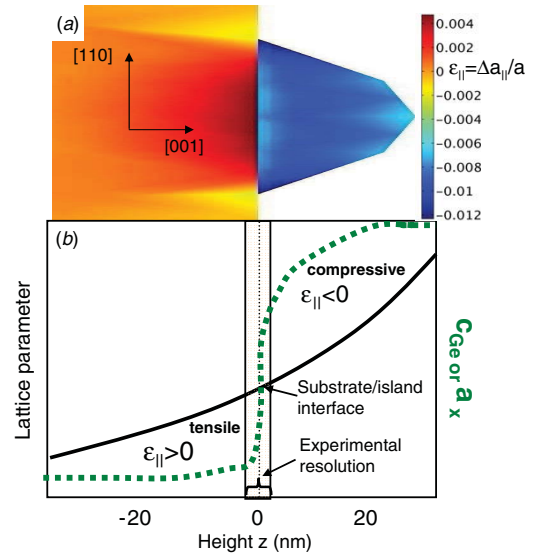


Figure 11. (a) Simulation of the strain inside a SiGe island on Si(001) (note that the shape is not to scale). (b) Sketch of the mean evolution of the lattice parameter (full line) and the Ge content or the equilibrium lattice parameter a_x (dashed line) as a function of height inside the substrate and the island. The experimental resolution is indicated as a shaded bar. Image courtesy of Nina Hrauda.

limitations of this direct determination of elastic energy are set by the regions where ϵ changes its sign. These are generally the regions close to the substrate surface, at the bottom of an island. For Ge on Si(001) the upper part of the substrate suffers from tensile stress, whereas the island is compressed. In figure 11(b), a graphical representation of the evolution of the lattice parameter (full line) and composition (and thus the equilibrium lattice parameter a_x) inside an island as a function of height above the substrate is shown. As the composition evolves rather abruptly at the island/substrate interface, the strain ϵ changes its sign from positive (tensile) to negative (compressive). This is indicated in the color coded image shown in figure 11(a) which presents a simulated cross section of the strain distribution in the {110} plane of a SiGe island on Si(001). The in-plane strain ϵ_{\parallel} is showing positive values inside the substrate and negative values inside the compressed island. Note that the simulation takes into account the composition gradient inside the island and hence the evaluation of ϵ in every point refers to the equilibrium lattice parameter of the corresponding $\text{Si}_x\text{Ge}_{1-x}$ alloy. Limited lattice parameter resolution will now affect the resolution of strain and composition gradients. Regions with similar lattice parameter will yield an average over their Ge content and lattice parameter. The intrinsic resolution limit that will affect such a measurement is generally determined by the size of the strained nanostructure [26, 67]. By way of example we may consider a small crystal of size D and its diffraction at the Bragg point hkl with a corresponding lattice spacing d_{hkl} . The corresponding momentum transfer at this Bragg diffraction then reads

$$Q_{hkl} = \frac{2\pi}{d_{hkl}} \quad (8)$$

Due to the finite size D of the crystal, the FWHM of the observed Bragg peak is then spread as

$$\Delta Q_{\text{size}} = \frac{2\pi}{D} \quad (9)$$

and thus independent of the position hkl . Equation (9) is referred to as size-broadening. In order to resolve strain, we have to look at the deviations Δd_{hkl} from the equilibrium or the reference lattice spacing d_{hkl} . In general, we will expect the Bragg signal to be spread out in reciprocal space due to these deviations. According to equation (8) we can calculate the difference in the momentum transfer ΔQ_{hkl} caused by a small difference in the lattice parameter Δd_{hkl} as

$$\Delta Q_{hkl} = \frac{2\pi}{d_{hkl}^2} \Delta d_{hkl}. \quad (10)$$

It becomes clear from equations (9) and (10) that size broadening may ‘hide’ the effect of strain on the spread of the diffracted intensity in reciprocal space. Furthermore, one can enhance the effects of strain by choosing a high indexed reflection and thus a small lattice spacing d_{hkl} . When performing anomalous scattering however, the x-ray energy and thus achievable range in reciprocal space, is limited.

For the investigation of SK-grown islands this resolution limit Δd_{hkl} can be translated into an integration over a certain volume or height inside the island, as the lattice parameter generally evolves as a function of height (including lateral variations). In the example of Ge islands on Si(001), for an island size of 600 Å, equation (9) results in a ΔQ_{size} of about 0.01 \AA^{-1} . At the (400) Bragg reflection, using equation (10) this translates into a resolvable lattice parameter difference Δd_{hkl} of 0.2 %. This still permits an appreciable strain resolution in the system Ge on Si with a lattice mismatch of 4.2% and typical lattice parameter evolutions of 1–3 % throughout SK islands [60]. Such convolution effects do not change the average value of ϵ over the whole integration range, but may well affect the average of E_v . In regions where ϵ is averaged to 0, the E_v cannot be determined directly (as otherwise it would average out to 0 as well), but can be estimated if the gradient of ϵ can be interpolated in the questionable regions. When the lattice parameter evolution inside the island is expressed as a function of height, such resolution limits are translated into an averaging over a certain height inside the islands. As discussed, this becomes of particular importance for regions close to the substrate interface as sketched in figure 11. The method allows thus a direct evaluation of elastic energy only outside the shaded region where the strain ϵ changes its sign and falls into the intrinsic experimental resolution. Here, fitting procedures can close this gap [68].

2.5. Dislocated islands

The formation of defects during growth may be induced by lattice strain and subsequent plastic relaxation. The energy necessary to form a defect generally comes from the local elastic energy and from thermal activation. Prominent defects in SK islands for Ge on Si(001) are stacking faults, i.e.

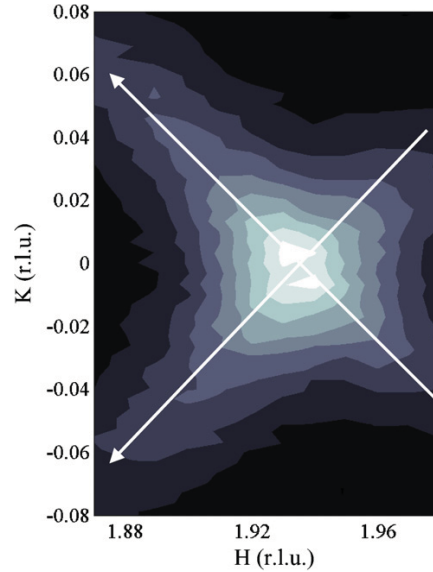


Figure 12. Reciprocal space map in the vicinity of the (200) ‘forbidden’ reflection of SiGe island on Si(001) containing stacking faults. The streaks of the cross-shaped intensity are pointing in $\langle 111 \rangle$ directions (here only their projections in the $\{001\}$ plane are visible) and are caused by the 2D nature of the extra $\{111\}$ plane forming the stacking fault.

extra $\{111\}$ planes that are introduced and cause a rupture of the ABCABC... stacking sequence. This leads to a local change of the extinction rules of the diamond fcc lattice and to apparition of diffracted intensity at forbidden reflections as is the case for e.g. the intensity apparition at the (200) reflection in implanted Si [69]. In particular, as the perturbation is caused by a 2D structure (the extra $\{111\}$ plane), the features observed in reciprocal space consist of streaks pointing in all $\langle 111 \rangle$ directions. As in the case of SK islands, the introduction of dislocations generally occurs in a ‘late’ stage of growth, most of the studies dealing with these can thus be performed *ex situ*. An example for the observation of such defects by x-rays is shown in figure 12. An in-plane map is recorded in the vicinity of the (200) reciprocal lattice point for islands grown by the deposition of 10 ML of Ge on Si(001) at a growth temperature of 450 °C. At this temperature, stacking faults are easily observable. A cross-like distribution of scattered intensity is visible, the cross arms are projections of the corresponding $\langle 111 \rangle$ on the $\langle 110 \rangle$ vectors in the $\{001\}$ plane. For higher growth temperature and during SK growth, the *in situ* observation of the appearance of stacking faults with x-rays is still a challenge, although first studies reveal the possibility. The main problem is the weak intensity and thus the measurement time that becomes problematic during *in situ* experiments. However, a particular interest in this method is definitely given by the possibility of evaluating not only the appearance but also the size of the stacking faults (corresponding to the FWHM of the streaks visible in figure 12) and their evolution during growth.

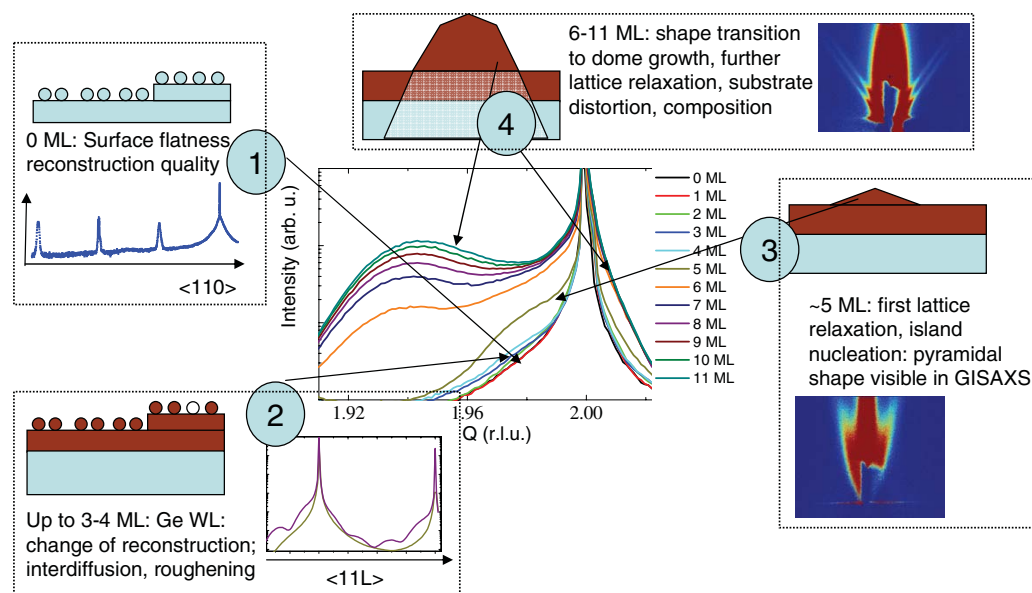


Figure 13. Summary of all relevant growth stages of Ge on Si(001) as observed by x-ray diffraction. As an example, the intensity in the vicinity of the Si(220) Bragg peak is plotted for 0–11 ML of Ge deposition. For 0–4 ML the focus of interest lies in the evolution of the surface reconstruction. After island nucleation, the combination of GISAXS and GID attributes an island shape to a certain degree of relaxation.

2.6. Summary of observables during heteroepitaxial growth

The tools and the parameters permitted to be explored as described in sections 2.1–2.4 are easily extensible to other heteroepitaxial systems. Figure 13 summarizes the information accessible throughout the growth process of Ge on Si(001). During surface preparation and 2D growth the most compelling information is found on truncation rods and reconstruction peaks and their evolution. This gives access to the nature of the reconstruction as the size of its unit cell in all three dimensions as well as its internal structure (atomic displacements). For island nucleation, the centers of interest are on the one hand the vicinity of Bragg peaks, where islands manifest in the form of lattice relaxation, and on the other hand the GISAXS region where the morphology of 3D structures can be probed. The combined information as accessible by utilizing diffraction in the vicinity of the (220) Bragg reflection, CTRs, RRs and GISAXS during island growth shows the complementarity of both scattering methods: from 0 to 4 deposited ML of Ge, the Bragg signal does not show any evolution, as no lattice relaxation is present. With the first facet streaks appearing in the GISAXS signal a first relaxation of the crystal lattice is visible in the form of a shoulder to the left of the Si(220) position. For ongoing deposition, this evolves quickly toward higher relaxation indicating the formation of dome-shaped islands, which themselves strain the underlying substrate. Eventual further shape changes can be detected, as well as the formation of defects, often correlated with these.

3. Current development and future

The increase in availability of synchrotron beamlines enables more specialized instruments dedicated to *in situ* growth. The instrumentation that has been installed 10–15 years ago under the perspective of surface diffraction for the analysis of perfect crystal surfaces and reconstructions is nowadays often extended to full MBE systems that allow a multitude of elements to grow. As extremely good vacuum conditions are a concern for these instruments, candidates such as As and Se are often excluded due to their incompatibility with other systems. The growth of group III–V semiconductors is, as long as As is excluded, compatible with multiple source MBE *in situ* growth systems as presented in the works of [63, 70]. The growing complexity of functional nanomaterials and devices as potential candidates for high density storage, fuel cells or batteries, renders x-rays as an *in situ* or *in operando* tool extremely compelling. Very recent works in the field of studies on the structure and failure of devices during use clearly show the way *in situ* x-rays are able to go. One of the most interesting topics might be metal organic chemical vapor deposition (MOCVD) growth, which in the future might attract broad interest. In principle, the required installations can be built compact and easy to adapt to the requirements of x-ray diffraction. The vast amount of technically relevant material grown with this process ranges from perovskites [10], known for their multitude of interesting properties, up to semiconductors [23] where CVD and MOCVD processes are still the most technically exploited processes in thin-film and nanostructure growth.

Acknowledgments

For their help and for their collaboration during the x-ray experiments, special thanks go to G Renaud and M-I Richard as well as to the staff of Beamline BM32 of the ESRF. The author would also like to acknowledge G Bauer for inspiration and fruitful discussions.

References

- [1] Warren B E 1990 *X-Ray Diffraction* (New York: Dover)
- [2] Binnig G, Rohrer H, Gerber C and Weibel E 1983 *Phys. Rev. Lett.* **50** 120
- [3] Voigtländer B 2001 *Surf. Sci. Rep.* **43** 127
- [4] Ross F M, Tromp R M and Reuter M C 1999 *Science* **286** 1931
- [5] Horn M and Henzler M 1987 *J. Cryst. Growth* **81** 428
- [6] Rous P J and Pendry J B 1989 *Surf. Sci.* **219** 355
- [7] Hopkins B J and Watts G D 1974 *Surf. Sci.* **44** 237
- [8] Holy T, Baumbach V and Pietsch U 1999 *High Resolution X-Ray Diffraction from Thin Films and Multilayers* (Berlin: Springer)
- [9] Bernard P, Peters K, Alvarez J and Ferrer S 1999 *Rev. Sci. Instrum.* **70** 1478
- [10] Fong D D, Eastman J A, Stephenson G B, Fuoss P H, Streiffer S K, Thompson C and Auciello O 2005 *J. Synchrotron Radiat.* **12** 163
- [11] Teubner Th *et al* 2008 *Cryst. Res. Technol.* **43** 1278
- [12] Resel R *et al* 2006 *Surf. Sci.* **600** 4645
- [13] Bohr J, Feidenhansl R, Nielsen M, Toney M, Johnson R L and Robinson I K 1985 *Phys. Rev. Lett.* **54** 1275
- [14] Robinson I K 1983 *Phys. Rev. Lett.* **50** 1145
- [15] Feidenhansl R 1989 *Surf. Sci. Rep.* **10** 105
- [16] Renaud G, Villette B, Vilfan I and Bourret A 1994 *Phys. Rev. Lett.* **73** 1825
- [17] Williams A A, Thornton J M C, MacDonald J E, Vanshilfhout R G, Vanderwee J F, Finney M S, Johnson A D and Norris C 1991 *Phys. Rev. B* **43** 5001
- [18] Norris C 1993 *Phil. Trans. R. Soc. A* **344** 1673
- [19] Fuoss P H, Kisker D W, Renaud G, Tokuda K L, Brennan S and Kahn J L 1989 *Phys. Rev. Lett.* **63** 2389
- [20] Jenichen B *et al* 2003 *Rev. Sci. Instrum.* **74** 1267
- [21] Takahasi M, Yoneda Y, Inoue H, Yamamoto N and Mizuki J 2002 *Japan. J. Appl. Phys.* **41** 6247
- [22] Fuoss P H, Kisker D W, Stephenson G B and Brennan S 1995 *Mater. Sci. Eng. B* **30** 99
- [23] Richard M I, Highland M J, Fister T T, Munkholm A, Mei J, Streiffer S K, Thompson C I, Fuoss P H and Stephenson G B 2010 *Appl. Phys. Lett.* **96** 051911
- [24] Cowley J M 1975 *Diffraction Physics* (Amsterdam: North-Holland)
- [25] Rauscher M, Paniago R, Metzger H, Kovats Z, Domke H D, Pfannes J, Schulze J and Eisele I 1999 *J. Appl. Phys.* **86** 6763
- [26] Kegel I, Metzger T-H, Lorke A, Peisl J, Stangl J, Bauer G, Garcia J M and Petroff P 2000 *Phys. Rev. Lett.* **85** 1694
- [27] Lazzari R 2002 *J. Appl. Cryst.* **35** 406
- [28] Richard M I, Favre-Nicolin V, Renaud G, Schüllli T U, Priestler C, Zhong Z and Metzger T H 2009 *Appl. Phys. Lett.* **94** 013112
- [29] Stranski I N and Krastanow L 1938 *Sitzber. Akad. Wiss. Wien, Math.-Nat.wiss. Kl.*, 2B **146** 747
- [30] Renaud G *et al* 2003 *Science* **300** 1416
- [31] Bloch J M 1985 *J. Appl. Cryst.* **18** 33
- [32] Teichert C 2002 *Phys. Rep.* **365** 335
- [33] Ignatiev A, Jona F, Debe M, Johnson D E, White S J and Woodruff D P 1977 *J. Phys. C: Solid State Phys.* **10** 1109
- [34] Ueda K, Kinoshita K and Mannami M 1984 *Surf. Sci.* **145** 261
- [35] Mark Peter, Levine J D and McFarlane S H 1977 *Phys. Rev. Lett.* **38** 1408
- [36] White S J and Woodruff D P 1977 *Surf. Sci.* **64** 131
- [37] Felici R, Robinson I K, Ottaviani C, Imperatori P, Eng P and Perfetti P 1997 *Surf. Sci.* **375** 55
- [38] Robinson I K 1992 *Rep. Prog. Phys.* **55** 599
- [39] Renaud G 1998 *Surf. Sci. Rep.* **32** 1
- [40] Miki K, Sakamoto K and Sakamoto T 1998 *Surf. Sci.* **406** 312
- [41] Shiraki Y and Ishiwara A 1986 *J. Electrochem. Soc.* **133** 666
- [42] Eastman D E 1980 *J. Vac. Sci. Technol.* **17** 492
- [43] Takahasi T, Nakatani S, Okamoto N, Ishikawa T and Kikuta S 1989 *Rev. Sci. Instrum.* **60** 2365
- [44] Braun W, Jenichen B, Kaganer V M, Shtukenberg A G, Däweritz L and Ploog K H 2003 *Surf. Sci.* **525** 126
- [45] Kaganer V M, Braun W, Jenichen B, Däweritz L and Ploog K H 2003 *Phys. Rev. Lett.* **90** 016101
- [46] Chen X, Wu F, Zhang Z Y and Lagally M G 1994 *Phys. Rev. Lett.* **73** 850
- [47] Zhou T, Revenant C, Issartel J, Renaud G and Schüllli T U 2011 In-depth atomic structure and composition of the 2×N reconstruction of the 1 to 3 monolayer Ge wetting layer on Si(001) by surface x-ray diffraction *Phys. Rev. B* at press
- [48] Eaglesham D J and Cerullo M 1990 *Phys. Rev. Lett.* **64** 1943
- [49] Takahasi M, Kaizu T and Mizuki J 2006 *Appl. Phys. Lett.* **88** 101917
- [50] Medeiros-Ribeiro G, Bratkovski A M, Kamins T I, Ohlberg D A A and Williams R S 1998 *Science* **279** 353
- [51] Mo Y-W, Savage D E, Schwartzentruber B S and Lagally M G 1990 *Phys. Rev. Lett.* **65** 1020
- [52] Renaud G 2009 *Surf. Sci. Rep.* **64** 255
- [53] Rastelli A and von Känel H 2002 *Surf. Sci.* **515** L493
- [54] Richard M I, Schüllli T U, Renaud G, Wintersberger E, Chen G, Bauer G and Holy V 2009 *Phys. Rev. B* **80** 045313
- [55] Schüllli T U, Richard M I, Renaud G, Favre-Nicolin V, Wintersberger E and Bauer G 2006 *Appl. Phys. Lett.* **89** 143114
- [56] Schmidt O G, Denker U and Stoffel M 2003 *Phys. Rev. Lett.* **90** 196102
- [57] Rastelli A, Stoffel M, Merdzhanova T and Schmidt O G 2008 *J. Phys. Condens. Matter* **20** 454214
- [58] Ratto F *et al* 2004 *Appl. Phys. Lett.* **84** 4526
- [59] Hesse A, Stangl J, Holy V, Roch T, Bauer G, Schmidt O G, Denker U and Struth B 2002 *Phys. Rev. B* **66** 085321
- [60] Schüllli T U *et al* 2005 *Phys. Rev. B* **71** 035326
- [61] Magalhaes-Paniago R, Medeiros-Ribeiro G, Malachias A, Kycia S, Kamins T I and Williams R S 2002 *Phys. Rev. B* **66** 245312
- [62] Schüllli T U, Stangl J, Zhong Z, Lechner R T, Sztucki M, Metzger T H and Bauer G 2003 *Phys. Rev. Lett.* **90** 066105
- [63] Coraux J, Renevier H, Favre-Nicolin V, Renaud G and Daudin B 2006 *Appl. Phys. Lett.* **88** 153125
- [64] Liao X Z, Zou J, Cockayne D J H, Wan J, Jiang Z M, Jin G and Wang K L 2001 *Appl. Phys. Lett.* **79** 1258
- [65] Dismukes J P, Ekstrom L and Paff R J 1964 *J. Phys. Chem.* **68** 3021
- [66] De Salvador D *et al* 2001 *Phys. Rev. B* **63** 045314
- [67] Metzger T H, Schüllli T U and Schmidbauer M 2005 *C. R. Phys.* **6** 47
- [68] Schüllli T U *et al* 2009 *Phys. Rev. Lett.* **102** 025502
- [69] Richard M I, Metzger T H, Holy V and Nordlund K 2007 *Phys. Rev. Lett.* **99** 225504
- [70] Landre O, Camacho D, Bougerol C, Niquet Y M, Favre-Nicolin V, Renaud G, Renevier H and Daudin B 2009 *Phys. Rev. B* **80** 045313

2.2 The 2xN reconstruction on the Ge wettinglayer

As a first stage of growth of Ge on Si(001) the formation of a ultra thin Ge film is observed. This film is generally referred to as the wettinglayer. In this film, the Ge lattice is expanded to coherently match the lattice of the Si host crystal. Although highly strained, this film remains stable. Beyond a critical thickness proper to the system Ge on Si(001), it becomes energetically more favorable to increase the surface of the system and allow for the growth of islands on top of this wettinglayer in order to partially relax the elastic energy. It has been observed however that even prior to island growth, a modification of the last atomic layer on this wettinglayer modifies its structure as a function of deposited thickness in order to optimize the strain accommodation. Details on the periodic structure of this reconstruction have been reported in microscopy studies, but the studies presented here result in a full 3D resolution of this reconstructed surface. The atoms on top of a Si(001) surface arrange in dimers to reduce the number of dangling bonds. This changes the local symmetry and doubles the periodic repetition length of the atomic structure of the surface along one $[110]$ direction, whereas in the perpendicular $[1\bar{1}0]$ direction the periodicity remains the same as in the bulk. This surface structure is called the Si(001) 2x1 reconstruction.

In the case of a Ge wettinglayer deposited on Si(001), the atoms of the topmost atomic layer arrange in a way to limit the dangling bonds and to reduce the elastic strain. This leads to a periodic arrangement of missing dimers to optimize strain reduction, leaving entire dimer vacancy lines on the surface. In that way, if every N_{th} dimer line is missing, a new periodicity is formed called the 2XN reconstruction. It is found that N depends on the deposited Ge thickness and that the resulting strain relaxation extends up to several atomic layers into the crystal. The following work investigates in detail the structure of this 2xN reconstruction and analyzes the deformation and the chemical composition of the Ge wettinglayer. The presented experiments have been carried out on beamlines BM32 and ID03 at the ESRF.

- 2.2.1** *In-depth atomic structure and composition of the 2 times N reconstruction of the initial growth stages of the Ge wetting layer on Si(001) by surface x-ray diffraction*
T. Zhou, G. Renaud, J. Issartel, C. Revenant, T. U. Schüllli, R. Felici, A. Malachias
Phys. Rev. B 83, 195426 (2011).

PHYSICAL REVIEW B **83**, 195426 (2011)

Atomic structure and composition of the $2 \times N$ reconstruction of the Ge wetting layer on Si(001) investigated by surface x-ray diffraction

T. Zhou,¹ G. Renaud,¹ C. Revenant,¹ J. Issartel,¹ T. U. Schüllli,¹ R. Felici,² and A. Malachias²¹CEA, Institut Nanosciences et Cryogénie, SP2M, NRS, F-38054 Grenoble, France²ESRF, Boite Postale 220, F-38043 Grenoble, France

(Received 21 May 2010; revised manuscript received 7 March 2011; published 17 May 2011)

The $2 \times N$ reconstruction of the Ge/Si(001) wetting layer has been investigated by surface x-ray diffraction. At a substrate temperature of 670 °C, the average N periodicity decreases from $N = 11.5$ to 8 with an increasing Ge coverage from one to three monolayers (ML). The top layer consists of asymmetric dimers with a bond length in the range of 2.50–2.60 Å and a buckling angle in the range of 9.4°–15.6°, depending on the Ge coverage. The obtained dimer bond lengths are similar to those calculated for alternating asymmetric mixed dimers. Intermixing of Ge with Si is found down to the sixth (eighth) layer for 2 (from 3 to 5) ML coverage. For 2 ML coverage, a quantitative surface x-ray diffraction data set has been measured. It is analyzed using a model describing the atomic structure and Ge occupation probability with a limited set of parameters to bypass the intrinsic lack of appreciable reflections of the $2 \times N$ ($N = 9$) reconstruction. The Ge occupation probability varies periodically along the N direction, having its minimum value below the dimer vacancy lines. In addition, a more direct calculation of the Lorentz and detector acceptance corrections is given for rocking and radial scans.

DOI: 10.1103/PhysRevB.83.195426

PACS number(s): 68.35.B-, 68.47.Fg, 61.05.cp

I. INTRODUCTION

Ge islands on Si(001) have been studied extensively because of their novel electronic and optical properties related to quantum confinement.¹ Apart from its relevance to applications, the heteroepitaxy of Ge on Si has become a prototype system for the investigation of the Stranski-Krastanow growth mode. Because of an identical crystal structure and atomic bonding but a 4.2% mismatch in lattice parameter, Ge first forms a wetting layer (WL) before islands start to nucleate for Ge deposits larger than four monolayers (ML). Island structure, nucleation,² ripening,³ facet evolution,^{4,5} and alloying⁶ have been studied intensively, and many of the underlying mechanisms are now reasonably understood. However, less attention has been paid to the structure and composition of the WL, despite the fact that they are intimately linked to the growth of the Ge islands. The process of island nucleation on the WL cannot just be described by the capture of newly deposited Ge atoms, since it also involves a diffusive interaction with the WL.⁷ At growth temperatures around 600 °C, a substantial amount of material is transferred from the WL to the islands during the initial stages of their formation.⁸ Thus, a quantitative determination of the WL structure and composition is essential for a better understanding of island formation and intermixing.

The top layer of the Ge WL on Si(001) is composed of dimers, as are the clean, 2×1 reconstructed Si(001) and Ge(001) surfaces. The structure and symmetry of these dimers have been the object of quite a few studies. X-ray standing waves⁹ and high-resolution photoemission spectroscopy concluded to the dimer asymmetry, i.e., dimers with two atoms at different heights. Moreover, mixed Si-Ge asymmetric dimers were found at the beginning of the growth; Ge occupying the up site and Si the down site.¹⁰ A first-principles molecular cluster total-energy and atomic-force calculation confirmed that asymmetric dimers are energetically more stable than symmetric ones, thanks to a charge transfer from down to

up dimer atoms.¹¹ Photoelectron diffraction studies further suggested that the buckling angle of a mixed dimer is significantly larger than that of a pure Si dimer.¹² A theoretical study confirmed that buckling of Si-Ge dimers is energetically favorable, Si (Ge) occupying the down (up) site. The higher buckling angle for these dimers is also confirmed by theory.¹³ It was also shown that, as in the cases of 2×1 reconstructed Si and Ge (001) surfaces, the uppermost Ge layer can be composed of alternating asymmetric dimer structures, where in-phase or out-of-phase buckling of adjacent dimer rows leads to $p(2 \times 2)$ or $c(4 \times 2)$ reconstructions, respectively.¹⁴ Theoretical calculations further predicted that alternating asymmetric dimers correspond to the most stable structure for Ge/Si(001).¹⁵ A room-temperature (RT) scanning tunneling microscopy (STM) study of the Ge(001) surface showed that, within a single substrate dimer row, neighboring dimers buckle in opposite directions.¹⁶ Atom-tracking STM showed that mixed dimers are highly buckled and appear to “rock” between two configuration states with 180° rotational symmetry.^{17,18}

The lattice mismatch is partially accommodated in the WL by removing every N th line of dimers: the WL is characterized by a $(2 \times N)$ reconstruction¹⁹ consisting of a periodic arrangement of dimer vacancy lines (DVLs) of the (2×1) dimer reconstruction. The value of N results from a balance between the energy gain from strain relief and the energy cost of forming dimer vacancies. N varies with the WL thickness, and depends on the Si-Ge intermixing, which is another mechanism for strain relief. Intermixing in the WL was confirmed by several experimental means: X-ray photoelectron diffraction and Auger electron diffraction,²⁰ transmission electron microscopy, Raman spectroscopy and photoluminescence,²¹ and high-resolution Rutherford backscattering spectroscopy.²² For example, this last study yielded Ge concentrations in the first four layers to be 64.5%, 38%, 22.5%, and 11% for 1.5 ML of Ge deposited at 500 °C. Besides these experiments, intermixing was also studied theoretically. A Monte Carlo (MC) simulation showed that, for 1 ML coverage, entropy

T. ZHOU *et al.*PHYSICAL REVIEW B **83**, 195426 (2011)

counteracts the wetting nature of Ge and mixes the two top layers. As an example, at a deposition temperature of 677 °C and 1.2 ML coverage (with enough Ge to completely coat the surface), 14% of the surface atoms were found to be Si.²³ In the same study, the occupation probabilities of Ge in the first four layers were calculated as a function of Ge coverage. For 2 ML, the Ge concentration of the second layer was found to be only 1/3 at 600 °C. Another MC simulation concluded to a site selectivity of intermixing, mainly induced by the dimer rows and DVLs.²⁴ The DVLs induce atomic displacements in their vicinity, corresponding to a local compressive strain. Hence, the surrounding of the DVLs is unfavorable for larger atoms, and in this case, Ge.²⁴

When the Ge coverage exceeds the value corresponding to the minimal equilibrium dimer vacancy separation, the stress cannot be further relieved by additional dimer vacancies. The additional stress relaxation is achieved by forming dimer-row vacancies (DRVs) every M dimer rows. The resulting structure is called a patched structure or $M \times N$ reconstruction.^{25,26} Because DRVs are less efficient than the DVLs in relieving the strain, M decreases faster than N with increasing coverage. The state of the art of the Ge/Si(001) WL reveals a fragmented knowledge of the Ge/Si(001) $2 \times N$ (and $M \times N$) reconstruction. To the best of our knowledge, no precise experimental determination of the WL structure exists, nor does that of the in-depth displacements and composition below the surface. The present study aims at determining the structure and composition of the $2 \times N$ reconstruction, with special attention to the dimer configuration and the predicted site selectivity.

The $2 \times N$ reconstruction has been investigated by surface x-ray diffraction (SXRD),²⁷ which is a powerful technique to determine the atomic positions, as well as the intermixing, at a surface and within a few layers below, with high sensitivity during growth at a chosen substrate temperature, in an ultrahigh-vacuum (UHV) environment. The SXRD experimental setups are described in Sec. II. The value of the deposition temperature (670 °C) was chosen to favor a possible atomic order in the WL. As a matter of fact, zones of atomic order were claimed to exist in Ge/Si(001) domes grown in this temperature range.²⁸ In Sec. III, general characteristics of the reconstruction are presented, such as the size of the reconstructed domains and terraces, the N periodicity, and intermixing. Then, the 2×1 reconstruction of 1, 2, and 3 ML coverage is studied, followed by the $2 \times N$ reconstruction at 2 ML coverage. In Sec. IV, the discussion deals with the configuration of the buckling dimers, the N periodicity, the atomic displacements, intermixing, and the site selectivity of Si and Ge. Finally, the Appendix presents calculations of specific corrections (Lorentz, detector acceptance) that are mandatory to correctly evaluate the integrated intensities of the $\times N$ diffraction rods.

II. SXRD EXPERIMENTS

The experiments were carried out at two surface diffraction beamlines at the European Synchrotron Radiation Facility (ESRF). The first measurements, in which only the $\times 2$ diffraction rods were measured, were performed at the BM32²⁹ bending magnet beamline for 0, 1, 2, and 3 ML Ge deposits at

670 °C. The $\times N$ reconstruction data were recorded in a second run at the ID03³⁰ undulator beamline, for 2 ML Ge coverage at 670 °C. Both beamlines are equipped with a z -axis type diffractometer, holding a heavy-duty UHV chamber equipped with beryllium windows to let the x-ray beam enter and exit the chamber. In both cases, the x-ray energy was set to 11 keV and the openings of the detector slit (located 570 mm from the sample center) were set to 2 mm in both directions, parallel and perpendicular to the sample surface. A standard scintillation detector was used. The incident angle was equal to the critical angle (0.163°) for total external reflection of Si at this energy. At BM32, the doubly focused incident x-ray beam size was $0.3 \times 0.3 \text{ mm}^2$ ($H \times V$); it had a divergence of $1 \times 0.1 \text{ mrad}^2$ ($H \times V$). At ID03, the beam was doubly focused to a size of $0.05 \times 0.1 \text{ mm}^2$ ($H \times V$), with a divergence of $0.1 \times 0.01 \text{ mrad}^2$ ($H \times V$).

In both cases, the base vacuum was below 1×10^{-10} mbar. The Si(001) surface was deoxidized by heating up to 930 °C for 30 min under a very low flux ($<0.1 \text{ \AA}/\text{min}$) of silicon, resulting in a nice, carbide-free, Si(001)-(2×1) reconstruction as checked by reflection high-energy electron diffraction (RHEED) (at BM32) and grazing incidence x-ray diffraction.

Ge was deposited by molecular beam epitaxy using a Knudsen cell (fluxes of $0.5 \text{ \AA}/\text{min}$ on BM32 and $0.4 \text{ \AA}/\text{min}$ on ID03) monolayer (1.412 Å) after monolayer at 670 °C. The sample growth temperature was measured with a calibrated pyrometer. The measurements were performed at RT.

Since the $\times 2$ reconstruction rods were narrow enough to be integrated along the slit directions, they were measured by rocking scans of the sample around its surface normal, then integrated before standard monitor, area, polarization, and Lorentz corrections were applied.^{31,32} Because the $\times N$ rods were too large to be fully integrated by the detector slits, they were all measured through two perpendicular scans: radial and rocking. Specific Lorentz and detector acceptance corrections had to be calculated, as shown in the Appendix. Radial and rocking measurements yielded very close structure factor amplitudes after corrections, thus validating the calculations and measurements (cf. the Appendix).

A real-space lattice is chosen with respect to the conventional fcc lattice. The surface lattice vectors \mathbf{a}_s (x direction) and \mathbf{b}_s (y direction) are parallel to the direction of the dimer ($[1\bar{1}0]$ direction) and of the dimer rows ($[110]$ direction), respectively (Fig. 1).

The basis vectors of the unreconstructed (1×1) surface unit cell are

$$\mathbf{a}_s = \begin{bmatrix} 1 & \bar{1} \\ 2 & 2 \end{bmatrix} 0, \quad \mathbf{b}_s = \begin{bmatrix} 1 & 1 \\ 2 & 2 \end{bmatrix} 0, \quad \mathbf{c}_s = [001], \quad (1)$$

with lengths $|\mathbf{a}_s| = \frac{1}{\sqrt{2}}a_0$, $|\mathbf{b}_s| = \frac{1}{\sqrt{2}}a_0$, $|\mathbf{c}_s| = a_0$,

where a_0 is the silicon bulk lattice constant (0.5431 nm).

For the surface unit cell of the 2×1 reconstruction, \mathbf{a}_s is replaced by $\mathbf{a}_s^{2 \times 1} = 2 \times \mathbf{a}_s$. For the $2 \times N$ reconstruction,

$$\mathbf{a}_s^{2 \times N} = 2 \times \mathbf{a}_s, \quad \mathbf{b}_s^{2 \times N} = N \times \mathbf{b}_s, \quad \mathbf{c}_s^{2 \times N} = \mathbf{c}_s, \quad (2)$$

with $|\mathbf{a}_s^{2 \times N}| = \sqrt{2}a_0$, $|\mathbf{b}_s^{2 \times N}| = \frac{N}{\sqrt{2}}a_0$, $|\mathbf{c}_s^{2 \times N}| = a_0$.

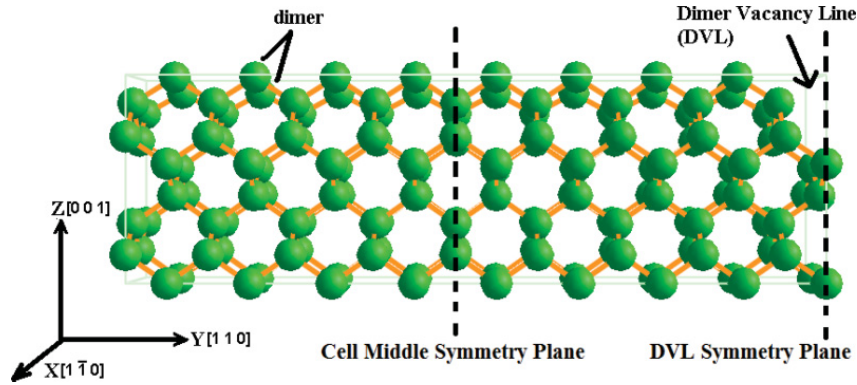


FIG. 1. (Color online) 2×9 reconstruction cell for 2 ML Ge/Si(001). There are two symmetry planes parallel to the (xz) plane, the cell middle symmetry plane, and the DVL symmetry plane.

For example, a 2×9 reconstruction has a surface lattice cell of dimensions $7.681 \times 34.563 \text{ \AA}^2$. Unless otherwise specified (index “ b ” when the bulk fcc unit cell is used), the (h,k) reciprocal space units are given in reduced lattice units of the (1×1) or (2×1) surface unit cell.

III. RESULTS

A. General characteristics of the reconstruction

First, the average sizes of terraces and reconstructed domains are evaluated. The reconstruction rods and crystal truncation rods (CTRs) give access to the average size D of the reconstructed domains and terraces, respectively, according to

$$D = \frac{2\pi}{\Delta Q_t} \text{ with } \Delta Q_t = Q_{\parallel} \cdot \Delta\omega, \quad (3)$$

where Q_{\parallel} is the in-plane component of the momentum transfer and $\Delta\omega$ is the angular full width at half maximum (FWHM) of the peak situated at \mathbf{Q} in reciprocal space measured with

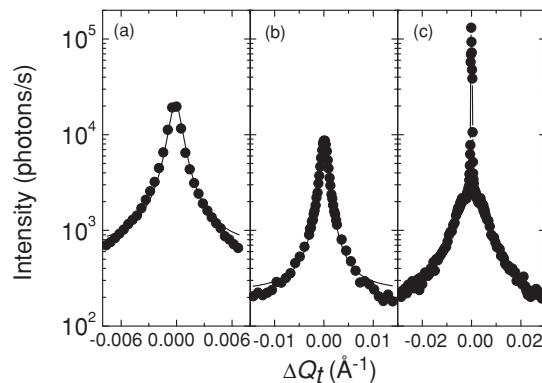


FIG. 2. Some rocking scans of the Si(001)- (2×1) reconstruction (a) $(0.5,0.5,0)_b$, (b) $(1.5,1.5,0)_b$, and (c) $(1 1 0)_b$, in which a CTR is also present. The lines are Lorentzian fits through the experimental data.

an in-plane rocking scan.³³ The FWHM of the rocking scans [Figs. 2(a) and 2(b)] of the 2×1 reconstruction rods of the clean Si(001) surface are $\sim 1.64 \times 10^{-3} \text{ \AA}^{-1}$, which yields an average size of the reconstruction domains of $\sim 0.38 \mu\text{m}$. The $(110)_b$ peak in Fig. 2(c) is the superposition of a 2×1 reconstruction rod and a more intense CTR, whose FWHM ($4.28 \times 10^{-4} \text{ \AA}^{-1}$) yields an average terrace size of $\sim 1.5 \mu\text{m}$. Hence, a terrace includes approximately four 2×1 reconstructed domains on average. For comparison, the coherence length of the x-ray beam is determined to be $\sim 3.6 \mu\text{m}$ at BM32 (from the FWHM of the Si Bragg peak).

Figure 3 shows h scans along the $(hh0)_b$ direction for clean Si and for increasing Ge coverage. Due to the crystal symmetry of the diamond lattice, the unit cell is rotated by 90° on two adjacent terraces separated by a monatomic step. Hence, peaks

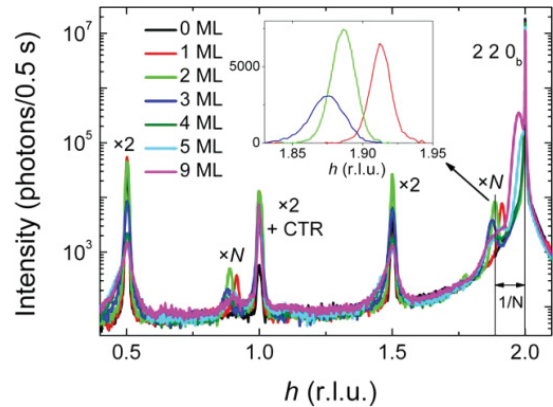


FIG. 3. (Color online) Measured intensity (logarithmic units) at BM32 during radial scans along the $(hh0)_b$ direction for clean Si- (2×1) and for increasing Ge coverage. The separation between the $(220)_b$ peak and its closest $\times N$ reconstruction peak, for example, is equal to $1/N$. The $\times N$ reconstruction peaks are much wider and less intense than those of the $\times 2$ reconstruction. Inset: background-subtracted $\times N$ rods for 1 (right), 2 (middle), and 3 (left) ML coverage.

T. ZHOU *et al.*PHYSICAL REVIEW B **83**, 195426 (2011)

from the $\times 2$ and $\times N$ reconstructions can be found on the same h scans. The Si surface is characterized by the $(220)_b$ Bragg peak and $\times 2$ reconstruction peaks: $(0.5, 0.5, 0)_b$, $(110)_b$, $(1.5, 1.5, 0)_b$, and $(220)_b$. As soon as the first ML is deposited, a satellite peak of the $(110)_b$ [$(220)_b$] peak appears. This satellite is characteristic of the periodic DVLS with a separation from the main peak inversely proportional to N and is present up to a coverage of at least 9 ML. With an increasing coverage up to 4 ML, this satellite shifts farther away from the $(110)_b$ [$(220)_b$] peak, revealing a decrease of the N periodicity from 11.5 for 1 ML to 9 for 2 ML and to 8 for 3 ML. This satellite (displayed at h slightly smaller than 2 in the inset of Fig. 3) is symmetric and becomes wider with increasing Ge coverage. Its Δh FWHM of 0.016 ± 0.001 for 1 ML, 0.020 ± 0.001 for 2 ML, and 0.029 ± 0.001 for 3 ML yields the size $D = (a_0/\sqrt{2})/\Delta h$ of the $\times N$ reconstructed domain in the in-plane $(hh0)_b$ direction. The D size is $240 \pm 15 \text{ \AA}$ for 1 ML, $192 \pm 10 \text{ \AA}$ for 2 ML, and $132 \pm 5 \text{ \AA}$ for 3 ML. Hence, the domains of the $\times N$ reconstruction are small and become even smaller with increasing Ge coverage. Above 5 ML coverage, the satellite peaks broaden due to an additional contribution from the $\times M$ periodicity. In addition, a shoulder appears on the left side of the Bragg peak, corresponding to the formation of strained islands in the very early stages of the nucleation. At 9 ML coverage, the shoulder moves toward smaller h , indicating a strain relief in larger islands. Remarkably, the $(M \times N)$ reconstruction still exists during the island growth, implying that the WL is still reconstructed in between islands. However, the reconstruction is not as well ordered above 4 ML, once 3D islands have nucleated.

Figure 4 shows h scans along the $(h, h, 0.5)_b$ direction, i.e., with a nonzero out-of-plane momentum transfer ($Q_z = 2\pi \ell/c_s$, $\ell = 0.5$) for clean Si and for increasing Ge coverage. This scan is more sensitive to the reconstruction peaks than the in-plane scan thanks to a much lower thermal diffuse scattering background. At 4 ML coverage, the $\times N$ reconstruction peak is less intense and wider than those for smaller Ge deposition. This confirms the presence of a substantial amount of disorder in the $\times N$ reconstruction once islands are formed on the WL.

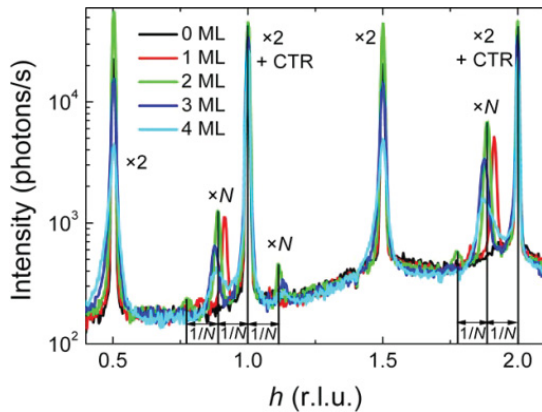


FIG. 4. (Color online) Measured intensity (logarithmic units) at BM32 during radial scans along the $(h, h, 0.5)_b$ direction for clean Si and for increasing Ge coverage.

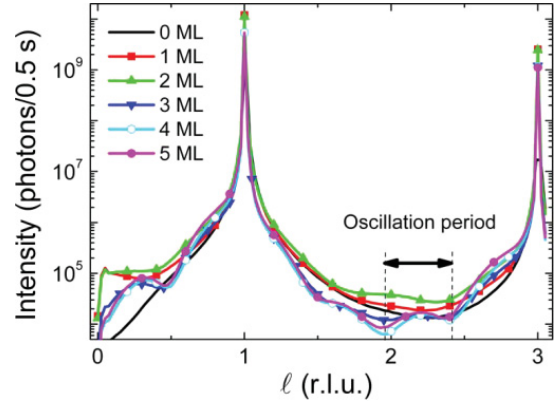


FIG. 5. (Color online) Measured intensity on BM32 (logarithmic units, uncorrected, and not integrated) during a scan along the $(11\ell)_b$ direction for clean Si and increasing Ge coverage.

Figure 5 shows ℓ scans along the $(11\ell)_b$ direction from 0 to 5 Ge ML coverage. The oscillation period observed on the CTR can be used for a rough estimate of the reconstruction depth.²⁷ For 2 ML coverage, the reconstruction depth is approximately six layers. From 3 to 5 ML coverage, the oscillation period decreases and the reconstruction depth increases to approximately eight layers. No clear oscillations are visible for 1 ML coverage, implying that the reconstruction does not affect the substrate in depth.

In short, the transitions $2 \times 1 \rightarrow 2 \times N$ ($N \sim 11.5-8$) $\rightarrow 2 \times 8 + M \times N$ ($M \leq 11$) + islands have been identified from 0 to 9 ML coverage. The $\times N$ reconstruction domains are found to be much smaller than those of the $\times 2$ reconstruction.

B. 2×1 reconstruction of 1, 2, and 3 ML Ge/Si(001)

1. Model presentation

The aim of this section is to determine the structure and the composition of the 1, 2, and 3 ML Ge/Si(001) WL. In a first step, only the data collected at BM32 are used, and the dimer vacancy lines (the $\times N$ reconstruction) are neglected. Because only the $\times 2$ data are analyzed, the positions and compositions along the y direction are in fact averaged. A surface structure model is refined on the SXRD data. The model has eight layers, which corresponds to the maximum of the reconstruction depth (see Sec. III A). Each layer consists of two atoms that can be displaced along the $[1\bar{1}0]$ and $[001]$ directions. Thus, a complete model comprises 32 displacements. To limit the number of parameters, the model is reduced to only 20 displacements as shown in Fig. 6, similar to the disordered model of Torrelles *et al.*³⁴ The horizontal atomic displacements in layers (3), (4), (7), and (8) are assumed to be zero, and, in the fifth and sixth layers, the horizontal displacements, as well as the vertical ones, are assumed to be equal within each layer. A vertical symmetry axis is assumed from the third to the eighth layer. The Debye-Waller (DW) factor of the dimer layer is taken anisotropic, i.e., split into in-plane and out-of-plane parameters. The other DW factors are taken isotropic. For the clean Si surface, five independent DW parameters are used

ATOMIC STRUCTURE AND COMPOSITION OF THE ...

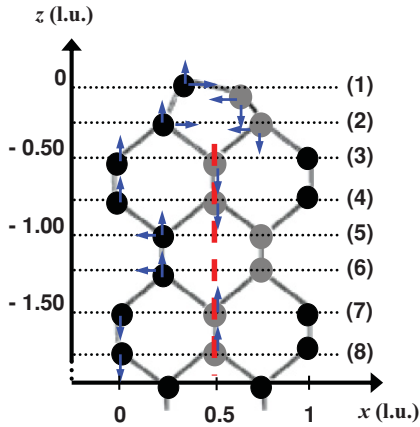


FIG. 6. (Color online) Schematic representation of the atomic positions in the top eight layers. The arrows indicate the displacements of the atoms from their bulk positions (not to scale). The dashed line represents the vertical symmetry axis. In each atomic layer, the black (gray) atom is identified by b (g) in Table I.

to account for the different vibration amplitudes of the dimer layer and the layers below. For the Ge/Si(001) WL, the DW parameters are fixed. For the dimer layer, they are taken equal to those obtained by Torrelles *et al.*³⁴ for a pure Ge surface, while for the next sublayers, they are fixed to those obtained from the fit of the clean Si(001)-(2 × 1) surface. This simplified model will be validated *a posteriori*.

Because different terraces separated by monatomic steps are present with a 90° rotation of the dimers, two surface structures with equal probability are introduced, namely the above-described one as well as a second one deduced from the first by a 90° rotation plus a $c_s/4$ shift along z [cf. Fig. 7(a)]. As the coherence length of the x-ray beam is close to the terrace size, the waves scattered by up and down terraces are considered to add incoherently.

In addition, the other orientation of the dimer tilt is taken into account by duplicating the above procedures and applying an additional 180° rotation [cf. Fig. 7(b)]. As STM studies showed couplings of Si(001) dimers within a row and also between rows,³⁵ similar dimer couplings probably exist also for the Ge/Si(001) WL. Hence, the structure factors corresponding to both tilts in the same terrace are added coherently. Each tilt orientation has 1/2 probability.

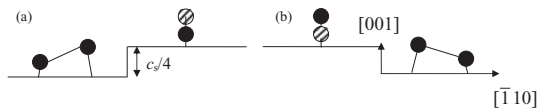


FIG. 7. Schematic representation of the dimer orientation. Up and down adjacent terraces are shifted by $c_s/4$ in the direction normal to the surface. They are equally occupied and are supposed to scatter incoherently. The hatched atoms are at the back. The dimers in (b) correspond to those in (a) rotated by 180°.

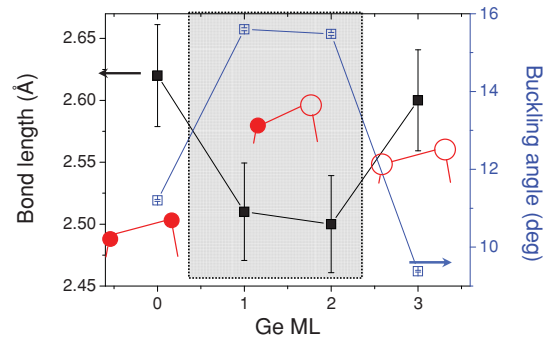
PHYSICAL REVIEW B **83**, 195426 (2011)

FIG. 8. (Color online) Dimer bond length (filled squares) and buckling angle (open squares) as a function of the Ge coverage. The dimers are represented in three different regimes. The small filled (large open) circles represent the Si (Ge) atoms. The differences in bond lengths and buckling angles are schematic.

2. Best-fit results

For each deposition, i.e., Si(001) and 1, 2, and 3 ML Ge/Si(001), six reconstruction rods and six CTRs were measured at BM32 up to an out-of-plane momentum transfer of 3.47 \AA^{-1} ($\ell = 3$) with a step size of 0.1 \AA^{-1} , totaling 312 independent structure factors. The structure refinement was performed with an adapted version of the ROD software for surface x-ray crystallography,³⁶ with a χ^2 minimization using the Levenberg-Marquardt method.³⁷

The fit of the well-known Si(001)-(2 × 1) reconstruction is first discussed to validate the model. There are in all 27 free parameters (20 displacements, 5 DW parameters, a scale factor, and a fraction of crystal that is covered by the surface layer). This yields a reasonable factor of approximately 11 points per parameter. The best fit leads to $\chi^2 = 1.05$. The corresponding displacement values (listed in Table I) are in good agreement with reported SXRD results on Si(001).^{38,39} The bond length and the buckling angle of the dimers are deduced from these displacements (cf. Fig. 8).

The results obtained for the Si(001) surface are satisfactory (as will be shown below) and will serve as the starting point for studying the Ge/Si(001) WL, beginning with a study of its atomic structure along the $\times 2$ (dimer) direction (i.e., averaging over the $\times N$ reconstruction direction).

For the Ge/Si(001) WL, a Ge occupation probability is included in the first four layers for 1 ML and in the first eight layers for 2 and 3 ML. Hence, there are 26 (30) free parameters for 1 (2 and 3) ML (20 displacements, a scale factor, a fraction of covered crystal, and Ge occupation probabilities). This yields a reasonable factor of approximately 12 (10) structure factors per parameter for 1 (2 and 3) ML. The best fit leads to $\chi^2 = 1.3$ for 1 ML, 2.30 for 2 ML, and 2.05 for 3 ML. To illustrate the fit quality, the measured structure factors of reconstruction rods and CTRs are plotted for 1 and 3 ML coverage in Figs. 9(a) and 9(b). The displacements for the best-fit model are listed in Table I. For 1 ML coverage, the displacement values are close to those for clean Si. The Ge occupation probabilities are plotted in Fig. 10. To take into account the DVL, a $1-1/N$ correction is applied to the

T. ZHOU *et al.*PHYSICAL REVIEW B **83**, 195426 (2011)TABLE I. Displacement values in Ångströms for the best fit for clean Si-(2×1) (0 ML) and 1, 2, and 3 ML Ge/Si(001)-(2×1). The atomic layer number refers to Fig. 6. For each atomic layer, the atoms are identified by “*b*” (black color in Fig. 6) or “*g*” (gray color in Fig. 6).

Direction	Atomic layer number	Atoms	0 ML	1 ML	2 ML	3 ML
<i>x</i>	1	<i>b</i>	0.407 ± 0.015	0.530	0.492	0.315
		<i>g</i>	−0.860 ± 0.015	−0.891	−0.937	−0.960
	2	<i>b</i>	0.046 ± 0.023	0.123	0.046	0.092
		<i>g</i>	−0.177 ± 0.015	−0.092	−0.038	−0.077
	3	<i>b</i>	0	0	0	0
		<i>g</i>	0	0	0	0
	4	<i>b</i>	0	0	0	0
		<i>g</i>	0	0	0	0
	5	<i>b</i>	−0.046 ± 0.008	−0.046	−0.038	−0.038
		<i>g</i>	0.046 ± 0.008	0.046	0.038	0.038
	6	<i>b</i>	−0.031 ± 0.008	−0.046	−0.046	−0.023
		<i>g</i>	0.031 ± 0.008	0.046	0.046	0.023
	7	<i>b</i>	0	0	0	0
		<i>g</i>	0	0	0	0
	8	<i>b</i>	0	0	0	0
		<i>g</i>	0	0	0	0
<i>z</i>	1	<i>b</i>	0.081 ± 0.027	0.206	0.005	0.234
		<i>g</i>	−0.429 ± 0.038	−0.467	−0.663	−0.19
	2	<i>b</i>	0.163 ± 0.022	0.31	0.125	0.282
		<i>g</i>	−0.250 ± 0.027	−0.081	0.13	0.239
	3	<i>b</i>	0.054 ± 0.016	0.038	−0.038	0.147
		<i>g</i>	−0.076 ± 0.016	−0.103	−0.152	−0.011
	4	<i>b</i>	0.054 ± 0.011	0.125	0.071	0.168
		<i>g</i>	−0.092 ± 0.016	−0.076	−0.06	0.054
	5	<i>b</i>	−0.016 ± 0.011	−0.011	−0.027	0.049
		<i>g</i>	−0.016 ± 0.011	−0.011	−0.027	0.049
	6	<i>b</i>	0.005 ± 0.011	0.005	0.005	0.06
		<i>g</i>	0.005 ± 0.011	0.005	0.005	0.06
	7	<i>b</i>	−0.043 ± 0.011	−0.043	−0.065	−0.005
		<i>g</i>	0.005 ± 0.011	0.027	−0.038	0.054
	8	<i>b</i>	−0.005 ± 0.011	−0.022	−0.049	−0.011
		<i>g</i>	0.033 ± 0.011	0.022	−0.016	0.016

occupancy in the first layer. The Ge occupation probability is high (60%–80%) at the surface level and quickly decreases right from the second layer. For a 1 ML Ge deposit, the obtained values are similar to those deduced from a theoretical calculation at 600 °C.⁴⁰ The values of the dimer bond length and buckling angle are displayed in Fig. 8.

The complete model with 32 displacements was also tested, but no significant improvement was observed. Moreover, the additional displacements were found to be negligible, and the other displacements were basically unchanged. This validates the 20 displacement model and confirms the vertical symmetry axis at $x = 0.5$.

To conclude, a model of the atomic displacements and the Ge occupation probability of the WL is proposed for 1, 2, and 3 ML coverage. The dimer bond length and buckling angle were then deduced from the displacements. The use of BM32 was appropriate for measuring the ×2 reconstruction peaks.

C. 2 × *N* reconstruction of 2 ML Ge/Si(001)

1. Qualitative analysis and model presentation

Because of the inherent vacancy structure and long period of the ×*N* reconstruction, its diffraction rods are not only much weaker than those of the ×2 reconstruction, but most of them are negligible, i.e., below the background. This was confirmed by many line scans performed on both BM32 and ID03 beamlines. For instance, Fig. 11 compares a radial scan along the $(hh0)_b$ direction for 2 ML Ge coverage measured at BM32 and at ID03. On BM32, only the first-order ×*N* reconstruction rods on the left side of the CTRs (i.e., at $h = \text{integer} - 1/N$, $h = 0.89$ and 1.89 in this case) were visible above the background, while on ID03, some of the higher-order rods were also measurable (typically those at $h = \text{integer} - 2/N$, $\text{integer} + 1/N$, and sometimes $\text{integer} + 2/N$) thanks to the 20-fold gain in intensity.

ATOMIC STRUCTURE AND COMPOSITION OF THE ...

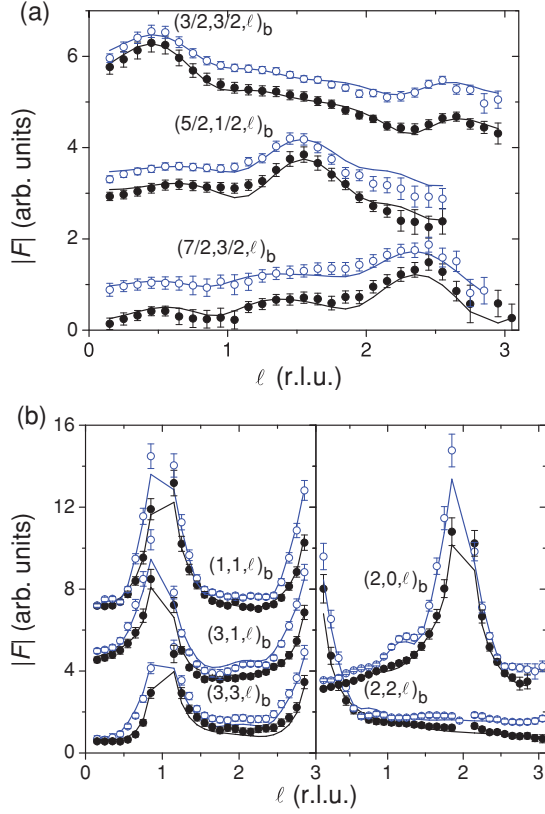
PHYSICAL REVIEW B **83**, 195426 (2011)

FIG. 9. (Color online) Measured structure factor moduli vs index ℓ of (a) reconstruction rods and (b) CTRs for 1 ML (filled black circle) and 3 ML (open blue circle) coverage. The continuous lines are the theoretical values.

Using ID03, all k lines at h constant (integer or half-integer) were performed to look for reflections. A total of 113 independent in-plane reconstruction reflections were experimentally confirmed to be below the background. The remaining visible reflections underwent a careful selection that reduced the total number of suitable reflections from 73 to 38 by keeping only the reflections that yielded reasonable and consistent FWHM from both radial and rocking scans. These 38 reflections were further reduced to 19 due to symmetry. In addition, a total number of 193 out-of-plane reflections were measured, which was reduced to 112 nonequivalent intensities corresponding to seven rods [(0.889, 0, ℓ), (0.889, 0.5, ℓ), (1.889, 0, ℓ), (1.889, 0.5, ℓ), (1.889, 1, ℓ), (1.889, 1.5, ℓ), and (2.889, 0.5, ℓ)] with a systematic error of 0.09. The rods were measured up to a maximum value $\ell = 2.30$.

The starting model to analyze the 2×9 reconstruction of the 2 ML Ge/Si(001) WL was the structure averaged over y deduced from the above-described analysis of the $\times 2$ reflections. The surface unit cell of the 2×9 reconstruction has two atoms in each plane along the x direction, nine along the y direction (eight for the surface layer), and six planes along the z direction due to intermixing. Hence, the total number of

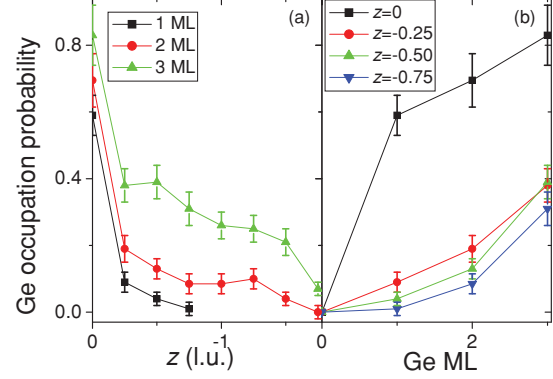


FIG. 10. (Color online) Ge occupation probability (a) for 1, 2, and 3 ML Ge/Si(001) as a function of z and (b) in each of the top four atomic layers ($z = 0, -0.25, -0.50, -0.75$) as a function of the Ge coverage.

atoms is 106. Each atom is defined by its position (xyz) and its Ge (or Si) occupation probability. Hence, a full description of this system calls for 424 parameters. As the number of available data was far from sufficient for a standard structure refinement, we resorted to a simpler model that is inspired by a MC simulation.²⁴ For 2 ML Ge on Si(001), the simulation showed that the evolution of the atomic displacements as a function of y is a smooth function and could be thus easily accounted for by a low-order polynomial. In our model, each displacement is described by a third-order polynomial as a function of y , multiplied by a decreasing exponential function as a function of z .

Taking into account the cell middle symmetry plane (cf. Fig. 1), the z displacement within each atomic layer is modeled by an even function with respect to this symmetry plane:

$$dz = [b_0 + b_2(y - \bar{y})^2]e^{b_4 \times z} + d_{z0}, \quad (4)$$

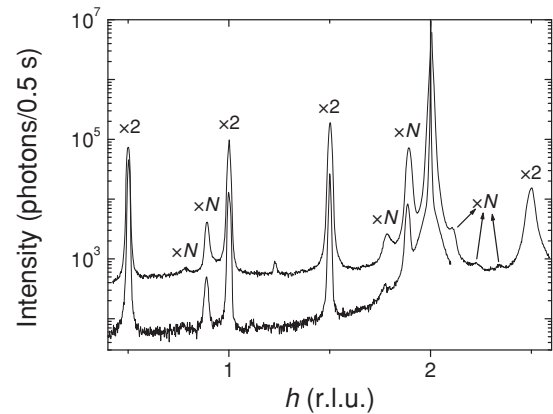


FIG. 11. Measured intensity (logarithmic units) during a radial scan along the $(hh0)_b$ direction for 2 ML Ge coverage measured at BM32 (bottom curve) and at ID03 (top curve).

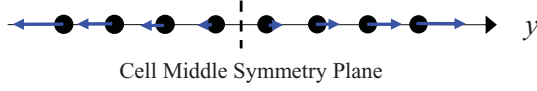
T. ZHOU *et al.*PHYSICAL REVIEW B **83**, 195426 (2011)

FIG. 12. (Color online) Schematic representation of the atoms in the first layer. The arrows indicate the y displacements.

where \bar{y} is the y position of the atom in the cell middle symmetry plane and d_{z0} is the displacement found for the 2×1 reconstruction. Fitting the z displacements thus requires three parameters.

Along the y axis, the MC simulation showed that the distance between neighboring dimers increases significantly near the DVL.²⁴ The closer the atoms are from the DVL, the larger is the absolute value of their displacement from their $\times 2$ reconstruction origin (cf. Fig. 12). The y displacement for atoms in a same layer is thus antisymmetric with respect to the cell middle symmetry plane and is modeled by an odd function. Similar to the precedent case (dz displacement), fitting the dy displacement requires three parameters:

$$dy = [c_1(y - \bar{y}) + c_3(y - \bar{y})^3]e^{c_4 \times z}. \quad (5)$$

Initially, a polynomial had been introduced also along the x axis, but all displacements happened to be very small and ill-defined. A qualitative study was thus undertaken with only two parameters (see below).

Taking into account the cell middle symmetry plane, the Si (Ge) θ_{occ} occupation probability was modeled by an even function with respect to this symmetry plane,

$$\theta_{\text{occ}} = d_0 + [d_2(y - \bar{y})^2]e^{d_4 \times z}. \quad (6)$$

Note that the d_0 parameter varies with the atomic layer. Fitting the occupancies thus requires eight additional parameters.

In all, 131 quantitatively measured structure factors (19 in-plane and 112 out-of-plane) were fitted with 17 parameters (three for z , three for y , two for x , eight for θ_{occ} , and an overall scale factor). This yields a rather reasonable factor of approximately eight reflections per parameter. However, a reduced set of parameters usually implies an increase in their correlations. These correlations were partially taken into account by calculating the error bars with the covariance matrix.³⁷ The best fit yields the z and y atomic displacement as a function of y and z .

2. Best-fit results

A total of ten parameters (three for y , six d_0 parameters for θ_{occ} , and an overall scale factor) were initially refined using the 19 in-plane structure factors. The θ_{occ} evolution was only obtained at the end along with other out-of-plane parameters, since it contributes relatively less to the overall structure factor. The corresponding error bars were evaluated following the same order. For the in-plane measurements, the best fit of the structure factors ($\chi^2 = 2.35$) is displayed in Fig. 13.

Below-background diffractions were recorded at the location where intensities calculated with the model are very weak. This good agreement between experimental and calculated intensities accounts for 113 independent reflections.

For the out-of-plane measurements, the best fit of the structure factors ($\chi^2 = 1.51$) is displayed for four rods

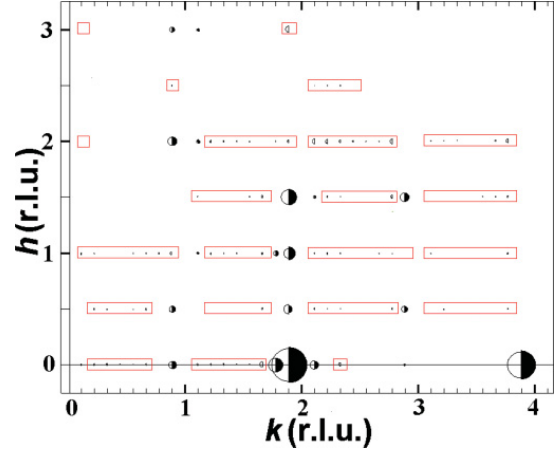


FIG. 13. (Color online) Top view of the in-plane diffraction pattern. The measured reflections are drawn as right black half-disks of radius (area) proportional to the structure factor amplitude (intensity). The left half-circles represent the fitted structure factors according to the model. The confirmed below-background diffractions are surrounded by the rectangles. Corresponding values calculated with the model are also drawn. The h and k indexes are those of the unreconstructed surface unit cell (1×1)_s.

[[0.889,0, ℓ], [0.889,0.5, ℓ], [1.889,0, ℓ], and [1.889,1.5, ℓ]] in Fig. 14. The overall agreement is good, supporting the idea that the model should not be far from the real situation.

The z displacements with respect to the initial values of the 2×1 reconstruction are shown in Fig. 15. In each layer, the atoms close to the DVL symmetry plane are found to have the largest vertical motions.

The relative uncertainty on the z atomic displacement can be estimated by $\Delta(dz)/dz = \Delta b_4 \times z$, as the uncertainties on the fit parameters b_0 and b_2 in Eq. (4) are negligible with

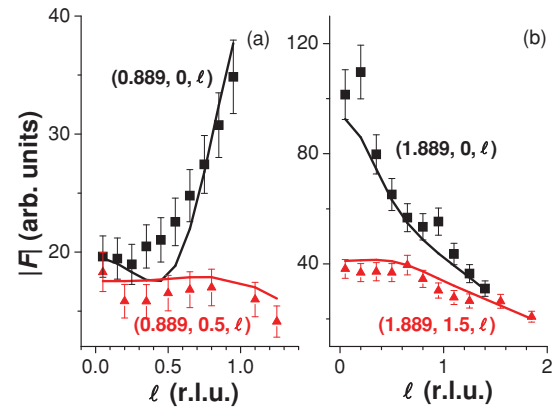


FIG. 14. (Color online) Experimental structure factors for four measured rods vs index ℓ : (a) (0.889,0, ℓ) and (0.889,0.5, ℓ), (b) (1.889,0, ℓ) and (1.889,1.5, ℓ). The lines correspond to the best fits with the chosen model.

ATOMIC STRUCTURE AND COMPOSITION OF THE ...

PHYSICAL REVIEW B 83, 195426 (2011)

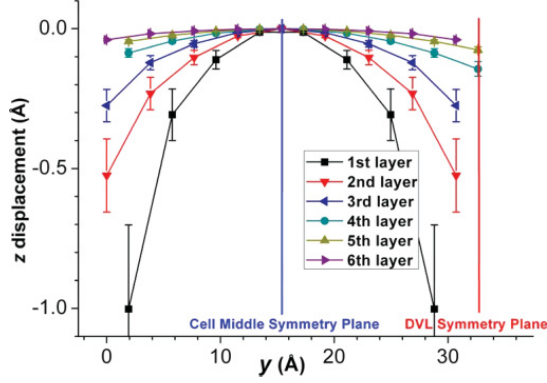


FIG. 15. (Color online) The z atomic displacement with respect to the initial values of the 2×1 reconstruction for 2 ML coverage in layers (1) to (6).

respect to that of b_4 ($\Delta b_4/b_4 \sim 5\%$). Hence, the uncertainties are approximately 30% for the first layer, 25% for the second layer, 21% for the third layer, 18% for the fourth layer, 14% for the fifth layer, and 10% for the sixth layer, decreasing linearly with depth.

The y displacement is displayed in Fig. 16. Again, in each layer, the largest displacements are undergone by the atoms closest to the DVL symmetry plane. The atoms indicated as P in layers (4) and (5) in Fig. 16 do not move along y as they are in the DVL symmetry plane. Moreover, these atoms move down along z (cf. Fig. 15) and prevent the atom indicated as P' in the layer (6) to move along y (cf. Fig. 16).

The uncertainty on the y atomic displacement can be estimated by $\Delta(dy)/dy = \Delta c_4 \times z$, as the uncertainties on the c_1 and c_3 parameters in Eq. (5) are negligible with respect to that of c_4 ($\Delta c_4/c_4 \sim 1.2\%$). Hence, the uncertainties on the y atomic displacement are around 5% for the first layer, 4% for the second and third layers, 3% for the fourth layer, and 2% for the fifth and sixth layers.

A preliminary polynomial modelization revealed that the x displacements of most atoms are negligible with respect to their original positions in the $\times 2$ reconstruction. Hence, a qualitative study was carried out specifically on the two atoms in layer (2) near the DVL where the x displacements are expected to be the largest. The study showed that these

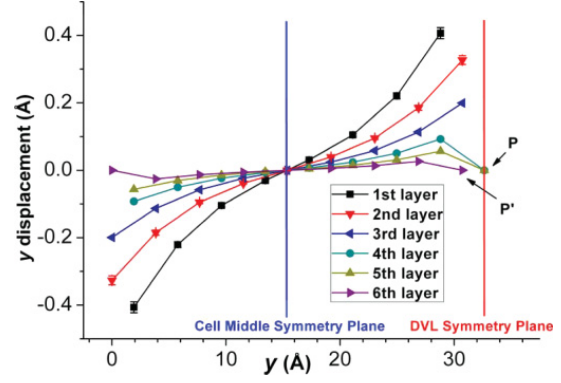


FIG. 16. (Color online) The y atomic displacement in layers (1) to (6) for 2 ML coverage. Most error bars are smaller than the symbol size.

two atoms (cf. Fig. 17) tend to move slightly away from each other from their initial positions in the $\times 2$ reconstruction, thus partially compensating the compressive strain induced by the large z displacement of their nearest neighbor in layer (1).

The best fit also yields the average Ge occupation probability with reasonable uncertainties (cf. Table II).

The evolution of the Ge occupation probability is displayed in Fig. 18 for layers (3), (4), and (5). The SXRD shows that, from layer (3), the Ge occupation decreases from the cell middle symmetry plane to the DVL one. However, no such variation was found for layers (1) and (2).

To conclude, the available x-ray data are well fitted with the chosen model. The best fits yielded the z and y atomic displacement as a function of y and z , as well as the Ge occupation probability in each atomic layer by using 17 parameters.

IV. DISCUSSION

A. Asymmetric dimer bond lengths and buckling angles

The best fits of the 2×1 reconstruction for Si and 1, 2, and 3 ML Ge/Si(001) confirm the dimer asymmetry. Let us compare the deduced dimer bond length and buckling angle (cf. Fig. 8) with those found in the literature. Previous SXRD measurements of the Si(001) reconstruction yielded a bond

TABLE II. Average Ge occupation probability in each atomic layer for 2 ML Ge/Si(001) WL grown at 670 °C, obtained from the present SXRD study. For comparison, the average Ge occupation probabilities obtained from MC simulations at 600 °C are also reported.²⁴ In this case, the intermixing region covers layers 1–5 or the whole bulk region (see Sec. IV for discussion).

Layer	SXRD	MC	
		Intermixing in five layers	Intermixing in the whole bulk
1	79.6% \pm 8%	91%	66%
2	49.3% \pm 12%	33.5%	10%
3	14.7% \pm 21%	26%	8%
4	14.2% \pm 27%	24.5%	8%
5	11.7% \pm 28%		
Sum	1.70 ML	1.75 ML	0.92 ML

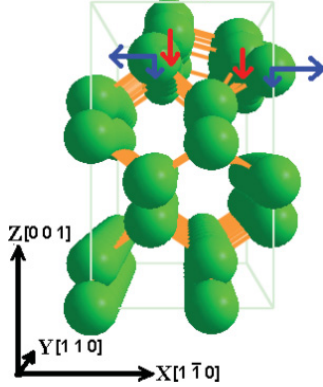
T. ZHOU *et al.*

FIG. 17. (Color online) Schematic of the 2×9 reconstruction for 2 ML coverage. The arrows show the displacements of the atoms in the second layer and the z displacements of the dimer atoms near the DVL.

length of $2.67 \pm 0.07 \text{ \AA}$ and a buckling angle of $20^\circ \pm 3^\circ$.³⁹ Another SXRD study of the Ge(001) reconstruction indicated a bond length of $2.55 \pm 0.01 \text{ \AA}$ and a buckling angle of $15.6^\circ \pm 0.6^\circ$.³⁴ X-ray standing-wave measurements of 1 ML Ge/Si(001) determined a bond length of $2.60 \pm 0.04 \text{ \AA}$ and a buckling angle of $12.1^\circ \pm 0.2^\circ$.⁹ A first-principles local-density molecular-cluster total-energy and atomic-force study of Ge dimers on Si(001) yielded a buckling angle of 14.2° .¹¹ In addition, final-state pseudopotential theory for 1 ML Ge/Si(001) gave a buckling angle of 16° .⁴¹ Globally, the buckling angles deduced from the present SXRD measurements (between 9.4° and 15.6° depending on Ge coverage) are in good agreement with those found in the literature. Surface-extended x-ray-absorption fine structure indicated that the bond length is $2.51 \pm 0.04 \text{ \AA}$ for 1 ML Ge/Si(001).⁴² Furthermore, first-principles total-energy calculations yielded a bond length of 2.54 \AA for a $p(2 \times 2)$ reconstruction for 1 or more ML coverage.¹⁵ Another first-principles study of 1 ML Ge/Si(001) in the $p(2 \times 2)$ reconstruction found a bond length of 2.55 \AA .⁴³ X-ray diffraction of the $c(4 \times 2)$ reconstruction of Ge(001) at 150 K yielded a bond length of 2.55 \AA .⁴⁴ The calculated bond length using a (4×2) unit cell is 2.51 \AA .⁴⁵ Globally, the bond lengths obtained by SXRD for the 1, 2, and 3 ML coverage (between 2.5 and 2.62 \AA depending on coverage) are also in good agreement with those experimentally determined or calculated for alternating asymmetric dimers. This indicates that the alternating asymmetric dimers correspond to the most stable structure. The calculated bond lengths for a (4×2) unit cell are longer than those calculated for a (2×1) symmetry,^{46,47} showing that the bond length depends strongly on the long-range interaction between dimers or on the surface stress extending over several dimer units.

More precisely, the measured bond lengths (buckling angles) of the 1 and 2 ML Ge/Si(001), displayed in Fig. 8, are smaller (larger) than those of clean Si and of 3 ML Ge/Si(001). For 3 ML coverage, since the Ge occupation probability is larger than 80%, most dimers are Ge-Ge dimers, while for

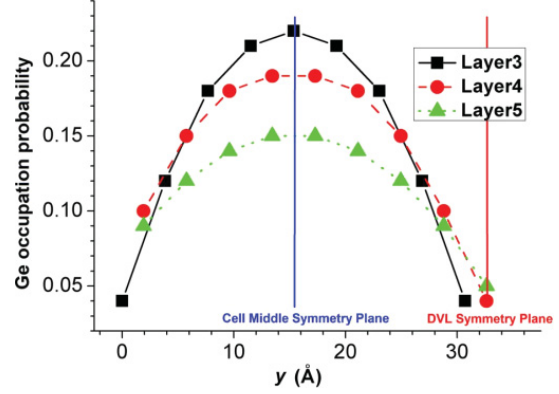
PHYSICAL REVIEW B **83**, 195426 (2011)

FIG. 18. (Color online) Ge occupation probability as a function of y for layers (3), (4), and (5) for 2 ML coverage. The uncertainties on the Ge occupation probability within a layer are large (typically 80% for the fifth layer).

low coverage, mixed Si-Ge dimers are favored.¹⁰ Hence, the present SXRD study confirms that the buckling angle of a Si-Ge dimer is significantly larger than that of a pure Si dimer.¹² In addition, our results show that the buckling angles of mixed dimers are also larger than those of pure Ge dimers. As a matter of fact, the surface total-energy reduction due to the buckling of the dimers has been evaluated to 0.13 eV/dimer for the Si-Si dimer,¹³ 0.28 eV/dimer for the Si-Ge dimer,¹³ and 0.13 eV/dimer for the Ge-Ge dimer.¹¹ Therefore, the buckling of the mixed dimer is energetically the most favorable process. This can be attributed to the strain relief of the dimers, which reduces the strain energy of the surface, as the lattice constant of Ge is larger than that of Si. Since Ge is coherent with the Si(001) substrate, a tetragonal distortion of the Si-Ge dimers along the [001] direction reduces the strain in the Ge/Si(001) interfaces. In short, the bond length of Si-Ge dimers is smaller ($\sim 2.50 \text{ \AA}$) than those of pure Si or pure Ge dimers, while the buckling angle of mixed dimers is larger ($\sim 16^\circ$). This structural difference comes from the strain associated with the lattice mismatch between Si and Ge.

B. The $DVL \times N$ reconstruction

The average N value is found to decrease from 11.5 to 8 with increasing Ge coverage from 1 to 3 ML. This value is in good agreement with previous theoretical and experimental studies. A MC simulation shows that, in the absence of intermixing (e.g., at low growth temperatures), N first decreases with increasing coverage and then saturates at $N = 8$ at approximately 2 ML coverage.²⁴ Taking into account intermixing, the calculated N value shifts from 8 to larger values for 2 ML coverage and $N \sim 8$ for 3 ML coverage.²⁴ Moreover, a high-temperature STM study showed that N decreases from 10 for 1.2 ML coverage to 8–9 for 2 ML coverage.⁴⁸

Besides, the intermixing depth is found to increase from six to eight layers with increasing Ge coverage from 2 to 3 ML. This is also in good agreement with previous theoretical and experimental studies. The MC method shows that at

ATOMIC STRUCTURE AND COMPOSITION OF THE ...

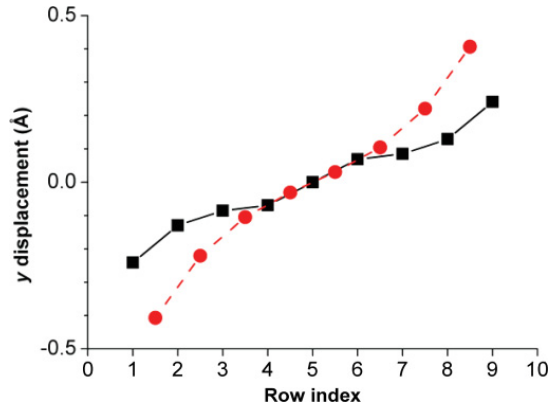
PHYSICAL REVIEW B **83**, 195426 (2011)

FIG. 19. (Color online) Evolution of the y displacement in the first layer as a function of the dimer line index. The y displacement of the 2×9 reconstruction obtained from the present SXR data is represented by filled circles and the one from a theoretical study for a 2×10 reconstruction without intermixing at $T = 11$ K is represented by filled squares.²⁴ The uncertainty on the experimental y displacement for the first layer is 4%.

600 °C, a significant Ge amount is present throughout the surface region, with the third and fourth layers becoming populated even at low coverages.²⁴ Previous experiments showed that Ge is present at least in the fourth layer for monolayer or even submonolayer deposits.^{49–52}

Regarding the atomic displacements of the $2 \times N$ reconstruction, the obtained y displacement in the first layer is plotted together with that calculated in an MC simulation for a 2×10 reconstruction without intermixing at $T = 11$ K in Fig. 19.²⁴ The evolution of both curves is similar, i.e., the y displacement in absolute value increases from the middle of the lattice toward the DVL. Interestingly, near the DVL, the y displacement obtained for the 2×9 reconstruction is larger than the theoretical one for the 2×10 reconstruction. This can probably be attributed to the fact that the DVLs act as a misfit strain relief mechanism by providing space for the expansion of the Ge-rich overlayer. This effect is expected to be larger

for a DVL every ninth line than for a DVL every tenth line. In addition, the atomic displacements may be larger at RT (current study) than at $T = 11$ K (MC simulation).²⁴

The average Ge occupation probability at 2 ML coverage is shown in comparison (Table II) with theoretical results.²⁴ The experimental average Ge occupation probability is similar to that obtained from the MC simulations. More precisely, SXR shows that the Ge occupation probability is maximum in the middle of the lattice and minimum near the DVLs below the surface from the third layer (cf. Fig. 18). This site selectivity agrees well with a MC simulation that shows that the region under the DVL is unfavorable to Ge occupation.²⁴ Indeed, the inward relaxation leads to a compressively strained region near the DVL that becomes unfavorable to Ge occupation. The site selectivity is due to the strain coming from the lattice mismatch between Si and Ge. Finally, the atomic structure of the 2×9 reconstruction with the effect of the DVL is schematically represented in Fig. 20.

Last but not least, the literature suggests that a small disturbance in the WL locally modifies the strain configuration, leading to the formation of prepyramids.⁵³ Our results suggest that the top of the Ge-rich region might be a preferable site for island nucleation due to larger strain relief for Ge atoms.

V. CONCLUSION

The $2 \times N$ reconstruction of the Ge/Si(001) WL was investigated by SXR for Ge coverages between 1 and 3 ML.

The structure of its cornerstone, the surface dimers, was first studied. The buckling angle was found between 9.4° and 15.6° and the dimer bond length was between 2.50 and 2.60 Å depending on the coverage. The bond lengths correspond to those calculated for alternating asymmetric dimers, which are smaller than those of pure Si and pure Ge dimers, while the buckling angles are larger. These results suggest that a significant proportion of the dimers are mixed dimers.

The overall $2 \times N$ reconstruction was then investigated. The average N periodicity is found to decrease from 11.5 to 8 with increasing Ge coverage from 1 to 3 ML. Intermixing is found to extend below the surface down to six (eight) layers for 2 (3) ML coverage.

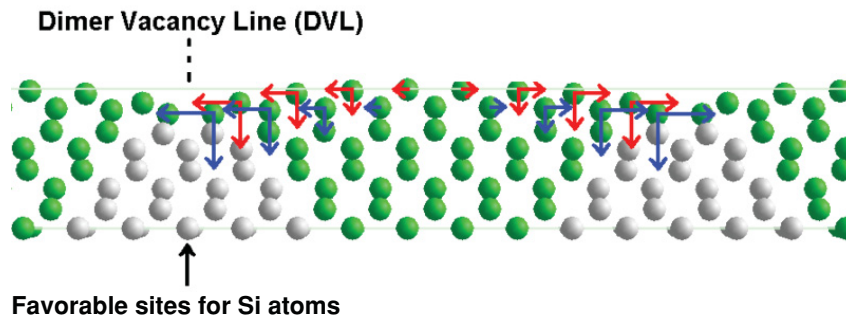


FIG. 20. (Color online) Schematic representation of the atomic structure of the 2×9 reconstruction. The red (gray) [blue (dark)] arrows indicate the displacements of the atoms in layer (1) [(2)]. Lattice sites that are under tensile strain and thus richer in Ge atoms are represented by green (dark gray) disks. Sites under compression and thus richer in Si atoms are represented by light gray disks.

T. ZHOU *et al.*PHYSICAL REVIEW B **83**, 195426 (2011)

For 2 ML coverage, a model of the atomic displacements and the Ge occupation probability for the 2×9 reconstruction is proposed. The largest displacements are located below the DVLs, with a smooth decrease with increasing distance from the DVLs. The average Ge occupation probability decreases from approximately 80% in the first layer down to 12% in the fifth layer. An experimental proof for the site selectivity in intermixing is also provided, which reveals that the regions under the DVLs are unfavorable to Ge. The top of the Ge-rich region between the DVLs might then be a preferable site for prepyramid nucleation. The intermixing in the WL may be responsible for the observed intermixing in the prepyramids and pyramids that form at the 2D-3D transition, atomic motion being favored by the stress present in the wetting layer, especially in the Si-richer regions below the DVLs.

ACKNOWLEDGMENTS

We would like to thank D. Vermeille of the ESRF ID03 beamline for his invaluable help during the measurements. We would also like to thank D. Hauser for his help in analyzing the SXRD data, and C. Metzger for guiding Monte Carlo simulations. The 2×9 reconstruction was displayed with V_Sim, a free 3D visualization tool available at [http://inac.cea.fr/L_Sim/V_Sim/]. We acknowledge support by the University Joseph Fourier, Grenoble, France, with which the SP2M laboratory is associated.

APPENDIX

A. Lorentz factor

The differential scattering cross section is expressed in reciprocal space as the integration is performed on the scan angles. The Lorentz factor is a geometrical correction factor whose value is equal to the determinant (also called Jacobian) of the transformation matrices between both volumes. The Lorentz factor for a rocking scan is given, for example, in Ref. 31. This factor is calculated here with another approach. Once this approach is validated for a rocking scan, it will be

used for a radial scan for which the Lorentz factor is rarely given.

In the case of a rocking scan, the integration volume V expressed in terms of angles is given by³¹

$$V = (K_f d\psi \times K_f d\gamma) \cdot d\mathbf{Q} = K d\psi K d\gamma \cos \gamma dQ_{\parallel}^*, \quad (\text{A1})$$

where $\mathbf{Q} = \mathbf{K}_f - \mathbf{K}_i$ is the momentum transfer, $K = K_i = K_f$ is the wave-vector value, and dQ_{\parallel}^* is the component of $d\mathbf{Q}$ parallel to the direction of \mathbf{K}_f . The dQ_{\parallel}^* parameter can be expressed as

$$dQ_{\parallel}^* = d\mathbf{Q}_{\parallel}^* \cdot \frac{\mathbf{K}_{f\parallel}}{K_{f\parallel}} = dQ_{\parallel} \sin \tau = Q_{\parallel} d\omega \sin \tau, \quad (\text{A2})$$

where τ is the angle between \mathbf{Q}_{\parallel} and $\mathbf{K}_{f\parallel}$. Let us now compare two expressions of the surface A of the triangle $O-S'-P'$ in Fig. 21:

$$\begin{aligned} S &= \frac{1}{2} Q_{\parallel} K_{f\parallel} \sin \tau = \frac{1}{2} K_{i\parallel} K_{f\parallel} \sin \delta \Leftrightarrow \sin \tau \\ &= \frac{K_{i\parallel} \sin \delta}{Q_{\parallel}} = \frac{K \cos \alpha \sin \delta}{Q_{\parallel}}. \end{aligned} \quad (\text{A3})$$

Hence, one obtains

$$\begin{aligned} V &= K d\psi K d\gamma \cos \gamma Q_{\parallel} d\omega \frac{K \cos \alpha \sin \delta}{Q_{\parallel}} \\ &= K^3 \cos \alpha \sin \delta \cos \gamma d\psi d\gamma d\omega, \end{aligned} \quad (\text{A4})$$

which is the expression given in the literature for an in-plane rocking scan (i.e., ω scan).³¹

For a radial scan, the calculation is similar except that the scan direction is along \mathbf{Q}_{\parallel} . The integration volume can be described as

$$V = K d\psi K d\gamma \cos \gamma dQ_{\parallel}^{**} \quad (\text{A5})$$

with

$$dQ_{\parallel}^{**} = d\mathbf{Q}_{\parallel}^{**} \cdot \frac{\mathbf{K}_{f\parallel}}{K_{f\parallel}} = dQ_{\parallel} \sin \left(\frac{\pi}{2} - \tau \right) = dQ_{\parallel} \cos \tau. \quad (\text{A6})$$

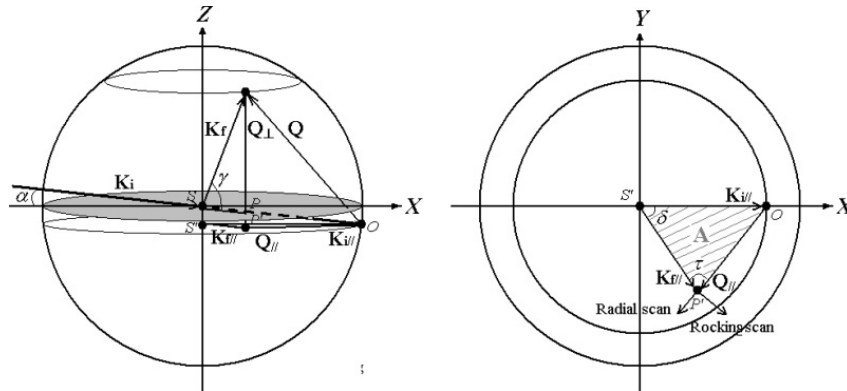


FIG. 21. Construction of the Ewald sphere for the z -axis diffractometer geometry.

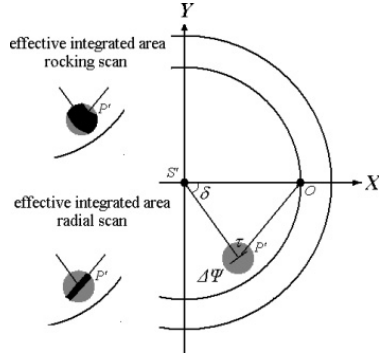


FIG. 22. Construction of the Ewald sphere (top view of the surface plane) for the z -axis diffractometer geometry and effective integrated area for a rocking scan or a radial one.

The law of cosines is next applied (for the same triangle as before in Fig. 21) to get an analytical expression,

$$Q_{\parallel}^2 = K^2 \cos^2 \gamma + K^2 \cos^2 \alpha - 2K^2 \cos \alpha \cos \gamma \cos \delta \Leftrightarrow dQ_{\parallel} = \frac{K^2 \cos \alpha \cos \gamma \sin \delta}{Q_{\parallel}} d\delta, \quad (\text{A7})$$

$$K^2 \cos^2 \alpha = Q_{\parallel}^2 + K^2 \cos^2 \gamma - 2Q_{\parallel} K \cos \gamma \cos \tau \Leftrightarrow \cos \tau = \frac{Q_{\parallel}^2 + K^2 \cos^2 \gamma - K^2 \cos^2 \alpha}{2Q_{\parallel} K \cos \gamma}. \quad (\text{A8})$$

Finally, the expression for V becomes

$$V = K d\psi K d\gamma \cos \gamma \frac{K^2 \cos \alpha \cos \gamma \sin \delta}{Q_{\parallel}} \times d\delta \frac{2K^2 \cos^2 \gamma - 2K^2 \cos \alpha \cos \gamma \cos \delta}{2Q_{\parallel} K \cos \gamma}, \quad (\text{A9})$$

and with the help of (A7), a simpler result is obtained:

$$V = K^3 d\psi d\gamma d\delta \frac{\cos \alpha \sin \delta \cos^2 \gamma (\cos \gamma - \cos \alpha \cos \delta)}{\cos^2 \gamma + \cos^2 \alpha - 2 \cos \alpha \cos \gamma \cos \delta}. \quad (\text{A10})$$

B. Detector acceptance

The square of the structure factor is proportional to the integrated intensity of the corresponding peak. However, the angular acceptance of the detector may not be large enough in certain cases. For example, when the surface is not well organized, the FWHM of the peaks can be extremely large. It is often possible to perform a very wide scan so that along the scan direction, the peak can be fully integrated. On the contrary, the integration along the other direction (perpendicular to the scan direction) is still limited by the detector angular acceptance. Figure 22 illustrates the effective integrated area of a wide peak during a rocking scan or a radial scan when the detector angular acceptance cannot be made large enough. When this happens, an additional correction factor has to be applied, equal to the ratio between the effective integrated intensity and the entire peak intensity. For in-plane data sets, an analytical correction factor for a rocking scan is given for a Lorentzian or Gaussian line shape in the literature. For a general setting, a numerical correction factor is given for a rocking scan but not for a radial scan.³¹

Let us derive an analytical correction factor for a more general setting. A much simpler calculation using the τ angle will be described later. First, consider the common case of a two-dimensional Lorentzian line shape, for which

$$I = \int_{-\infty}^{+\infty} \int_{-\infty}^{+\infty} f_{\text{Lor}}(x, y; x_0, y_0, w) dx dy = \int_{-\infty}^{+\infty} \int_{-\infty}^{+\infty} \frac{w}{4\pi} \frac{1}{\left(\frac{w^2}{4} + \Delta x^2 + \Delta y^2\right)^{3/2}} dx dy, \quad (\text{A11})$$

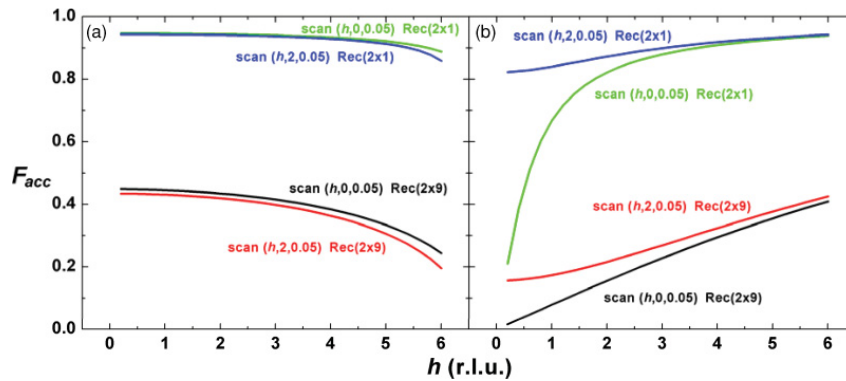


FIG. 23. (Color online) The correction factor of detector acceptance for a Lorentzian line shape in the case of (a) a rocking scan and (b) a radial scan. The parameters are drawn from our case with a horizontal opening angle of the detector $\Delta\Psi = 0.2^\circ$, corresponding to 0.02 \AA^{-1} in reciprocal space. The factors for the two surface reconstructions ($\times 2$ and $\times 9$) are presented for two different peaks $(h, 0, 0.05)$ and $(h, 2, 0.05)$. The $\times 2$ reconstruction has a typical FWHM of $L_{\times 2} = 1.65 \times 10^{-3} \text{ \AA}^{-1}$ and the $\times 9$ reconstruction has a typical FWHM of $2.3 \times 10^{-2} \text{ \AA}^{-1}$, i.e., approximately $14 \times L_{\times 2}$.

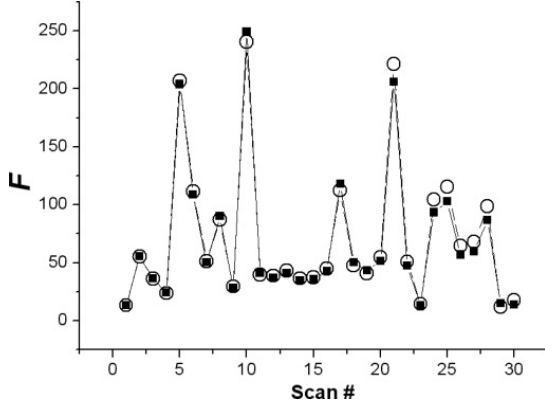
T. ZHOU *et al.*PHYSICAL REVIEW B **83**, 195426 (2011)

FIG. 24. Comparison of the structure factor after correction for the corresponding rocking (filled squares) and radial (open circles) scans.

where w is the FWHM of the distribution and Δx and Δy denote the deviation from the position of the distribution maximum given by x_0 and y_0 . The distribution is two-dimensionally homogeneous so that the integral is the same for two other variables of integration orthogonal to each other: $d\mathbf{q}_t$ (the transverse component of $d\mathbf{Q}$) and dq_r (the radial component of $d\mathbf{Q}$). The total integrated intensity is

$$I_{\text{tot}} = \int_{-\infty}^{+\infty} \int_{-\infty}^{+\infty} \frac{w}{4\pi} \frac{1}{\left(\frac{w^2}{4} + \Delta q_t^2 + \Delta q_r^2\right)^{3/2}} dq_t dq_r. \quad (\text{A12})$$

In the case of a rocking scan, where the detector moves transversally with respect to \mathbf{Q} , the integral interval over dq_t can have the maximum value while the one over dq_r depends on the effective length of the detector slit ($L_{\text{eff}} = 2T$), which is perpendicular to the scan direction. The effective integrated intensity is thus

$$I_{\text{eff}} = \int_{-T}^{+T} \int_{-\infty}^{+\infty} \frac{w}{4\pi} \frac{1}{\left(\frac{w^2}{4} + \Delta q_t^2 + \Delta q_r^2\right)^{3/2}} dq_t dq_r. \quad (\text{A13})$$

The detector acceptance correction factor acceptance is then the quotient of both integrated intensities:

$$F_{\text{acc}} = I_{\text{eff}}/I_{\text{tot}} = \frac{2}{\pi} \arctan\left(\frac{2T}{w}\right). \quad (\text{A14})$$

For a radial scan, the expression of the factor is the same as in formula (A13) while the value of the effective length $L_{\text{eff}} = 2T$ is different because it is now the integral over dq_t , which is limited. By calculating L_{eff} for both cases, we obtain

$$2T = \frac{L_{\text{oslit}}}{D_{\text{sample detector}}} K_f \times \begin{cases} \sin \tau, & \text{rocking scan} \\ \cos \tau, & \text{radial scan,} \end{cases} \quad (\text{A15})$$

where we can replace directly the part related to τ with the expression given in formulas (A3) and (A7), respectively. A similar calculation can also be done for a Gaussian line shape.

The detector acceptance correction factors for rocking and radial scans are shown in Fig. 23. For a rocking scan, let us consider that most data are measured at $h < 4$. The correction factor can be thought to be constant (0.93) for the 2×1 reconstruction. Neglecting the correction factor results only in a slight constant underestimation of the structure factor, easily taken into account by the overall scale factor. For the $\times 9$ reconstruction, only about 40% of the peak would be integrated, nevertheless neglecting the same factor would cause a variation of up to 20% throughout the in-plane data set.

For a radial scan, the factor becomes crucial even for the 2×1 reconstruction. In an extreme case, such as the $(h,0,0.05)$ scan, the correction factor increases dramatically from 20% for $h = 0.2$ (because at small $|\mathbf{Q}|$, the detector is practically parallel to the radial direction) to 91% for $h = 4$. For the $\times 9$ reconstruction, the factor changes linearly with h . Even in the best cases [i.e., $(h,2,0.05)$], neglecting the correction factor would cause a variation of up to 50% throughout the in-plane data set.

Finally, Fig. 24 shows that both kinds of measurements (rocking and radial scans) yield the same structure factor amplitude after corrections, thus validating the corrections applied in this work.

¹B. Voigtländer, *Surf. Sci. Rep.* **43**, 127 (2001).

²Y. W. Mo, D. E. Savage, B. S. Swartzentruber, and M. G. Lagally, *Phys. Rev. Lett.* **65**, 1020 (1990).

³A. Vailionis, B. Cho, G. Glass, P. Desjardins, D. G. Cahill, and J. E. Greene, *Phys. Rev. Lett.* **85**, 3672 (2000).

⁴G. Medeiros-Ribeiro, A. M. Bratkovski, T. I. Kamins, D. A. A. Ohlberg, and R. S. Williams, *Science* **279**, 353 (1998).

⁵M.-I. Richard, T. U. Schüllli, G. Renaud, E. Wintersberger, G. Chen, G. Bauer, and V. Holý, *Phys. Rev. B* **80**, 045313 (2009).

⁶T. U. Schüllli, J. Stangl, Z. Zhong, R. T. Lechner, M. Sztucki, T. H. Metzger, and G. Bauer, *Phys. Rev. Lett.* **90**, 066105 (2003).

⁷S. Miyamoto, O. Moutanabbir, E. E. Haller, and K. M. Itoh, *Phys. Rev. B* **79**, 165415 (2009).

⁸T. U. Schüllli, M.-I. Richard, G. Renaud, V. Favre-Nicolin, E. Wintersberger, and G. Bauer, *Appl. Phys. Lett.* **89**, 143114 (2006).

⁹E. Fontes, J. R. Patel, and F. Comin, *Phys. Rev. Lett.* **70**, 2790 (1993).

¹⁰L. Patthey, E. L. Bullock, T. Abukawa, S. Kono, and L. S. O. Johansson, *Phys. Rev. Lett.* **75**, 2538 (1995).

¹¹S. Tang and A. J. Freeman, *Phys. Rev. B* **50**, 10941 (1994).

¹²X. Chen, D. K. Saldin, E. L. Bullock, L. Patthey, L. S. O. Johansson, J. Tani, T. Abukawa, and S. Kono, *Phys. Rev. B* **55**, R7319 (1997).

¹³R. H. Miwa, *Surf. Sci.* **418**, 55 (1998).

ATOMIC STRUCTURE AND COMPOSITION OF THE ...

PHYSICAL REVIEW B **83**, 195426 (2011)

- ¹⁴H. J. W. Zandvliet, *Rev. Mod. Phys.* **72**, 593 (2000).
- ¹⁵K. Varga, L. G. Wang, S. T. Pantelides, and Z. Zhang, *Surf. Sci. Lett.* **562**, L225 (2004).
- ¹⁶A. van Houselt, R. van Gastel, B. Poelsema, and H. J. W. Zandvliet, *Phys. Rev. Lett.* **97**, 266104 (2006).
- ¹⁷X. R. Qin, B. S. Swartzentruber, and M. G. Lagally, *Phys. Rev. Lett.* **85**, 3660 (2000).
- ¹⁸Z.-Y. Lu, F. Liu, C.-Z. Wang, X. R. Qin, B. S. Swartzentruber, M. G. Lagally, and K.-M. Ho, *Phys. Rev. Lett.* **85**, 5603 (2000).
- ¹⁹F. Liu, F. Wu, and M. G. Lagally, *Chem. Rev.* **97**, 1045 (1997), and references therein.
- ²⁰R. Gunnella, P. Castrucci, N. Pinto, I. Davoli, D. Sébilleau, and M. De Crescenzi, *Phys. Rev. B* **54**, 8882 (1996).
- ²¹J. Wan, Y. H. Luo, Z. M. Jiang, G. Jin, J. L. Liu, K. L. Wang, X. Z. Liao, and J. Zou, *J. Appl. Phys.* **90**, 4290 (2001).
- ²²K. Nakajima, A. Konishi, and K. Kimura, *Phys. Rev. Lett.* **83**, 1802 (1999).
- ²³R. J. Wagner and E. Gulari, *Phys. Rev. B* **69**, 195312 (2004).
- ²⁴L. Nurminen, F. Tavazza, D. P. Landau, A. Kuronen, and K. Kaski, *Phys. Rev. B* **68**, 085326 (2003).
- ²⁵I. Goldfarb, J. H. G. Owen, P. T. Hayden, D. R. Bowler, K. Miki, and G. A. D. Briggs, *Surf. Sci.* **394**, 105 (1997).
- ²⁶M. Tomitori, K. Watanabe, M. Kobayashi, and O. Nishikawa, *Appl. Surf. Sci.* **76-77**, 322 (1994).
- ²⁷I. K. Robinson and D. J. Tweet, *Rep. Prog. Phys.* **55**, 599 (1992).
- ²⁸A. Malachias, T. U. Schüllli, G. Medeiros-Ribeiro, L. G. Cançado, M. Stoffel, O. G. Schmidt, T. H. Metzger, and R. Magalhães-Paniago, *Phys. Rev. B* **72**, 165315 (2005).
- ²⁹R. Baudouin-Savois, M. De Santis, M. Saint-Lager, P. Dolle, O. Geaymond, P. Tautier, P. Jeantet, J. Roux, G. Renaud, and A. Barbier, *Nucl. Instrum. Methods Phys. Res. B* **149**, 213 (1999).
- ³⁰S. Ferrer and F. Comin, *Rev. Sci. Instrum.* **66**, 1674 (1995).
- ³¹E. Vlieg, *J. Appl. Cryst.* **30**, 532 (1997).
- ³²O. Robach, Y. Garreau, K. Aid, and M. B. Véron-Jolliot, *J. Appl. Cryst.* **33**, 1006 (2000).
- ³³G. Renaud, *Surf. Sci. Rep.* **32**, 1 (1998).
- ³⁴X. Torrelles, H. A. van der Vegt, V. H. Etgens, P. Fajardo, J. Alvarez, and S. Ferrer, *Surf. Sci.* **364**, 242 (1996).
- ³⁵R. A. Wolkow, *Phys. Rev. Lett.* **68**, 2636 (1992).
- ³⁶E. Vlieg, *J. Appl. Cryst.* **33**, 401 (2000).
- ³⁷W. H. Pres, B. P. Flannery, S. A. Teukolsky, and W. T. Vetterling, *Numerical Recipes in C* (Cambridge University Press, Cambridge, 1988).
- ³⁸M. Takahashi, S. Nakatani, Y. Ito, T. Takahashi, X. W. Zhang, and M. Ando, *Surf. Sci.* **338**, L846 (1995).
- ³⁹R. Felici, I. K. Robinson, C. Ottaviani, P. Imperatori, P. Eng, and P. Perfetti, *Surf. Sci.* **375**, 55 (1997).
- ⁴⁰J.-H. Cho and M.-H. Kang, *Phys. Rev. B* **61**, 1688 (2000).
- ⁴¹J.-H. Cho, S. Jeong, and M.-H. Kang, *Phys. Rev. B* **50**, 17139 (1994).
- ⁴²H. Oyanagi, K. Sakamoto, R. Shioda, Y. Kuwahara, and K. Haga, *Phys. Rev. B* **52**, 5824 (1995).
- ⁴³J. Oviedo, D. R. Bowler, and M. J. Gillan, *Surf. Sci.* **515**, 483 (2002).
- ⁴⁴S. Ferrer, X. Torrelles, V. H. Etgens, H. A. van der Vegt, and P. Fajardo, *Phys. Rev. Lett.* **75**, 1771 (1995).
- ⁴⁵Y. Miyamoto, *Phys. Rev. B* **49**, 1947 (1994).
- ⁴⁶P. Kruger and J. Pollmann, *Phys. Rev. B* **47**, 1898 (1993).
- ⁴⁷J.-H. Cho and M.-H. Kang, *Phys. Rev. B* **49**, 13670 (1994).
- ⁴⁸B. Voigtländer and M. Kästner, *Phys. Rev. B* **60**, R5121 (1999).
- ⁴⁹M. Sasaki, T. Abukawa, H. W. Yeom, M. Yamada, S. Suzuki, S. Sato, and S. Kono, *Appl. Surf. Sci.* **82-83**, 387 (1994).
- ⁵⁰A. Ikeda, K. Sumitomo, T. Nishioka, T. Yasue, T. Koshikawa, and Y. Kido, *Surf. Sci.* **385**, 200 (1997).
- ⁵¹H. W. Yeom, M. Sasaki, S. Suzuki, S. Sato, S. Hosoi, M. Iwabuchi, K. Higashiyama, H. Fukutani, M. Nakamura, T. Abukawa, and S. Kono, *Surf. Sci.* **381**, L533 (1997).
- ⁵²B. P. Uberuaga, M. Leskovar, A. P. Smith, H. Jónsson, and M. Olmstead, *Phys. Rev. Lett.* **84**, 2441 (2000).
- ⁵³A. Rastelli, H. Von Känel, B. J. Spencer, and J. Tersoff, *Phys. Rev. B* **68**, 115301 (2003).

2.3 *In situ* monitoring of Ge-island growth on Si(001)

The following publications describe the second important step of the growth morphology of Ge on Si(001): The nucleation of islands. The x-ray *in situ* methods GISAXS and GID as introduced in section 2.1 are applied in order to follow the evolution of size, shape, and strain of the islands.

2.3.1 *In situ* investigation of the island nucleation of Ge on Si(001) using x-ray scattering methods

T. U. Schülli, M.-I. Richard, G. Renaud, V. Favre-Nicolin, E. Wintersberger, G. Bauer

Applied Physics Letters 89, 143114 (2006)

An often discussed point during the SK growth of Ge on Si(001) is the influence of intermixing on the different island shapes observed during the growth. Furthermore, it is of interest to know how far the wettinglayer itself is already subject to intermixing and how this may affect its stability. In case of a highly strained and thus poorly intermixed wettinglayer, one may expect that a part of the latter is mobilized and contributes to the island formation once their nucleation has set in. Of particular interest is the observation of a shape change of the islands during growth: The first nucleation stage consists of flat {105}-faceted pyramids. These transform into a multi-faceted island type with higher aspect ratio once a certain amount of Ge is deposited. These islands are generally referred to as domes. On the following pages, this problem is treated by a comparison of GISAXS images (that show the presence and the shape of islands on a surface) with the integrated intensity of the diffraction signal stemming from the islands. As the latter one is proportional to the island volume, an eventual contribution of the wettinglayer to the island formation can be tracked during continuous deposition. It is found that in the presence of high elastic strain in the wettinglayer some parts of it become mobilized when the growing islands undergo themselves a shape transition from flat pyramid shaped island type to a multi-faceted dome like growth. This phenomenon is observed for a growth temperature of 500°C. For higher growth temperatures Si-Ge intermixing is already present in the wettinglayer, leading to a significant reduction of the elastic strain. Thus at elevated temperatures, such transport phenomena depend on the growth kinetics and therefore the deposition rate.

APPLIED PHYSICS LETTERS 89, 143114 (2006)

In situ investigation of the island nucleation of Ge on Si(001) using x-ray scattering methodsT. U. Schüllli,^{a)} M.-I. Richard, G. Renaud, and V. Favre-Nicolin
CEA Grenoble, DRFMC/SP2M, 17 rue des martyrs, F-38054 Grenoble, FranceE. Wintersberger and G. Bauer
Institute for Semiconductor Physics, Johannes Kepler Universität Linz, A-4040 Linz, Austria

(Received 22 March 2006; accepted 28 August 2006; published online 5 October 2006)

The growth of Ge on Si(001) is investigated *in situ* at 500 and 600 °C, combining grazing incidence diffraction, multiple wavelength anomalous diffraction, and small angle scattering. This allows probing simultaneously the island shape, strain state, composition, and the transition from wetting layer to island growth. At 500 °C no intermixing occurs. The wetting layer is found to decrease by one atomic layer at the onset of island nucleation. At 600 °C interdiffusion plays an important role in strain relaxation leading to a more stable wetting layer. Small angle scattering yields the island morphology and shows the transition from pyramids to multifaceted domes. © 2006 American Institute of Physics. [DOI: 10.1063/1.2358300]

Self-organized growth of semiconductor islands has been studied in great detail on a variety of heteroepitaxial systems.^{1–3} The first devices based on zero dimensionally confined objects are now commercially exploited.⁴ This technology requires a certain tunability of structural properties of the quantum dots. Thus fundamental aspects of the Stranski Krastanow (SK) growth instability still attract vital interest. These are, e.g., the dependences of interdiffusion, lattice relaxation, and island shape on the growth conditions. Most structural studies are done *ex situ* using scanning probe microscopy or luminescence spectroscopy from sample series. In these studies, several stages of the morphological evolution of islands have been described (see Refs. 5–7 and references therein). In electron microscopy, the morphological evolution has even been followed *in situ*.^{8–10} Apart from these latter studies, most methods are limited by high temperatures or make shadowing effects during molecular beam epitaxy (MBE). Furthermore it was so far not possible to go beyond the description of the morphological evolution. Structural parameters such as strain and interdiffusion are hardly accessible by these methods. Recently Takahasi *et al.* applied *in situ* x-ray diffraction to growing InAs nanostructures.¹¹ For the growth of self-organized Ge quantum dots on Si(001), the question about the origin of interdiffusion is still discussed as experimental data are scarce. In particular, the role of kinetic effects at different stages of the growth is not yet fully understood. This also raises the question for a possible transport of material from the wetting layer or the substrate into the islands during or after the transition from two dimensional to three dimensional growth (2D-3D transition) of the SK instability. We address these issues in the present work using *in situ* scattering methods during growth that do not suffer from restrictions of high temperatures. The diffraction pattern of reflected high-energy electrons (RHEED) often serves for a qualitative analysis of different stages of MBE growth. X-ray scattering methods offer the advantage of a much higher resolution and the possibility of quantitative analysis. Furthermore, the exploitation of the small angle scattering regime together with diffraction

at higher angles allows to record data over a broad range of momentum transfers, extending from 0.003 to 10 Å⁻¹, thus probing length scales from several 100 nm down to atomic distances. To answer the above questions, we coupled *in situ* three x-ray techniques during the MBE growth of Ge on Si(001). The first, grazing incidence small angle x-ray scattering (GISAXS), is sensitive to the morphology of nucleating islands and can easily detect 2D-3D and shape transitions.¹² The second, grazing incidence x-ray diffraction (GIXD), in particular, when recording reciprocal space maps in the vicinity of Bragg reflections, allows to follow the lattice relaxation during the nucleation of the islands. It is a very sensitive measure of the strain state of the islands and of the 2D-3D transition from wetting layer to island growth. The third, grazing incidence multiple wavelength anomalous diffraction (GI-MAD), allows to separate the Si and Ge contributions to the diffraction and thus to determine the composition of the growing islands.¹³ Figure 1 sketches the different probed regions in reciprocal space of such a sample.

The experimental station BM32 at the European Synchrotron Radiation Facility is equipped with a MBE growth chamber. The epitaxial growth of Ge and Si can be per-

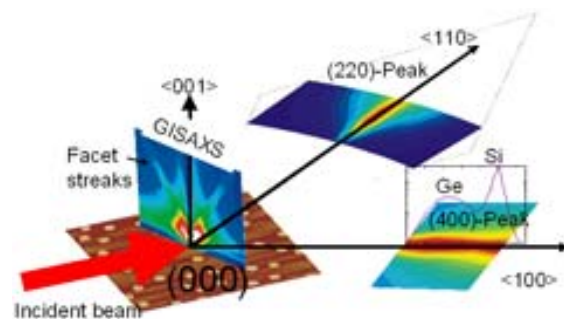


FIG. 1. (Color online) Sketch of the *in situ* x-ray scattering setup. Under grazing incidence conditions, the evolution of the sample morphology can be followed in the small angle regime; the formation of facets is indicated in the GISAXS pattern. The lattice relaxation is monitored by the appearance of Bragg peaks in GIXD. Intensity maps around the (220) and (400) Si and Ge Bragg peaks, integrated perpendicular to the surface, are also shown.

^{a)}Electronic mail: schullli@esrf.fr

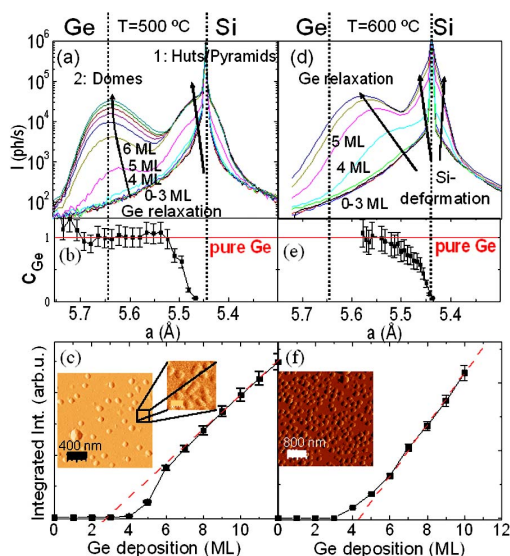


FIG. 2. (Color online) Evolution of the lattice relaxation during the growth of Ge on Si(001) for depositions from 0 to 11 ML at 500 °C (a) and from 0 to 7 ML at 600 °C (d). The Ge concentration for a deposit of 7 ML as a function of lattice parameter is plotted below for the corresponding temperatures [(b) and (e)]. Vertical dotted lines mark the lattice parameters of Ge and Si. In (c) and (f), the integrated Bragg peak intensity is plotted as a function of the deposited Ge amount. Insets show AFM images after the growth.

formed at a base pressure of 10^{-10} mbar. A cylindrical Be window allows to perform the x-ray experiments during the growth procedure. All Si(001) surfaces were deoxidized at 900 °C under ultrahigh vacuum conditions and characterized for their surface quality with GIXD and RHEED. The surfaces showed a 2×1 reconstruction whose average domain size was $\sim 1 \mu\text{m}$. During the growth of Ge, reciprocal space maps (see Fig. 1) were recorded in the vicinity of the (220) and (400) in-plane Bragg reflections of Ge and Si (the Ge lattice parameter is 4.2% larger than the Si one). For each deposited Ge monolayer, GISAXS patterns were collected in the azimuthal orientations $\langle 110 \rangle$, $\langle 100 \rangle$, and $\langle 15 3 0 \rangle$. In this letter, we present the results for substrate temperatures of 500 and 600 °C. For a growth temperature of 500 °C, a series of radial scans across the (400) reflection is shown in Fig. 2(a). No lattice relaxation is visible up to 4 ML coverage. For 5 and 6 ML deposit, two shoulders (indicated as 1 and 2 in the graph) are developing. This indicates a bimodal growth in this temperature regime. The shoulder one, closest to the Si peak, corresponds to highly strained islands that form in very early stages of the nucleation. For depositions higher than 6 ML, only more relaxed islands (shoulder 2) continue to grow. The maximum in intensity for these more relaxed islands is located at about 5.64 Å, very close to the Ge bulk value of 5.646 Å. Its position hardly evolves for deposits higher than 6 ML. After the growth, domes of variable size and hut clusters were observed by atomic force microscopy (AFM) [inset in Fig. 2(c)]. In order to further characterize this morphological transition, the recorded GISAXS patterns have to be considered. For the bare Si(001) surface, a typical GISAXS pattern is shown in Fig. 3(a). It is dominated in its central part by stray radiation from the direct beam (blocked by a beam stop) and by diffuse scattering

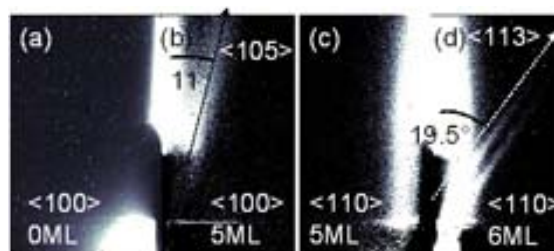


FIG. 3. (Color online) GISAXS images for different deposition stages and azimuthal orientations for a deposition temperature of $T=500$ °C. For symmetry reasons, only the left or the right parts of the images are presented. (a) Scattering image (left half) from a flat surface in the $\langle 100 \rangle$ sample azimuth; the central beam is blocked by a beam stop. (b) $\{105\}$ facets attributed to pyramids at deposited 5 ML. The bare substrate GISAXS from (a) was subtracted. The indicated angle of 11° corresponds to the angle between the facet normal $\langle 105 \rangle$ and the surface normal $\langle 100 \rangle$. For comparison with (a), only the right half of the GISAXS image is shown. (c) The $\langle 110 \rangle$ azimuth for a deposition of 5 ML (left half of the GISAXS image). (d) At 6 ML the sharp pyramid to dome transition is reached and $\{113\}$ facets appear. 19.5° corresponds to the angle between $\langle 113 \rangle$ and $\langle 001 \rangle$.

from the surface. To record the appearance of islands and, in particular, of facets, different low-index azimuthal orientations were regarded. Figure 3(b) shows a GISAXS image in the $\langle 100 \rangle$ azimuth for early nucleation stages at 500 °C. Broad and diffuse streaks in the $\langle 105 \rangle$ direction (traced by arrows) indicate the formation of $\{105\}$ faceted hut clusters and/or pyramids. Due to the flat facet orientation [11° with respect to the (001) surface], these islands are highly strained. For the $\langle 110 \rangle$ azimuth, no evolution can be observed for low deposits [see Fig. 3(c) for 5 ML deposit]. For 6 ML deposition [Fig. 3(d)], streaks in the $\langle 113 \rangle$ direction appear. The splitting of the streaks occurs as a consequence of a fourfold scattering process when working close to the critical angle.¹⁴

The same behavior is observed for $\langle 15 3 0 \rangle$ azimuth, where $\{15 3 23\}$ facets appear at 6 ML (not shown here). The previously described $\{105\}$ facets remain almost unchanged at this point. These latter three orientations describe the multifaceted dome shape as reported in earlier works.⁶ To obtain a measure for material transport, reciprocal space maps (see Fig. 1) of the scattered intensity in the vicinity of the (220) and (400) Bragg reflections were recorded. The principal probe here is the relaxation of the lattice parameter. Integrating the scattered intensity over all three dimensions in reciprocal space, one can extract a measure that is directly proportional to the growing scattering volume in the nanostructures. Material deposited to the wetting layer does not contribute to these intensities, as it remains pseudomorphic to the substrate and thus scatters at the same reciprocal position as the Si peak. For each added monolayer, the reciprocal space map of the bare Si substrate was subtracted. The remaining integrated intensity as a function of the deposition is plotted in Fig. 2(c) for a deposition temperature of 500 °C. As expected, up to 4 ML, no change in the integrated intensity is observed as the deposited Ge forms a pseudomorphic wetting layer. The onset of relaxation is revealed by a small rise at 5 ML. It follows a steeper slope between 6 and 8 ML and a linear evolution for higher deposits. The linear evolution indicated by the dashed line can be understood, if the complete amount of deposited Ge crystallizes in the form of islands. In the transitional region from 5

to 6 ML, the quantity of Ge added to the islands is larger than the deposited amount. The additional material is either Ge from the previously deposited wetting layer or Si that migrates into the island. To distinguish between these two possibilities, we performed GI-MAD to probe for possible interdiffusion. The diffracted intensity was measured in the vicinity of the (220) and (400) reflections at 12 energies close to the Ge *K* edge. Using the measured real and imaginary resonant corrections of the atomic scattering factor of Ge, $f_{\text{Ge}}^{\prime}(E)$ and $f_{\text{Ge}}^{\prime\prime}(E)$, it is possible¹⁵ to quantitatively separate the momentum of the scattering amplitudes for Ge, $|F_{\text{Ge}}|$, and for all scattering atoms, $|F_T|$, through a least-squares minimization. The $\text{Ge}_x\text{Si}_{1-x}$ content can be deduced using the relation

$$\frac{|F_{\text{Ge}}|}{|F_T|} = \frac{x f_{\text{Ge}}^0}{x f_{\text{Ge}}^0 + (1-x) f_{\text{Si}}^0}.$$

For a deposition of 7 ML, the Ge concentration is plotted as a function of lattice parameter in Fig. 2(b). At 500 °C, no Si signal is found inside the islands, excluding interdiffusion effects. The combination of the addressed parameters in the data presented in Figs. 3 and 2(a)–2(c) allows the following conclusions. The first nucleation step leads to the formation of {105} faceted hut clusters and pyramids. A part of these transforms into domes for ongoing deposition. During the pyramid formation as well as during the pyramid to dome transition, thus in the regime of deposited 5–6 ML, the equivalent of ~1 ML of Ge is transported from the wetting layer into the islands. A depletion of the previously formed wetting layer has been assumed in earlier publications.^{16,17} Our results for the critical thickness at 500 °C as well as for the remaining wetting layer thickness are in good agreement with recently published simulations.¹⁸

At 600 °C interdiffusion effects are known to exist, and we repeated the measurement and data treatment as described above to trace the material transport during the growth. These data are shown in Figs. 2(d)–2(f). While the morphological states remain qualitatively the same during the growth, the kink in the rise of the integrated intensity of the growing islands is not observed. The growing intensity close to the Si substrate peak in Fig. 2(d) can be attributed to deformations in the Si substrate as the scattering from silicon strongly dominates this region and as its intensity continues to grow with the growth of the SiGe domes.¹⁹ The relaxation of the lattice parameter during the dome growth is less important in the beginning and increases for ongoing deposition. This can be explained by interdiffusion that is already

present in the wetting layer at 600 °C. The material that forms the first islands (at 4 ML at this temperature) consists of a SiGe alloy that is formed at the surface due to ongoing intermixing at the interface. Ongoing deposition of pure Ge leads to a progressing increase of the Ge concentration and further relaxation of the growing domes. The smooth rise of the integrated intensity at 600 °C [Fig. 2(e)] shows that no partial dewetting of the interdiffused wetting layer occurs after the island nucleation. Furthermore the material exchange that takes place between wetting layer and substrate lowers the strain energy per atom in the wetting layer. The comparison of Figs. 2(b) and 2(e) shows that at 600 °C the nucleation occurs at 1 ML earlier than at 500 °C, preventing the effect of a supersaturated wetting layer.¹⁷ The resulting island ensemble consists only of domes with a narrower size distribution than for 500 °C. At 600 °C the lattice relaxation increases with every monolayer, whereas at 500 °C the islands approach the Ge lattice constant already right after nucleation.

¹V. A. Shchukin, N. N. Ledentsov, and D. Bimberg, *Epitaxy of Nanostructures* (Springer, Berlin, 2003).

²C. Teichert, *Phys. Rep.* **365**, 335 (2002).

³G. Meideiros-Ribeiro, A. M. Bratkowski, T. I. Kamins, D. A. A. Ohlberg, and R. S. Williams, *Science* **279**, 353 (1998).

⁴www.fujitsu.com

⁵T. I. Kamins, G. Meideiros-Ribeiro, D. A. A. Ohlberg, and R. S. Williams, *Appl. Phys. A: Mater. Sci. Process.* **67**, 727 (1998).

⁶A. Rastelli and H. von Känel, *Surf. Sci.* **515**, L493 (2002).

⁷F. Montalenti, P. Raiteri, D. B. Migas, H. von Känel, A. Rastelli, C. Manzano, G. Costantini, U. Denker, O. G. Schmidt, K. Kern, and L. Miglio, *Phys. Rev. Lett.* **93**, 216102 (2004).

⁸F. M. Ross, R. M. Tromp, and M. C. Reuter, *Science* **286**, 1931 (1999).

⁹P. Sutter and M. C. Lagally, *Phys. Rev. Lett.* **84**, 4637 (2000).

¹⁰B. Voigtlander, *Surf. Sci. Rep.* **43**, 127 (2001).

¹¹M. Takahashi, T. Kaizu, and J. Mizuki, *Appl. Phys. Lett.* **88**, 101917 (2006).

¹²G. Renaud, R. Lazzari, C. Revenant, A. Barbier, M. Noblet, O. Ulrich, F. Leroy, J. Jupille, I. Borensztein, C. R. Henry, J.-P. Deville, F. Scheurer, C. Mane-Mane, and O. Fruchart, *Science* **300**, 1416 (2003).

¹³A. Letoublon, V. Favre-Nicolin, H. Renevier, M. G. Proietti, C. Monat, M. Gendry, O. Marty, and C. Priester, *Phys. Rev. Lett.* **92**, 186101 (2004).

¹⁴M. Rauscher, R. Paniago, H. Metzger, Z. Kovats, J. Domke, J. Peisl, H.-D. Pfannes, J. Schulze, and I. Eisele, *J. Appl. Phys.* **86**, 6763 (1999).

¹⁵W. A. Hendrickson, *Trans. Am. Crystallogr. Assoc.* **21**, 11 (1985).

¹⁶A. V. Osipov, F. Schmitt, S. A. Kukushkin, and P. Hess, *Appl. Surf. Sci.* **188**, 156 (2002).

¹⁷Y. Zhang and J. Drucker, *J. Appl. Phys.* **93**, 9583 (2003).

¹⁸V. G. Dubrowski, G. E. Cirlin, and V. M. Ustinov, *Phys. Rev. B* **68**, 075409 (2003).

¹⁹T. U. Schülli, J. Stangl, Z. Zhong, R. T. Lechner, M. Sztucki, T. H. Metzger, and G. Bauer, *Phys. Rev. Lett.* **90**, 066105 (2003).

2.4 Evolution of Ge-domes on Si(001) during growth

2.4.1 *In situ x-ray scattering study on the evolution of Ge island morphology and relaxation for low growth rate: Advanced transition to superdomes*

M.-I. Richard, T. U. Schüllli, G. Renaud, E. Wintersberger, G. Chen, G. Bauer, V. Holý
Physical Review B 80, 045313 (2009)

As compared to the pyramids, often observed as a transition stage that exists only for a narrow window of temperature regime and deposited amount of Ge, dome-shaped islands are stable over a vast temperature regime and even for high Ge deposits. Beyond a certain critical size, these coherently growing domes build in defects to relax strain. Such dislocated islands are referred to as superdomes. Their appearance has been described to depend on temperature and deposition. More generally as the island size itself is decisive for the nucleation of dislocations, the total Ge amount expressed in deposited atomic layers necessary to form dislocated islands may also be dependent on growth speed. This implies that Ostwald ripening effects may be present during the growth phase of coherent domes. In the investigation presented here, performed during growth and following the island size as a function of deposit, one can make the following two statements: Firstly that slow growth rates indeed lead to an earlier (in terms of deposited amount of Ge) introduction of defects and the formation of superdomes (thus Ostwald ripening takes place at this stage). Secondly that once dislocations are formed, the island volume growth proportional to the amount of deposited material. In this phase Ostwald ripening and island coalescence thus plays no decisive role. To obtain these results, the main limiting facets have been analyzed in terms of size as a function of Ge deposit via a quantitative data treatment of GISAXS images.

PHYSICAL REVIEW B **80**, 045313 (2009)***In situ* x-ray scattering study on the evolution of Ge island morphology and relaxation for low growth rate: Advanced transition to superdomes**M.-I. Richard,^{1,2} T. U. Schüllli,¹ G. Renaud,¹ E. Wintersberger,³ G. Chen,³ G. Bauer,³ and V. Holý⁴¹*Département de Recherche Fondamentale sur la Matière Condensée/SP2M/NRS, CEA Grenoble, 17 Avenue des Martyrs, F-38054 Grenoble Cedex 9, France*²*ID01/ESRF, 6 rue Jules Horowitz, BP 220, F-38043 Grenoble Cedex, France*³*Institut für Halbleiter- und Festkörperphysik, Johannes Kepler Universität Linz, 4040 Linz, Austria*⁴*Faculty of Mathematics and Physics, Charles University, Ke Karlovu 5, 121 16 Prague, Czech Republic*

(Received 17 July 2008; revised manuscript received 17 June 2009; published 16 July 2009)

The kinetics of the growth of Ge superdomes and their facets on Si(001) surfaces are analyzed as a function of deposited Ge thickness for different growth temperatures and at a low growth rate by *in situ* grazing-incidence small-angle x-ray scattering in combination with *in situ* grazing-incidence x-ray diffraction. At a low growth rate, intermixing is found to be enhanced and superdomes are formed already at lower coverages than previously reported. In addition, we observe that at the dome-to-superdome transition, a large amount of material is transferred into dislocated islands, either by dome coalescence or by anomalous coarsening. Once dislocated islands are formed, island coalescence is a rare event and introduction of dislocations is preferred. The superdome growth is thus stabilized by the insertion of dislocations during growth.

DOI: [10.1103/PhysRevB.80.045313](https://doi.org/10.1103/PhysRevB.80.045313)

PACS number(s): 61.05.C-, 81.07.Ta, 81.15.-z, 61.82.Fk

I. INTRODUCTION

The physical properties of semiconductor nanostructures depend entirely on their size, shape, and internal structure (strain and composition), which thus have to be fully controlled and understood. Semiconductor nanostructures are classically grown by the Stranski-Krastanow (SK) mechanism for which, beyond a critical thickness, islands are formed on a two-dimensional (2D) wetting layer. This is the case for the growth of Ge on Si(001) for which the 2D-three-dimensional (3D) transition is driven by the 4.16% lattice mismatch between Ge and Si, Ge having the larger lattice parameter. The mechanism of the SK growth of Ge layers on Si(001) substrates has been investigated extensively (see, e.g., Refs. 1 and 2 for a review). By increasing the Ge coverage above a critical thickness of ~ 4 monolayers (ML), islands that are coherent (i.e., without defects) appear. Square pyramids exposing {105} facets first form, followed by dome-shaped islands with {105}, {113}, and {15 3 23} facets, and a top (001) facet.³ Another type of coherent islands called “barns” with additional {111} and {20 4 23} facets^{4,5} may follow. For depositions higher than a threshold of about 9 ML,^{5,6} the misfit strain can no longer be accommodated coherently and larger islands named “superdomes” with interfacial misfit dislocations appear. They expose similar facets as barns but with different relative sizes.

The coherent pyramid and dome-shaped islands have been the subject of many very detailed recent studies that deal with their growth^{5,7,8} as well as with their strain and composition.^{9–11} For instance, different concepts on the role of strain relaxation, diffusion and temperature activation have been reported to describe Ge-Si intermixing in Ge nanostructures on Si(001) (Ref. 1) and Si(111).^{12,13} In contrast, much less work¹⁴ has been done in characterizing the superdomes. The kinetics of the superdome growth and of their shape transitions is still not completely understood. In particular, the evolution with the *growth rate*, with

temperature,¹⁵ and *deposited thickness* of the superdome apparition, size, and shape were not fully determined during growth. For example, Eaglesham *et al.*¹⁶ reported that islands grown at 773 K and with a height above 50 nm are no more dislocation-free. From x-ray reflectivity measurements¹⁷ on islands grown at 823 K with a very low growth rate, the island-height evolution was determined as a function of Ge deposition, exhibiting a sudden increase in island height at ~ 6 ML coverage. Apparently, at the transition, a huge amount of material is transferred into dislocated islands, either by island coalescence or by anomalous coarsening.

In this work we report on extensive *in situ* investigations of Ge island growth. The morphology of islands during their growth has been investigated so far by several *in situ* methods, such as electron or x-ray diffraction,¹⁸ scanning tunneling, or low-energy electron microscopies.^{8,19} Recently, grazing-incidence x-ray scattering (GISAXS) (Ref. 20) was used to analyze the shape and size of growing metallic islands. It has been shown to be a powerful tool in analyzing the faceting of semiconductor islands and in indexing their facets.²¹ With *in situ* GISAXS, contrary to other *in situ* techniques, not only the average diameter and height of the islands but also the average size of each facet can be directly determined during growth. In addition, *in situ* GISAXS was combined with grazing-incidence x-ray diffraction (GIXD), which allows monitoring the island nucleation by the beginning of lattice relaxation and following the evolution of the strain state. We report here on a combined GISAXS-GIXD study performed *in situ*, during the growth of Ge on Si(001) at a low growth rate and at different temperatures. The transition from the wetting layer to the dome and superdome formations is detected and quantitatively characterized by both techniques.

II. EXPERIMENTS

The samples were grown by molecular-beam epitaxy (MBE) in a dedicated ultrahigh vacuum chamber equipped

RICHARD *et al.*PHYSICAL REVIEW B **80**, 045313 (2009)

with large beryllium windows and coupled to a surface diffractometer for GIXD and GISAXS measurements, on the BM32 synchrotron beamline at the ESRF, Grenoble.²² The base pressure of the ultrahigh vacuum chamber is a few 10^{-11} mbar. The Si(001) substrates were deoxidized by annealing at 1200 K until a sharp 2×1 reconstructed reflection high-energy electron diffraction (RHEED) pattern was observed. Germanium was deposited with a Knudsen cell with a slow deposition rate of 170 s for one Ge ML (~ 0.006 ML/s), which was *in situ* calibrated using both a quartz microbalance and x-ray reflectivity. This rate is about seven times smaller than the deposition rate usually used for Ge/Si MBE experiments.⁷ Ge was deposited monolayer after monolayer at four growth temperatures (773, 823, 873, and 923 K). After growth, no damage induced by x rays was observed. We have experimentally determined with GISAXS and GIXD that no evolution of the island morphology, internal structure, or composition happens during annealing below 773 K. At 823 K, small changes were found to start only after 30 s of annealing, which confirms the observation of Medeiros-Ribeiro *et al.*²³ To avoid any evolution of the islands between successive depositions, the samples were immediately cooled down to 723 K after each added monolayer, the reference temperature at which the x-ray measurements were performed. These typically lasted 50 min, after which the temperature was raised again to the deposition temperature. During cooling or heating, the sample never stayed more than 30 s at intermediate temperatures between 773 K and the growth temperature so that significant morphological evolution or Si-Ge intermixing between successive depositions can be safely neglected.^{8,21,23} We actually checked that, for a growth temperature of 923 K, almost the same final state (as probed with GISAXS and GIXD) was obtained for a 7 ML deposition realized with the procedure described above, and a 7 ML deposition without growth interruption. Consequently, our successive depositions are equivalent to a continuous deposition with constant rate as a function of time; the deposited amount θ (Ge coverage) is proportional to an equivalent deposition time t .

For all x-ray measurements, the x-ray beam energy was set at 11 043 eV and the incident angle fixed at the critical angle for total external reflection of Si, $\alpha_i = 0.163^\circ$. The incident beam of 1 mrad (horizontal— H) \times 0.1 mrad (vertical— V) divergence, was defined by a pair of slits to 0.1 mm(H) \times 0.3 mm(V) at the sample position, the horizontal direction being perpendicular to the surface.

For GIXD measurements, the scattered beam direction was defined by a slit opening of 1 mm parallel to the surface and an 8 mm slit perpendicular to it. The slit-to-sample distances were 200 and 600 mm, respectively. For GISAXS measurements, slits and a beam stop were used in vacuum to avoid background scattering by the beryllium windows. The scattered intensity was detected by a two-dimensional low-noise charge-coupled device detector from Princeton (1152×1242 pixels of $56.25 \times 56.25 \mu\text{m}^2$) placed 1.68 m away from the sample. All direct- or reciprocal-space notations refer to the bulk Si unit cell ($a=b=c=5.431 \text{ \AA}$ and $\alpha=\beta=\gamma=90^\circ$). The Miller indexes (h , k , and l) are expressed in reciprocal-lattice units of Si.

GIXD measurements were performed mostly along the $\langle h0l \rangle$ direction (h being variable and l being small: $l=0.04$),

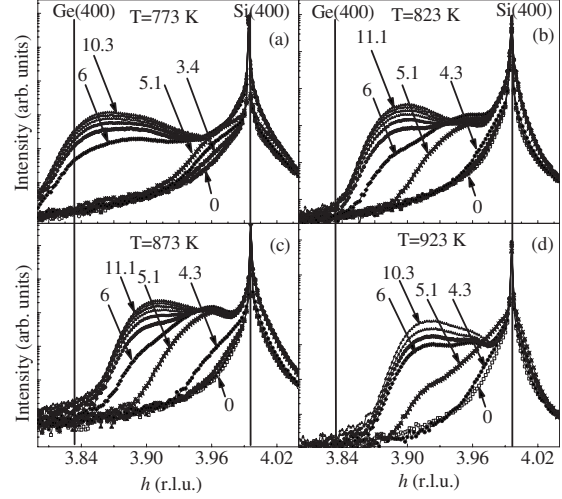


FIG. 1. GIXD data: radial scans along the $\langle h0l \rangle$ direction, with $l=0.04$, in the vicinity of the Si(400) reflection, for different Ge depositions indicated in the graphs in equivalent monolayers (ML). The vertical lines show the position of the bulk Si(400) and Ge(400) Bragg peaks. The growth temperatures are (a) 773 K (from 0 to 10.3 ML), (b) 823 K (from 0 to 11.1 ML), (c) 873 K (from 0 to 10.3 ML), and (d) 923 K (from 0 to 11.1 ML).

with finer measurements in the vicinity of the Si(400) and Ge(400) Bragg peaks (Fig. 1). These radial scans were recorded *in situ* for each added monolayer. GISAXS measurements consisted in recording two-dimensional GISAXS intensity distributions with the x-ray beam aligned along the substrate's $[100]$, $[110]$, (Fig. 2) and $[15\ 3\ 0]$ (Fig. 3) directions. The GISAXS maps represent cuts of the three-dimensional intensity distribution in reciprocal space with

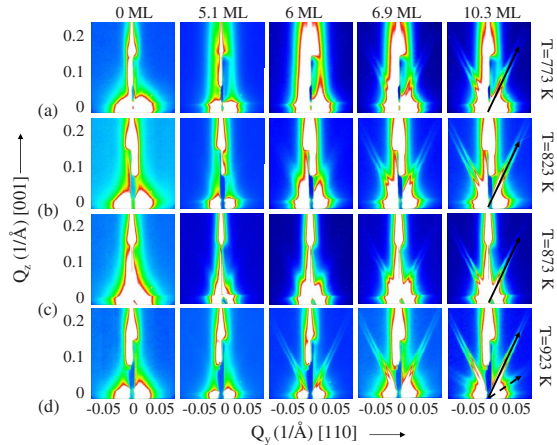


FIG. 2. (Color online) GISAXS intensity maps along the $[110]$ azimuth obtained at growth temperatures of (a) 773, (b) 823, (c) 873, and (d) 923 K; the numbers denote the number of deposited Ge monolayers, the arrows are along $\langle 113 \rangle$ (full arrows) and $\langle 111 \rangle$ (dashed arrow).

IN SITU X-RAY SCATTERING STUDY ON THE...

PHYSICAL REVIEW B 80, 045313 (2009)

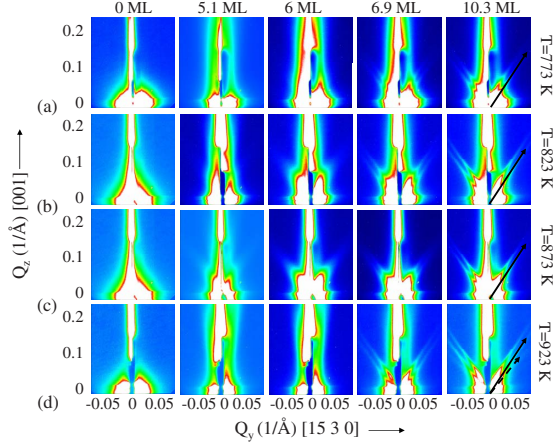


FIG. 3. (Color online) GISAXS intensity maps along the $[15\ 3\ 0]$ azimuth obtained at growth temperatures of (a) 773, (b) 823, (c) 873, and (d) 923 K; the numbers denote the number of deposited Ge monolayers, the arrows are along $\langle 15\ 3\ 23 \rangle$ (full arrows) and $\langle 20\ 4\ 23 \rangle$ (dashed arrow).

the Ewald sphere. The scattering vector is defined as $\mathbf{Q} = \mathbf{K}_f - \mathbf{K}_i$ ($\mathbf{K}_{i,f}$ are the wave vectors of the primary and scattered beams, respectively, having the angles $\alpha_{i,f}$ with the mean sample surface). The collected images correspond to (Q_y, Q_z) planes, which are tangential to the Ewald sphere.

III. GISAXS ANALYSIS

For the analysis of the GISAXS data we have used the distorted-wave Born approximation.²⁴ From this approach it follows that the intensity scattered by a noncapped island is a coherent superposition of four scattering processes. If we assume that the island positions are completely random and that the islands are far apart from each other, the intensity of the scattered radiation is an incoherent superposition of intensities scattered by individual islands

$$I(\mathbf{Q}) = \text{const} \sum_{n=1}^4 \sum_{m=1}^4 A_n A_m^* \langle \Omega^{\text{FT}}(\mathbf{Q}_n) \Omega^{\text{FT}*}(\mathbf{Q}_m) \rangle, \quad (1)$$

where the sums run over the scattering processes, and A_n and \mathbf{Q}_n are the amplitude and scattering vector of process n . The direct (kinematical) process $n=1$ is the scattering of the incident wave while the indirect processes $n=2, 3, 4$ imply reflections on the substrate and correspond to the multiple-scattering paths displayed in Fig. 4—see Ref. 24 for details. $\Omega^{\text{FT}}(\mathbf{Q})$ is the Fourier transform of the shape function $\Omega(\mathbf{r})$ of a single island and the averaging in Eq. (1) is carried out over all island sizes.

In the case of islands with flat facets, it is suitable to convert the volume integral calculating $\Omega^{\text{FT}}(\mathbf{Q})$ into an integral over the island surface $S(\Omega) = \cup_j S^{(j)}$ using the Stokes formula, which yields

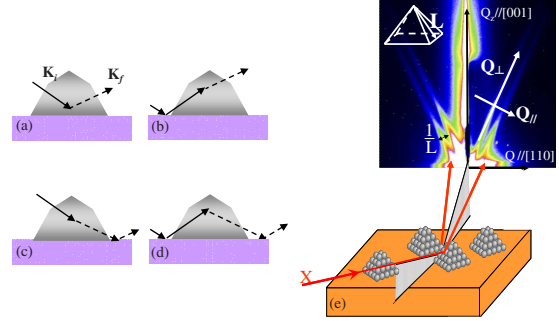


FIG. 4. (Color online) [(a)–(d)] Four scattering processes in GISAXS. $\mathbf{K}_{i,f}$ are the wave vectors of the primary and scattered beams, respectively. (e) Schematic drawing of islands and their corresponding GISAXS intensity map. The width of the streak is inversely proportional to the facet size L .

$$\Omega^{\text{FT}}(\mathbf{Q}) = \frac{i}{Q^2} \sum_j Q_{\perp}^{(j)} e^{-iQ_{\perp}^{(j)} r_{\perp}^{(j)}} F_j(\mathbf{Q}_{\parallel}^{(j)}). \quad (2)$$

In this equation, if we denote by $\mathbf{n}^{(j)}$ the unit vector of the outer normal of the facet j with the area $S^{(j)}$, then $r_{\perp}^{(j)} = \mathbf{r} \cdot \mathbf{n}^{(j)}$ is the distance of this facet from the origin (located at the center of the bottom of the islands), $Q_{\perp}^{(j)} = \mathbf{Q} \cdot \mathbf{n}^{(j)}$ is the component of \mathbf{Q} perpendicular to the facet, and $\mathbf{Q}_{\parallel}^{(j)} = \mathbf{n}^{(j)} \times (\mathbf{Q} \times \mathbf{n}^{(j)})$ is the component of \mathbf{Q} parallel to the facet. We have also denoted $F_j(\mathbf{Q}_{\parallel}^{(j)}) = \int_{S^{(j)}} d^2\mathbf{r}_{\parallel}^{(j)} e^{-i\mathbf{Q}_{\parallel}^{(j)} \cdot \mathbf{r}_{\parallel}^{(j)}}$ as the Fourier transformation of the shape function of the facet j .

Equation (2) makes it possible to analyze the contribution of individual facets to the intensity $I(\mathbf{Q})$. If we neglect tiny interference fringes (that are smeared out by the size averaging anyway), we can simplify the expression for the scattered intensity as follows:

$$I(\mathbf{Q}) \approx \text{const} \sum_j \sum_{n=1}^4 |A_n|^2 \left(\frac{Q_{\perp}^{(j)}}{Q_n^2} \right)^2 \langle |F_j(\mathbf{Q}_{\parallel}^{(j)})|^2 \rangle. \quad (3)$$

Within this approximation, the intensity is a sum of the contributions of individual facets. Each facet gives rise to a narrow streak in reciprocal space parallel to $\mathbf{n}^{(j)}$. The intensity distribution across the streaks is determined by $\langle |F(\mathbf{Q}_{\parallel})|^2 \rangle$, where the average is taken over by the distribution of facet sizes. A detailed numerical calculation of the shapes of the diffraction peaks from a set of facets with various shapes was performed using fast Fourier transform. It showed that the peak tails behave as Q_{\parallel}^{-3} , independently on the dispersion of the facet sizes. The full width at half maximum (FWHM) ΔQ_{\parallel} of the streak is inversely proportional to the mean facet size $L_0 \equiv \langle L \rangle$ (Fig. 4); however, the proportionality factor decreases with increasing root mean square (rms) deviation σ_L of L . For $\sigma_L \rightarrow 0$, $L_0 \rightarrow 2\pi / \Delta Q_{\parallel}$ holds. Along the streak, the intensity drops as $(Q_{\parallel}^{(j)})^{-2}$. In the case of a nonfaceted island with a rounded surface, the scattered intensity decreases as Q^{-4} (the Debye-Porod law²⁵) so that from the asymptotic intensity decrease it is possible to identify individual facets.

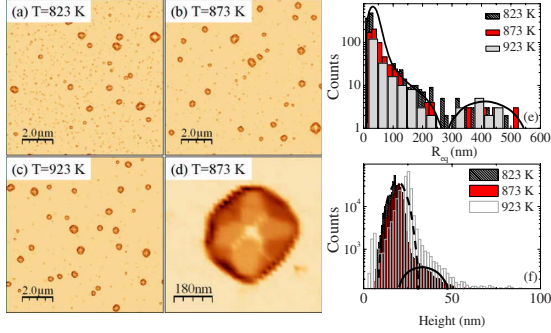
RICHARD *et al.*PHYSICAL REVIEW B **80**, 045313 (2009)

FIG. 5. (Color online) (a) AFM images of samples obtained after the deposition of 10–11 ML of Ge at (a) 823, (b) 873, and (c) 923 K, on a large scale, showing the presence of two island “families” with different mean sizes. (d) AFM zoom of a superdome island grown at 873 K. The measured mean sizes of {113} and {15 3 23} facets are ~ 145 and ~ 92 nm, respectively. They correspond to the simulated values observed in Figs. 8(a) and 8(b). (e) AFM histogram of the equivalent radii of the islands obtained from the island-projected area and (f) AFM histogram of the island heights as a function of the growth temperatures.

The indirect scattering processes ($n=2,3,4$) give rise to an additional streak for each facet if $Q_{nz} > 0$. Due to the reflection from the free surface, the additional streak is shifted vertically by $2K \sin \alpha_i$ and its intensity depends on the incidence or exit angles due to the reflectivity coefficients $r_{i,f}$. This effect has to be taken into account in the determination of the facet size from the streak width. The influence of the indirect scattering processes is visible in the experimental data taken along the [110] and [15 3 0] azimuths in Fig. 2 and 3, where the streaks are twofold.

Atomic force microscopy (AFM) measurements were performed *ex situ* on the samples after growth, i.e., for conditions corresponding to the total amount of deposited Ge. The AFM pictures of the surfaces [Figs. 5(a)–5(d)], and the histograms of the equivalent disk radius and heights of the islands [Figs. 5(e) and 5(f)] revealed that the island-size distribution is bimodal; small islands coexist with islands having a width and a height larger than 400 and 25 nm, respectively. Due to their larger scattering volume, the large ones dominate the GISAXS. Taking only into account the population of large islands, the rms deviation of the island sizes, $\sigma_L/L_0 = 0.17 \pm 0.03$, was obtained from the analysis of the AFM images.

In order to determine the evolution of the facet sizes, we have extracted line scans perpendicular to the streaks from the measured intensity maps and we have fitted the streak profile by a pair of modified Lorentzian functions $f(Q_{||}) = \text{const}[1 + (2Q_{||}/\Delta Q_{||})^2(2^{2/3} - 1)]^{-3/2}$ ($\Delta Q_{||}$ is the FWHM of the function), obeying the asymptotic decrease ($|Q_{||}|^{-3}$) of the scattered intensity and yielding perfect fits. From direct numerical simulations it follows that, for this value of σ_L , the FWHM of the streak is $\Delta Q_{||} \approx 2\pi/L_0$ with the accuracy of about 10%. The distance between the peaks stemming from various scattering processes is $\delta Q_{||} = 2K \sin \alpha_i \sin \beta$, where β is the angle of the facet with the surface normal (001).

Figure 6 shows an example of a fit of a line scan extracted from the GISAXS measurement in the [110] azimuth for a

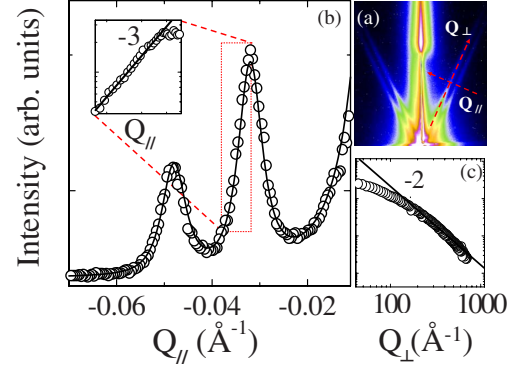


FIG. 6. (Color online) (a) GISAXS image (azimuth [110], $\theta = 10$ ML), from which the line scans in panels (b) and (c) are extracted along the $Q_{||}$ and Q_{\perp} axes. (b) The linear scan extracted from the GISAXS intensity map across the {113} facet streak (points) and its fit by a sum of three $f(Q_{||})$ functions (see text); the inset shows the tail of this line scan in a log-log representation. (c) Line scan along the facet streak. From (b) and (c), the Q_{\perp}^{-2} and $Q_{||}^{-3}$ slopes are visible.

deposition of 10 ML of Ge for the growth temperature of 873 K. This line scan is fitted by the sum of three modified Lorentzian functions, one corresponds to the streak of the top facet (001) (on the right side of the figure) while the other two stem from {113} facets. The study was not performed for the {105} facets appearing in the [100] azimuth because the flat-facet orientation (11° with respect to the [001] axis) and the small facet size induce a broadening of the {105} diffuse streaks that makes the extraction difficult. Therefore, only the {113} and {15 3 23} facet sizes were characterized. The insets in Fig. 6 show the linear scans extracted from the intensity map in the [110] azimuth for $\theta=10$ ML at a growth temperature of 873 K along and across the intensity streaks. The above predicted $Q_{||}^{-3}$ asymptotic dependence is clearly visible. The values of the mean sizes L_0 for the islands corresponding to the total amount of deposited Ge deduced from these fits are consistent with those deduced from the *ex situ* AFM measurements performed after growth (Fig. 5).

IV. EXPERIMENTAL RESULTS AND ANALYSIS

GIXD (Fig. 1) and GISAXS (Figs. 2 and 3) measurements were combined to have access to composition and strain (GIXD) as well as also to the morphology (GISAXS) of the growing islands. Figure 1 shows the GIXD measurements performed around the Si(400) Bragg peak at 773, 823, 873, and 923 K. Figures 2 and 3 show the corresponding GISAXS maps as a function of the Q_y and Q_z coordinates of the scattering vector, i.e., parallel and perpendicular to the sample surface, respectively, for the [110] (Fig. 2) and [15 3 0] (Fig. 3) azimuthal directions of the primary beam. The maps measured along the [100] azimuth are not shown because the expected scattering from {105} facets is hardly visible, being too close to the specular rod.

Below 2.6–3.4 ML (depending on the growth temperature) both GIXD and GISAXS measurements remain un-

changed. This is because of the growth of a perfectly strained (pseudomorphic) flat two-dimensional wetting layer, which scatters at the same location as the Si substrate. For depositions of 3–4 ML of Ge, depending on temperature, diffuse scattering appears in GIXD radial scans below the Si(400) Bragg peak, as well as faint changes in the GISAXS maps. These changes are in the form of diffuse intensity streaks (which are doubled as a consequence of the indirect scattering processes—see Sec. III) along $\langle 113 \rangle$ directions for the maps measured in the $[110]$ azimuth (Fig. 2) and along $\langle 15\ 3\ 23 \rangle$ directions (Fig. 3) for the maps measured in the $[15\ 3\ 0]$ azimuth. These streaks are signatures of the 2D-3D transition, with the formation of 3D islands on top of the wetting layer. These results show that GIXD is very sensitive to the onset of island nucleation by detecting the very first stages of relaxation of the island lattice.

Interpreting our results for GIXD and GISAXS, we can state that for $T=773$ K, the partially relaxed island volume does not increase rapidly until a coverage of about 5.1 ML is reached (Fig. 2). At this stage, no dome facets ($\{113\}$ and $\{15\ 3\ 23\}$) are detected on the GISAXS images. $\{105\}$ facets were detected but their streaks are too broad to be analyzed. Pyramid islands have thus been formed. These small islands are almost fully strained by the substrate: they have an in-plane lattice parameter very close to the Si one and the measured diffuse scattering mostly arises because of their small size. The scattered intensity is modulated by the form factor of pyramids.

At 6 ML, a huge increase in the diffuse scattering is observed on the GIXD scan [see Fig. 1(a)] and the diffuse signal moves toward much smaller h values. The signal can be attributed to much more relaxed islands. Indeed, due to the larger lattice parameter of Ge, the partially relaxed component due to germanium shifts to lower values of h and adopts a position close to that of bulk germanium. This coincides with the appearance of weak rods on the GISAXS pictures, corresponding to scattering by $\{113\}$ and $\{15\ 3\ 23\}$ facets, which are known to be present on Ge domes, barns, or superdomes on Si(001). The large lattice parameter of these islands, close to the value for bulk Ge, can only be explained by large plastically relaxed islands because coherent islands such as domes or barns are much more strained by the Si substrate.²⁶

To demonstrate this, we performed finite element method (FEM) simulations, using a program developed by Priester and co-workers.²⁷ Assuming a coherent, i.e., pseudomorphically strained dome-shaped island of the size of ~ 100 nm (as measured by GISAXS) of *even* pure Ge, the in-plane strain component ϵ_{xx} , defined with respect to the Si substrate lattice, was calculated [see Fig. 7(a)], and the scattered intensity was simulated [see Fig. 7(b)]. The main part of the simulated scattering is located around $h=3.945$. Only a weak shoulder is found around $h=3.89$, at the position of the experimental scattering intensity maximum: the average relaxation of the simulated island is far from being centered at the position of the experimental data and is shifted toward the position of the Si bulk Bragg peak. This demonstrates that the experimentally observed relaxation cannot be achieved by coherent elastic relaxation.

These large relaxed islands can thus be identified as large plastically relaxed, i.e., dislocated superdomes, exposing side

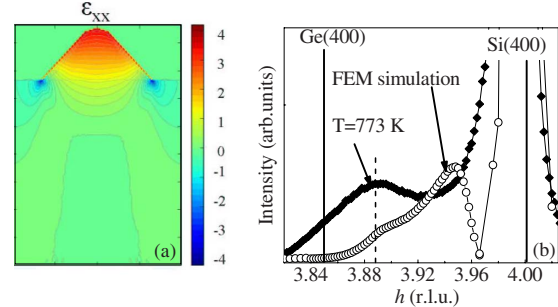


FIG. 7. (Color online) (a) FEM simulation of the in-plane deformation ϵ_{xx} in the island and the Si substrate underneath the island (with respect to Si bulk) in a 100-nm-large dome of pure Ge without dislocations. $\epsilon_{xx}=4.2\%$ means that Ge atoms are no more strained. In the region of the Si substrate, where $\epsilon_{xx}<0\%$, the Si lattice is compressed and where $\epsilon_{xx}>0\%$, the Si lattice is expanded. (b) Experimental and simulated scattered intensities. Finite element simulations of the strain state of coherent dome-shaped islands, and the corresponding simulation of the scattered intensity around the (400) reciprocal-lattice point show that their lattice parameter is much closer to that of Si than experimentally observed.

$\{113\}$ and $\{15\ 3\ 23\}$ facets. The GISAXS signal emanating from $\{111\}$ facets of the superdomes is so small compared to the $\{113\}$ ones that it is hardly detectable in the feet of the rods due to $\{113\}$ facets. In contrast, the average relaxation at coverage of 5.1 ML in Figs. 1(b) and 1(c) could be achieved by coherent elastic relaxation, showing that, at this stage, coherent domes are formed. Thus, in the present study, superdomes appear for lower coverages than previously reported.^{5,6} This can be explained by the much smaller deposition rate (0.0006 ML/s as opposed to 0.3 ML/s) in the present study. Rastelli *et al.*⁶ observed the formation of superdomes after a deposition of 8 ML of Ge at 823 K at a rate of 0.3 ML/s. A slow growth rate leads to a more complete relaxation¹⁷ by the introduction of dislocations, which can explain why dislocated islands are observed already at 6–6.9 ML for a growth temperature of 773 K in our case; this point will be discussed in next section in more detail. Note that very weak additional scattering streaks along $\langle 111 \rangle$ directions can be observed in the $[110]$ azimuth for a deposition of 7–8 ML at 873 K and for a deposition of 10 ML at 823 K. At $T=923$ K, weak additional streaks along $\langle 111 \rangle$ appear in the $[110]$ azimuth as early as 6 ML. The signal from the $\langle 111 \rangle$ streaks is clearly visible at 10 ML in Fig. 2(d). An onset of $\langle 20\ 4\ 23 \rangle$ streaks is also visible in Fig. 2(d), where its direction is denoted by a black arrow. The observation of the $\{111\}$ and $\{20\ 4\ 23\}$ facets in addition with AFM and the results of FEM simulations confirms the formation of dislocated superdomes after a deposit of 6 ML for the four studied temperatures. In GIXD scans, the pyramid- or dome-to-superdome transition is thus characterized by a strong strain relief causing a shift of the island-related maximum on the h axis to smaller h values.

In Fig. 8 we have plotted the dependence of the mean vertical sizes L_0 of the $\{113\}$ and $\{15\ 3\ 23\}$ facets for the growth temperatures of 773, 823, 873, and 923 K as a function of the deposited Ge coverage θ . Between 6 and 6.9 ML,

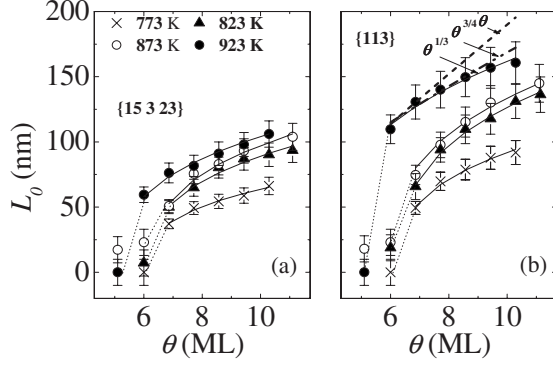
RICHARD *et al.*PHYSICAL REVIEW B **80**, 045313 (2009)

FIG. 8. The dependence of the mean facet sizes L_0 on the nominal coverage θ of the number of the deposited Ge monolayers is shown for the (a) {15 3 23} and (b) {113} facets, respectively. Above 6 ML at 923 K and 6.9 ML for the three other growth temperatures, the data were fitted to a $B(\theta - \theta_c)^{1/3}$ function (full lines).

a significant increase in the {113} and {15 3 23} facet sizes (Fig. 8) is observed. For instance, the mean size of the {113} facets increases from (0 ± 10) to (50 ± 5) nm between 6 and 6.9 ML deposits for the growth temperature of 773 K.

For $T=773$ K, above 6.9 ML, the facet size is found to evolve as $\theta^{1/3}$. This is shown in Fig. 8(b), where the dashed lines correspond to $\theta^{1/3}$, $\theta^{3/4}$, and θ^1 power laws. This $\theta^{1/3}$ power law implies that, given certain assumptions, the island volume V is proportional to the deposited Ge coverage θ . The assumptions are that (i) the apparent shape anisotropy of the superdomes is neglected, and (ii) small volume variations possibly induced by a different size variation in the {105}, {111}, or {20 4 23} facet areas are also neglected. The first hypothesis, which postulates that the apparent anisotropy of the superdomes does not influence the analysis of the GISAXS data with respect to the 1/3 power law, is justified as GISAXS measurements average over the facet sizes. During the superdome evolution, the island shape is changed, which causes changes in the relative sizes of different facet types; however, the area limited by the {105} facets is negligible with respect to that limited by the other dome or superdome facets^{5,6} so that the assumption (ii) is approximately valid as well. Furthermore, AFM images show that the area limited by the steep superdome facets ({111} and {20 4 23}) is almost negligible compared to the {113} and {15 3 23} superdome facets.

The 1/3 power-law observation excludes the possibility of the Ostwald ripening for which, according to Lifshitz-Slyozov,²⁸ Wagner,²⁹ and Chakraverty,^{30,31} the island size should increase as $t^{3/4}$ or t^1 , where t is the deposition time. Our results suggest that island coalescence occurs at the transition and, once dislocated islands are formed, the coalescence of islands is a rather rare event.^{32,33} This is consistent with AFM images, which reveal a large separation of superdome islands. Besides, no depletion region is evident around the dislocated islands. This was previously observed by Merdzhanova *et al.*¹⁴ for a faster growth rate (0.04 ML/s) and for a growth temperature around 843 K, and interpreted as the signature of a comparatively small efficiency of

anomalous coarsening at low temperatures. Note that the 1/3 power evolution of superdome facet sizes is valid supposing that the number of superdomes remains constant with increasing Ge deposition, after the coherent-to-incoherent growth transition, whereas their size increases accordingly. Moreover, the total volume of the domes remain constant after this transition; this is confirmed by the GIXD data since, in Figs. 1(b) and 1(c), the signal from the domes, located in between the signal from superdomes and the Si Bragg peak, does not change beyond the deposition of 7 ML. As no decrease or increase in the intensity of the scattering from domes is observed, dome coalescence is a rare event and in average, domes do not increase in size. This implies that, when superdomes are formed, the deposited Ge atoms preferentially attach to superdomes and their mean facet sizes will follow a 1/3 power law. Nevertheless, island capture induced by diffusion-mediated processes^{34–36} or anomalous coarsening^{8,14} cannot be excluded as it corresponds to a small amount of captured material compared to the volume of superdomes.

During the superdome growth, the GIXD data show that the maximum of relaxation stays almost constant but that the corresponding intensity increases [see Fig. 1(a), between 6 and 10.3 ML]. This is interpreted as being caused by the growth of superdomes as confirmed by the increase in the {113} and {15 3 23} facet sizes found by GISAXS. In the following, we define ϵ^{Ge} as the residual strain of a Ge island (with respect to the relaxed Ge lattice) and $\epsilon_0=4.16\%$ as the mismatch between bulk Ge and Si. In a one-dimensional model of an island of width w , relaxed by n dislocations of Burgers vector b , one has $\epsilon^{\text{Ge}} = \epsilon_0 - nb/w$ (Ref. 37). The above results show that ϵ^{Ge} is constant above $\theta=6$ ML while w increases with $\theta^{1/3}$. Thus, n also increases with θ . This implies that during the superdome growth, the introduction of dislocations is prevalent compared to the coalescence of islands and it reduces the need for strain energy relief by elastic deformation.

The same phenomena are observed for the other studied growth temperatures. The strong strain relief and the shift of the island relaxation toward the position of the Ge bulk Bragg peak in GIXD can be correlated with the introduction of dislocations inside the islands and to the formation of superdomes. If we consider the growth temperature of 923 K, at the dome-to-superdome transition (between 5.1 and 6 ML), the mean size of the {113} and {15 3 23} facets increases from (0 ± 10) nm to (110 ± 11) nm and to (60 ± 6) nm, respectively, whereas the mean {113} facet size is around 30 nm for a domelike island according to Ref. 38. The transition from domes to superdomes does not only explain the significant increase in the facet sizes; a large amount of material is transferred into dislocated islands at the transition as seen by the huge increase in the scattered intensity in GIXD.

The superdome growth is thus characterized by two phenomena. First, at the transition, the coalescence of domes is the dominant pathway toward the formation of dislocated islands. Second, during the growth of superdomes, the fact that their volume growth is proportional to the deposit implies that superdome coalescence is a rare event. The introduction of dislocations prevails and the superdomes are char-

IN SITU X-RAY SCATTERING STUDY ON THE...

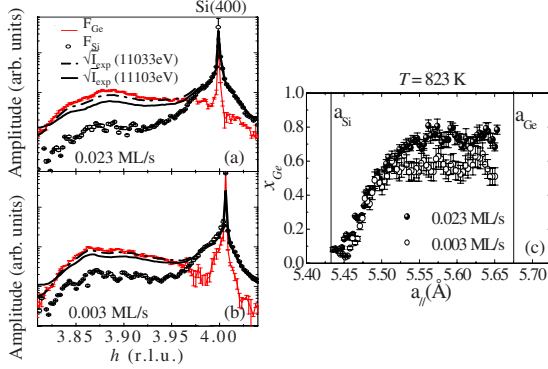
PHYSICAL REVIEW B **80**, 045313 (2009)

FIG. 9. (Color online) Experimental anomalous x-ray diffraction data (\sqrt{I}_{exp}) measured at two energies (11 033 and 11 103 eV), and Ge and Si structure factors (F_{Ge} and F_{Si}) calculated from the experimental anomalous x-ray diffraction data. The curves are plotted as a function of lattice parameter for a growth temperature of 873 K, a deposit of 8 ML, and for two growth rates: (a) 0.023 and (b) 0.003 ML/s. (c) Ge content of the islands determined from the ratio of the Ge and Si structure factors versus in-plane lattice constant.

acterized roughly by a self-similar volume increase. The $\{113\}$ and $\{15\ 3\ 23\}$ facets continue to grow and are not suppressed by the introduction of the steeper $\{111\}$ and $\{20\ 4\ 23\}$ facets.

From the fit of the experimentally determined mean facet sizes L_0 to the $\theta^{1/3}$ power law $L_0=B(\theta-\theta_c)^{1/3}$, where B and θ_c are constant, we determined the temperature dependence of the constant B for both investigated facet types. The value of $B_{\{113\}}/B_{\{15323\}}$ is found to be constant, around 1.5 ± 0.1 in the investigated temperature range, which implies that the superdome shape does not strongly depend on temperature.

From GIXD data taken after completing the deposition of Ge (10–11 ML), the average lateral lattice parameter of the superdomes was obtained as a function of temperature: 5.62 Å at 773 K, 5.58 Å at 823 K, 5.57 Å at 873 K, and 5.55 Å at 923 K. With increasing temperature, the average lattice parameter of the islands decreases. According to the findings in Ref. 14, this dependence is caused by the increase in the Si content for increasing growth temperature (see also Refs. 39–41). This has been confirmed by multiwavelength anomalous diffraction measurements performed at the end of each growth. As superdomes are formed at 6 ML at $T=923$ K and 6–6.9 ML at $T=773$ K, it appears that for a low growth rate the nucleation of dislocations is almost temperature independent. To determine if intermixing increases with growth rate, we performed multiwavelength anomalous x-ray diffraction measurements for two different growth rates (0.023 and 0.003 ML/s) at a growth temperature of 823 K for a deposit of 8 ML of Ge. In this experiment, we have compared the GIXD intensities measured for various photon energies around the Ge K edge, in various positions h in reciprocal space,²¹ and we have extracted the Si and Ge structure factors (F_{Ge} and F_{Si}) as illustrated in Figs. 9(a) and 9(b). From the ratio of the Si and Ge structure factors, we determined the Ge content x_{Ge} of the islands as a function of in-plane lattice parameter [Fig. 9(c)]. From the figure it fol-

lows that the maximum Ge content in the island volume decreases with decreasing growth rate. Since the superdome shapes grown by different growth rates are similar, we conclude that the average Ge content in the island decreases with decreasing growth rate. This is the evidence that Si intermixing is enhanced for lower growth rates.

V. DISCUSSION

In the following, we propose a model to explain these observations. For this purpose, we will use the phenomenological relation given in Ref. 14, which links the critical volume to incorporate a dislocation to the Ge content: $x_{Ge} = 3.7V_c^{-1/6}$, where V_c is expressed in nm^3 [see Fig. 2(d) of Ref. 14]. This relation was proven theoretically to be appropriate by Marzegalli *et al.*⁴² who computed this critical volume for the onset of plastic strain relaxation in SiGe islands on Si(001) for different Ge contents and realistic shapes by using a three-dimensional model, with position-dependent dislocation energy. The average island volume expressed in nm^3 depends on the island density ρ (islands/ nm^2), Ge coverage θ (atoms/ nm^2), and island lattice parameter a (nm) as $V = \frac{a^3 \theta}{8 \rho}$. The critical coverage, θ_c expressed in atoms/ nm^2 at the dome-to-superdome transition is thus given by

$$\theta_c = \frac{8\rho V_c}{a^3} = \frac{8 \times 3.7^6 \rho}{x_{Ge}^6 a^3}, \quad (4)$$

where ρ , a , and V_c are expressed in islands/ nm^2 , nm, and nm^3 , respectively. The Ge concentration x_{Ge} and the island density ρ can be written as a function of flux F at a given temperature. From Ref. 43, it can be shown that the average Ge fraction x_{Ge} decreases almost linearly with decreasing growth rate, F at 923 K: $x_{Ge} = x_1 + x_2 F$, x_1 , and x_2 (min/ML) are some positive constants, with F expressed in ML/min. A decrease in the x_{Ge} value with decreasing F follows from our anomalous diffraction experiment (see Fig. 9).

From Ref. 44 (see Fig. 2) at 873 K, the island density increases with increasing F ; $\rho = \beta F^{2/3}$, where β is a constant, ρ and F are expressed in islands/ nm^2 and ML/min, respectively. Thus the critical coverage (expressed in atoms/ nm^2) of the dome-to-superdome transition as a function of flux F at growth temperatures in the 873–923 K range is given by the following empirical relation:

$$\theta_c = \frac{8 \times 3.7^6 \beta F^{2/3}}{a^3 (x_1 + x_2 F)^6}. \quad (5)$$

For small fluxes F , θ_c is growing while for fluxes above $\frac{x_1}{8x_2}$, it is decreasing [see Fig. 10(b)]. If we estimate $x_1=0.5$ and $x_2=0.006$ min/ML (Refs. 14 and 43) at 873–923 K, the critical coverage is an increasing function of the flux F for fluxes smaller than 0.174 ML/s. The flux of 0.006 ML/s [dashed line in Fig. 10(a)] used in this work is much smaller than the flux of 0.04 ML/s reported in Ref. 14 [full line in Fig. 10(a)], i.e., the one usually used in MBE growth of Ge islands. This explains our experimental results, namely, the advanced transition of domes to superdomes for the substantially lower Ge growth rate. From the rough estimation of the critical island volume for the dome-to-superdome transition, from the criti-

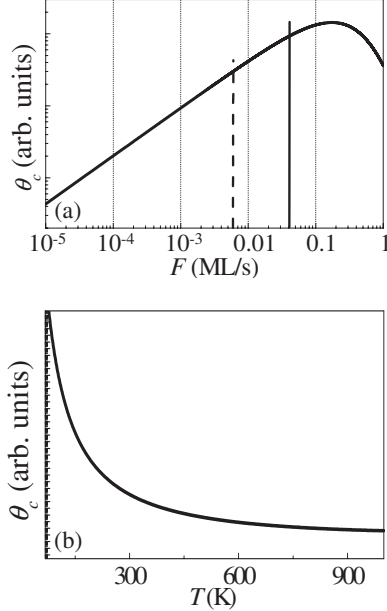
RICHARD *et al.*PHYSICAL REVIEW B **80**, 045313 (2009)

FIG. 10. Evolution of the critical coverage θ_c for which dislocations appear, as a function of (a) flux F and (b) growth temperatures. The dashed and full lines in (a) indicate the growth rates used in this work and the one used in Ref. 14, respectively.

cal coverage θ_c , the critical Ge concentration $x_{\text{Ge}}^{\text{crit}} \approx 0.6$, and from the island density, we roughly estimated that the amount of Ge transferred from the wetting layer to the island is negligible at this transition. This finding is confirmed by experimental results published earlier,²¹ showing that approximately 1 ML of Ge is transferred from the wetting layer to the dome volumes. However, above the dome-to-superdome transition, the superdome volumes were found to grow linearly with the coverage, i.e., no Ge transfer from the wetting layer to the superdome volume was detectable.

The Ge content of the islands x_{Ge} and the island density ρ can also be written as a function of temperature at a given flux. With increasing temperature T , x_{Ge} decreases due to intermixing^{41,45} and ρ decreases as well, fulfilling the Arrhenius law.⁴⁶ From Refs. 41 and 45, a phenomenological relation can be obtained for x_{Ge} : $x_{\text{Ge}} \sim -0.1746 + 6.15 \times 10^8 T^{-3}$ (T is expressed in K) in the 0.035–0.33 ML/s range. In the following, we suppose that, at our growth rate (0.006 ML/s), this tendency is still applicable. From the AFM measurements of the studied samples, the evolution of the island density as a function of time has been determined as $\rho \sim 0.24 \times 10^{-9} e^{\delta/T}$ islands/nm², with $\delta \sim 7380$ K and T is the temperature. The critical coverage of the dome-to-superdome transition at a flux of 0.006 ML/s and as a function of temperature is then given by the following phenomenological relation:

$$\theta_c \sim \frac{8 \times 3.7^6 \times 0.24 \times 10^{-9} e^{\delta/T}}{a^3 [-0.1746 + 6.15 \times 10^8 T^{-3}]^6}. \quad (6)$$

For T higher than 205 K, the critical coverage is decreasing as a function of growth temperature [see Fig. 10(b)]. At 973

K, dislocations will appear at a coverage that is only about ~ 0.25 ML smaller compared to one for which superdomes appear at a growth temperature of 723 K: $|\theta_c(T=923 \text{ K}) - \theta_c(T=723 \text{ K})| \sim 1.54 \text{ atoms/nm}^2 \sim 0.25 \text{ ML}$, assuming that the islands consist of pure Ge. Thus for our work follows that the critical coverage is almost temperature independent, as experimentally observed.

VI. CONCLUSION

We have studied the evolution of the size of superdome facets of Ge islands on (001) Si substrates and their relaxation state for comparatively low growth rates, using *in situ* grazing-incidence small-angle x-ray scattering and diffraction. From the evolution of the widths of GISAXS intensity streaks in reciprocal space, we have determined the growth kinetics of the superdome {113} and {15 3 23} facets. The 1/3 power-law dependence of the superdome facet size on the amount of deposited Ge indicates that once dislocated islands are formed, the coalescence of islands, if any, is a rare event. However, Ostwald ripening and anomalous coarsening cannot be excluded. At the dome-to-superdome transition, a huge amount of material is transferred into dislocated islands either by dome coalescence or anomalous coarsening. From *in situ* grazing-incidence diffraction experiment it follows that the mean lateral lattice parameter of the superdomes remains constant during their growth. Thus, superdomes are stabilized by the insertion of dislocations during their growth. We also demonstrate that a low growth rate shifts the onset for dislocation formation to lower Ge coverages than for higher growth rates.

The strength of the present work lies in the direct determination, *in situ*, of the evolution of the statistical average of the facet sizes as a function of deposited material during the MBE growth under UHV conditions.

We show that *in situ* UHV-GISAXS measurements during MBE growth complement microscopic techniques and allows for a systematic study of the statistical average of facet sizes as a function of the deposited amount of Ge and of growth temperatures. Combined with *in situ* GIXD, it leads to a complete understanding of both strain status and composition as well as of the morphology of the islands.

We expect that the island evolution reported here can be employed for the study of other Stranski-Krastanow islands systems. A further step will consist in the characterization of defect formation and their evolution during the *in situ* growth of superdomes using quasiforbidden x-ray diffraction.^{47,48}

ACKNOWLEDGMENTS

The authors thank C. Priester and V. Favre-Nicolin for the development of the FEM and diffraction simulation programs. This work is a part of the research program MSM under Grant No. 0021620834 that is financed by the Ministry of Education of the Czech Republic. E.W., G.C., and G.B thank the FWF, Vienna, Austria (Project No. SFB025) for support. The authors acknowledge additional support from the EC network SANDiE.

IN SITU X-RAY SCATTERING STUDY ON THE...

PHYSICAL REVIEW B **80**, 045313 (2009)

- ¹F. Ratto, G. Costantini, A. Rastelli, O. G. Schmidt, K. Kern, and F. Rosei, *J. Exp. Nanosci.* **1**, 279 (2006).
- ²J. Stangl, V. Holý, and G. Bauer, *Rev. Mod. Phys.* **76**, 725 (2004).
- ³G. Medeiros-Ribeiro, A. M. Bratkowski, T. I. Kamins, D. A. A. Ohlberg, and R. S. Williams, *Science* **279**, 353 (1998).
- ⁴E. Sutter, P. Sutter, and J. E. Bernard, *Appl. Phys. Lett.* **84**, 2100 (2004).
- ⁵M. Stoffel, A. Rastelli, J. Tersoff, T. Merdzhanova, and O. G. Schmidt, *Phys. Rev. B* **74**, 155326 (2006).
- ⁶A. Rastelli and H. Von Känel, *Surf. Sci. Lett.* **515**, L493 (2002).
- ⁷A. Rastelli, M. Stoffel, J. Tersoff, G. S. Kar, and O. G. Schmidt, *Phys. Rev. Lett.* **95**, 026103 (2005).
- ⁸F. M. Ross, R. M. Tromp, and M. C. Reuter, *Science* **286**, 3 (1999).
- ⁹G. Katsaros, G. Costantini, M. Stoffel, R. Esteban, A. M. Bittner, A. Rastelli, U. Denker, O. G. Schmidt, and K. Kern, *Phys. Rev. B* **72**, 195320 (2005).
- ¹⁰A. Malachias, S. Kycia, G. Medeiros-Ribeiro, R. Magalhães-Paniago, T. I. Kamins, and R. Stanley Williams, *Phys. Rev. Lett.* **91**, 176101 (2003).
- ¹¹U. Denker, M. Stoffel, and O. G. Schmidt, *Phys. Rev. Lett.* **90**, 196102 (2003).
- ¹²F. Ratto, A. Locatelli, S. Fontana, S. Kharrazi, S. Ashtaputre, S. K. Kulkarni, S. Heun, and F. Rosei, *Small* **2**, 401 (2006).
- ¹³N. Motta, F. Boscherini, A. Sgarlata, A. Balzarotti, G. Capellini, F. Ratto, and F. Rosei, *Phys. Rev. B* **75**, 035337 (2007).
- ¹⁴T. Merdzhanova, S. Kiravittaya, A. Rastelli, M. Stoffel, U. Denker, and O. G. Schmidt, *Phys. Rev. Lett.* **96**, 226103 (2006).
- ¹⁵D. J. Eaglesham and R. Hull, *Mater. Sci. Eng., B* **30**, 197 (1995).
- ¹⁶D. J. Eaglesham and M. Cerullo, *Phys. Rev. Lett.* **64**, 1943 (1990).
- ¹⁷A. A. Williams, J. M. C. Thornton, J. E. Macdonald, R. G. van Silfhout, J. F. van der Veen, M. S. Finney, A. D. Johnson, and C. Norris, *Phys. Rev. B* **43**, 5001 (1991).
- ¹⁸M. Takahashi, T. Kaizu, and J. Mizuki, *Appl. Phys. Lett.* **88**, 101917 (2006).
- ¹⁹O. Kirfel, E. Müller, D. Grützmacher, K. Kern, A. Hesse, J. Stangl, V. Holý, and G. Bauer, *Appl. Surf. Sci.* **224**, 139 (2004).
- ²⁰G. Renaud, R. Lazzari, Ch. Revenant, A. Barbier, M. Noblet, O. Ulrich, F. Leroy, J. Jupille, Y. Borensztein, C. R. Henry, J.-P. Deville, F. Scheurer, J. Mane-Mane, and O. Fruchart, *Science* **300**, 1416 (2003).
- ²¹T. U. Schüllli, M.-I. Richard, G. Renaud, V. Favre-Nicolin, E. Wintersberger, and G. Bauer, *Appl. Phys. Lett.* **89**, 143114 (2006).
- ²²<http://www.esrf.eu/UsersAndScience/Experiments/CRG/BM32>
- ²³G. Medeiros-Ribeiro, T. I. Kamins, D. A. A. Ohlberg, and R. Stanley Williams, *Phys. Rev. B* **58**, 3533 (1998).
- ²⁴M. Rauscher, R. Paniago, H. Metzger, Z. Kovats, J. Domke, J. Peisl, H.-D. Pfannes, J. Schulze, and I. Eisele, *J. Appl. Phys.* **86**, 6763 (1999).
- ²⁵A. Guinier and G. Fournet, *Small Angle Scattering of X-rays* (Wiley, New York, 1955).
- ²⁶M.-I. Richard, T. U. Schüllli, C. Priester, V. Favre-Nicolin, and G. Renaud (unpublished).
- ²⁷V. Ranjan, G. Allan, C. Priester, and C. Delerue, *Phys. Rev. B* **68**, 115305 (2003).
- ²⁸I. M. Lifshitz and V. V. Slyozov, *J. Phys. Chem. Solids* **19**, 35 (1961).
- ²⁹C. Wagner, *Z. Elektrochem.* **65**, 581 (1961).
- ³⁰B. K. Chakraverty, *J. Phys. Chem. Solids* **28**, 2401 (1967).
- ³¹B. K. Chakraverty, *J. Phys. Chem. Solids* **28**, 2413 (1967).
- ³²P. Meakin, *Rep. Prog. Phys.* **55**, 157 (1992).
- ³³J. L. Viovy, D. Beysens, and C. M. Knobler, *Phys. Rev. A* **37**, 4965 (1988).
- ³⁴P. A. Mulheran and J. A. Blackman, *Phys. Rev. B* **53**, 10261 (1996).
- ³⁵F. Ratto, T. W. Johnston, S. Heun, and F. Rosei, *Surf. Sci.* **602**, 249 (2008).
- ³⁶F. Ratto, A. Locatelli, S. Fontana, S. Kharrazi, S. Ashtaputre, S. K. Kulkarni, S. Heun, and F. Rosei, *Phys. Rev. Lett.* **96**, 096103 (2006).
- ³⁷F. K. LeGoues, M. C. Reuter, J. Tersoff, M. Hammar, and R. M. Tromp, *Phys. Rev. Lett.* **73**, 300 (1994).
- ³⁸A. Rastelli, M. Kummer, and H. von Kanel, *Phys. Rev. Lett.* **87**, 256101 (2001).
- ³⁹D. J. Smith, D. Chandrasekhar, S. A. Chaperro, P. A. Crozier, J. Drucker, M. Floyd, M. R. McCartney, and Y. Zhang, *J. Cryst. Growth* **259**, 232 (2003).
- ⁴⁰M. Floyd and Y. Zhang, *Appl. Phys. Lett.* **82**, 1473 (2003).
- ⁴¹T. U. Schüllli, M. Stoffel, A. Hesse, J. Stangl, R. T. Lechner, E. Wintersberger, M. Sztucki, T. H. Metzger, O. G. Schmidt, and G. Bauer, *Phys. Rev. B* **71**, 035326 (2005).
- ⁴²A. Marzegalli, V. A. Zinoviyev, F. Montalenti, A. Rastelli, M. Stoffel, T. Merdzhanova, O. G. Schmidt, and L. Miglio, *Phys. Rev. Lett.* **99**, 235505 (2007).
- ⁴³E. P. McDaniels, Q. Jiang, P. A. Crozier, J. Drucker, and D. J. Smith, *Appl. Phys. Lett.* **87**, 223101 (2005).
- ⁴⁴B. Cho, T. Schwarz-Selinger, K. Ohmori, D. G. Cahill, and J. E. Greene, *Phys. Rev. B* **66**, 195407 (2002).
- ⁴⁵G. Capellini, M. De Seta, and F. Evangelisti, *Appl. Phys. Lett.* **78**, 303 (2001).
- ⁴⁶J. S. Sullivan, H. Evans, D. E. Savage, M. R. Wilson, and M. G. Lagally, *J. Electron Mater.* **28**, 426 (1999).
- ⁴⁷M.-I. Richard, T. H. Metzger, V. Holý, and K. Nordlund, *Phys. Rev. Lett.* **99**, 225504 (2007).
- ⁴⁸M.-I. Richard, A. Malachias, J.-L. Rouvière, T.-S. Yoon, Y.-H. Xie, V. Holý, E. Holmström, K. Nordlund, and T.-H. Metzger, (unpublished).

2.4.2 *In situ x-ray study of the formation of defects in Ge islands on Si(001)***M.-I. Richard, T. U. Schülli, G. Renaud****submitted to Applied Physics Letters (2011)**

The introduction of defects at a certain growth stage leads to partial plastic relaxation of strain inside the islands. Such defects negatively influence the electronic properties of such islands and thus compromise their potential for future optoelectronic applications. It is thus of crucial importance to study their appearance and evolution during island growth in order to conclude on the driving forces governing their formation. The following study makes use of the high symmetry of the Diamond-type structure of Si and Ge. The arrangement of atoms in one unit cell leads to destructive interference of x-rays at reciprocal lattice points (hkl) with $h + k + l = 2(2N + 1)$, N being an integer number. One generally speaks of forbidden reflections in this case. Typical defects observed in strained SiGe structures are stacking faults caused by extra $\{111\}$ planes or missing ones. This leads to a break of the lattice symmetry and thus to an incomplete destructive interference at the position of forbidden reflections. As stacking faults represent 2D objects, their "footprint" in reciprocal space are streaks along the $[111]$ direction. Their appearance during growth allows to detect the stage of defect formation. Quantitative information about their size and the lattice parameter of the dislocated region can be extracted.

***In situ* x-ray study of the formation of defects in Ge islands on Si(001).**M.-I. Richard^{1*}, T. U. Schülli², G. Renaud³¹Université Paul Cézanne Aix-Marseille, IM2NP-CNRS,

Faculté des Sciences de St Jérôme, 13397 Marseille, France

²ID01/ESRF, 6 rue Jules Horowitz, BP220, F-38043 Grenoble Cedex, France and³CEA-UJF, INAC, SP2M, 17 rue des martyrs, F-38054 Grenoble, France

(Dated: April 1, 2011)

Plastic relaxation and formation of defects is a crucial issue in the epitaxial growth of nanoparticles and thin films. Here, we report an *in situ* non-destructive method based on x-ray diffuse scattering close to forbidden reflections to study the formation of defects during the growth of Ge islands on Si(001). The dependence of in-plane spacing between interfacial dislocations, defect size and density is analyzed as a function of Ge-deposit. It is found that the introduction of additional defects is preferred to relieve strain during growth.

PACS numbers: 61.10.Eq, 61.10.Nz, 81.07.-b

The mechanism of island formation of Ge on Si(001) via the Stranski-Krastanow growth mode has been extensively investigated in the past years. In a simplified general scenario the growth of Ge islands proceeds as follows. After deposition of 3-4 monolayers (ML), the strain energy stored in the wetting-layer is partially relaxed by the formation of three-dimensional (3D) islands. They evolve from pyramids to domes, *i.e.* from shallower to steeper morphologies, increasing their size and therefore their total volume [1, 2]. Finally, when the island volume exceeds a critical value elastic relaxation stops being effective for driving the system to a metastable equilibrium state, and plastic relaxation occurs with the formation of large dislocated islands called superdomes [1–4]. These dislocated islands contain mostly {111}-type stacking-faults which originate at the Ge/Si interface [5] and strain-relieving misfit dislocations [3, 4, 6–8].

In this letter, the evolution of defects is studied using *in situ* x-ray diffraction during molecular beam epitaxy (MBE) growth of Ge islands on Si(001). X-ray reciprocal space mapping around forbidden reflections has proven to be a powerful tool to probe the type of defects as well as their average size and the strain fields inside Si crystals [9] or Ge islands grown on Si(001) [10, 11]. The technique has allowed to study planar faults (stacking-faults) and twin faults in nanostructures, as well as to study the structure of the core of defects in a Si crystal. Here we apply this technique *in situ* during Ge island growth to observe the mechanism of defect formation. Investigations were carried out using a system for *in situ* x-ray studies of MBE growth located at beamline BM32 of ESRF [12]. The base pressure of the ultra-high vacuum chamber was below 10^{-10} mbar. The Si(001) substrate was deoxidized by annealing at 1200 K until a sharp, 2x1 reconstructed, Reflection High Energy Electron Diffraction (RHEED) pattern was observed. Germanium was deposited with a Knudsen cell with a slow deposition rate of ~ 0.006

ML/s, which was *in situ* calibrated using both a quartz microbalance and x-ray reflectivity. Ge was deposited monolayer after monolayer at 923 K. To avoid any evolution of the islands between successive depositions, the sample was immediately cooled down to 723 K after each added monolayer, the reference temperature at which the x-ray measurements were performed. During cooling or heating, the sample never stayed more than 30 s at intermediate temperatures between 723 K and the growth temperature, so that significant morphological evolution or Si-Ge intermixing between successive depositions can be safely neglected [2, 13, 14]. Consequently, our successive depositions can be considered equivalent to a continuous deposition with constant rate, as a function of time: the deposited amount θ (Ge-coverage) is proportional to an equivalent deposition time t .

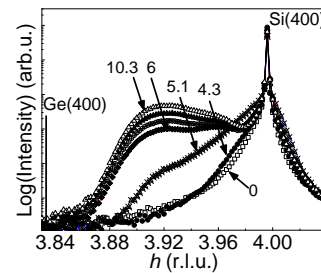


FIG. 1: GIXD data: radial scans along the $\langle h0l \rangle$ direction, with $l=0.04$, in the vicinity of the Si(400) reflection, for different Ge depositions indicated in the graphs in equivalent monolayers ML.

During the growth, *in situ* grazing-incidence small angle x-ray scattering (GISAXS) was combined to grazing-incidence x-ray diffraction (GIXD). GISAXS has been shown to be a powerful tool to analyze the faceting of nano-islands and to index their facets [13, 15]. GIXD allows monitoring the island nucleation by the beginning of lattice relaxation and following the strain state. Figure 1 displays GIXD measurements performed along the $\langle h0l \rangle$

*marie-ingrid.richard@im2np.fr

direction (h being variable and l being small: $l=0.04$), with finer measurements in the vicinity of the Si(400) and Ge(400) Bragg peaks. These radial scans were recorded *in situ* for each added monolayer. GISAXS intensity maps measurements along the [110] and [15 3 0] azimuths are displayed in Figs. 2(b) and 3(b) of Reference [16]. Below 2.6 ML, GIXD and GISAXS measurements remain unchanged. This is because of the growth of a perfectly strained (pseudomorphic) flat two-dimensional wetting layer, which scatters at the same location as the Si substrate. At $\theta=4.3$ ML, diffuse scattering appears in the GIXD radial scan below the Si(400) Bragg peak, which corresponds to the formation of strained pyramids. At $\theta=5.1$ ML, the diffuse signal moves towards small h values due to the formation of relaxed domes as confirmed by the observation of rods of scattering from {113} and {15 3 23} facets in the GISAXS images. At 6 ML, a change of the relaxation state is observed in GIXD. It can be related to the formation of other islands, called barns or superdomes as rods of scattering from {111} facets are observed in GISAXS images.

To monitor the formation of defects during growth, scans were performed around the (200) basis-forbidden reflection as a function of Ge deposit. Figure 2 depicts an in-plane reciprocal space map of diffuse scattering measured around the Si(200) position. The intensity was measured by a position sensitive detector collecting the diffracted signal between $\alpha_f \sim 0^\circ$ and $\alpha_f \sim 1.5^\circ$ for a deposit of 10.3 ML of Ge. According to previous studies [10, 11], the integrated hump-like intensity, which follows the $\langle 110 \rangle$ directions in the plane, is a characteristic footprint of {111} stacking-faults (SFs) or twin faults. Stacking-faults, which lie in {111} planes, result from the incorporation or removal of a double plane in the usual stacking sequence. From symmetry considerations, it follows that the reciprocal-space distribution of the intensity scattered by stacking-faults or twins, what we call hereafter {111}-type defects, is concentrated along $\langle 111 \rangle$ lines. Thus, the projected $\langle 110 \rangle$ streaks reveal the presence of {111}-type defects in the SiGe islands. Interstitial-type defects result from a local lattice compression and will exhibit a higher diffuse intensity for $\mathbf{G} \cdot \delta \mathbf{h} < 0$, where $\delta \mathbf{h}$ indicates the deviation of a point in the reciprocal space along the h direction from the Bragg reflection $\mathbf{G}=(200)$. The asymmetric intensity distribution of the streaks with higher intensity for lower h values as shown in Fig. 2 indicates that the {111} defects are interstitial-type defects.

Figures 3 (a) and (b) display angular scans at $h=1.94$ and radial scans around the (200) reflection, respectively (see the lines denoted (b) and (c) in Fig. 2). At $h=1.94$, the signal comes entirely from {111}-type defects. Intensity is observed after a deposit of 6.0 ML. This is the signature of the formation of streaks along the $\langle 111 \rangle$ directions associated to the formation of {111}-type defects. This confirms the formation of dislocated islands for this deposit. Figure 3 (a) and (b) shows an increase of the integrated intensity of the streaks with increasing

Ge deposit.

To quantify the evolution of the average size of {111}-type defects, perpendicularly to the $\langle 111 \rangle$ directions, as a function of Ge deposit, the full width at half maximum along the angular direction of the streaks ($\Delta k_{[010]}$) was fitted using Gaussian functions. Taking into account the broadening conditioned by the intersection angle at 45° , the average size of the {111}-type defects, perpendicularly to the [111] direction is then: $d = a/(\cos(\pi/4) \cdot \Delta k_{[010]})$, where a is the average lattice parameter of the islands (here $a = 5.54 \text{ \AA}$ with an average Ge content of $x_{Ge} \sim 0.5$ determined by multiwavelength anomalous diffraction). The size evolution is displayed in Fig. 3 (c) and reveals that during growth and for $6.0 \text{ ML} \leq \theta \leq 10.3 \text{ ML}$, the average size of the {111}-type defects is relatively constant: $d = (20 \pm 2) \text{ nm}$. Figure 3 (d) displays the evolution of the integrated intensity measured from scans in Fig. 3 (a) as a function of Ge deposit. A linear increase of the integrated intensity is observed with Ge deposit, implying that the number of {111}-type defects increases linearly with Ge deposit as the integrated intensity is proportional to the numbers of scattered atoms. Contrary to annealing [17], the introduction of additional defects is preferred to relieve strain during growth.

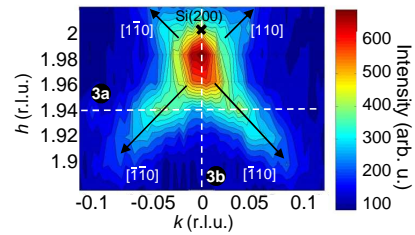


FIG. 2: Integrated reciprocal space map of diffuse scattering measured around the Si basis-forbidden reflection (200). The dashed lines labeled (3a) and (3b) denote the trajectory, along which the line scans in Figs. 3 (a) and (b) were performed respectively.

Recently, x-ray diffraction measurements at the (200) forbidden reflection allowed to determine the average in-plane spacing Λ between interfacial dislocations, which was confirmed by extensive atomic force microscopy with selective etching [11]. This leads to $\Lambda = b_{\text{eff}}/\epsilon_{200}$, where b_{eff} is the effective Burgers vector of the dislocations and ϵ_{200} the average strain value measured at the (200) forbidden reflection with respect to the Si as an absolute reference. 60° dislocations are commonly observed in SiGe islands at high growth temperatures [3, 4]. They accommodate misfit strain at the Ge/Si interface as they reduce the total free energy of growing strained islands [18]. Their effective Burgers vector contributing to the in-plane relaxation is $b_{\text{eff}} = \frac{a}{\sqrt{2}} \cos(\pi/3)$. Radial scans around the (200) forbidden reflection are displayed in Fig. 3 (b). The trajectory of the radial scans is shown as a dashed line in Fig. 2. The average strain value ϵ_{200} is

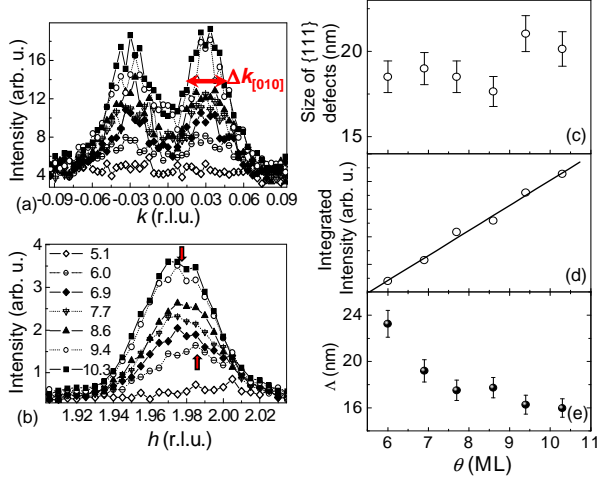


FIG. 3: (a) Angular scans at $h=1.94$ for several Ge deposit along the correspondent line denoted in Fig. 2. (b) Radial scans at the (200) reflection as a function of Ge deposit along the correspondent line denoted in Fig. 2. Evolution of (c) the size along the $\langle 110 \rangle$ direction, *i.e.* the lateral extension of the defects, of (d) the integrated intensity of the $\{111\}$ defects as a function of Ge deposit, θ and (e) the average in-plane spacing Λ between interfacial dislocations.

given by $\Delta h/h$, *i.e.* here $(h_{200} - 2)/2$, where h_{200} corresponds to the h value at the maximum of intensity of the peak measured at the (200) forbidden reflection. The h_{200} position is indicated by arrows in Fig. 3 (b) for a deposit of 6.0 and 10.3 ML. The absolute value of ϵ_{200} in-

creases from 0.84% at 6.0 ML to 1.23% at 10.3 ML. The in-plane distance between two interfacial 60° dislocations thus evolves from 23 ± 2 to 16 ± 2 nm with increasing Ge deposition (see Fig. 3 (e)). The average in-plane distance between two interfacial dislocations is decreasing as a function of Ge deposit. This is in agreement with the work of Boioli *et al.* [19], in which the ring width obtained after selective etching, which is associated to the distance between dislocations, decreases to converge to a nearly constant value as a function of the number of rings (*i.e.* dislocations). This implies that the number of dislocations inside islands increases, whereas their average in-plane spacing decreases with Ge deposit. Interestingly, during the superdome growth regime ($6.0 \leq \theta \leq 10.3$ ML), the GIXD data (see Fig. 1) show that the h -position of the maximum of relaxation stays rather constant but that its corresponding intensity increases. The average in-plane elastic strain $\epsilon_{//}$ of superdomes, given by $\epsilon_{//} = \Delta a/a - b_{\text{eff}}/\Lambda$ (where $\Delta a/a = \Delta h/h$ is calculated from the h position of the dislocated island hump at the (400) reflection) is thus decreasing as a function of Ge deposit. When superdomes form, elastic relaxation stops being effective and plastic relaxation is prevalent.

In conclusion, mapping around the (200) basis-forbidden reflection allows to follow the formation of defects during growth. The onset of the nucleation of $\{111\}$ defects was determined as a function of Ge deposit as well as the in-plane distance between interfacial dislocations. The average size of $\{111\}$ defects is relatively constant during growth, whereas their density increases linearly with deposited Ge. Insertion of defects is preferred to relieve strain during growth.

-
- [1] G. Medeiros-Ribeiro, A. M. Bratkovski, T. I. Kamins, D. A. A. Ohlberg, and R. S. Williams, *Science* **279**, 353 (1998).
- [2] F. M. Ross, R. M. Tromp, and M. Reuter, *Science* **286**, 1931 (1999).
- [3] F. K. LeGoues, M. C. Reuter, J. Tersoff, M. Hammar, and R. M. Tromp, *Phys. Rev. Lett.* **300**, 73 (1994).
- [4] M. Hammar, F. K. LeGoues, J. Tersoff, M. C. Reuter, and R. M. Tromp, *Surf. Sci.* **349**, 129 (1996).
- [5] D. J. Smith and *et al.*, *J. Cryst. Growth* **259**, 232 (2003).
- [6] B. J. Spencer and J. Tersoff, *Appl. Phys. Lett.* **77**, 2533 (2000).
- [7] B. J. Spencer and J. Tersoff, *Appl. Phys. Lett.* **63**, 205424 (2001).
- [8] T. Merdzhanova and *et al.*, *Phys. Rev. Lett.* **96**, 226103 (2006).
- [9] M. I. Richard, T. H. Metzger, V. Holý, and K. Nordlund, *Phys. Rev. Lett.* **99**, 225504 (2007).
- [10] M. I. Richard, A. Malachias, J.-L. Rouvière, T.-S. Yoon, E. Holmström, Y.-H. Xie, V. Favre-Nicolin, V. Holý, K. Nordlund, G. Renaud, *et al.*, *Phys. Rev. B* (2011).
- [11] M. I. Richard, A. Malachias, M. Stoffel, T. Merdzhanova, O. G. Schmidt, and T. H. Metzger, *Phys. Rev. B* (2011).
- [12] <http://www.esrf.eu/UsersAndScience/Experiments/CRG/BM32/>.
- [13] T. U. Schüllli, M.-I. Richard, G. Renaud, V. Favre-Nicolin, E. Wintersberger, and G. Bauer, *Appl. Phys. Lett.* **89**, 143114 (2006).
- [14] G. Medeiros-Ribeiro, T. Kamins, D. Ohlberg, and R. Williams, *Phys. Rev. B* **58**, 7 (1998).
- [15] G. Renaud, R. Lazzari, C. Revenant, A. Barbier, M. Noblet, O. Ulrich, F. Leroy, J. Jupille, Y. Borensztein, C. Henry, *et al.*, *Phys. Rev. B* **300**, 1416 (2003).
- [16] M. I. Richard, T. Schüllli, G. Renaud, E. Wintersberger, G. Chen, G. Bauer, and V. Holý, *Phys. Rev. B* **80**, 045313 (2009).
- [17] M. Stoffel, A. Rastelli, J. Stangl, T. Merdzhanova, G. Bauer, and O. Schmidt, *Phys. Rev. B* **75**, 113307 (2007).
- [18] H. T. Johnson and L. B. Freund, *J. Appl. Phys.* **91**, 9 (1997).
- [19] F. Boioli and *et al.*, *J. Appl. Phys.* submitted (2011).

Chapter 3

Ge growth on prepatterned Si(001)

The work presented in this chapter address the growth of Ge nanostructures on Si(001) substrates that have undergone a patterning procedure. This pre patterning can have multiple motivations: It allows for an ordered growth of islands being highly homogeneous in size and density. Eventually smaller sizes or higher Ge concentrations are possible while preserving dislocation free growth. The growth of SiGe islands on prepatterned substrates may open up the way to highly homogeneous ensembles of Ge rich, dislocation free and highly relaxed islands, thus lifting the natural conflict present between these parameters present for growth on a flat substrate.

3.1 SiGe islands on nominal and prepatterned Si(001)

In order to obtain a direct comparison of the parameters strain, Ge composition and shape, a simultaneous deposition of Ge on Si(001) was carried out on a patterned part and on a non-patterned part of the substrate. The experiments were carried out in the MBE chamber of BM32 after a sample transfer under inert gas atmosphere. The use of this chamber was thus not for *in situ* growth but rather to avoid oxidation of the sample. The patterning was obtained by electron beam lithography and subsequent Si- overgrowth of the etched surface. This leaves a patterned but defect free surface as a prerequisite to defect free SiGe island growth. The x-ray measurements in the following work were performed at several photon energies close to the Ge K-edge, allowing for an extraction of the Ge concentration. A direct fitting of the x-ray data with 3D inverse Monte Carlo modeling of the Si-Ge distribution and the lattice parameter profile inside the islands yield a higher elastic energy in Islands grown on the flat Si(001) as compared to the growth on the patterned area.

3.1.1 *Enhanced Relaxation and Intermixing in Ge Islands Grown on Pit-Patterned Si(001) Substrates*

T. U. Schüllli, G. Vastola, M.-I. Richard, A. Malachias, F. Uhlik, F. Montalenti, G. Chen, L. Miglio, F. Schäffler, G. Bauer,
Phys. Rev. Lett. 102, 025502 (2009).

Enhanced Relaxation and Intermixing in Ge Islands Grown on Pit-Patterned Si(001) SubstratesT. U. Schüllli,^{1,*} G. Vastola,³ M.-I. Richard,^{1,2} A. Malachias,² G. Renaud,¹ F. Uhlík,³ F. Montalenti,³ G. Chen,⁴ L. Miglio,³ F. Schäffler,⁴ and G. Bauer⁴¹CEA Grenoble, INAC/SP2M, 17 rue des martyrs, F-38054 Grenoble, France²ESRF, Grenoble 6 rue J. Horowitz, F-38043 Grenoble, France³L-NESS and Materials Science Department, University of Milano-Bicocca, Via R. Cozzi 53, I-20125 Milano, Italy⁴Johannes Kepler Universität Linz, A-4040 Linz, Austria

(Received 24 October 2008; published 16 January 2009)

We compare elastic relaxation and Si-Ge distribution in epitaxial islands grown on both pit-patterned and flat Si(001) substrates. Anomalous x-ray diffraction yields that nucleation in the pits provides a higher relaxation. Using an innovative, model-free fitting procedure based on self-consistent solutions of the elastic problem, we provide compositional and elastic-energy maps. Islands grown on flat substrates exhibit stronger composition gradients and do not show a monotonic decrease of elastic energy with height. Both phenomena are explained using both thermodynamic and kinetic arguments.

DOI: 10.1103/PhysRevLett.102.025502

PACS numbers: 81.16.Nd, 61.46.-w, 71.15.Pd, 81.07.-b

Ordering, shape and size uniformity of epitaxial Ge (or SiGe) islands on Si(001) is very important whenever microelectronic applications based on such nanostructures are concerned [1]. Island formation is known to follow the Stranski-Krastanow (SK) growth mode [2], allowing for partial elastic energy relaxation. Significant intermixing between Si and Ge within the islands has been reported [3–8], and the role of alloying for growth has been theoretically investigated [9–13]. Since on flat substrates islands tend to nucleate randomly, substrate patterning can be used to achieve controlled positioning [14]. Remarkably, patterning was also shown to increase size uniformity, possibly because of a more regular distribution of capture areas [15]. The growth of ordered nanometric islands with a narrow distribution in shape and size is already exciting *per se*, but recent results [15,16] indicate that the influence of patterning can be even more far reaching. Self organized patterning in ultra high vacuum (UHV) may also be used in the future, in order to control size and relaxation in SiGe islands [17]. We recall that SiGe islands on Si are coherent up to a critical volume V_c , characteristic for the onset of the formation of misfit dislocations [18]. In Ref. [15], it was demonstrated that patterning of Si(001) extends the allowed volume range for coherent islands. According to atomistic and finite element method (FEM) calculations reported in the same paper, this can be explained by an extra relaxation, caused by the pit, which lowers the substrate or island misfit. The possibility of controlling also the relaxation level of the islands by growth on patterned substrates appears extremely intriguing. In this Letter, we report an experimental proof of the abovementioned effect, and we show that the pits influence both, average relaxation and distribution of Ge within the islands.

Pit-patterned substrates were prepared by lithography, following the procedure used in [19]. Seven ML of Ge were deposited at 650 Å °C on a Si(001) substrate with a 900 ×

900 μm^2 part of it being patterned with pits at a periodic spacing of 495 nm. The growth of a Si buffer prior to Ge deposition leaves periodic downward pyramid-shaped {1110} pits [19]. The sample was transferred under N_2 atmosphere into the UHV chamber of beam line BM32 at the ESRF in Grenoble. AFM analysis shows that Ge islands nucleate at the bottom of these pits and form dome-shaped islands with identical facets as on the flat part of the substrate. The average island density per surface unit area is 5 μm^{-2} for the patterned part and 20 μm^{-2} for the flat one. The domes on the patterned (flat) part have an average height of 28 nm (23 nm) and a diameter of 130 nm (110 nm).

The islands were characterized by grazing incidence x-ray diffraction (GIXD) at an x-ray energy of 11.04 keV. The incident beam and the collimation on the detection side were translated in order to select between patterned and flat regions. Reciprocal space maps in the vicinity of the (400) Bragg reflection were recorded, as shown in Figs. 1(a) and 1(b) together with corresponding AFM images (insets). The intensity distribution along the radial direction clearly extends to higher lattice parameters for the patterned region. The islands grown on the flat have their main lattice parameter around 5.465 Å (in reciprocal lattice units of $H = 3.975$) whereas for the patterned part, the lattice parameters are stretched in reciprocal space, showing a maximum at ~ 5.51 Å ($H = 3.943$).

To understand the observed differences, we related the lattice-parameter to the local Ge content inside the islands by exploiting anomalous x-ray scattering. By monitoring the scattered intensity when varying the x-ray energy in the vicinity of the Ge K edge ($E_e = 11.103$ keV) at a fixed momentum transfer Q , the corresponding average Ge concentration can be determined, so that in-plane lattice parameter a_{\parallel} vs Ge content (c_{Ge}) data are extracted without any model assumption [5,20]. It is found that for the islands

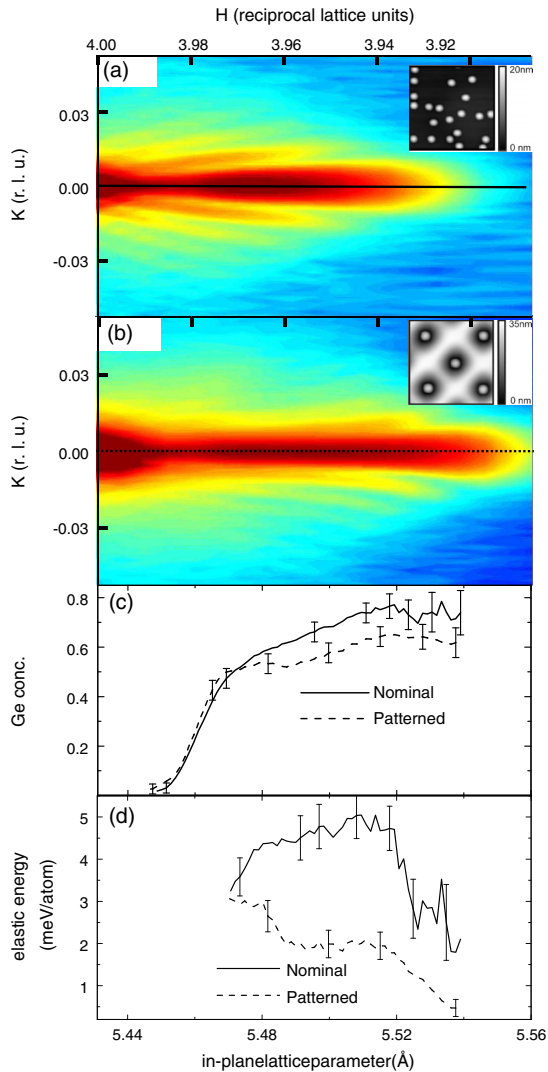


FIG. 1 (color online). Logarithmic intensity distribution in the vicinity of the (400) Bragg reflection for Ge islands grown on the flat (a) and patterned (b) sample part. Corresponding AFM images ($1 \mu\text{m}^2$ in size) are shown as insets. (c) Ge content inside the islands as a function of lattice parameter for growth on the flat (full line) and on the patterned part (dashed line). (d) elastic energy as a function of lattice parameter as extracted from the x-ray data. All figures correspond to the same lattice-parameter scale.

grown on the flat, the maximum Ge concentration for highest lattice parameters is slightly higher than for the patterned case [Fig. 1(c)]. However, as visible from the intensity distribution in Figs. 1(a) and 1(b), these relaxed regions contribute little to the total diffracted intensity. The combined analysis of the x-ray size oscillations, and the island shape as resolved by AFM, yield that the major part

of the island volume is situated at lattice parameters below 5.48 \AA for islands on the flat. Combining x-ray diffraction and AFM, the mean Ge content is determined to be $c_{\text{Ge}} \simeq (60 \pm 5)\%$ for both island types. Hence, the presence of the pits does neither influence the shape nor the mean SiGe composition of the islands. Let us see where, instead, differences exist. Figure 1(c) shows c_{Ge} vs a_{\parallel} for the flat (full lines) and the patterned region (dashed lines). The continuous broadening of H-constant profiles for lower H values points to a monotonic lattice parameter increase as a function of height in the islands [21]. The flatness of the dashed curve indicates lower gradients for c_{Ge} inside the islands grown in pits in comparison to the flat case. It is thus clear that the elastic energy at comparable c_{Ge} must be significantly lower for islands nucleating in the pits, as the intensity in reciprocal space stretches out to much higher lattice parameters. The volumetric elastic energy can be extracted from these data, as performed in Refs. [7,20]. It is plotted as a function of lattice parameter in Fig. 1(d). In the narrow region that forms the interface between island and substrate, and hence the region where the in-plane strain ϵ_{\parallel} changes sign from expansive to compressive nature, our method does not allow for a precise determination of the elastic energy since regions with similar lattice parameter and slightly different composition will have a mean $\bar{\epsilon}_{\parallel}$ that amounts to zero. However, with the elastic energy $E_e \propto \epsilon_{\parallel}^2$, its mean value does not average to zero. In the region of validity, our method yields a remarkable decrease of elastic energy throughout the islands grown on the pit-patterned part. One has to state that such x-ray measurements carry information on the in-plane lattice parameter, but effects of local hydrostatic compression cannot be taken into account when determining the elastic energy directly from the data.

More insights can be gained by extracting the actual 3D Ge distribution and the elastic-energy profile throughout the island. Over the last ten years, x-ray methods have been developed, coupling lattice parameter with lateral size [21] and chemical composition of an object, to reconstruct a concentration profile inside nanostructures [4,5,22]. These methods are limited, however, by model assumptions concerning the shape of the considered isostrain regions. A combination of x-ray methods and FEM calculations is thus necessary in order to overcome the lack of experimentally accessible information. We have used a fitting procedure that exploits a FEM-based treatment of nonuniform concentration profiles, to determine the local Ge content without any constraint. After the island and substrate geometry is created based on AFM images, nonuniform concentration values are assigned on a discrete mesh [13]. The elastic problem is then solved exploiting linear interpolation, $(c_{\text{Ge}}, a_{\parallel})$ data are extracted, and the statistical χ^2 is evaluated by comparison with the corresponding x-ray data. Using an iterative procedure based on local concentration exchanges, χ^2 is minimized. Technical details on the way we handle nonuniform distributions within FEM can be found in [13] where the elastic energy was

minimized. In the present work, the deviation from the experimental data is minimized. It is important to emphasize that particular care is required in assigning the correct statistical weight to the data. During the fit, $(c_{\text{Ge}}, a_{\parallel})$ pairs from the FEM grid were computed from the island interior and from a surrounding region in the substrate with a lateral extension inferred from the experimental island density, and a depth of 12 nm, i.e., the estimated penetration depth of the x-rays in our setup. This allowed us to filter out the substrate contribution from the experimental data which, as shown in Fig. 1(c) for the flat case, causes a sudden drop of the average Ge content at low lattice parameters, due to the strong scattering contribution from the Si-substrate. From the x-ray data, it is thus difficult to analyze the region of the substrate-island interface. Another difficulty stems from the vanishing experimental scattering volume of the regions with lattice parameters close to bulk Ge. In the fit shown in Fig. 2, the local value of c_{Ge} was extrapolated from experiments, assigning a large error bar in order not to bias the region where real data were present. Finally, a satisfactory fit (requiring $\sim 10^4$ iterations) is obtained, the full solution of the elastic problem being required at each step. The FEM fitted data (small dots in Fig. 2) show that several concentration values can be associated with a single value of lattice parameter, which is not obvious from the experimental curve which averages them out.

The 3D compositional maps corresponding to our best fits are displayed in Figs. 3(a)–3(d) together with their horizontally averaged values [Fig. 3(e)], while the elastic energy per atom is reported in Fig. 3(f), where a comparison with the uniform composition case is also shown. In the flat case—Figs. 3(a) and 3(b)—an almost pure Si region is found close to the base edges, a result fully compatible with selective-etching data [23]. From Figs. 3(c) and 3(d), one sees that Si enrichment at the base is less evident in the pit case where the overall Ge distribution is more uniform, but for more localized irregularities. This is particularly evident from the horizontally averaged c_{Ge} values dis-

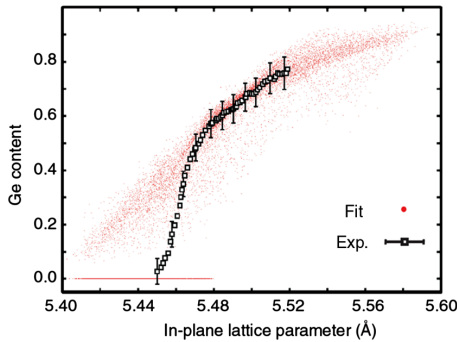


FIG. 2 (color online). Experimental data of the Ge-content as a function of lattice parameter together with FEM fitted data after proper separation of the Si substrate contribution (flat case).

played in Fig. 3(e). The different Ge distribution of the island apex along the [100] and [110] cross sections is due to the fact that the island boundary is composed by a set of facets and edges which is different for the two sections. It has thus a direct influence on the local elastic relaxation and hence the Ge concentration profile [24]. The above observations can be justified using both thermodynamic and kinetic arguments. The edges of the islands grown on flat substrates are the most compressed regions in case a uniform Ge distribution is considered [25], so that replacing Ge with Si atoms produces significant relaxation. Comparing the elastic energy in flat vs pit-patterned substrates [Fig. 3(f)] in the case of a uniform distribution, one sees that the driving force for Si segregation at the island base is weaker in pits, since the energy difference between base and top is smaller. Entropy of mixing could then prevail over elastic relaxation, forcing enhanced intermixing. While this thermodynamic argument supports our

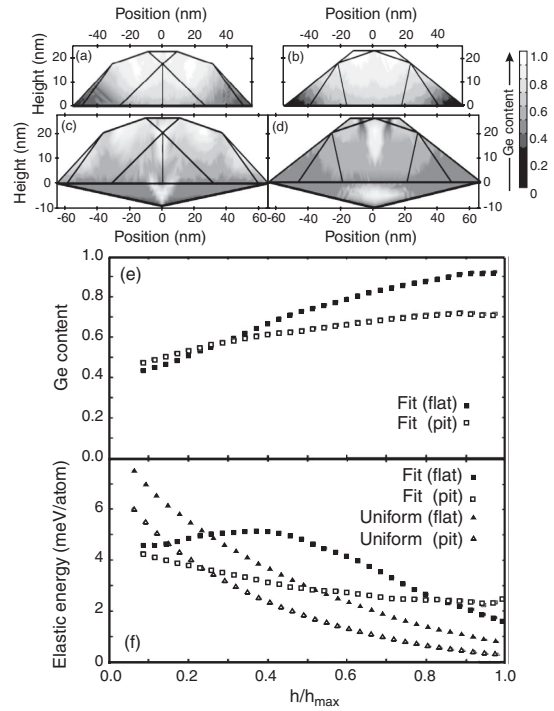


FIG. 3. Cross section map of the 3D-reconstructed Ge content profile for islands grown on flat (a), (b) and patterned (c), (d) samples. Sections are shown along the [100] (a), (c) and the [110] (b), (d) crystallographic directions. Panel (e) displays the average Ge content as a function of height. Panel (f) reports the elastic energy profile corresponding to the fitted Ge distribution on flat (filled box) and patterned (empty box) substrates. Plots made for the case of uniform concentration are analogously displayed for flat (filled triangles) and pit (empty triangles) case. The quantity h/h_{max} is a normalized height to allow the proper comparison between both island types at every height h .

results, it is important to consider that during growth, kinetic limitations are present, so that one should always check whether the proposed scenario is favored or simply made possible by plausible kinetic paths. On flat substrates, large amounts of Si become available during growth when the strong compressive stress at the edges produces trenches penetrating the Si substrate [26]. These Si atoms coming out close to the island periphery could easily be incorporated in the regions which are most favorable from the energetic point of view. As a result, the final profile resembles the minimum-energy one [13]. In the initial stages of growth, trenches are not yet present, providing a kinetic justification for the limited lateral extension of the external Si-rich region. Our results do not confirm the formation of a central Si-rich region ([4,7]), whose presence seems to be difficult to explain from both the thermodynamic and kinetic point of views. In pits, the Si-supply mechanism could be different. In Ref. [27], data collected on pit-patterned samples similar to ours indicated that the condition of a perfect WL completed prior to island formation is not fulfilled. Since preliminary results on the present samples confirm this observation, we believe that in pits, enhanced Si supply prior to trench formation is possible, i.e., from detachment of uncovered Si atoms from the steps of the pits' facets. These could reach the growing islands by surface diffusion, leading to a more uniform intermixing profile.

Let us now analyze quantitatively the main differences between the flat and the patterned case in terms of elastic energy. From Fig. 3(f), one sees that the presence of the pit allows for a significant decrease ($\sim 30\%$ on average) in elastic energy. Since this effect is confirmed also for uniform Ge distributions [triangles in Fig. 3(f)], the key role must be played by the different geometry. Before island formation, the pit is filled by Ge forming an inverted pyramid. This redistributes the load between Ge and the surrounding Si resulting in better strain relaxation with respect to a flat WL so that islands on pits nucleate on a substrate with a lower effective misfit. This relaxation mechanism was demonstrated in [15]. Additionally, the behavior of the elastic energy shows that the usual picture of a base-to-top stress relaxation breaks down in the case of a flat substrate [25]: the curve displayed in Fig. 3(f) clearly displays a maximum. Combining this with Fig. 3(e), one sees that Si enrichment at the base guarantees a lowering of the elastic energy. As soon as c_{Ge} approaches its average value (at around $h/h_{\text{max}} = 0.3$), elastic-energy lowering becomes less efficient: the strong elastic load determined by the high Ge content cannot be relieved by the limited deformation in regions still close to the base. In the proximity of the island top, instead, the elastic energy is nicely lowered in spite of the maximum Ge content in the island.

If prepatterning is already seen as a powerful tool to control positioning and homogeneity of heteroepitaxial islands, we have shown that it also allows one to control

elastic-energy release and thus to grow islands with the desired relaxation. The kinetics of Si supply seems to be also influenced by the pit, calling for further studies for achieving full control.

Financial support by the EU-funded project "D-DotFET" and the FWF (Vienna, project SFB025) and GMe (Vienna) are gratefully acknowledged, together with technical help received from R. Gatti.

*schulli@esrf.fr

- [1] F. Schäffler, *Semicond. Sci. Technol.* **12**, 1515 (1997).
- [2] V. A. Shchukin and D. Bimberg, *Rev. Mod. Phys.* **71**, 1125 (1999).
- [3] G. Capellini, M. De Seta, and F. Evangelisti, *Appl. Phys. Lett.* **78**, 303 (2001).
- [4] A. Malachias *et al.*, *Phys. Rev. Lett.* **91**, 176101 (2003).
- [5] T. U. Schüllli *et al.*, *Phys. Rev. Lett.* **90**, 066105 (2003).
- [6] G. Medeiros-Ribeiro *et al.*, *Appl. Phys. A* **80**, 1211 (2005).
- [7] G. Medeiros-Ribeiro and R. S. Williams, *Nano Lett.* **7**, 223 (2007).
- [8] A. Rastelli *et al.*, *Nano Lett.* **8**, 1404 (2008).
- [9] C. Lang, D. J. H. Cockayne, and D. Nguyen-Manh, *Phys. Rev. B* **72**, 155328 (2005).
- [10] G. Hadjisavvas and P. C. Kelires, *Phys. Rev. B* **72**, 075334 (2005).
- [11] Y. Tu and J. Tersoff, *Phys. Rev. Lett.* **98**, 096103 (2007).
- [12] N. V. Medhekar, V. Hegadekatte, and V. B. Shenoy, *Phys. Rev. Lett.* **100**, 106104 (2008).
- [13] R. Gatti, F. Uhlík, and F. Montalenti, *New J. Phys.* **10**, 083039 (2008).
- [14] Z. Zhong and G. Bauer, *Appl. Phys. Lett.* **84**, 1922 (2004).
- [15] Z. Zhong *et al.*, *Phys. Rev. Lett.* **98**, 176102 (2007).
- [16] H. Hu, H. J. Gao, and F. Liu, *Phys. Rev. Lett.* **101**, 216102 (2008).
- [17] G. Katsaros *et al.*, *Phys. Rev. Lett.* **101**, 096103 (2008).
- [18] A. Marzegalli *et al.*, *Phys. Rev. Lett.* **99**, 235505 (2007).
- [19] G. Chen *et al.*, *Phys. Rev. B* **74**, 035302 (2006).
- [20] R. Magalhães-Paniago *et al.*, *Phys. Rev. B* **66**, 245312 (2002).
- [21] I. Kegel *et al.*, *Phys. Rev. Lett.* **85**, 1694 (2000).
- [22] A. Letoublon *et al.*, *Phys. Rev. Lett.* **92**, 186101 (2004).
- [23] G. Katsaros *et al.*, *Phys. Rev. B* **72**, 195320 (2005).
- [24] In Figs. 3(c) and 3(d), the calculations show Ge rich regions of the pit bottoms which do not appear in 3(e). In this figure, we make the comparison between the average composition between islands on flat and patterned substrates. Since the material at the bottom of the pit is of course not present in the island on flat substrate, the averaged compositions of Fig. 3(e) do not take into account this volume.
- [25] G. Vastola, R. Gatti, A. Marzegalli, F. Montalenti, and Leo Miglio, *Detailed Analysis of the Shape-Dependent Deformation Field in 3D Ge Islands on Si(001)* (Springer, Berlin, 2008), pp. 421–438.
- [26] S. A. Chaparro, Y. Zhang, and J. Drucker, *Appl. Phys. Lett.* **76**, 3534 (2000).
- [27] T. Stoica *et al.*, *Nanotechnology* **18**, 455307 (2007).

Chapter 4

Atomic ordering in SiGe islands

Atomic ordering in SiGe alloys is not observed as a state of thermodynamic equilibrium. It has been observed to be present in SiGe films grown on Si(001) and is attributed to the specific growth kinetics of the Si(001) surface and its reconstruction. In an x-ray diffraction experiment, atomic ordering in alloys leads to extra peaks at positions of forbidden reflections. While the observation of such phenomena *in situ* during growth so far failed due to the weak intensity scattered from the ordered regions, the investigation of order in as grown samples can yield information about the growth kinetics. Samples grown at different conditions in terms of temperature and deposition rate or by using different growth methods as MBE, chemical vapour deposition (CVD) or liquid phase epitaxy (LPE) may show different degree of Si-Ge ordering. Once the process responsible for such ordering is identified, its presence may allow to shed light on different kinetic growth processes as for example the interplay between surface and volume diffusion mechanisms.

4.1 Atomic ordering in MBE grown SiGe islands

- 4.1.1 *X-ray study of atomic ordering in self-assembled Ge islands grown on Si(001)*
A. Malachias, T. U. Schüllli, G. Medeiros-Ribeiro, L. G. Cancado, M. Stoffel, O. G. Schmidt, T. H. Metzger, R. Magalhaes-Paniago,
Phys. Rev. B **72**, 165315 (2005).

An investigation of the diffuse intensity present at the forbidden (200) reflection from SK-grown SiGe islands led to the interpretation that atomic ordering must be at its origin. Unlike the intensity distribution observed by stacking faults as discussed in 2.4, the observations could not be explained by simple defects but needed consideration of a 3D-model of the internal structure of the islands. A model that can describe the complex intensity distribution at the (200) reflections consists of ordered domains with anti phase domain walls in the island centre. The existing order has been quantified respecting the local SiGe concentration and was compared to Raman scattering measurements.

PHYSICAL REVIEW B 72, 165315 (2005)

X-ray study of atomic ordering in self-assembled Ge islands grown on Si(001)A. Malachias,^{1,2,*} T. U. Schüllli,³ G. Medeiros-Ribeiro,⁴ L. G. Cançado,¹ M. Stoffel,⁵ O. G. Schmidt,⁵ T. H. Metzger,² and R. Magalhães-Paniago^{1,4}¹*Departamento de Física, Universidade Federal de Minas Gerais, C.P. 702, CEP 30123-970, Belo Horizonte, MG, Brazil*²*European Synchrotron Radiation Facility, BP 220, F-38043 Grenoble Cedex, France*³*CEA/Grenoble, 17 rue des Martyrs, 38054 Grenoble Cedex 9, France*⁴*Laboratório Nacional de Luz Síncrotron, C.P. 6192, CEP 13084-971, Campinas, SP, Brazil*⁵*Max-Planck-Institut für Festkörperforschung, Heisenbergstraße 1, D-70569 Stuttgart, Germany*

(Received 6 July 2005; revised manuscript received 8 August 2005; published 12 October 2005)

X-ray diffuse scattering in the vicinity of basis-forbidden Bragg reflections were measured for samples with uncapped self-assembled Ge islands epitaxially grown on Si(001). Our results provide evidence of atomically ordered SiGe domains in both islands and wetting layer. The modeling of x-ray profiles reveals the presence of antiphase boundaries separating the ordered domains in a limited region of the islands. X-ray order parameter results were independently supported by Raman measurements.

DOI: [10.1103/PhysRevB.72.165315](https://doi.org/10.1103/PhysRevB.72.165315)

PACS number(s): 68.65.Hb, 61.10.-i

I. INTRODUCTION

The possibility of producing spontaneous order on a nanometer scale has become one of the most important driving forces in nanoscience research during the last two decades. Stacked lipid membranes,¹ ordered arrays of quantum dots² and atomically ordered short-period alloy superlattices^{3,4} are examples of self-organization of atoms on very short length scales. In particular, for self-assembled quantum dots a variety of atomlike behavior has been observed, like single electron charging⁵ and Pauli blocking.⁶ In order to further explore band structure engineering in these systems some crucial parameters must be controlled. From the mesoscopic point of view, island shape and size distribution are the most important factors that must be managed. In the case of heteroepitaxial self-assembled islands, strain and composition may vary from one atomic layer to another. Hence, it is imperative to understand and control the growth conditions not only at the mesoscopic level but also at the atomic scale for rational quantum structures design.

Detailed near-surface studies have shown that spontaneous atomic ordering is observed in some semiconductor alloys.^{3,4} In particular, SiGe had been considered as a model for random alloys since long-range order cannot be produced by time-prolonged anneals in a wide temperature range (170 °C–925 °C).⁷ The thermodynamical description of SiGe alloys considers that these two atomic species interact with each other in the same way as they do among themselves.⁸ This so-called “ideal solution” is extremely useful to understand SiGe alloy growth since it fits very well the solid-liquid alloy phase diagrams.⁹

In 1985 Ourmazd and Bean¹⁰ performed an electron diffraction experiment on Si_{0.6}Ge_{0.4} superlattices grown by MBE at 550 °C on Si(001) and observed a clear evidence of atomic ordering. Besides the fundamental electron diffraction peaks they noticed the occurrence of superstructure reflections such as $(\frac{1}{2} \frac{1}{2} \frac{1}{2})$, $(\frac{3}{2} \frac{1}{2} \frac{1}{2})$, and $(\frac{3}{2} \frac{3}{2} \frac{1}{2})$. Despite of trying different annealing procedures (at several temperatures, anneal times, and cooling rates) the authors could not pre-

vent the ordering in the $\langle 111 \rangle$ direction. They deduced that the superposition of ordered domains with a pseudodiamond structure (later called RS1) could explain the width and shape of the superstructure reflections.

After this first work several authors^{11,12} tried to explain the ordering phenomena combining strain and thermodynamic arguments. While the hypothesis of strain driven ordering remained unclear, it was found that ordering should occur only for temperatures lower than ~ 150 K. The proof that strain does not induce ordering appeared in a work by Muller *et al.*¹³ Electron diffraction experiments were performed in a set of samples grown on alloy substrates, i.e., no strain, and superstructure reflections were also observed. This was also true for thick relaxed Si_{0.5}Ge_{0.5} films.¹⁴ In both works the growing temperature was in the range between 400 °C and 500 °C and the substrates were oriented in the $\langle 001 \rangle$ direction. By analyzing and simulating the electron diffraction patterns they found a different pseudodiamond structure (later called RS2).

LeGoues *et al.*¹⁵ showed unambiguously that ordering was not an equilibrium bulk phenomenon but it was tied to surface reconstruction. SiGe relaxed alloy films were grown on Si(001) with the typical 2×1 surface reconstruction and an artificially induced 1×1 reconstruction. Superstructure reflections were not observed at the 1×1 film although they had been measured at the 2×1 alloy. Moreover, films grown in Si(111) substrates exhibited no ordering. The suggested ordering mechanism was linked to the lower energy of completely ordered $\langle 111 \rangle$ planes instead of reverting the registry by zig-zagging. This $\langle 111 \rangle$ structure is energetically favorable over the arbitrary zig-zag domains by an energy difference of 80 meV per dimer.

A complete x-ray investigation about possible Si_{0.5}Ge_{0.5} structures in thin films was performed by Tischler *et al.*¹⁶ The crystallographic measurements of the superstructure reflection intensities lead to a modified RS2 ordering model (called RS3), with the coexistence of two different structures, the main $\langle 111 \rangle$ order and a secondary CuAu-I type order along the $\langle 100 \rangle$ direction. More recently, metastable ordered structures were discovered near the surface.¹⁸ The kinetic

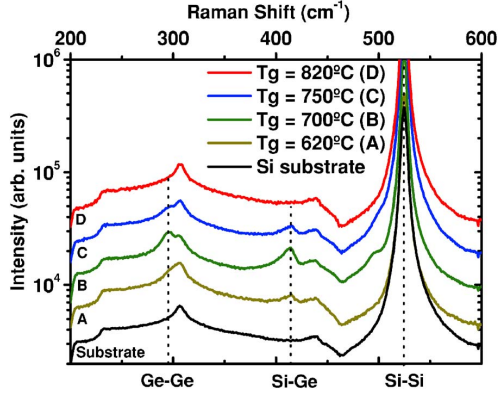
MALACHIAS *et al.*PHYSICAL REVIEW B **72**, 165315 (2005)

FIG. 1. (Color online) Raman spectra of a Si(001) substrate and samples A, B, C and D. The Ge-Ge and Si-Ge Raman peaks are indicated by dashed lines.

origin of ordering has been continuously corroborated during the last years.^{15,17–19}

Despite of all the work done the possibility of atomic ordering for deposition of pure Ge on Si(001) was neglected due to island formation. In this paper basis forbidden reflections were measured in Ge:Si(001) islands to unambiguously determine the existence of an ordered alloy phase inside these nanostructures and at the wetting layer (WL). We clearly observe atomic ordering inside self-assembled islands, evidencing the important role of surface kinetics to the island final structure and composition.

II. EXPERIMENT

The samples investigated in this work were grown on Si(001) substrates by solid source molecular beam epitaxy²⁰ at temperatures of 620 °C (sample A), 700 °C (sample B), 750 °C (sample C), and 840 °C (sample D). The amount of deposited Ge for samples A–D in monolayers (ML) is, respectively, 6.7 ML (A), 11 ML (B), 11 ML (C), and 6 ML (D). Atomic force microscopy measurements showed that dome islands were formed with monodisperse size distributions.²⁰ The average Ge:Si interdiffusion inside each sample was studied by x-ray anomalous scattering in Ref. 20. The Ge average content was found to be 0.62 for sample A, 0.48 for sample B, 0.45 for sample C, and 0.22 for sample D.²⁰

In order to qualitatively evaluate interdiffusion and short-range ordering in these Ge islands Raman scattering measurements were performed. The samples were excited by a 5145 Å Ar laser set to a power of 8 mW at the sample surface. Raman spectra were recorded using a triple grating spectrometer. This experiment essentially reveals the existence and relative abundance of Ge-Ge and Si-Ge bonds inside the islands. Figure 1 shows the Raman signal in a range between 200 and 600 cm⁻¹ from the four samples and a Si substrate. The Ge-Ge, Si-Ge, and Si-Si vibrational modes are observed around 300, 400, and 500 cm⁻¹, respectively.

A qualitative analysis can be drawn by comparing the intensities of the Si-Ge peak (around 415 cm⁻¹) for all

samples. This intensity is roughly proportional to (a) interdiffusion that introduces Si atoms inside the Ge islands and; (b) short-range atomic ordering that maximizes the number of Si-Ge bonds.^{21,22} From the measurements of Fig. 1 one observes an increase in the Si-Ge mode intensity with the growth temperature comparing samples A and B essentially due to the larger coverage and higher degree of intermixing. However, the intensity of this Raman peak decreases for growth temperatures higher than 700 °C, most notably by comparing samples B and C where the same amount of Ge (11 ML) was deposited. This suggests a dependence of the short-range ordering degree with the growth temperature as observed by electron diffraction experiments.¹⁹ Since sample B exhibited the strongest Si-Ge Raman peak it was chosen for a complete analysis.

The x-ray experiments were performed in grazing incidence geometry at Beamline ID1 of the European Synchrotron Radiation Facility. The incident angle was set to 0.17°. X-ray scattering was collected in a range of exit angles from 0° to 1.5° by a position sensitive detector. The x-ray photon energy was set to 8.0 keV. Reciprocal space maps were recorded next to surface Bragg reflections. The x-ray scattering was measured as a function of $q_{\text{radial}} = q_r = (4\pi/\lambda)\sin(2\theta/2)$, which is strain sensitive, and $q_{\text{angular}} = q_a = q_r \sin(2\theta/2 - \omega)$, which is size sensitive.

Two types of scans were done. A radial scan was performed coupling θ to 2θ . Thus, by Bragg's law $\lambda = 2d \sin(2\theta/2)$, this scan was sensitive to the strain of the sample, since for each value of 2θ (q_r), regions of different lattice parameter $a' = 2\pi/q_r$ were probed. Angular scans were performed solely by θ (q_a), with fixed 2θ (q_r). These scans were size sensitive, since the size of each region with a given lattice parameter can be inferred from the width of the q_a -scan profile.^{23–26} The regions of interest were mapped by a series of angular scans perpendicular to the radial direction over a range between the corresponding reciprocal lattice points of pure Ge and Si. This procedure has been published earlier and can be used to separate the contributions of size and strain broadening in reciprocal space.^{23,26}

III. RESULTS AND ANALYSIS

A. Complete analysis of sample B

A radial scan along the [100] direction near the (400) Si reciprocal lattice point is shown in Fig. 2(a), where the q_r axis was directly converted into the in-plane lattice parameter (upper scale). Next to the Si peak at 5.431 Å one observes a broad intensity distribution up to 5.6 Å indicating that the lattice parameter, which was initially constrained to the Si value, relaxes continuously with increasing height inside the islands. A rather unexpected result is obtained when the scattered intensity is measured in the vicinity of the (200) reflection, which is forbidden for pure Si and pure Ge crystals. Under this Bragg condition, scattered intensity is expected only when the SiGe alloy is, at least, partially ordered. Figure 2(b) thus represents the first evidence that long-range ordering is present in this system. While the total Ge relaxation reaches 5.60 Å [Fig. 2(a)], the ordered alloy is restricted to lattice parameters between 5.44 and 5.54 Å. The

X-RAY STUDY OF ATOMIC ORDERING IN SELF-...

PHYSICAL REVIEW B 72, 165315 (2005)

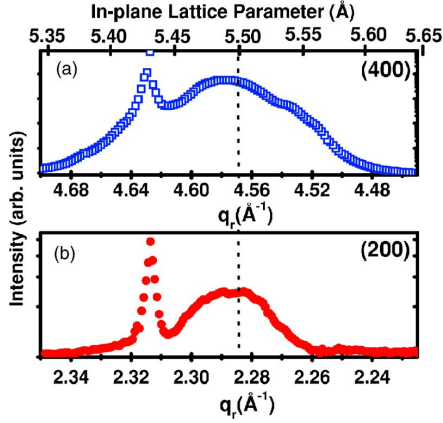


FIG. 2. (Color online) Radial scans along q_r in the vicinity of (a) Si (400) reflection (open squares) and (b) Si (200) reflection (solid circles) for sample B. The upper scale indicates the in-plane lattice parameter.

narrow peak observed at 5.431 \AA is generated by the ordered SiGe wetting layer, which is pseudomorphically strained to the Si in-plane lattice parameter.

The strain information is only partially revealed by radial θ - 2θ scans and a complete analysis relating the region which is constrained to a given lattice parameter and its position inside an island depends on the information of angular scans. In this case it is necessary to know the form factor of an iso-lattice parameter region of the island which is given by integrating the charge density inside the scattering object.²⁶

Performing an angular scan for a fixed lattice parameter [dashed lines in Fig. 2(a) or 2(b)], one can probe the corresponding Fourier transform of a region with constant lattice parameter. One angular profile close to the (400) reflection is shown in Fig. 3(a). It exhibits a broad peak centered at $q_a=0$ and subsidiary maxima, indicating the finite size and narrow size distribution of these constant-lattice parameter regions.²⁶ The lateral size of this region is evaluated from the q_a -peak width [using, e.g., Eq. (2)], which is inversely proportional to the lateral size L of this region in real space.

In contrast to the (400) reflection, an angular scan performed at the (200) reflection at $q_r=2 \times 2\pi/(5.50 \text{ \AA})$ yields a very different profile as seen in Fig. 3(a). A pronounced minimum is observed at $q_a=0$, which cannot be generated by structures that are interfering constructively, i.e., such a profile can only be modeled by introducing antiphase boundaries between domains inside the islands [using, e.g., Eq. (3)].

Other superstructure reflections consistent with Ref. 16 were also measured. Angular scans for three superstructure reflections at a fixed lattice parameter $d=5.50 \text{ \AA}$ are shown in Fig. 3(a). At the (420) and (200) reflections the antiphase pattern is clearly observed. The angular scan at the (110) reflection reveals a superposition of line shapes due to the contribution from domains in in-phase and out-of-phase con-

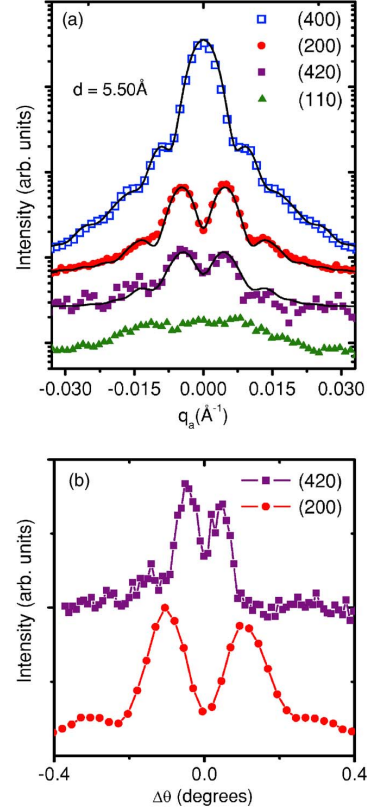


FIG. 3. (Color online) (a) Angular scans for sample B performed at 5.50 \AA at four reflections: (400) open squares, (200) solid circles, (420) solid squares, and (110) solid triangles. The (400) intensity was divided by a factor of 100 when compared to the (200). (420) and (110) angular scan intensities were multiplied by 2 when compared to (200). (b) (200) and (420) angular scans seen in (a) plotted in angular space.

ditions. The angular scans at the (420) and (200) reflections have different angular distances in real space as shown in Fig. 3(b), excluding the possibility of scattering by two or more rotated structures.

B. X-ray scattering formalism

Two distinct form factors were used here. At the (400) fundamental reflection all material inside a Ge dome will scatter since its intensity is proportional to the square of the sum of the atomic scattering factors of Ge/Si atoms.^{25,27} Since the surface diffraction technique used here is fairly insensitive to the shape of the nanostructures one can consider, for simplicity, that the islands have a square-shaped section. In this case the scattered intensity for an island with M planes parallel to the surface is given by²⁷

MALACHIAS *et al.*

PHYSICAL REVIEW B 72, 165315 (2005)

$$I(q_r, q_a, q_z) = \frac{I_{\max}}{M^2 N^4} \left| \sum_{j=0}^{M-1} \left(\sum_{m=1}^{N_j} e^{imd_j q_r} \sum_{n=1}^{N_j} e^{ind_j q_a} \right) e^{ih_j q_z} \right|^2, \quad (1)$$

where I_{\max} is the maximum scattered intensity of the angular profile,²⁶ N_j , d_j , and h_j are the number of atomic lines, lattice parameter, and height of layer j . Thus, the side length L_j of one layer is given by $L_j = N_j d_j$.

The result of Eq. (1) in the angular direction (constant q_r) at a fixed q_z can be simplified into^{26,27}

$$I(q_a) = \frac{I_{\max}}{L^2} \left| \frac{\sin\left(\frac{L}{2} q_a\right)}{\sin(q_a)} \right|^2. \quad (2)$$

In contrast to the (400) reflection, the shape of an angular scan performed at the superstructure (200) reflection will depend on the existence of an ordered SiGe alloy. If the isotlattice parameter region is completely ordered the angular scan will exhibit an intensity profile given by Eq. (2). However, an atomic layer may be divided into smaller ordered regions separated by antiphase boundaries. These boundaries are generated by mistakes in the in-plane atomic sequence. Instead of a layer with an atomic sequence such as \cdots Si-Ge-Si-Ge-Si-Ge- \cdots , a broken sequence of atoms (e.g., \cdots Si-Ge-Si-Si-Ge-Si-) is formed. Considering that the lattice parameter is nearly constant for a plane parallel to the substrate, the Si-Si or Ge-Ge stacking faults lead to phase inversions in the x-ray wave.^{4,27} To calculate the scattering amplitudes in this case one must introduce an inversion term $e^{i\pi}$ at each boundary, describing the phase shift between one domain and its neighbor. For an island with M atomic planes divided in four domains the scattered intensity can be calculated from^{4,27}

$$I(q_r, q_a, q_z) = I_{\max} \frac{2 \sin^4\left(\frac{\pi}{4N}\right)}{3M^2} \times \left| \sum_{j=0}^{M-1} \left(\sum_{m=0}^{N_j-1} e^{imd_j q_r} + e^{i\pi} \sum_{m=N_j}^{2N_j-1} e^{imd_j q_r} \right) \times \left(\sum_{n=0}^{N_j-1} e^{ind_j q_a} + e^{i\pi} \sum_{n=N_j}^{2N_j-1} e^{ind_j q_a} \right) e^{ih_j q_z} \right|^2, \quad (3)$$

where N_j is the number of atoms within each domain at layer j .

The presence of antiphase boundaries in islands is evident only in angular scans since in the radial direction the measured intensity results from a convolution between strain, domain size, and antiphase relation between them. This effect produces the well-known broadening of the superstructure peaks in the radial direction.^{4,27} Similarly to Eq. (1), at a fixed q_r and q_z , Eq. (3) can be simplified to²⁷

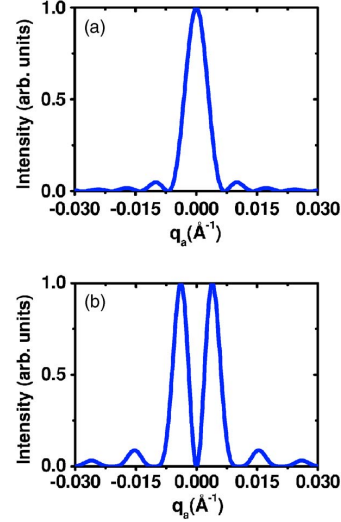


FIG. 4. (Color online) Form factors for (a) a 900 Å atomic layer [Eq. (2)] and (b) two domains with 300 Å each one [Eq. (4)].

$$I(q_a) = I_{\max} \sin\left(\frac{\pi}{2Nd}\right) \left| \frac{\sin(Ndq_a)}{\sin(q_a)} \right|^2. \quad (4)$$

Equations (3) and (4) were normalized by the maximum measured intensity (I_{\max}) at $q = \pi/(2Nd)$ since $I(q_a=0)=0$ for an ordered crystal with antiphase boundaries.

The resulting function of Eq. (4) represents a layer of atoms with local lattice parameter d divided into two domains with the same domain size Nd . The angular intensity shape resulting from Eqs. (2) and (4) are shown in Fig. 4.

In order to explain angular scans observed at the superstructure reflections discussed above it is necessary to understand the atomic arrangement for a SiGe ordered alloy. The schematic crystal structure of Fig. 5 follows the RS3 model of Ge-rich (α, β) and Si-rich (δ, γ) sites proposed in Refs. 16 and 17. According to these references, Ge atoms deposited on a (2×1) reconstructed Si(001) select specific sites and produce rows with the same atomic species along the $[1\ 1\ 0]$ or $[1\ -1\ 0]$ direction. Antiphase boundaries are formed when they are shifted by one atomic distance in the direction perpendicular to these rows. At this intersection an antiphase boundary in the $[010]$ direction can be created, as represented by the (red) lines in Fig. 5. The model used to fit the (200) and (420) angular scans in Fig. 3(a) is described by Eq. (3) and represented as four square-shaped domains with opposite phases. The model is consistent with this fourfold symmetry, since the scattering pattern measured for reflections (200) and (020) exhibited the same intensity distribution. Each ordered domain is then surrounded by domains with opposite phases. Antiphase boundaries are always located in between domains since only two atomic species are involved. Changing one atom from Si to Ge (or vice versa) in an ordered atomic row will always generate an antiphase configuration. In this structural model the antiphase walls are

X-RAY STUDY OF ATOMIC ORDERING IN SELF-...

PHYSICAL REVIEW B 72, 165315 (2005)

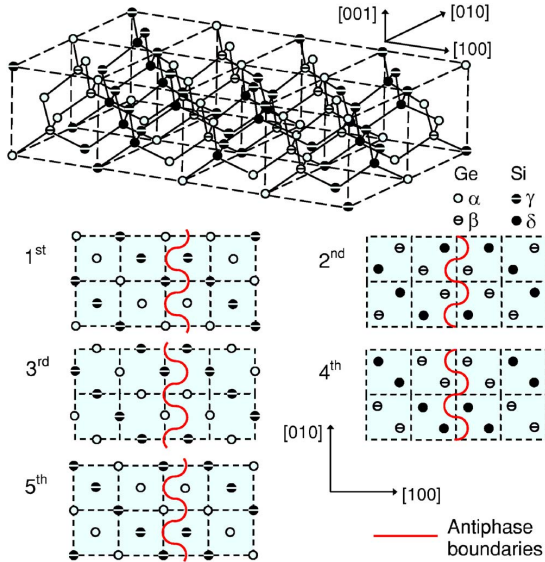


FIG. 5. (Color online) Schematic representation of the Si/Ge atomic ordering arrangement in the RS3 model. Ge-rich sites (α and β) correspond to white atoms while Si-rich sites (δ and γ) are represented by dark atoms. Five atomic layers along $[001]$ are shown to indicate antiphase boundaries in each layer. This structural model is consistent with measurements of Fig. 3(a).

always located along the $\langle 100 \rangle$ directions. For this reason the angular scans that have antiphase profiles are always found along these directions while angular scans performed in the $\langle 110 \rangle$ directions result in a sum of scattering intensities from in-phase and out-of-phase atomic domains.

Superstructure reflections such as (100), (210), and (300)—that would indicate the presence of different ordered alloy phases—were not observed. Half-integral reflections such as $(\frac{1}{2} \frac{1}{2} \frac{1}{2})$ and $(\frac{3}{2} \frac{3}{2} \frac{3}{2})$, which could indicate ordering along the $\langle 111 \rangle$ direction as observed in 2D SiGe alloy layers,¹⁶ were also not observed. LeGoues *et al.*¹⁵ have found that, at high growth temperatures such as the one used in our experiment, the vertical registry is lost since there are four possible $\langle 111 \rangle$ ordering directions.

The complete q_r/q_a measured intensity map in the vicinity of the Si (200) reflection is shown in Fig. 6(a). Spanning from q_r values higher than the Si position ($q_r=2.314 \text{ \AA}^{-1}$) up to $q_r=2.27 \text{ \AA}^{-1}$ two different structures are seen. In the region of the strained alloy ($q_r < 2.31 \text{ \AA}^{-1}$) the double peak structure along q_a is always present. For lower q_r , the width of this profile slightly increases, indicating a decreasing lateral size of the domains in real space. A weak narrow peak is seen exactly at the Si (200) position, indicating that the wetting layer (WL) is partially ordered, but without establishing antiphase boundaries. This evidences that alloying and ordering begin as soon as Ge is deposited. Si atoms are incorporated into the WL in the initial phase of growth and into the islands after the beginning of their nucleation.

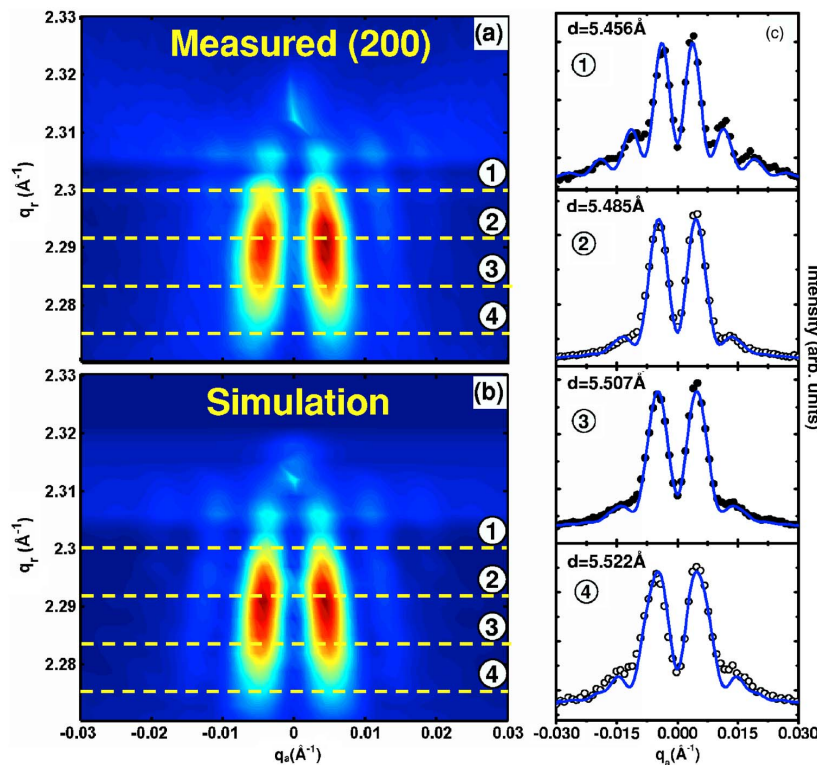


FIG. 6. (Color online) (a) Measured q_r, q_a intensity map for sample B in the vicinity of the Si (200) reflection. (b) Fitted intensity map based on selected angular scans. Four numbered q_a scans [dashed lines in maps (a) and (b)] are shown in (c). In these cuts the dots represent the measured data of (a) and the solid lines are the fits obtained from (b). A linear color intensity scale was used in maps (a) and (b).

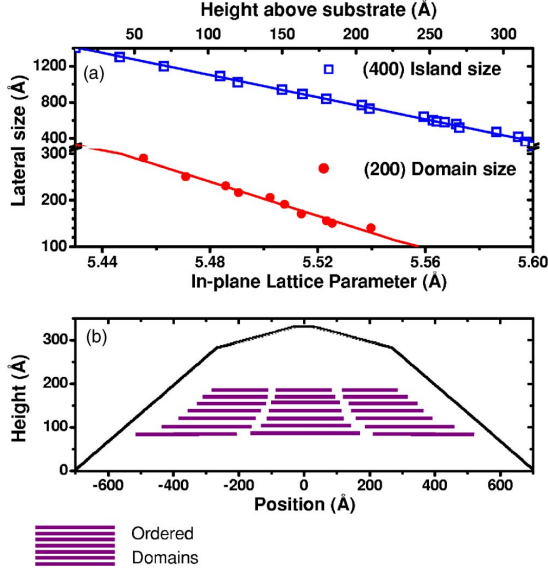
MALACHIAS *et al.*PHYSICAL REVIEW B **72**, 165315 (2005)

FIG. 7. (Color online) (a) Size of the islands and domains of sample B as a function of in-plane lattice parameter. Notice the y-axis break in the lateral size (scale is linear). (b) Schematic map for the islands of sample B, showing the location of the ordered domains.

The map shown in Fig. 6(b) was obtained using Eq. (3), consisting of the ordered domain distribution inside the islands, taking into account the interference between neighboring layers with different lattice parameters, square shaped domains, and corresponding composition profiles. The WL peak was included in the simulation describing the scattering from a thin SiGe film at the surface, strained to the Si bulk lattice parameter. Selected angular cuts from the experimental and calculated maps are shown in Fig. 6(c). The possible interference between antiphase domains belonging to different islands was ruled out by performing simulations using correlation functions, which could not reproduce the scattering data.

A comparison between the island and domain size in sample B is shown in Fig. 7(a), where the domain size was obtained from fits of the (200) map and the island size from scans at the (400) reflection (not shown here). The height information was introduced by correlating the size of an iso-lattice parameter region in the (400) reflection with a height inside the island obtained from AFM profiles.^{23,24} Assuming that the strain status of the ordered alloy at the (200) reflection follows the strain relaxation of the whole island this association was extended to the ordered regions.²⁸ For both island and domain there is an approximate linear variation of size with lattice parameter and height. It can be inferred that nine ordered domains could fit inside each constant lattice parameter layer. There is a clear variation of domain size with increasing lattice parameter and height, suggesting the existence of a stress-mediated mechanism that determines the domain size. Figure 7(b) depicts schematically what should be the distribution of domains inside the islands of sample B.

C. Bragg-Williams order parameter of samples grown at different temperatures

The influence of the growth temperature on ordering was evaluated for the whole temperature sample series. Figure 8 shows q_r - q_a maps in the vicinity of the (400) reflection (maps a, c, e, g) and the (200) reflection (maps b, d, f, h) for samples A (a, b), B (c, d), C (e, f), and D (g, h). The equivalent lattice parameter region is the same in both reflections for each sample. Intensity scales are logarithmic in the (400) maps and linear in the (200) maps for a better visualization of their profiles. Reciprocal space regions that were not measured appear in white at the (200) maps.

In all samples the (200) scattered intensity is observed up to 60% of the q_r range that is measured in the (400) maps. This indicates that ordering is possibly strain stabilized. In all (200) maps the scan step is larger than the width of a (200) multiple scattering peak that is usually observed exactly at the Si (200) position. Hence, the structures observed at the Si (200) position in Figs. 8 (b, d, f) are due to the presence of partially ordered alloys in the WL. In the (200) map of Fig. 8(f) (sample C) one observes a broad peak at the Si position. At this temperature range the (200) ordering starts to be destructed due to the annealing that takes place at the equivalent sample growth time.¹⁸ For sample D that was grown at 840 °C the (200) ordering at the WL disappears.

Figure 9 shows the relationship between islands and/or domains strain, size, and height for samples A (a), C (b), and D (c). The height position of ordered domains starts always after a minimum height of 50 Å due to the Si-rich island basis.^{25,20}

The degree of ordering inside Ge islands can be estimated by comparing the intensities of fundamental and superstructure reflections.²⁷ For the Ge islands this comparison was done between the in-plane (400) and (200) reflections. The intensity of the (400) reflection is proportional to the square of the sum of atomic scattering factors of Si (f_{Si}) and Ge (f_{Ge}),²⁷ i.e.,

$$I_{(400)} = c4V_{400}(C_{\text{Ge}}f_{\text{Ge}} + C_{\text{Si}}f_{\text{Si}})^2, \quad (5)$$

where C_{Ge} and C_{Si} are the concentrations of Ge and Si, respectively, V_{400} is the volume of the region at the Bragg condition and c is a constant that includes all scattering parameters (such as sample area, photon flux, etc.). In contrast, the intensity measured at the (200) reflection is proportional to the square of the difference of the atomic scattering factors and depends on the degree of ordering expressed by the Bragg-Williams order parameter S ,²⁷ i.e.,

$$I_{(200)} = cV_{200}S^2(f_{\text{Ge}} - f_{\text{Si}})^2. \quad (6)$$

The order parameter S can be experimentally obtained by comparing the ratio of the measured intensities. Assuming that the intensities were measured in a region of reciprocal space with equal volume ($V_{400} = V_{200}$) the ratio between the three-dimensional integrated intensities will be given by

$$\frac{I_{200}}{I_{400}} = \frac{S^2(f_{\text{Ge}} - f_{\text{Si}})^2}{4(f_{\text{Ge}}n_{\text{Ge}} + f_{\text{Si}}n_{\text{Si}})^2}. \quad (7)$$

X-RAY STUDY OF ATOMIC ORDERING IN SELF-...

PHYSICAL REVIEW B 72, 165315 (2005)

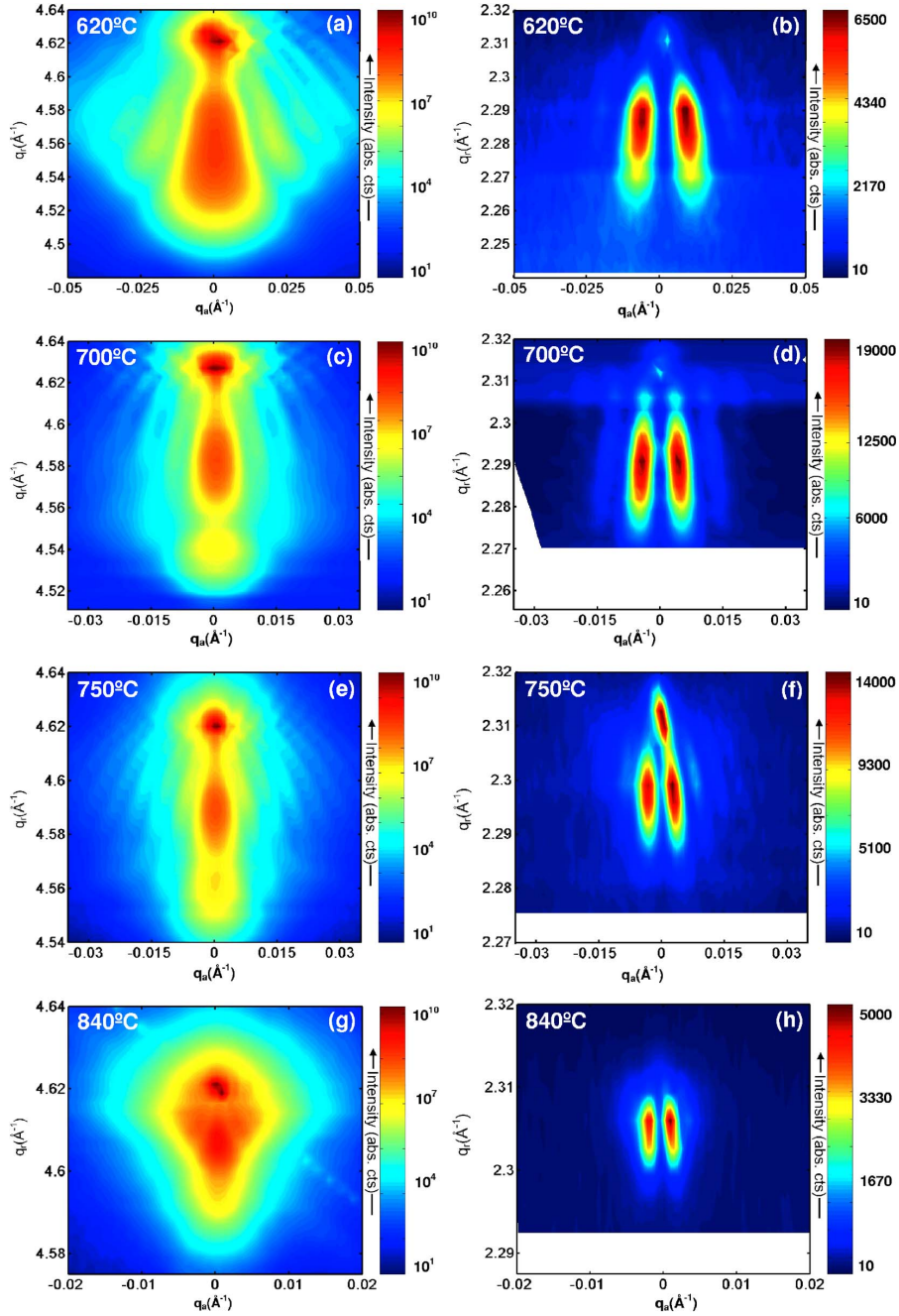


FIG. 8. (Color online) Measured q_r - q_a (400) and (200) maps for samples A (a, b), B (c, d), C (e, f), and D (g, h). The color scale is logarithmic in the (400) maps and linear in the (200) maps for better visualization. Due to the large variation in island size, composition and strain from samples A–D (see Ref. 20) the q_r - q_a axis were set to allow a direct comparison between (400) and (200) scattering profile widths for each sample. Intensities are shown in absolute counts. White regions in the (200) maps correspond to reciprocal space positions that were not measured. The strain relaxation of the ordered alloy is observed at the (200) reflection maps up to 60% of the q_r -range measured at the (400) reflection. This relation holds up if intensities are compared in logarithmic or linear scales.

MALACHIAS *et al.*

PHYSICAL REVIEW B 72, 165315 (2005)

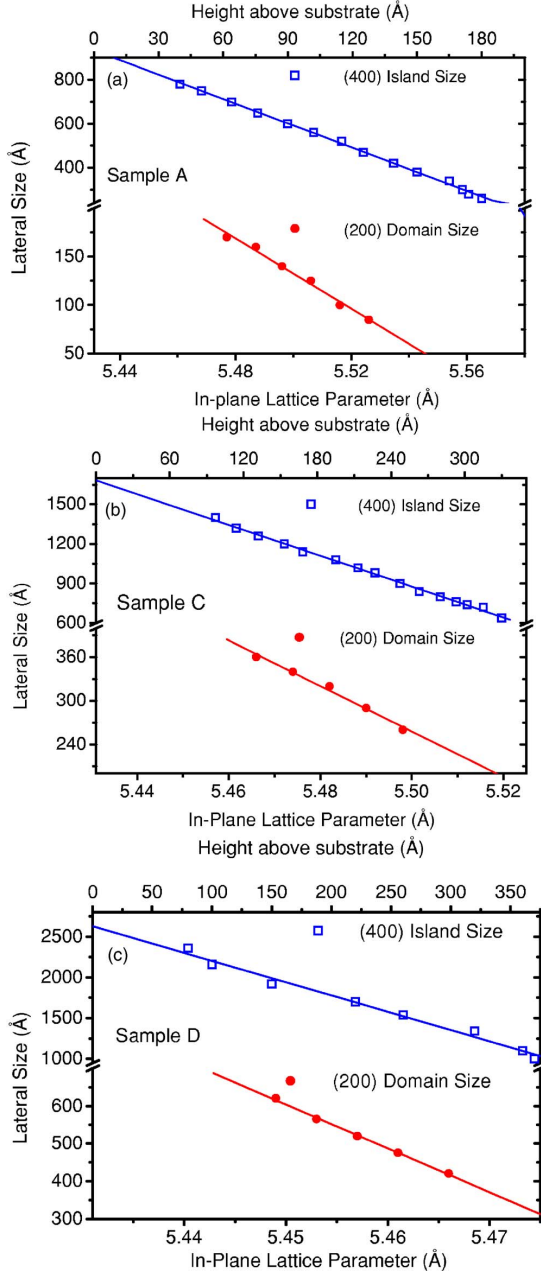


FIG. 9. (Color online) Island and domain size as a function of lattice parameter and height for samples A (a), C (b), and D (c).

For an atomic in-plane layer with two types of sites α (Ge) and γ (Si) the ordering parameter S is defined as $S = r_\alpha + r_\gamma - 1$,²⁷ where r_α and r_γ are fractions of α and γ sites occupied by the right atom. The value $S=0$ indicates that 50% of the atoms are in their wrong sites, denoting a com-

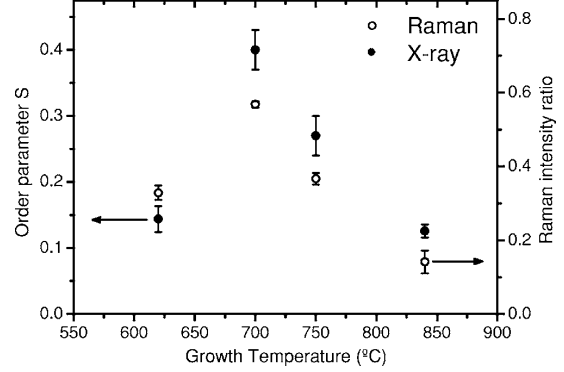


FIG. 10. Order parameter S and Raman integrated intensity ratio between Si-Ge and Ge-Ge peaks ($I_{\text{SiGe}}/I_{\text{GeGe}}$).

pletely random alloy, while $S=1$ represents a perfectly ordered arrangement.

Comparing the measured q_a -integrated intensities of (200) and (400) reflections of sample B an order parameter $S = 0.40 \pm 0.03$ was obtained, which represents a lower bound for the degree of ordering, since $V_{400} > V_{200}$. This value indicates a high degree of ordering when compared to $S = 0.18$, obtained for $\text{Si}_{0.5}\text{Ge}_{0.5}$ alloy layers.¹⁶ The stress caused by the deposition of pure Ge on Si is higher than for an alloy layer, possibly increasing the efficiency of the ordering mechanism.¹⁷ According to Jesson *et al.* and Tischler *et al.*,^{16,17} each atomic plane parallel to the substrate has only one type of Ge-rich site (α or β) and only one type of Si-rich site (γ or δ) as shown in Fig. 5. Thus, S can be considered an average value over the whole crystal (all domains). Using the definition $S = r_\alpha + r_\gamma - 1$,²⁷ where r_α and r_γ are fractions of α and γ sites occupied by the right atoms, we obtain that at least 70% of the atoms inside the islands of sample B are in their correct positions. Bragg-Williams ordering parameters for all samples were calculated comparing the experimental intensities of (400) and (200) maps.

Order parameter results for all samples are shown in Fig. 10 together with the ratio of the integrated intensities of the Si-Ge and Ge-Ge Raman peaks. As mentioned before this Raman intensity ratio ($I_{\text{SiGe}}/I_{\text{GeGe}}$) between the 295 cm^{-1} and 414 cm^{-1} vibrational modes reveals the relative abundance of Si-Ge bonds inside the islands^{22,29} and can be semiquantitatively compared with the ordering parameter S . The growth-temperature dependence of these parameters seen in Fig. 10 exhibits an excellent agreement between these techniques, indicating that Raman measurements support the x-ray results.

IV. DISCUSSION AND CONCLUSIONS

It is worth noting that ordered domains may influence the electronic and/or optical properties of these islands. The presence of ordered domains may result in a shift of the phonon frequency, band edge alignment, and even the semiconductor gap.³⁰ Thus, any realistic calculation of quantum dot properties should take this into account. Changing the

X-RAY STUDY OF ATOMIC ORDERING IN SELF-...

PHYSICAL REVIEW B **72**, 165315 (2005)

growth temperature it is possible to favor or avoid the formation of ordered alloy regions inside Ge domes. The ordering efficiency may be also modified by tuning the growth rate, which was fixed for the sample series used here.

In summary, by measuring basis-forbidden x-ray reflections of self-assembled Ge:Si(001) islands we have demonstrated the existence of atomically ordered regions inside these nanostructures. X-ray scattering maps evidenced that these small ordered domains are separated by antiphase

boundaries. Order parameters were calculated to all samples and corroborated by Raman measurements.

ACKNOWLEDGMENTS

This work was supported by ESRF and Brazilian agencies CAPES (BEX-0017/03-5), FAPESP (Grant No. 03/13136-6), and CNPq.

*Electronic address: angeloms@fisica.ufmg.br

- ¹G. C. L. Wong, J. X. Tang, A. Lin, Y. L. Li, P. A. Janmey, and C. R. Safinya, *Science* **288**, 2035 (2000).
- ²G. Springholz, V. Holy, M. Pinczolits, and G. Bauer, *Science* **282**, 734 (1998).
- ³P. Venezuela, J. Tersoff, J. A. Floro, E. Chason, D. M. Follstaedt, F. Liu, and M. G. Lagally, *Nature (London)* **397**, 678 (1999).
- ⁴J. H. Li, S. C. Moss, Y. Zhang, A. Mascarenhas, L. N. Pfeiffer, K. W. West, W. K. Ge, and J. Bai, *Phys. Rev. Lett.* **91**, 106103 (2003).
- ⁵G. Medeiros-Ribeiro, F. G. Pikus, P. M. Petroff, and A. L. Efros, *Phys. Rev. B* **55**, 1568 (1997).
- ⁶R. J. Warburton, C. S. Dürr, K. Karrai, J. P. Kotthaus, G. Medeiros-Ribeiro, and P. M. Petroff, *Phys. Rev. Lett.* **79**, 5282 (1997).
- ⁷M. Hansen, *Constitution of Binary Alloys*, 2nd ed. (McGraw-Hill, New York, 1958).
- ⁸J. Y. Tsao, *Materials Fundamentals of Molecular Beam Epitaxy* (Academic, San Diego, 1993).
- ⁹A. Qteish and R. Resta, *Phys. Rev. B* **37**, 6983 (1988).
- ¹⁰A. Ourmazd and J. C. Bean, *Phys. Rev. Lett.* **55**, 765 (1985).
- ¹¹J. L. Martins and A. Zunger, *Phys. Rev. Lett.* **56**, 1400 (1986).
- ¹²P. B. Littlewood, *Phys. Rev. B* **34**, 1363 (1986).
- ¹³E. Muller, H.-U. Nissen, M. Ospelt, and H. von Kanel, *Phys. Rev. Lett.* **63**, 1819 (1989).
- ¹⁴F. K. LeGoues, V. P. Kesan, and S. S. Iyer, *Phys. Rev. Lett.* **64**, 40 (1990).
- ¹⁵F. K. LeGoues, V. P. Kesan, S. S. Iyer, J. Tersoff, and R. Tromp, *Phys. Rev. Lett.* **64**, 2038 (1990).
- ¹⁶J. Z. Tischler, J. D. Budai, D. E. Jesson, G. Eres, P. Zschack, J.-M. Baribeau, and D. C. Houghton, *Phys. Rev. B* **51**, 10947 (1995).
- ¹⁷D. E. Jesson, S. J. Pennycook, and J.-M. Baribeau, *Phys. Rev. Lett.* **66**, 750 (1991); D. E. Jesson, S. J. Pennycook, J.-M. Baribeau, and D. C. Houghton, *ibid.* **68**, 2062 (1992); D. E. Jesson, S. J. Pennycook, J. Z. Tischler, J. D. Budai, J.-M. Baribeau, and D. C. Houghton, *ibid.* **70**, 2293 (1993).
- ¹⁸H. Reichert, S. C. Moss, P. Imperatori, and K. Evans-Lutterodt, *Appl. Phys. Lett.* **74**, 531 (1999).
- ¹⁹V. P. Kesan, F. K. LeGoues, and S. S. Iyer, *Phys. Rev. B* **46**, 1576 (1992).
- ²⁰T. U. Schüllli, M. Stoffel, A. Hesse, J. Stangl, R. T. Lechner, E. Wintersberger, M. Sztucki, T. H. Metzger, O. G. Schmidt, and G. Bauer, *Phys. Rev. B* **71**, 035326 (2005).
- ²¹D. J. Lockwood, K. Rajan, E. W. Fenton, J.-M. Baribeau, and M. W. Denhoff, *Solid State Commun.* **61**, 465 (1987).
- ²²E. Finkman, F. Meyer, and M. Mamor, *J. Appl. Phys.* **89**, 2580 (2001).
- ²³R. Magalhães-Paniago, G. Medeiros-Ribeiro, A. Malachias, S. Kycia, T. I. Kamins, and R. S. Williams, *Phys. Rev. B* **66**, 245312 (2002).
- ²⁴T. U. Schüllli, J. Stangl, Z. Zhong, R. T. Lechner, M. Sztucki, T. H. Metzger, and G. Bauer, *Phys. Rev. Lett.* **90**, 066105 (2003).
- ²⁵A. Malachias, S. Kycia, G. Medeiros-Ribeiro, R. Magalhães-Paniago, T. I. Kamins, and R. S. Williams, *Phys. Rev. Lett.* **91**, 176101 (2003).
- ²⁶I. Kegel, T. H. Metzger, P. Fratzl, J. Peisl, A. Lorke, J. M. Garcia, and P. M. Petroff, *Europhys. Lett.* **45**, 222 (1999).
- ²⁷B. E. Warren, *X-ray Diffraction* (Dover, New York, 1969).
- ²⁸An alternative method to determine heights of iso-lattice parameter regions consists in the analysis of the q_z information measured by the PSD detector as discussed by I. Kegel *et al.*, *Phys. Rev. B* **63**, 035318 (2001). This analysis procedure was applied to the (200) reflection data, exhibiting quantitative agreement with the AFM method.
- ²⁹A. V. Dvurechenskii, Zh. V. Smagina, V. A. Zinov'ev, V. A. Armbrister, V. A. Volodin, and M. D. Efremov, *JETP Lett.* **79**, 333 (2004).
- ³⁰S. P. Ahrenkiel, S. W. Johnston, R. K. Ahrenkiel, D. J. Arent, M. C. Hanna, and M. W. Wanlass, *Appl. Phys. Lett.* **74**, 3534 (1999).

4.2 Growth dependence of atomic ordering in SiGe islands

4.2.1 *Atomic ordering dependence on growth method in Ge:Si(001) islands: Influence of surfacekinetic and thermodynamic interdiffusion mechanisms*

A. Malachias, M. Stoffel, M. Schmidtbauer, T. U. Schüllli, G. Medeiros-Ribeiro, O. G. Schmidt, R. Magalhaes-Paniago, T. H. Metzger, Phys. Rev. B 82, 035307 (2010).

As a follow-up of the investigations of atomic ordering in MBE grown islands, the presence of such ordering was interpreted as being of kinetic origin and a footprint for the importance of surface diffusion processes for island formation and as a Si-source of interdiffusion. We have thus studied different growth methods like MBE, where surface diffusion is the most important transport mechanism, and compared it to Chemical Vapour Deposition (CVD) and Liquid Phase Epitaxy (LPE) grown SiGe islands. The CVD grown islands showed less ordering than the MBE grown islands. LPE growth resulted in the poorest degree of order. This result is comforting the assumption of surface diffusion being the main driving force for atomic ordering. This diffusion mechanism has highest importance for the formation of MBE grown islands but is significantly less important when the semiconductor atoms are dissolved and transported in a liquid medium. At the same time, these results allow for the interpretation that surface diffusion is the main mechanism for Si-incorporation into SiGe islands produced by Ge MBE on Si(001).

PHYSICAL REVIEW B **82**, 035307 (2010)**Atomic ordering dependence on growth method in Ge:Si(001) islands: Influence of surface kinetic and thermodynamic interdiffusion mechanisms**A. Malachias,^{1,*} M. Stoffel,^{2,3} M. Schmidbauer,⁴ T. Ü. Schulli,⁵ G. Medeiros-Ribeiro,⁶ O. G. Schmidt,³ Rogerio Magalhães-Paniago,⁷ and T. H. Metzger^{5,8}¹*Laboratório Nacional de Luz Síncrotron, CP 6192, CEP 13083-970, Campinas, Brazil*²*Institut Jean Lamour, UMR CNRS 7198, Nancy-Université, BP 239, F-54506 Vandœuvre-lès-Nancy, France*³*Institute for Integrative Nanosciences, IFW Dresden, Helmholtzstr. 20, 01069 Dresden, Germany*⁴*Leibniz Institut für Kristallzüchtung, Max-Born-Str. 2, D-12489 Berlin, Germany*⁵*European Synchrotron Research Facility, BP 220, Grenoble, France*⁶*Hewlett-Packard Laboratories, Palo Alto, California 94304, USA*⁷*Departamento de Física, Universidade Federal de Minas Gerais, CP 702, 30123-970 Belo Horizonte, MG, Brazil*⁸*Department of Biomaterials, Max Planck Institute of Colloids and Interfaces, 14424 Potsdam, Germany*

(Received 15 April 2010; revised manuscript received 3 June 2010; published 15 July 2010)

Interdiffusion in self-assembled Ge:Si(001) islands has been explained by models based on either thermodynamic and/or surface kinetic considerations. In order to analyze the relevance of bulk and surface diffusion on the final composition state, we performed a set of controlled x-ray diffraction experiments to study both composition and atomic ordering in Ge:Si(001) islands grown by different methods. Surface diffusion strongly enhances the overall interdiffusion during island growth by solid source molecular beam epitaxy while chemical-vapor-deposited islands are closer to thermodynamic model systems. The growth conditions play a crucial role on the appearance of atomic ordering. In particular, a remarkable correlation between atomic ordering and surface diffusion kinetics is found.

DOI: [10.1103/PhysRevB.82.035307](https://doi.org/10.1103/PhysRevB.82.035307)

PACS number(s): 68.65.Hb, 61.05.C-

I. INTRODUCTION

Self-assembled semiconductor islands have gained a tremendous interest over the last years. Novel nanoscale devices based on such islands have been proposed¹ and their use as building blocks for such devices experimentally realized recently.² Furthermore, new possible applications in quantum computing³⁻⁵ and spintronics^{6,7} were envisaged. The island formation and subsequent evolution has been investigated thoroughly both experimentally and theoretically. Different models based on partially or fully thermodynamic or kinetic considerations have been proposed and are still a matter of controversy.

Most of the studies have concerned Ge:Si(001) islands, that follows Stranski-Krastanow growth mode with only two elements involved. In this specific case, island shapes are well described by thermodynamics⁸ while bimodal distributions (for instance) have been tackled by surface kinetics^{9,10} and thermal equilibrium arguments.^{8,11} Finally, shape transitions observed in ultrahigh vacuum (UHV) growth conditions¹² were found to be associated with strong mass transport effects of surface kinetic origin, referred before as anomalous coarsening.^{9,10} Such finding for UHV deposition is in contrast with chemical-vapor-deposition (CVD) studies, in which the range of coexistence for different island shapes, domes and pyramids, is considerably broader.¹¹ Chemical composition has been addressed in Ge:Si islands by using a variety of techniques such as transmission electron microscopy,¹³ anomalous x-ray diffraction,¹⁴ and selective wet chemical etching.¹⁵

Besides morphological and chemical composition studies, the microscopic organization of Si and Ge atoms after island formation has been addressed by x-ray atomic order studies.

It was found that dome-shaped islands in which alloying take place exhibit long-range order with the appearance of superstructure reflections.¹⁶ Although the first study on the subject was unable to elucidate the mechanism that lead to order, it was demonstrated that the atomic arrangement followed the in-plane organization observed in thin films.¹⁷

In this work we explore chemical composition and atomic order measurements performed using x-ray diffraction techniques to address the relevance of thermodynamic and surface effects to the final state of Ge islands after growth on Si(001). It is found that CVD islands are much closer to model thermodynamic systems while surface kinetics strongly enhances interdiffusion¹⁸ during island growth by molecular-beam epitaxy (MBE). We show here how Ge:Si(001) growth conditions play also a crucial role for the appearance of the recently found atomic order in Ge domes.¹⁶ Such phenomenon exhibits a remarkable correlation with the degree of relevance of surface kinetics on island composition.

II. EXPERIMENTAL

For a thorough investigation on SiGe interdiffusion and on the appearance of spontaneous atomic ordering in Ge:Si uncapped nanostructures, six samples were studied in this work. The first one, grown by liquid-phase epitaxy (LPE), can be considered a reference for stoichiometric alloy islands since Ge_{0.5}Si_{0.5} was nominally deposited on a Si(001) substrate. A second sample, grown by CVD, was obtained by depositing nominally pure Ge via germane precursor (GeH₄) on Si. The other four samples were grown by solid source MBE at different temperatures, also with deposition of a pure Ge nominal coverage. The growth parameters for all samples

TABLE I. List of Ge:Si samples used in this work, with growth parameters, average island dimensions and morphology (Ref. 19).

Sample name	Growth temperature (°C)	Coverage	Growth rate (ML/s)	Island width/height (nm)	Type of island
LPE	600	31.4 ML $\text{Si}_{0.5}\text{Ge}_{0.5}$ ^a	0.007	81/40	Truncated pyramids
CVD	600	11.2 ML Ge	0.05	32/14	Domes
MBE-a	620	6.7 ML Ge	0.05	87/19	Domes
MBE-b	700	11 ML Ge	0.05	143/36	Domes
MBE-c	750	11 ML Ge	0.05	170/34	Domes
MBE-d	840	6 ML Ge	0.05	338/37	Domes

^aThe monolayer thickness here is considered as 0.1413 nm for Ge, and 0.1385 nm for $\text{Si}_{0.5}\text{Ge}_{0.5}$.

are summarized in Table I.¹⁹ It must be noticed that LPE islands assume a truncated pyramid geometry with $\langle 111 \rangle$ side facets.^{20,21} Such morphology indicates that LPE growth takes place very close to bulk thermal equilibrium conditions while MBE- and CVD-grown samples exhibit multifaceted dome islands.^{8,9}

It is worth to state at this point that the aim of our work is not to directly compare punctual details of samples grown by different techniques in different machines, but to show how strong changes in interdiffusion and resulting atomic ordering arise from growth conditions, ultimately related to a predominance of bulk thermodynamic or surface kinetic mechanisms. As mentioned before, the apparent contrast found in the literature has been a reason for extensive debate¹⁰ and can be better understood under the general framework illustrated by this work.

The ability of quantitatively depicting strain and chemical composition in Ge islands by anomalous grazing incidence x-ray diffraction (GID) methods^{14,22} has continuously developed over the last few years, with several works focusing on the reconstruction of lattice parameter profiles,²² composition gradients^{14,23,24} and ultimately atomic ordering.¹⁶ The GID experiments performed for this work were carried out at the ID01 beamline at the ESRF (Grenoble, France) and at the XRD2 beamline at the LNLS (Campinas, Brazil). In GID geometry the diffraction takes place on atomic planes perpendicular to the Si(001) substrate surface, i.e., the in-plane lattice parameter is probed. All samples were illuminated at a grazing angle of 0.15° , below the critical angle of total external reflection for Si near 11 keV photon energies. This condition establishes a penetration depth of few tens of nanometers, allowing for a partial suppression of the signal from the Si substrate, and a relative enhancement of the signal diffracted by the Ge islands.^{14,22}

Chemical composition in Ge:Si nanostructures can be retrieved from reciprocal space data by performing measurements in the vicinity of the Ge K edge (11 103 eV). The intensity contrast obtained from measurements in different energies can then be directly correlated with the average Ge content, as depicted in Refs. 14 and 23.

A survey of the real-space reconstruction method using the anomalous-GID measurements performed on sample MBE-b is presented in Fig. 1. Figure 1(a) shows two longitudinal (θ - 2θ) scans near the Si(400) reciprocal space posi-

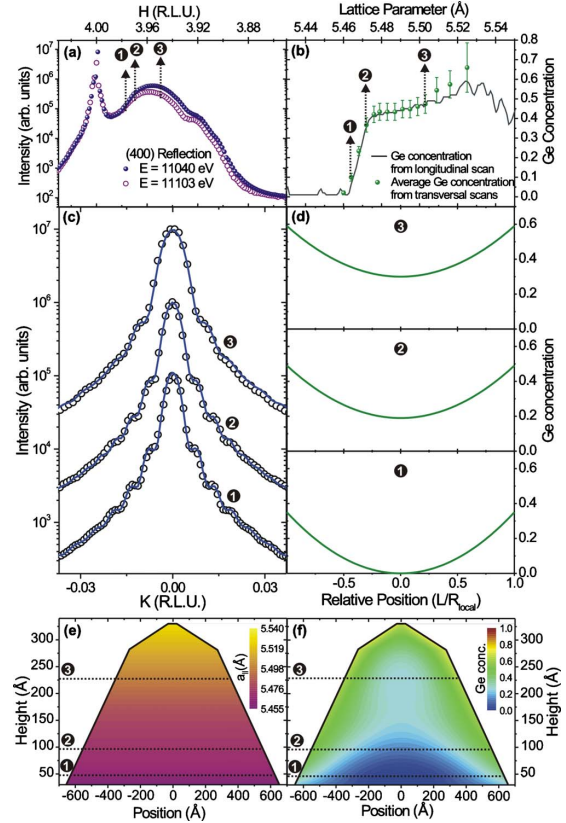


FIG. 1. (Color online) (a) Longitudinal (θ - 2θ) scans in the vicinity of the Si(400) reflection for sample MBE-b at two energies: 11 103 eV (Ge K edge) and 11 040 eV. (b) The solid line represents the vertical Ge concentration profile obtained from (a) as a function of the local in-plane lattice parameter (Ref. 14). The dots represent laterally averaged local compositions from the analysis of transversal scans. (c) Selected transversal (θ) scans performed at the positions labeled 1, 2, and 3 in (a). The open dots are measured data while the solid lines are fits with a lateral composition model (Ref. 24). (d) Lateral composition profiles used for fitting transversal scans. (e) Local lattice parameter map for MBE-b islands (Ref. 14). (f) Lateral concentration profile map for MBE-b islands.

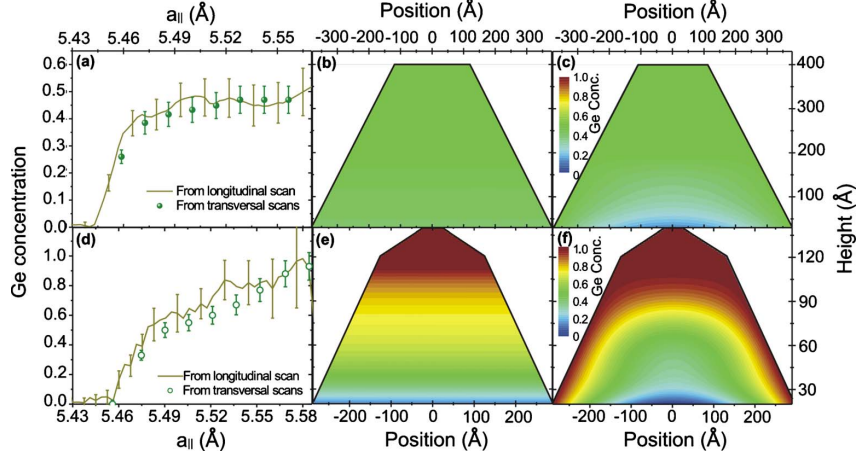


FIG. 2. (Color online) (a) Vertical (solid line) and laterally averaged (dots) Ge concentration profiles extracted from anomalous diffraction measurements on LPE islands. The concentration profiles are graphically represented as a function of height in (b) vertical only and (c) lateral. (d) Ge Vertical and laterally averaged concentration profiles for CVD islands (Ref. 24). These profiles are represented as a function of island height in (e) and (f), respectively.

tion. For both scans it is possible to notice a sharp peak at the $H=4$ position, corresponding to the diffraction from the Si substrate. A broad intensity profile is observed for $H < 4$, corresponding to regions with larger lattice parameter, inside the Ge islands.¹⁴ The spanning of such diffracted intensity is a direct indication that a lattice parameter gradient takes place inside Ge domes. For uncapped islands it is known that the scattering intensity closer to the substrate peak is originated from the bottom of the islands while the scattering at the lower H values (large in-plane lattice parameter) comes from partially relaxed regions on the island apexes.^{14,22}

By comparing the two measurements presented in Fig. 1(a) obtained at 11040 and 11103eV one observes an intensity reduction for lower values of H which is related to the presence of Ge atoms. Following Refs. 14 and 25, the Ge concentration was extracted, and is represented by the solid line in Fig. 1(b). The concentration profile obtained is still a function of the in-plane lattice parameter. It shows indirectly that the average Ge content at regions of the island with lattice parameter close to bulk Si (island base) reaches almost zero while a SiGe alloy with average 0.5 Ge concentration is found at regions with larger lattice parameter (island top).

In order to match lattice parameter and concentration information from reciprocal space and real space one must perform transversal scans at selected positions of the longitudinal scan of Fig. 1(a). Figure 1(c) shows three scans, corresponding to positions labeled 1, 2, and 3 in Fig. 1(a). The comparison of lateral widths from several transversal scans—obtained fitting the curves with appropriate form factor^{22,24}—with atomic force microscopy (AFM) profiles of the statistically average island allows to correlate the height in real space of a region with fixed lattice parameter.¹⁴ A map of lattice parameter distribution for a representative island of the ensemble is then built, as shown in Fig. 1(e).

Transversal (θ) scans also provide information on the lateral concentration profile of the islands. Using a lateral gra-

dient of composition allows to fit each of these scans [solid lines in Fig. 1(c)], extracting the lateral Ge composition.²⁴ Parabolic concentration profiles used to fit the scans of Fig. 1(c) are shown in Fig. 1(d). The method is finally able to fully depict concentration gradients inside the islands by plotting the profiles of Fig. 1(d) matching the lattice parameter positions in Fig. 1(e). A concentration map including lateral and vertical gradients is then obtained, as shown in Fig. 1(f).^{24,26,27} It is important to emphasize that the horizontally averaged lateral composition obtained here is fully consistent with the vertical gradient obtained directly from longitudinal scans,¹⁴ as shown by the solid dots in Fig. 1(b).

III. RESULTS AND DISCUSSION

A. Composition profiles and interdiffusion mechanisms

The composition profile of Fig. 1(f) is in agreement with recent findings using chemical selective etching procedures, as explored in Ref. 15. For such MBE grown samples a considerable Si diffusion is observed in the island bottom with an increasing Ge concentration observed toward the islands facets. However, the Ge concentration at the island surface/interface spans from 0.4 at the island bottom until 0.6 at the island surface.²⁵ This evidences that alloying takes place at the island bottom, as well as on facets, which are being continuously exposed to an incoming flux of Ge atoms. Such scenario points out the existence of a fast and efficient surface kinetic diffusion component that leads to a pronounced interdiffusion at the facets while the role of bulk diffusion is not significant for the resulting profile.

For LPE and CVD islands the composition profiles shown in Fig. 2 reveal a very different behavior. The average Ge concentration at the top of SiGe LPE islands is found to be 0.48, with a steplike gradient at the island bottom, as shown in Fig. 2(a). By applying only the vertical concentration profile one observes that the Ge content at the island bottom

MALACHIAS *et al.*PHYSICAL REVIEW B **82**, 035307 (2010)

decreases to about 35% [Fig. 2(b)] while the lateral concentration shows a more localized Si-rich core with only 20% Ge at the island center [Fig. 2(c)]. Similar plateaulike profiles ranging from the LPE island bottom until one third of its height have been obtained before from strain modeling.^{20,21} Most of the material inside LPE islands has the nominal alloy content with a reduced interdiffusion from Si atoms from the substrate. This scenario points out that the 50/50 Si-Ge mixture is thermodynamically favorable due to the low enthalpy of mixing. No phase segregation is observed if Figs. 2(b) and 2(c). The Si interdiffusion at the island bottom arises from a slow bulk diffusive process that minimizes the chemical gradient between island and substrate and consists therefore in a thermodynamic driving force for bulk diffusion. Since deposition involves a liquid precursor the process does not allow for quick changes among incoming atoms deposited on the surface and those from the substrate. Thus, with the surface growth front surrounded by the heated precursor stoichiometric alloy liquid, a suppression of any effective surface kinetic diffusion mechanisms is achieved.

For the CVD islands—the smallest of all nanostructures analyzed in this work—a smoother average vertical Ge concentration gradient is obtained [Figs. 2(d) and 2(e)]. However, when such gradient is analyzed by the lateral composition procedure²⁴ a Ge-rich shell is observed [Fig. 2(f)]. The pronounced composition gradient with a large Si diffusion at the island base is a result from its reduced height and the continuous flux of Ge atoms from the CVD precursor gas. Since a residual passivating hydrogen-rich atmosphere remains at the growth chamber a partial suppression of the kinetic Si interdiffusion mechanisms take place at the island facets (growth front). If the Ge precursor inflow is interrupted, maintaining the growth temperature, the island facets become more Si rich mainly due to bulk diffusion, as shown in Ref. 27 and corroborated by selective chemical etching.^{24,28} By introducing a modified atmosphere in the growth chamber Si and/or Ge surface diffusion can be enhanced/suppressed. In particular, H_2 environment strongly reduces Si and Ge surface diffusion, as evidenced experimentally in Ref. 27.

The average vertical composition data extracted from longitudinal scans in anomalous GID is generally a good approach to the local lateral concentration profiles for islands in which the lateral Ge composition gradient is less pronounced, as in MBE and LPE samples. In these islands the local composition is fairly similar in the vertical and three-dimensional profiles. For small islands grown in a surface kinetic limited technique such as CVD the lateral composition gradients are more pronounced and the average vertical concentration profile cannot be regarded as an adequate approximation to the local three-dimensional composition profile. In all cases the vertical averaged and the total Ge concentration obtained by the three-dimensional or by the vertical concentration analysis is the same.

In order to settle the discussion above into a more general and quantitative framework the vertical Ge composition profiles for MBE samples a, c, and d are depicted in Figs. 3(a)–3(c), following the results from Ref. 25. From selective etching experiments in this previous work it was shown that islands are strongly alloyed, with a considerable Si content at

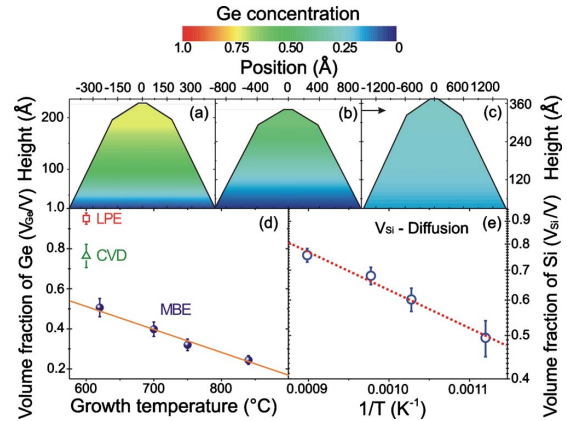


FIG. 3. (Color online) Representation of Ge vertical concentration profiles for islands of samples (a) MBE-a, (b) MBE-c, and (c) MBE-d. The ratio between integrated Ge volume fraction and nominal Ge concentration inside the islands studied in this work is shown in (d). The line plotted across solid dots for MBE islands is a guide to the eyes. An Arrhenius plot for Si volume inside the MBE samples is seen in (e).

their facets, as can be inferred from the vertical composition profiles.²⁵ By using vertical composition profiles it is possible to explore the volume fraction of alloyed material with respect to nominal deposition values as a function of the growth temperature for all islands. Figure 3(d) shows a representation of the ratio between the measured volume of Ge—or $Si_{0.5}Ge_{0.5}$ in the LPE case—observed in each island and the actual island volume. Figure 3(d) shows that in MBE grown islands a strong deviation with respect to the expected Ge nominal composition is observed for all samples, following a decreasing tendency with respect to temperature. Employing the same evaluation for the LPE sample one observes that the deviation from nominal composition in LPE islands is extremely reduced, which is compatible to a bulk diffusion scenario. For such case the incorporation of Si atoms from the substrate by a slow process results in a much less effective interdiffusion compared to MBE samples. Finally, the CVD grown domes are situated in between MBE and LPE islands, representing a growth condition where both surface or bulk diffusion may take place (depending on residual atmosphere). For these islands the surface kinetic diffusion activity will become clearer by analyzing atomic ordering, discussed in the following paragraphs.

For the MBE samples an Arrhenius plot based on the volume of Si atoms incorporated into the islands can be built, as shown in Fig. 3(e). We obtain an activation energy of 0.073eV for the Si adatoms. Such value is much smaller than the usual activation energies for bulk diffusion, which are on the order of a few electron volt²⁹ but compatible with kinetic atom step flow energies.^{30,31} This kinetic behavior becomes clearer by studying the atomic order of the SiGe-alloyed material inside the islands.

B. Atomic ordering and surface kinetics

SiGe atomic ordering has been observed in thin films and multilayers grown by MBE and CVD,¹⁷ and more recently in

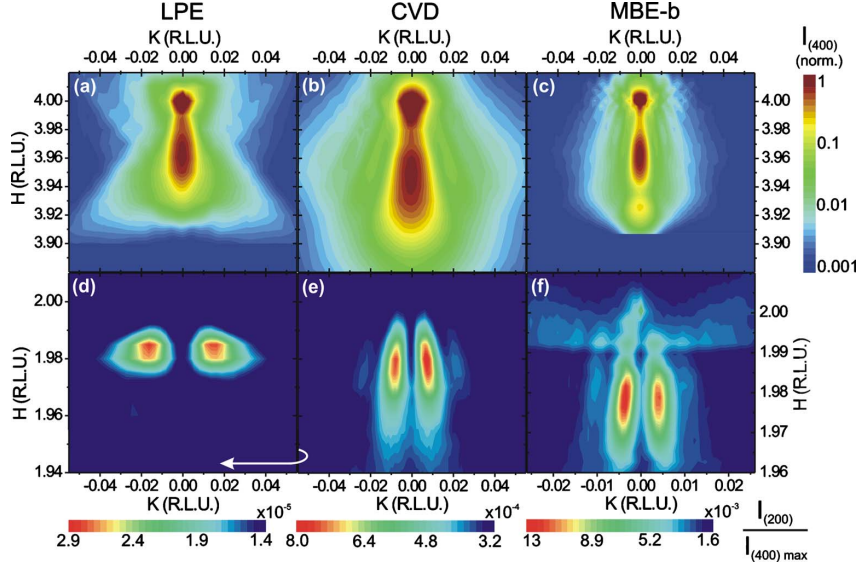


FIG. 4. (Color online) Reciprocal space maps of (400) [(a)–(c)] and (200) reflections [(d)–(f)] for [(a) and (d)] LPE, [(b) and (e)] CVD, and [(c) and (f)] MBE-b samples. The vertical H axis of (d) and (e) are equivalent. Intensity color scales in the (400) maps were normalized to the unit—taken at the island peak position—and to the intensity ratio relative to such maximum at the (200) maps.

Ge:Si(001) islands.¹⁶ In this case Si and Ge atoms are found to be periodically arranged in one (or more) crystallographic axis, giving rise to superstructure reflections that are not observed in elemental pure crystals or disordered alloys. The main evidence of ordering in Ge:Si islands is related to the appearance of nonzero intensity in basis-forbidden Ge/Si reflections such as (200) and (420).¹⁶ For a pure Si or Ge crystal as well as for a completely disordered alloy of both materials the structure factor of these reflections is zero, whereas for an ordered alloy the structure factor of such reflections is proportional to the difference of atomic scattering factors, i.e., $F(200) \propto S^2(f_{\text{Ge}} - f_{\text{Si}})^2$, where f_{Ge} and f_{Si} are the Ge and Si atomic scattering factors and S is the Bragg-Williams order parameter, discussed in the following paragraphs. Such superstructure reflection was found for all samples studied here. Reciprocal space maps in the vicinity of the Si(400) and (200) reflections are shown in Fig. 4 for selected samples.

The (400) maps of Figs. 4(a) and 4(c) corresponding to the LPE and MBE-b samples, respectively, exhibit diffraction intensity up to $H \sim 3.92$, showing that the alloy material inside both islands relax to approximately the lattice parameter of a $\text{Si}_{0.5}\text{Ge}_{0.5}$ alloy. Such composition matches the nominal SiGe content of the LPE grown alloy and is in agreement with the maximum Ge concentration of the MBE-b domes obtained in Fig. 1(b). The diffracted intensity at the (400) map obtained for the CVD sample—shown in Fig. 4(b)—spans up to $H \sim 3.87$, indicating that the CVD islands have a higher Ge content if compared to the LPE and MBE-b samples. The intensity data in all (400) reflection maps was normalized to unity at the island peak position of each sample.

On the (200) maps of Figs. 4(d)–4(f) one observes a double-peak feature along the K (transversal) direction. As

reported in previous works intensity from ordered alloys in SiGe islands exhibit a particular reciprocal space imprint with a two-peak structure along the transversal (K) direction, generated by the existence of antiphase boundaries.¹⁶ It is worth to compare the extent of the (200) intensity maps along the H direction relative to the extent of the (400) maps. For the LPE sample the (200) intensity [Fig. 4(d)] spans to a minimum H value of 1.975 while the (400) map [Fig. 4(a)] exhibits considerable diffracted intensity up to $H \sim 3.905$ (or 2×1.952). It is expected, therefore, that ordered alloys can be found only in regions of the islands where the local lattice parameter correspond to strained conditions. For the CVD sample, the reciprocal space extent of the (200) map reaches $H \sim 1.95$, still limited with respect to the extent of the (400) intensity, that reaches $H \sim 3.87$ (or 2×1.935). Finally, for the MBE-b sample the (200) intensity spans until $H \sim 1.96$ a value comparable to the extent of the (400) reflection $H \sim 3.91$ (2×1.955).

The quantification of the degree of order in the alloys of the samples studied here can be drawn by evaluating the intensity ratio between the (200) superstructure reflection and the (400) fundamental reflection. This ratio is shown in the different color scales of Figs. 4(d)–4(f), where the intensity normalization for each map was performed with respect to the maximum of diffraction intensity in the island position of (400) maps. Since Si, Ge, and SiGe alloy crystals have the diamond unit cell the Bragg-Williams order parameter S can be obtained from the ratio of intensities³² as

$$\frac{I_{(200)}}{I_{(400)}} = \frac{S^2(f_{\text{Ge}} - f_{\text{Si}})^2}{4(\langle f_{\text{GeSi}} \rangle)^2}, \quad (1)$$

where f_{Ge} and f_{Si} are the Ge and Si atomic scattering factors, respectively, and $\langle f_{\text{GeSi}} \rangle = C_{\text{Ge}}f_{\text{Ge}} + C_{\text{Si}}f_{\text{Si}}$ is the local effective

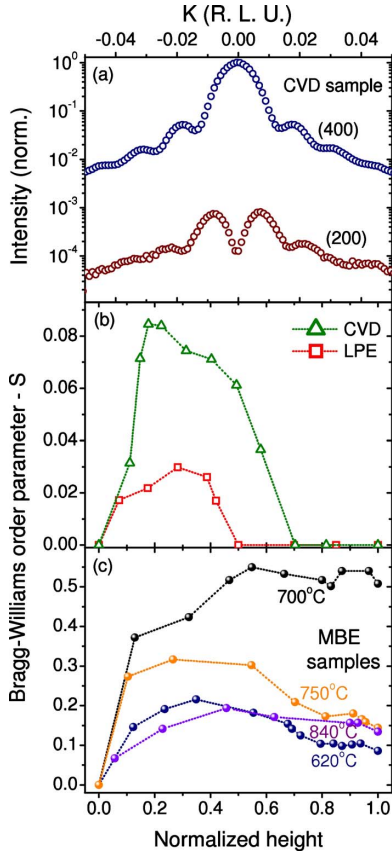
MALACHIAS *et al.*PHYSICAL REVIEW B **82**, 035307 (2010)

FIG. 5. (Color online) (a) Transversal scans at $H=3.95$ and $H=1.975$ for the (400) and (200) reciprocal space maps, respectively, measured for the CVD sample. (b) Bragg-Williams order parameter S as a function of the normalized height for LPE and CVD islands. (c) Values of S for all MBE samples measured in this work.

atomic scattering factor for a SiGe alloy. Typical S values range from zero to unity as the superstructure reflection is measured from a fully disordered alloy ($S=0$) until a completely ordered crystal ($S=1$).^{16,32}

All reciprocal space maps of Fig. 4 are composed of transversal scans. Transversal scans for the CVD islands obtained from Fig. 4(b) at $H=3.95$ and from Fig. 4(e) at $H=1.975$ are depicted in Fig. 5(a). For each transversal scan in a (400) map an equivalent transversal scan was performed to build the (200) map, allowing to integrate the diffracted intensity at each reciprocal space position along the map and evaluate the local order parameter on each sample. Finally, in order to express S as a function of the island height the procedure adopted is an extension of the procedure employed to build the maps of Fig. 1(e). Each transversal cut from the (400) map represents a local strain status inside the island that can be directly related to a region in real space by the lateral dimension extracted from the width of the transversal scan. Such width is then compared to a real space AFM profile and the height above the substrate for an isolat-

tice parameter region obtained. We assume, therefore, that a region with a given lattice parameter in the (200) map is located at the same height from the substrate in the island as a region assigned to the equivalent strain status in the (400) map. This assumption is valid since a monotonic vertical lattice parameter relaxation takes place in all islands and such vertical gradient is much more pronounced than possible lateral strain gradients inside these nanostructures.²² The lateral position of the ordered domains inside Ge:Si islands could not be addressed by our model.¹⁶ For this reason we follow our analysis exploring the vertical dependence of S .

Applying Eq. (1) for the integrated area of transversal scans at (400) and (200) maps one can obtain S and express it as a function of the island height. Since islands analyzed in this work have different heights a quick visualization procedure of the order degree in each case can be performed by plotting S as a function of the normalized island height, assumed to be unity at the apex of each island. Figures 5(b) and 5(c) show these results for the LPE, CVD, and all MBE islands. As shown in Fig. 4, (200) maps for all samples exhibit a very low intensity at the vicinity of the Si reciprocal space position, in contrast to a strong substrate peak at the (400) reflection. Since this condition is also related to Si-rich regions at the islands basis, the evaluation of S at such reciprocal space positions lead to very small values. For this reason graphs of Figs. 5(b) and 5(c) show $S=0$ for all island basis. Such values are reasonable for MBE samples where the Si diffusion is more severe at the islands bottom but certainly deviate from the expected in the LPE and CVD cases. S values obtained for corresponding positions in the (400) map where the island diffraction signal is predominant ($H < 3.99$) are accurate.

A first look to the S profile obtained for the LPE sample shows that a very reduced order is found in these alloyed islands. By evaluating the size of ordered regions by the procedure of Ref. 16 one finds an average domain size of 45 Å. Since the diffracted intensity from a superstructure reflection is proportional to the volume of ordered material, independently from the number of existing ordered domains³² such result indicates that a very small amount of material relative to the total islands volume is ordered from the LPE growth. In this system, in which the alloying process is much closer to expected thermodynamic behavior, the enthalpy of mixing for an ordered alloy is extremely high³³ and mixing entropy is maximized, leading to an almost fully random SiGe alloy. The ordered regions are mainly present at the island bottom part where the local strain has a maximum value. As shown in the S map of Fig. 6(a) the observed ordering is roughly limited to one-third of the island height.

CVD domes exhibit larger S values if compared to the LPE $\text{Si}_{0.5}\text{Ge}_{0.5}$ truncated pyramid islands. This result is rather unexpected for islands that have grown from the deposition of a pure Ge precursor (GeH_4). It is clear, therefore, that the incorporation of Si atoms by bulk and/or surface kinetic diffusion is responsible for generating the necessary stoichiometric conditions for alloying and ordering. As pointed out in Ref. 24 the incoming Ge atoms play a crucial role to the final concentration profile observed in CVD islands by producing a Ge-rich outer cap at the island, indicating that sur-

ATOMIC ORDERING DEPENDENCE ON GROWTH METHOD...

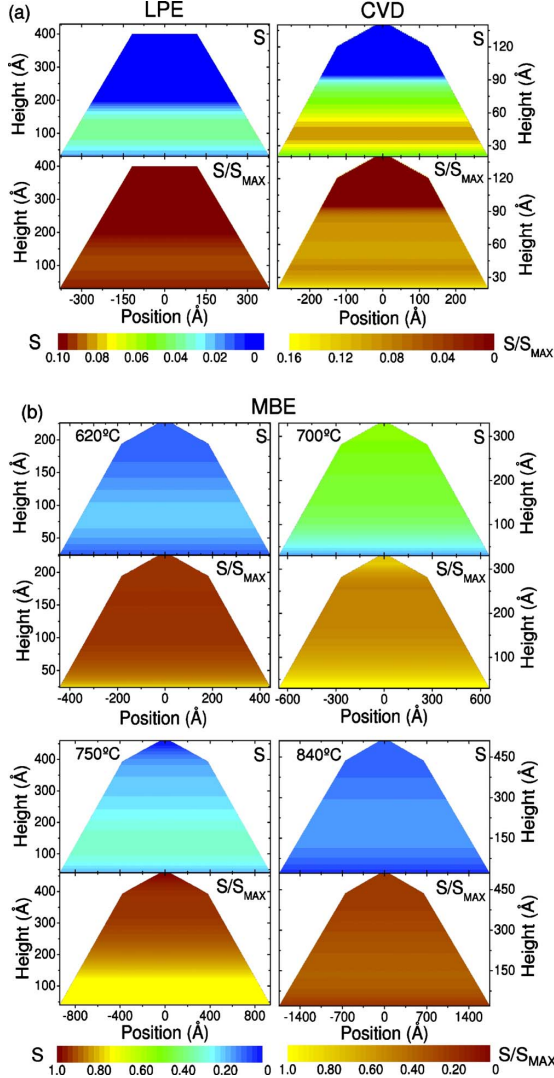
PHYSICAL REVIEW B **82**, 035307 (2010)

FIG. 6. (Color online) (a) Representation of Bragg-Williams order parameter S and the S/S_{MAX} ratio (see text) for LPE and CVD islands. The color scale for these maps is the same for both samples. (b) Maps of S and S/S_{MAX} for all MBE islands. The color scales for these four samples are shown in the bottom of the figure.

face kinetic diffusion—that would be responsible for alloying at the island facets—is reduced with respect to MBE samples [as also discussed for the results of Fig. 3(d)]. CVD islands behave, therefore, as systems in a condition much closer to thermodynamic equilibrium,⁸ due to partial hydrogen passivation of the surface, but with a non-negligible influence from surface kinetic phenomena. The proximity to thermal equilibrium leads to a pyramid-to-dome transition in which anomalous coarsening is much less effective than in MBE growth. Such transitions are related to the appearance of large island facets that differ from the expected equilibrium $\langle 111 \rangle$ or $\langle 100 \rangle$ Wulff construction symmetry, allowing

for surface reconstructions at the $\langle 113 \rangle$ and $\langle 15\ 3\ 23 \rangle$ facets that may be crucial for an increase in surface atomic mobility at multifaceted dome islands. These facets are steeper than those of shallow $\langle 105 \rangle$ faceted pyramids also obtained by MBE and/or CVD and will be hereafter referred as “steeper facets.” The resulting composition profile exhibits a vertically limited Si interdiffusion at the island center as a result from the combination of the slow Si bulk diffusion process and the continuous Ge atom flux. However, the incorporation of Si atoms is much stronger laterally—although a thin Ge-rich cap is still present—indicating that some small degree of surface Si-Ge diffusion takes place at the domes steeper facets. If Ge deposition is interrupted the steeper facets become more Si rich while the composition evolution at the island center is slower. This indicates the existence of a surface kinetic alloying mechanism for this growth method.²⁷ From the CVD S profile of Fig. 5(b), represented in the CVD S map of Fig. 6(a) one observes that ordered alloying is limited to the regions of the islands with steeper facets. This is also in agreement with the vertical extent of the Ge-pure region at the island top of Fig. 2(f). The average ordered domain size was found to be of 75 Å for CVD islands.

Finally, all MBE islands measured here exhibit S values much larger than for samples grown by other methods. From Fig. 5(c) one observes that S reaches considerably high values, having a maximum around 40% of the island height, and lower S values closer to the island top (except for sample MBE-b). Islands grown at 700 °C have shown an exceptionally high value of S , which results from matching the center of the temperature window in which order is more favorable with the conditions that provide a 50% Ge content into the islands. The nonvanishing S behavior for this growth temperature can be explained by the reciprocal space broadening of both (200) and (400) profiles along H due to finite size of isolattice parameter regions and ordered domains. Most notably for the MBE-b sample, for H values of transversal scans that correspond to the island apex at the (400) reflection, there is always diffracted intensity above the background at the equivalent transversal scan at the (200) map. For temperatures higher than 700 °C entropy of mixing increases, leading to lower values of S as shown in Fig. 5(c). Although islands may not be completely ordered from bottom to apex the values shown in Fig. 5(d) are more accurate at the middle height of these structures.

The difference in almost 1 order of magnitude for S values in the MBE islands with respect to LPE alloy islands is in clear contrast with the optimum composition for ordering since MBE islands exhibit stronger composition gradients. Such condition implies the existence of regions in which the stoichiometry deviates from 50/50. One can assume, therefore, that the mixing entropy is maximized in the LPE alloy system, as a tendency from thermodynamic equilibrium behavior, while another mechanism is responsible for the larger ordering in the MBE islands.

An alternative way to compare SiGe ordering in all islands can be established by evaluating the ratio S/S_{MAX} , where S_{MAX} is the maximum value of S that can be reached for a given local Ge/Si composition. S_{MAX} can be defined as $S_{\text{MAX}} = 1 - |C_{\text{Ge}} - C_{\text{Si}}|$, where C_{Ge} and C_{Si} are the local Ge and Si concentrations. This definition is in agreement with the

MALACHIAS *et al.*PHYSICAL REVIEW B **82**, 035307 (2010)

definition of S ,³² and leads to $S_{\max}=1$ for $C_{\text{Ge}}=C_{\text{Si}}=0.5$ and $S_{\max}=0$ for a pure material. Therefore, using the S/S_{\max} ratio it is possible to evaluate in which regions of the islands atomic order is more effective. Similar to the behavior of S , S/S_{\max} tends to be inaccurate at the island basis, where small finite S values are found in very Si-rich regions. For island regions where C_{Ge} is larger than 0.1 the S/S_{\max} ratio is more accurate and also indicates that order is more effective at the region of the islands where steeper facets are found.

IV. CONCLUSION

As discussed before, surface kinetic diffusion is strongly related to the larger incorporation of Si atoms in MBE growth in comparison with CVD and LPE. In this case, the surface reconstruction that takes place at the island facets is probably responsible for alloying Si and Ge atoms during the deposition process. The larger mobility obtained by UHV-MBE growth can, therefore, generate conditions that favor Si and Ge adatom bonding at the steeper island facets. Ordering would be, then, a result of alloying at the $\langle 113 \rangle$ and $\langle 15\ 3\ 23 \rangle$ dome facets. An indication of this facet mediated mechanism is observed by the presence of maximum S on the equivalent island height for these facets observed for the MBE and CVD samples in Figs. 6(a) and 6(b).

In conclusion, Ge:Si atomic ordering was evidenced in dome-faceted islands, with a remarkably strong signal from MBE-grown samples. Although the precise mechanism of ordering remains unclear we have shown that surface diffusion plays a key role in this phenomenon by comparing different growth methods. The poor degree of ordering mea-

sured for an alloyed LPE sample suggests that surface reconstruction at the domes steeper facets is the key for atomic ordering. We hence suggest that *in situ* scanning tunneling microscopy experiments at islands steeper facets (on the edge of a substrate) can shed some more light into the kinetic mixing that takes place in these regions. Although such kind of experiment cannot distinguish among Si and Ge atoms, it can surely provide the configuration of the surface atoms at the facets. The exact knowledge of such surface reconstruction and its energetic balance in dome islands will certainly improve the understanding of both kinetic diffusion and atomic ordering mechanisms in this system. CVD and MBE $\langle 105 \rangle$ faceted pyramids were also measured for this work and have shown no sign of ordering, corroborating the influence of dome facets on GeSi order. By assuming that steeper facets are responsible for atomic ordering one can explain the fourfold symmetry obtained when observing similar antiphase boundary diffraction profiles in all $\langle 100 \rangle$ orientations used to measure in-plane (200) reflections. In particular, measurements of the superstructure (200) reflection for Ge:Si islands have shown to be able to indicate and quantify relatively the existence of kinetic diffusion behavior during growth. Finally, the atomic order previously observed for the wetting layer formed on the $\langle 001 \rangle$ Si substrate surface is very reduced with respect to the order obtained in Ge domes, suggesting that different mechanisms are responsible for each of these phenomena.³⁴

ACKNOWLEDGMENTS

This work was supported by the Brazilian agencies CAPES and CNPq.

*Present address: Laboratório Nacional de Luz Síncrotron C.P. 6192–Campinas, Brazil; amalachias@lnls.br

¹G. S. Kar, S. Kiravittaya, U. Denker, B. Y. Nguyen, and O. G. Schmidt, *Appl. Phys. Lett.* **88**, 253108 (2006).

²G. Katsaros, P. Spathis, M. Stoffel, F. Fournel, M. Mongillo, V. Bouchiat, F. Lefloch, A. Rastelli, O. G. Schmidt, and S. De Franceschi, *Nat. Nanotechnol.* **5**, 458 (2010).

³M. Nomura, N. Kumagai, S. Iwamoto, Y. Ota, and Y. Arakawa, *Nat. Phys.* **6**, 279 (2010).

⁴H. Oka, P. A. Ignatiev, S. Wedekind, G. Rodary, L. Niebergall, V. Stepanyuk, D. Sander, and J. Kirschner, *Science* **327**, 843 (2010).

⁵L. Wang, A. Rastelli, S. Kiravittaya, M. Benyoucef, and O. G. Schmidt, *Adv. Mater.* **21**, 2601 (2009).

⁶A. F. Zinovieva, A. V. Dvurechenskii, N. P. Stepina, A. S. Deryabin, A. I. Nikiforov, R. M. Rubinger, N. A. Sobolev, J. P. Leitão, and M. C. Carmo, *Phys. Rev. B* **77**, 115319 (2008).

⁷F. Lipps, F. Pezzoli, M. Stoffel, C. Deneke, J. Thomas, A. Rastelli, V. Kataev, O. G. Schmidt, and B. Büchner, *Phys. Rev. B* **81**, 125312 (2010).

⁸G. Medeiros-Ribeiro, A. M. Bratkovski, T. I. Kamins, D. A. A. Ohlberg, and R. S. Williams, *Science* **279**, 353 (1998).

⁹F. M. Ross, J. Tersoff, and R. M. Tromp, *Phys. Rev. Lett.* **80**, 984 (1998).

¹⁰A. Rastelli, M. Stoffel, J. Tersoff, G. S. Kar, and O. G. Schmidt, *Phys. Rev. Lett.* **95**, 026103 (2005).

¹¹R. E. Rudd, G. A. Briggs, A. P. Sutton, G. Medeiros-Ribeiro, and R. S. Williams, *Phys. Rev. Lett.* **90**, 146101 (2003).

¹²F. Montalenti, P. Raiteri, D. B. Migas, H. von Känel, A. Rastelli, C. Manzano, G. Costantini, U. Denker, O. G. Schmidt, K. Kern, and L. Miglio, *Phys. Rev. Lett.* **93**, 216102 (2004).

¹³X. Z. Liao, J. Zou, D. J. H. Cockayne, J. Wan, Z. M. Jiang, G. Jin, and K. L. Wang, *Phys. Rev. B* **65**, 153306 (2002).

¹⁴R. Magalhães-Paniago, G. Medeiros-Ribeiro, A. Malachias, S. Kycia, T. I. Kamins, and R. Stan Williams, *Phys. Rev. B* **66**, 245312 (2002).

¹⁵A. Rastelli, M. Stoffel, A. Malachias, T. Merdzhanova, G. Katsaros, K. Kern, T. H. Metzger, and O. G. Schmidt, *Nano Lett.* **8**, 1404 (2008).

¹⁶A. Malachias, T. Ü. Schüllli, G. Medeiros-Ribeiro, L. G. Cançado, M. Stoffel, O. G. Schmidt, T. H. Metzger, and R. Magalhães-Paniago, *Phys. Rev. B* **72**, 165315 (2005).

¹⁷J. Z. Tischler, J. D. Budai, D. E. Jesson, G. Eres, P. Zsack, J. M. Baribeau, and D. C. Houghton, *Phys. Rev. B* **51**, 10947 (1995).

¹⁸Here the term interdiffusion refers to any general mixing mechanism. In the manuscript text the terms “surface diffusion” and “bulk diffusion” were used to refer specifically to these mechanisms, when they apply.

ATOMIC ORDERING DEPENDENCE ON GROWTH METHOD...

PHYSICAL REVIEW B **82**, 035307 (2010)

- ¹⁹The main type of island for all MBE samples studied here are dome-shaped and barn-shaped, both presenting $\langle 113 \rangle$ and $\langle 15\ 3\ 23 \rangle$ facets. In order to keep consistence with Ref. 25, in which the composition in these islands was firstly analyzed, the island type for MBE samples will be referred here as domes. A very reduced population of superdomes ($<5\%$), not statistically significant to influence the diffraction profiles, can be found in these samples.
- ²⁰Th. Wiebach, M. Schmidbauer, M. Hanke, H. Raidt, R. Köhler, and H. Wawra, *Phys. Rev. B* **61**, 5571 (2000).
- ²¹M. Hanke, M. Schmidbauer, D. Grigoriev, H. Raidt, P. Schäfer, R. Köhler, A.-K. Gerlitzke, and H. Wawra, *Phys. Rev. B* **69**, 075317 (2004).
- ²²I. Kegel, T. H. Metzger, A. Lorke, J. Peisl, J. Stangl, G. Bauer, K. Nordlund, W. V. Schoenfeld, and P. M. Petroff, *Phys. Rev. B* **63**, 035318 (2001).
- ²³T. U. Schüllli, J. Stangl, Z. Zhong, R. T. Lechner, M. Sztucki, T. H. Metzger, and G. Bauer, *Phys. Rev. Lett.* **90**, 066105 (2003).
- ²⁴A. Malachias, S. Kycia, G. Medeiros-Ribeiro, R. Magalhães-Paniago, T. I. Kamins, and R. S. Williams, *Phys. Rev. Lett.* **91**, 176101 (2003).
- ²⁵T. U. Schüllli, M. Stoffel, A. Hesse, J. Stangl, R. T. Lechner, E. Wintersberger, M. Sztucki, T. H. Metzger, O. G. Schmidt, and G. Bauer, *Phys. Rev. B* **71**, 035326 (2005).
- ²⁶G. Medeiros-Ribeiro, A. Malachias, S. Kycia, R. Magalhães-Paniago, T. I. Kamins, and R. Stanley Williams, *Appl. Phys. A: Mater. Sci. Process.* **80**, 1211 (2005).
- ²⁷M. S. Leite, A. Malachias, S. W. Kycia, T. I. Kamins, R. S. Williams, and G. Medeiros-Ribeiro, *Phys. Rev. Lett.* **100**, 226101 (2008).
- ²⁸M. S. Leite, G. Medeiros-Ribeiro, T. I. Kamins, and R. S. Williams, *Phys. Rev. Lett.* **98**, 165901 (2007).
- ²⁹M. Meduna, J. Novak, G. Bauer, V. Holy, C. V. Falub, S. Tsujino, and D. Grutzmacher, *Semicond. Sci. Technol.* **22**, 447 (2007).
- ³⁰J. B. Hannon, M. Copel, R. Stumpf, M. C. Reuter, and R. Tromp, *Phys. Rev. Lett.* **92**, 216104 (2004).
- ³¹D. E. Jesson, S. J. Pennycook, and J.-M. Baribeau, *Phys. Rev. Lett.* **66**, 750 (1991).
- ³²B. E. Warren, *X-Ray Diffraction* (Dover, New York, 1969).
- ³³J. E. Bernard and A. Zunger, *Phys. Rev. B* **44**, 1663 (1991).
- ³⁴A. Malachias, T. H. Metzger, M. Stoffel, O. G. Schmidt, and V. Holy, *Thin Solid Films* **515**, 5587 (2007).

Chapter 5

Solid-liquid-gas interaction during growth

While the investigation of MBE grown SiGe islands occupies the vast part of this work, x-ray *in situ* tools find intriguing applications not solely under UHV conditions. Whereas electron scattering and electron microscopy methods are working well under UHV, the presence of gas atmospheres as tolerated by x-rays maybe an obstacle for electron based probing. thus a particular interest of *in situ* probing of growth with x-rays may lie in the investigation *e.g.* CVD growth or processes in gas reactors in general. CVD growth represents one of the major industrial deposition processes in Si and SiGe technology and even for the growth of nanostructures it has gained new importance with the numerous studies of the potential of semiconductor nanowires. In this chapter, the investigation of nanowires with x-rays is introduced. As nanowires are mainly grown with metallic catalysts, a study of the liquid catalyst in interaction with the Si(111) surface is presented in section refsupercool. As a further example on gas-nanostructures interaction, outside semiconductor growth, the catalytic behaviour of metallic nanoparticles as exposed to O₂ and CO gases is investigated in section 5.3.1.

5.1 Complex faceting and strain in nanowires

5.1.1 *Structural investigation of silicon nanowires using GIXD and GISAXS: Evidence of complex saw-tooth faceting*

T. David, D. Buttard, T. U. Schüllli, F. Dallhuin, P. Gentile
Surf. Sci. 602, 2675 (2008).

Semiconductor nanowires, although known since many decades, have attracted enormous interest over the last years due to the theoretical potential of 1D semiconductors on the one hand, and the flexibility of combining different semiconductors in these structures on the other hand. The growth process makes use of liquid metal-semiconductor droplets, exposed to a gas source component carrying the semiconductor. It is generally referred to as the Vapour-Liquid-Solid (VLS) growth. For Si nanowires the most prominent procedure consists in a catalytic process

making use of the low temperature Gold-Silicon eutectic. Gold nanoparticles transform into liquid AuSi droplets, once exposed to Silane (SiH_4) in a CVD process at temperatures above the eutectic point $T_E=363^\circ$. Upon saturation, these droplets initiate the growth of a Si pillar. Samples grown by this CVD process have been transferred to the UHV chamber on BM32 and investigated to analyze the exact facet orientation on their sidewalls as well as the lattice parameter inside the wires.



Structural investigation of silicon nanowires using GIXD and GISAXS: Evidence of complex saw-tooth faceting

Thomas David *, Denis Buttard, Tobias Schüllli, Florian Dallhuin, Pascal Gentile

CEA/GRENOBLE-INAC/SP2M/SiNaPS, 17 rue des Martyrs, 38054 Grenoble Cedex 9, France

ARTICLE INFO

Article history:

Received 21 March 2008
Accepted for publication 24 June 2008
Available online 2 July 2008

Keywords:

X-ray scattering
Diffraction
GIXD
GISAXS
Epitaxy
Silicon
Nanowire
Facet

ABSTRACT

We present the results of X-ray experiments on silicon nanowires grown on $\langle 111 \rangle$ -oriented silicon substrate using the vapor liquid solid method. Grazing incidence X-ray diffraction shows that nanowires are in epitaxy on the substrate and have a hexagonal cross-section. The orientations of the sides are then determined. Grazing incidence small-angle X-ray scattering experiments reveal fine saw-tooth faceting of the sides of the nanowires. This fine saw-tooth faceting appears with alternating upward and downward orientations on each side of the nanowires, reflecting the trigonal symmetry of the nanowires. The crystallographic orientation of some of these facets is then determined. Finally, it is observed that large-diameter nanowires (diameter larger than 200 nm) exhibit six additional faces that truncate the edge of the usual hexagonal cross-section of the nanowires. These additional faces also show saw-tooth faceting which is tilted with respect to the horizontal and seems to be present only around the top of the nanowires.

© 2008 Elsevier B.V. All rights reserved.

1. Introduction

In many fields of physics today, there is a growing need for smaller and smaller structures. Microelectronics immediately comes to mind, but biology, optics and even mechanics have a similar need. This need has drawn the attention of many research people to nanostructures. Among these interesting structures, nanowires, grown by the vapor liquid solid (VLS) method [1], have attracted particular attention, one of the reasons being their many potential applications. Concerning the choice of material, silicon is extremely well-known and thus seems to be a good candidate. The first obvious use of such nanostructures would be in microelectronics, but nanowires could also be extremely useful in the field of sensors for instance. In order to use these basic structures, however, we need to understand their structural properties. A few studies have already shown interest in the structural and morphological properties of silicon nanowires grown by VLS [2–5], with the very small diameters (5–20 nm) attracting most attention. It seems that nanowires generally grow in epitaxy on the silicon substrate if the interface between the catalyst and the silicon is clean at the beginning of growth. In addition, ‘Big’

nanowires (with a diameter greater than 50 nm) appear to have six sides, one out of two presenting saw-tooth faceting [5], with the preferred growth direction being the $\langle 111 \rangle$ direction of the silicon crystal. In the case of smaller diameters, however, six faces also appear but the axis and the faces of the nanowire exhibit different directions [4,6]. In order to investigate the crystalline nature and faceting of an assembly of small objects, X-rays are a very suitable tool. With regard to shape in particular, grazing incidence small-angle X-ray scattering (GISAXS) has already proved its efficiency in the study of silicon nanocrystals [7]. We performed grazing incidence X-ray diffraction (GIXD) and GISAXS experiments on ‘big’ silicon nanowires (diameters from 50 to 500 nm) grown by VLS on $\langle 111 \rangle$ -oriented silicon substrate with a gold catalyst. Crystal orientation and structural properties of the nanowires were deduced from GIXD while GISAXS provided information about the shape of the nanowires, their faceting and the orientation of their facets.

2. Experimental details

2.1. Nanowire growth

Nanowires were grown on a $\langle 111 \rangle$ oriented silicon substrate. The catalysts used in the VLS reaction were gold droplets dewetted from a thin evaporated film (~ 2 nm thick). The growth took place

* Corresponding author. Tel.: +33 4 38 78 31 12; fax: +33 4 38 78 58 17.
E-mail address: thomas.david@cea.fr (T. David).

in a chemical vapor deposition (CVD) reactor, at 20 mbar and around 600 °C. The gaseous precursor was silane whereas the carrier gas was hydrogen. For additional details about controlled VLS growth of silicon nanowires see [8]. After growth, scanning electron microscopy (SEM) images of the resulting nanowires were produced (Fig. 1) and showed $\langle 111 \rangle$ oriented nanowires perpendicular to the surface of the substrate. Their diameters were not controlled because the diameters of the droplets obtained from the dewetting of a gold film are variable. However, we obtained a distribution of diameters around a given value fixed by the growth parameters (see [2,3] for details about the dependence of diameters on growth conditions). Their length was about 3.5 μm , determined by the duration of growth and was fairly independent of the diameter for a given set of parameters (except for small diameters as shown in [9]). Some kinks may appear but they can be reduced by changing growth parameters (temperature, silane partial pressure. . .) [3].

2.2. GIXD and GISAXS setup

GIXD and GISAXS experiments were performed at the European synchrotron radiation facility (ESRF) in the SUV instrument of the BM32 beamline under ultra high vacuum (UHV) conditions. The experimental configuration is shown in Fig. 2. The X-ray wavelength was $\lambda = 0.1062 \text{ nm}$ and the pressure was around 10^{-10} mbar. Grazing incidence was used in order to obtain as much signal as possible coming from the nanowires and not from the substrate (α_i typically around the critical angle for total reflection $\alpha_c = 0.15^\circ$ for the selected wavelength). In GIXD, the emergent angle α_e with respect to the sample surface remains small and comparable to α_i while the scattering angle 2δ in the plane of the sample surface can be large. In GISAXS, both emergent and scattering angles are small, and images of the scattered intensity are recorded just around the direct beam and specular reflection. For GIXD, a position sensitive detector (PSD) was used while for GISAXS a 1152×1242 pixels low-noise 16-bit CCD detector from Princeton was used.

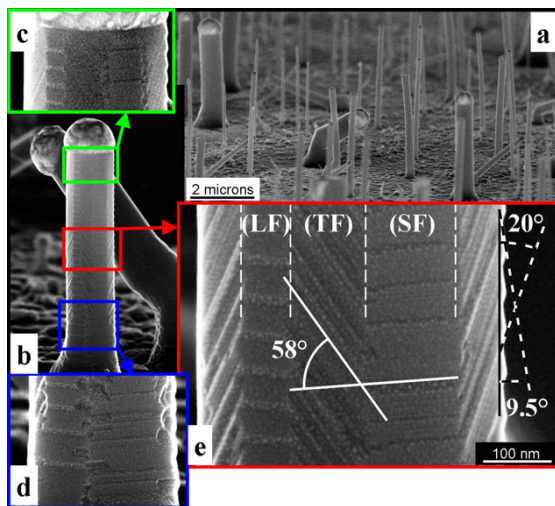


Fig. 1. SEM images of nanowires. (a) overall view, (b) single nanowire, (c), (d) and (e) detailed views from (b). Every face seems to be saw-tooth faceted with different types of facets oriented upwards. (SF) type faces have small upward-facing facets while (LF) type faces have large upward-facing facets. The edges of the hexagonal prism are truncated and the cross-section would thus be dodecagonal. These new faces are themselves finely faceted with tilted facets (TF), and appear wide at the top of the nanowire (c) and almost non-existent at the bottom (d).

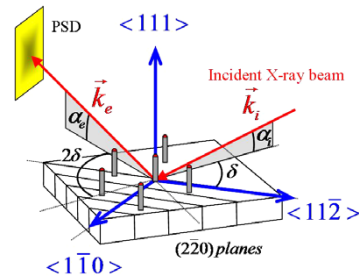


Fig. 2. Setup used for GIXD experiments. \vec{k}_i and \vec{k}_e are, respectively the incident and emergent wave vector. The scattering vector is $\vec{q} = \vec{k}_e - \vec{k}_i$ with $q = \frac{4\pi}{\lambda} \sin(\theta)$.

3. Results

3.1. GIXD: Shape and epitaxial orientation of the nanowires

Fig. 3a shows a profile of the diffracted intensity around the $(2\bar{2}0)$ reflection. We observe two diffraction peaks, the narrower (S) coming from the substrate and the broader (NW) from the wires, indicating that nanowires are single crystals and that their in-plane orientation is the same as the one of the substrate. Using Bragg's law $2d \sin \theta = \lambda$ for the selected wavelength $\lambda = 0.10619 \text{ nm}$ we can estimate the lattice parameter a_{si} and a_{nw} , respectively, of the substrate and the nanowires. We then deduce the lattice mismatch parameter $\delta a/a = (a_{nw} - a_{si})/a_{si} = -1.23 \times 10^{-3}$ corresponding to a compression. Analysis of this strain is in progress but it can be tentatively explained by surface effects in the nanowires coming from a thin oxide shell.

Fig. 3b shows a reciprocal space map of the diffracted intensity around the $(2\bar{2}0)$ peak of silicon. On this map, we see six diffraction streaks indicated by the dotted lines. These streaks are produced by vertical "planes". Consequently, they provide evidence of the hexagonal cross-section of the wires. The angle between two streaks is 60° and the directions of the six sides of the nanowires can be deduced from the directions of these streaks on the map. Thus, the directions of the six sides of the nanowires are $[\bar{1}\bar{1}2]$, $[\bar{1}2\bar{1}]$, $[2\bar{1}\bar{1}]$, $[11\bar{2}]$, $[1\bar{2}1]$ and $[\bar{2}11]$. Similarly, the directions of the edges between two faces are $[1\bar{1}0]$ and the five other equivalent directions. These results are consistent with previous electronic microscopy observations [10]. As this map shows the scattered intensity coming from the entire population of nanowires illuminated by the beam, we can be sure that these nanowires are all in epitaxy with the substrate and have the same in-plane orientation. Otherwise the map would show an arc following a Debye-Scherrer ring.

The same experiment was performed on another sample obtained after a shorter period of growth, resulting in nanowires at the very beginning of their growth. The corresponding map (not shown) has a round shape without streaks, showing that the hexagonal faces have not yet been formed.

3.2. GISAXS: fine saw-tooth faceting

Fig. 4a shows a GISAXS image obtained with the incident beam along the $[1\bar{1}0]$ direction (i.e., incoming on the nanowires through an edge), while Fig. 4b shows the same image obtained with the incident beam along the $[\bar{1}\bar{1}2]$ direction. The coordinates on the image correspond to the in-plane (q_x) and the out-of-plane (q_z) scattering vector. As there is no periodic vertical rod, no lateral periodicity of the wires is observed. However we can observe several tilted rods on the left and right of the image. As the rods are tilted, the facets do not correspond to the principal faces of the

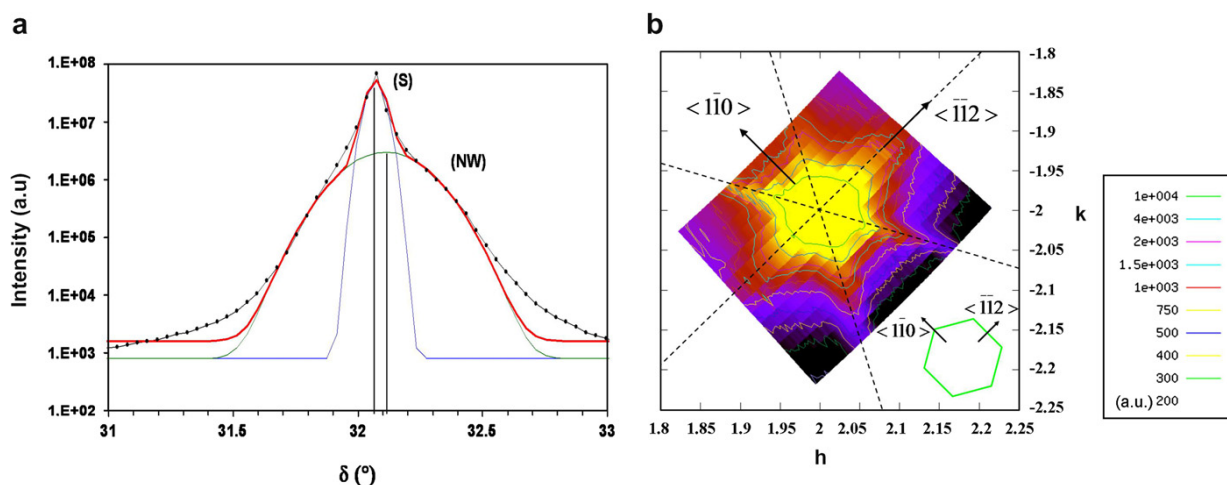


Fig. 3. (a) Experimental profile of diffraction (dotted line) close to the $(2\bar{2}0)$ peak of silicon with peak (S) from the substrate and peak (NW) from the nanowires. The solid lines correspond to fits for the center of the peaks in order to accurately determine the maximum peak position, (b) Reciprocal space map of scattered intensity (arbitrary units) around the $(2\bar{2}0)$ peak of silicon. h and k are the reciprocal space coordinates. There are six diffraction streaks spread regularly every 60° around the peak, providing evidence of the hexagonal cross-section of the nanowires and thus allowing determination of faces direction.

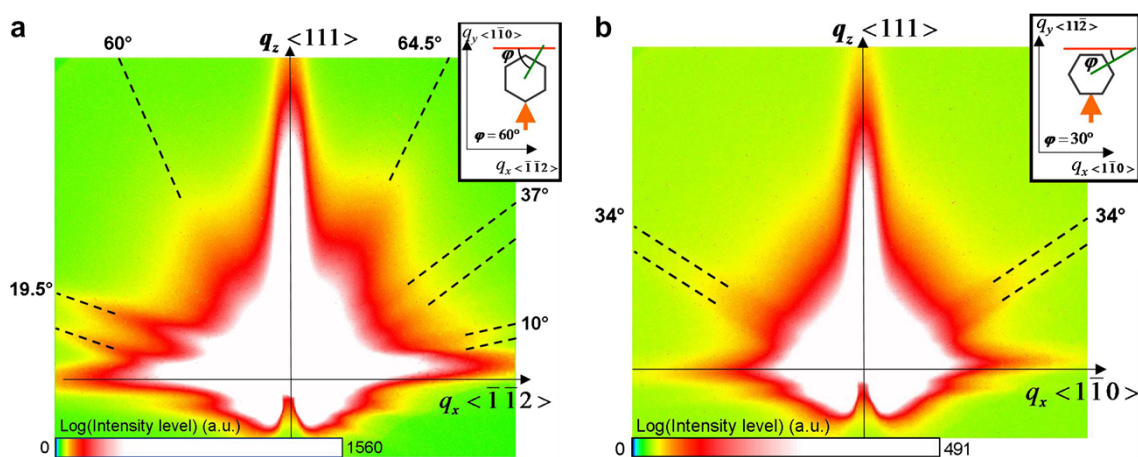


Fig. 4. GISAXS image obtained along (a) the $[1\bar{1}0]$ direction and (b) the $[\bar{1}\bar{1}2]$ direction. We see diffraction streaks tilted in relation to the vertical q_z direction, produced by different facet families. The angles indicated correspond to the measured angles $(90^\circ - \alpha_M) - \alpha_M$ and φ are defined in Fig. 5. In image (a) asymmetry between the left and right is noticeable, while image (b) is symmetrical. Intensity is given in a logarithmic scale. Inserts: schematic top view of a nanowire cross-section.

hexagonal cross-section of the wires shown earlier. These rods are produced by supplementary facets on the principal faces. This is consistent with the saw-tooth faceting observed earlier [5,10]. By measuring the tilt angle we can estimate the orientation of the facets.

Finally, on all GISAXS measurements, and especially in Fig. 4a, a splitting of the scattered streak may be observed. This phenomenon is due to multiple scattering effects and has already been investigated [11–15].

The diffuse streaks produced by facets are schematically represented in Fig. 5. The incident X-ray beam is scattered by facets and the scattering vector \vec{q} normal to these facets is located by angles α_R and φ . The axis x and z correspond to the plane of the CCD camera (respectively the horizontal and the wires axes), while y is the X-ray beam direction. In the plane of the camera, the projection of the vector \vec{q} has a measured angle α_M from the vertical. Depending on the facet orientation in relation to the CCD plane φ can take several values. If the facet is normal to the CCD plane $\varphi = 0^\circ$, so \vec{q}_{xy}

and \vec{q} are in the CCD plane and no correction is needed ($\alpha_R = \alpha_M$). But if $\varphi \neq 0^\circ$, \vec{q}_{xy} and \vec{q} are out of the CCD plane and a correction is needed as $\tan(\alpha_R) = \tan(\alpha_M) / \cos(\varphi)$. It is important to note that the visibility of streaks on the GISAXS image decreases quickly when φ increases. Facet indexation with the corrected angle is analysed in Section 4.

4. Analysis and discussion

4.1. Complex saw-tooth faceting

The asymmetry in Fig. 4a reflects the trigonal character of the nanowires. This is not in contradiction with the Friedel rule of centrosymmetry nor with the six symmetrical diffuse scattering streaks around the $(2\bar{2}0)$ reflection of silicon obtained in Fig. 3b. Indeed, in GISAXS the full inversion symmetry rule is eliminated [16,17]. This apparent trigonal character corroborate the observa-

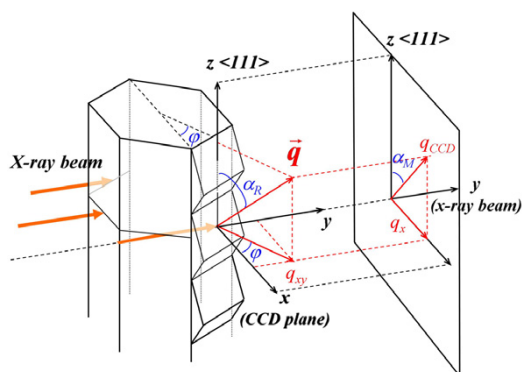


Fig. 5. Schematic representation of the faceted wire and the CCD camera plane. \vec{q} is the diffuse vector, x ; the horizontal axis in the CCD plane, y ; the X-ray beam direction, z ; the wire axis, α_R and α_M , respectively the real and measured angles between \vec{q} and the vertical and φ the angle between the normal of the facet and the CCD plane.

tions of Ross et al. in [5] which show that only one out of two sides are saw-tooth faceted. However, as shown in Fig. 1b–e, our SEM observations are not very consistent with the simple faceting model usually proposed. Indeed, we observe saw-tooth faceting on each side of the nanowire. For large-diameter wires (i.e. diameter larger than 200 nm) the hexagonal cross-section is replaced by a dodecagonal section. It seems that the six additional faces are wider at the top (Fig. 1c), while almost non-existent at the bottom (Fig. 1d).

All these observations lead us to reconsider the nanowire facet model and to propose a new one, as shown in Fig. 6. In Fig. 6a we can observe the dodecagonal section. The twelve faces are all saw-tooth faceted and distributed in three families. The (LF) family corresponds to large upward-oriented facets as indicated in Fig. 6b and the (SF) family corresponds to small upward-oriented facets. The two opposite faces are centrosymmetric. This is the reason why the GISAXS image in Fig. 4a is asymmetric. This is perfectly

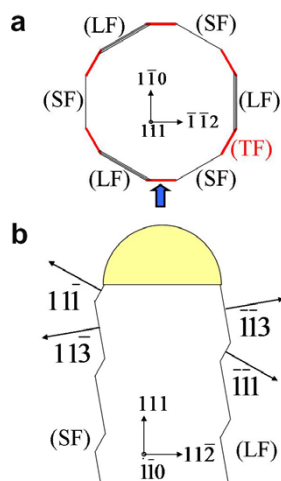


Fig. 6. Model of the nanowires. (a) The nanowire cross-section has the six usual faces, all saw-tooth faceted. Half of them (LF) present the large upward-facing facets and the other half (SF) present the small upward-facing facets. The six additional faces truncating the edges are represented in red and marked (TF). They also exhibit a saw-tooth faceting but with tilted facets. (b) shows a view in the vertical plane along the direction indicated by the blue arrow in (a). The two opposite faces are of different type, one being (LF) and the other (SF). This is the reason why the GISAXS image is asymmetric. (For interpretation of the references to colour in this figure legend, the reader is referred to the web version of this article.)

consistent with the trigonal character of the nanowires. For large diameter nanowires (diameter larger than 200 nm), six additional faces appear as a result of the truncation of the hexagonal edge, producing the (TF) family corresponding to tilted saw-tooth faceting.

The GISAXS image is consistent with this explanation, as shown in Fig. 7. On the GISAXS image in Fig. 7, the ‘large’ facets produce a streak at $10^\circ = (90^\circ - \alpha_{\text{Right}}) = (90^\circ - \alpha_R)$ on the right of the image and one at $19.5^\circ = (90^\circ - \alpha_{\text{Left}})$ on the left ($\tan(\alpha_{\text{Left}}) = \tan(\alpha_R) \times \cos(60^\circ)$). However, the streak at 19.5° should be much less intense than the one at 10° because of the in-plane angle correction explained earlier. In the same way, the ‘small’ facets would produce streaks at 19.5° (intense) and 37° (weak). Combining the two, we have one superimposed streak at 19.5° on the left of the image and two distinct streaks at 10° and 37° on the right. As the streak at 37° corresponds to a diffraction vector outside the detector plane ($\varphi \neq 0^\circ$), its intensity is very weak compared to the two other at 10° and 19.5° . This is exactly what we observe in Figs. 4a and 7 with an acceptable error of 1° . The SEM image in Fig. 1 corresponds well with this explanation since we measure an angle of about 9.5° with respect to the vertical for the large facets and 20° for the small ones. It is interesting to note that the angles determined locally by Ross et al. in [5] using SEM measure 11.2° and 23.3° values, which are close to ours. Similar results have also been reported with TEM observations [10]. In terms of direction, the facets tilted at 19.5° correspond to $(\bar{1}\bar{1}1)$ planes and those tilted at 10° correspond to $(\bar{1}\bar{1}3)$ planes.

Finally, we must explain the existence of the diffuse streaks at approximately 60° in Fig. 4a and at approximately 34° in Fig. 4b. For big wires with a diameter larger than 200 nm, tilted facets appear, as we can see in Fig. 1e, at an angle with respect to the horizontal $\omega \approx 58^\circ$. By applying corrections, we can find the approximate orientation of the diffuse streaks in Fig. 4a and b.

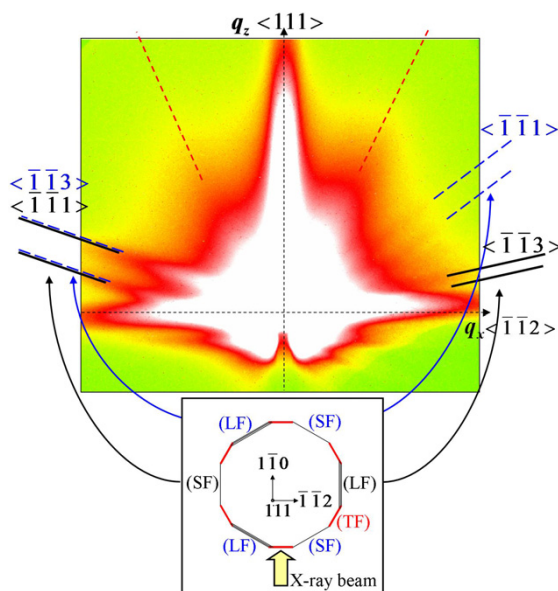


Fig. 7. Correspondence between the streaks visible on the GISAXS image and the different types of faces. The two streaks marked with black solid lines correspond to the facets whose normal is in the detector plane ($\varphi = 0^\circ$). These facets are present on two of the faces of types (LF) and (SF). The two streaks marked with large blue dashed lines correspond to the same facets but with $\varphi \neq 0^\circ$, present on the other faces of type (LF) and (SF). Finally, the two streaks marked with small red dashed lines probably correspond to the other tilted facets present on the faces of type (TF). These faces are only present on nanowires whose diameters are larger than 200 nm. The intensity is given in a logarithmic scale. (For interpretation of the references to colour in this figure legend, the reader is referred to the web version of this article.)

4.2. Other results concerning silicon faceting

Numerous theoretical articles have already been published on this topic. These have usually demonstrated that the orientation of these facets strongly depends on growth conditions and especially on temperature. Thus Bermond et al. [18] conducted experimental observations of silicon nanowhisker faceting at different temperatures. The results show facets of type $\{113\}$, $\{110\}$, $\{100\}$ and $\{111\}$ after annealing at $T > 1000$ K. The authors provide evidence that these facets depend on surface tension γ . They show that $\gamma_{110} = 0.98\gamma_{111}$, $\gamma_{113} = 0.98\gamma_{111}$ and $\gamma_{100} = 0.96\gamma_{111}$, leading to $\gamma_{111} > \gamma_{110} > \gamma_{113} > \gamma_{100}$, which is non-conventional.

On the other hand, Zhang et al. [19] carried out calculations for structures and energetics for hydrogen-terminated silicon nanowire surfaces that produced more classical results. The $\langle 112 \rangle$ silicon nanowires with only two $\{111\}$ and two $\{110\}$ surfaces appear to be more energetically favorable than the $\langle 110 \rangle$ wire surrounded by four $\{111\}$ surfaces. In the case of $\langle 111 \rangle$ nanowires, different faceting is possible, leading to different cross-sections such as triangular, truncated triangular or hexagonal. The stability of silicon nanowires is determined by competition between the minimization of surface energy of facets $\gamma_{111} < \gamma_{110} < \gamma_{100}$, in inverse proportion to the surface atomic density of these facets, and the minimization of the surface-to-volume ratio svr ($svr_{\text{hexag.}} > svr_{\text{rectangular}} > svr_{\text{triang.}}$).

Important among the theoretical studies is the article by Ruruli et al. [20] which studied the geometrical structure and electronic properties of $\langle 100 \rangle$ and $\langle 110 \rangle$ silicon nanowires in the absence of surface passivation. The authors showed that the reconstruction of the facets can lead to surface metallic states. Other studies on surface conduction and silicon nanotube faceting include Ruruli et al. [21], Kobayashi [22] or Zhao et al. [23]. An interesting study on simulated calculations was conducted by Justo et al. [24] in which, for different growth directions ($\langle 001 \rangle$, $\langle 110 \rangle$ and $\langle 112 \rangle$), various possible facet shapes, such as hexagonal or square, were calculated. In the case of growth direction $\langle 112 \rangle$ the wires comprised only $\{111\}$ and $\{110\}$ surfaces. This indicates that the surface plays a key role in nanowire energy and that the wire perimeter is a meaningful dimensional parameter.

Although some articles deal with molecular beam epitaxy (MBE) growth [25], VLS growth is usually performed in a CVD reactor. In the first study reported by Wagner and Ellis [1], the authors clearly demonstrate the growth of silicon wires on silicon $\langle 111 \rangle$ substrate using gold as a catalyst. Alternatively, $\{211\}$ and $\{110\}$ facets are observed resulting in a hexagonal wire cross-section. Although not discussed, microscopy images also exhibit non-periodic saw-tooth faceting. Pan et al. [26] obtained more “exotic” results with the growth of germanium islands on silicon nanowires. In this study, $\langle 112 \rangle$ silicon nanowires revealed $\{111\}$, $\{110\}$ and $\{113\}$ facets.

The most detailed studies on silicon nanowire faceting, however, are those by Hannon et al. [27] with sidewall morphology and Ross et al. [5] with saw-tooth faceting. They interpret this faceting term of both the role of the geometry and surface energy of the wire and the liquid droplet, and report that the period and amplitude of saw-tooth faceting are directly proportional to wire diameter. However, the origin of the facets presented in the literature is not really explained or understood, even if it is clear that the gold catalyst plays a key role.

4.3. Why these facets in our experiments?

As briefly shown above, surface faceting mechanisms have been attracting attention for years. See [28] for instance, for a general explanation of parameters determining stable facets. With regard to bulk silicon, many groups have studied different types of facet-

ing, especially in the presence of gold on the surface, and mostly using self-organised systems [29–31]. Most stable facet orientations in all these studies appear to depend on the gold covering of the silicon surface but $\langle 111 \rangle$ and $\langle 113 \rangle$ directions seem to be particularly stable, corroborating our results. Thus, each natural $\langle 112 \rangle$ side of our nanowires would show $\langle 111 \rangle$ and $\langle 113 \rangle$ facets.

Furthermore, the six additional tilted facets that truncate the edges produce another type of facet, with different orientations. Even if we cannot determine these orientations precisely, we can assume that their stability toward one of the $\langle 111 \rangle$ and $\langle 113 \rangle$ facets depends on gold coverage (just like every facet in the previously mentioned studies). Assuming these tilted facets become more stable than the others when gold coverage increases, this would explain why they are wider near the top of nanowires (where there is more gold diffusing from the gold catalyst droplet) than at the bottom (where less gold can diffuse). Obviously this still has to be investigated but, once again, as gold coverage often seems to influence the stability of the different facets, this could be a possible explanation.

5. Conclusion

Our investigations into the morphological and structural properties of epitaxial silicon nanowires grown by CVD/VLS on a $\langle 111 \rangle$ oriented silicon substrate have shown the nanowires to be epitaxial on the $\langle 111 \rangle$ -oriented substrate and to have a hexagonal cross-section with sides oriented in $\langle 112 \rangle$ directions.

We determined the direction of small saw-tooth facets ($\langle 111 \rangle$ and $\langle 113 \rangle$) and found that this saw-tooth faceting appeared on every side of the nanowires rather than on one of the two sides. However, the faceting proved to be head-to-tail on half of the sides, thus confirming the trigonal symmetry of the nanowires. As X-rays show the average signal from the nanowires over the whole sample, all these properties are visible only because of the overall homogeneity.

Finally, we observed a change in cross-section from hexagonal to dodecagonal near the top of the large nanowires. The new sides also seem to be saw-tooth faceted but with another kind of facet. The relative stability of these other facets compared with the ‘usual’ ones might be the result of a different level of surface gold coverage near the catalyst.

Acknowledgements

This work has been carried out as part of the PREEANS ANR project. We are sincerely grateful to T. Baron and P. Ferret for their fruitful discussions.

References

- [1] R.S. Wagner, W.C. Ellis, *Appl. Phys. Lett.* 4 (1964) 89.
- [2] F. Dhalluin, P.J. Desré, M.I. den Hertog, J.-L. Rouvière, P. Ferret, P. Gentile, T. Baron, *J. Appl. Phys.* 102 (2007) 094906.
- [3] J. Westwater, D.P. Gosain, S. Tomiya, S. Usui, H. Ruda, *J. Vac. Sci. Technol. B* 15 (1997) 554.
- [4] D.D.D. Ma, C.S. Lee, F.C.K. Au, S.Y. Tong, S.T. Lee, *Science* 299 (2003) 1874.
- [5] F.M. Ross, J. Tersoff, M.C. Reuter, *Phys. Rev. Lett.* 95 (2005) 146104.
- [6] Y. Wu, Y. Cui, L. Huynh, C.J. Barrelet, D.C. Bell, C.M. Lieber, *Nanoletters* 4 (2004) 433.
- [7] G. Renaud, R. Lazzari, C. Revenant, A. Barbier, M. Noblet, O. Ulrich, F. Leroy, J. Jupille, Y. Borensztein, C.R. Henry, J.-P. Deville, F. Scheurer, J. Mane-Mane, O. Fruchart, *Science* 300 (5624) (2003) 1416.
- [8] P. Gentile, T. David, F. Dhalluin, D. Buttard, N. Pauc, M. Den Hertog, P. Ferret, T. Baron, *Nanotechnology* 19 (2008) 125608.
- [9] J. Kikkawa, Y. Ohno, S. Takeda, *Appl. Phys. Lett.* 86 (2005).
- [10] M.I. Den Hertog, J.L. Rouvière, F. Dhalluin, P. Gentile, P. Ferret, C. Ternon, T. Baron, *Inst. Phys. Conf. Ser.* (in press).
- [11] M. Rauscher, R. Paniago, H. Metzger, Z. Kovats, J. Domke, J. Peisl, *J. Appl. Phys.* 86 (1999) 6763.

- [12] F. Leroy, J. Eymery, D. Buttard, G. Renaud, R. Lazzari, J. Cryst. Growth 275 (2005) e2195.
- [13] R. Lazzari, F. Leroy, G. Renaud, Phys. Rev. B 76 (2007) 125411.
- [14] R. Lazzari, G. Renaud, J. Jupille, F. Leroy, Phys. Rev. B 76 (2007) 125412.
- [15] C. Revenant, F. Leroy, G. Renaud, R. Lazzari, A. Letoublon, T. Madey, Surf. Sci. 601 (2007) 3431.
- [16] M. Rauscher, T. Salditt, H. Spohn, Phys. Rev. B 52 (1995) 16855.
- [17] P. Busch, M. Rauscher, D.-M. Smilgies, D. Posselt, C.M. Papadakis, J. Appl. Crystallogr. 39 (2006) 433.
- [18] J.M. Bermond, J.J. Métois, X. Egéa, F. Floret, Surf. Sci. 330 (1995) 48.
- [19] R.Q. Zhang, Y. Lifshitz, D.D.D. Ma, Y.L. Zhao, Th. Frauenheim, S.T. Lee, S.Y. Tong, J. Chem. Phys. 123 (2005) 144703.
- [20] R. Rurali, A. Poissier, N. Lorente, Phys. Rev. B 74 (2006) 165324.
- [21] R. Rurali, N. Lorente, Nanotechnology 16 (2005) S250.
- [22] K. Kobayashi, Phys. Rev. B 69 (2004) 115338.
- [23] M. Zhao, R.Q. Zhang, Y. Xia, C. Song, S.T. Lee, J. Phys. Chem. 111 (2007) 1234.
- [24] J.F. Justo, R.D. Menezes, L.V.C. Assali, Phys. Rev. B 75 (2007) 045303.
- [25] L. Schubert, P. Werner, N.D. Zakharov, G. Gerth, F.M. Kolb, L. Long, U. Gösele, T.Y. Tan, Appl. Phys. Lett. 84 (2004) 4968.
- [26] L. Pan, K.K. Lew, J.M. Redwing, E.C. Dickey, Nano Lett. 5 (2005) 1081.
- [27] J.B. Hannon, S. Kodambaka, F.M. Ross, R.M. Tromp, Nature 440 (2006) 69.
- [28] E.D. Williams, N.C. Bartelt, Ultramicroscopy 31 (1989) 36.
- [29] R. Hild, C. Seifert, M. Kammler, F.-J. Meyer zu Heringdorf, M. Horn-von-Hoegen, R.A. Zhachuk, B.Z. Olshanetsky, Surf. Sci. 512 (2002) 117.
- [30] D. Sanchez-Portal, R.M. Martin, Surf. Sci. 532–535 (2003) 655.
- [31] J.W. Dickinson, J.C. Moore, A.A. Baski, Surf. Sci. 561 (2004) 193.

5.2 Liquid AuSi droplets below the eutectic temperature

Various articles have been published in recent years, reporting on nanowire growth below the eutectic temperature. While some authors assume a novel type of growth called Vapour-Solid-Solid (VSS) growth, others clearly identify liquid droplets below the eutectic temperature. The following study sheds light on the latter case where supercooling is observed in AuSi droplets on a Si(111) surface. The system Au on Si(111) is one of the most prominent examples of catalytic nanowire growth. Therefore a profound understanding of such phenomena in the VLS growth process can be considered essential. During investigations of early growth stages of nanowires, a strong supercooling behavior of the catalyst was observed, its amplitude depending on the thermal history. To track details on the influence of the solid-liquid interaction on these phenomena, experiments were carried out studying Au or AuSi droplets on Si(111) surfaces obtained by MBE deposition of a few atomic Au layers on Si(111). For a comparison Au on Si(001) and on Ge(111) was studied as well, yielding significantly lower supercooling. In order to observe solid-liquid transitions in nanostructures, x-rays are definitely the best suited tool. In the case of droplets or islands on a surface, x-rays can probe the structure of the liquid or nanocrystals at the same time while observing the structure at the liquid-crystal interface.

Supercooling in liquid metals

Supercooling often also referred to also as undercooling describes the metastable state in which a liquid can be trapped below its solidification point. It can be explained by crystal nucleation theory where the stability of a nucleus or seed crystal in coexistence with its own melt depends on the size of the crystallite. Crystals of any size will turn liquid when the melting point T_m is reached. For smaller crystals of size d a reduced melting point $T_d = T_m - \Delta_d$, has been observed experimentally. This allows already to conclude qualitatively that when cooling down a pure liquid (in the absence of any crystal seed) even at a temperature $T_d < T_m$ solidification requires the spontaneous formation of a crystal grain of size d in order to be stable. Smaller grains, when formed, will dissolve again as their melting point T_d is higher. This reduces the point T_s where spontaneous solidification sets in. This comparison remains a qualitative one as the lowering of the melting point of nanoparticles generally is not observed once they are surrounded by their own liquid melt. Nevertheless, being experimentally less accessible, crystal nucleation theory can explain supercooling in homogeneous liquids due to the minimum size required for a grain in order to be stable in its own melt.

Supercooling was first described by D.G. Fahrenheit in 1724 [15] while investigating water. It has however attracted novel interest when important supercooling in metals was described by D. Turnbull and co-workers [16, 17]. Crystal nucleation theory explained the supercooling from a kinetic point of view: the size of thermodynamically stable nuclei at the melting point was supposed to be too large to be spontaneously formed in the liquid. This suggests that the homogeneous nucleation mechanism responsible for formation of the solid phase must present an energetic barrier to phase change. This critical size for homogeneous nucleation decreases with temperature and once a certain degree of supercooling is obtained, spontaneous solidification

sets in [17]. However, given the similar densities and properties of liquid and crystal phases, the barrier separating them in metals and alloys was too small to explain the unusually large degree of supercooling ($\Delta T = T_m - T_s$) observed in some liquid metals and alloys. Furthermore, supercooling in deep binary eutectics is from this point of view an unexpected phenomenon: At the origin of their low melting point is the absence of a common crystalline phase with the corresponding composition. Both elements of such a eutectic can thus be considered to be in a non-classical supercooled phase since no homogeneous nucleation is possible without phase separation. Once the phases are locally separated, at least one element is far below its' respective solidification temperatures and thus spontaneous solidification sets in. It was thus the observation of giant supercooling of some elements that solidify into close-packed structures and the supercooling of intermetallic eutectics that led to the interpretation that the internal structure of the liquid itself must be responsible for its metastable behaviour. F.C. Frank [18] proposed in the 1950s that as metallic liquids cool, local atomic structures containing icosahedral short-range order (ISRO) develop in the liquid phase. This ISRO presents the same coordination number, 12, as in the solid, but is locally more stable because it is denser. Moreover, this local icosahedral ordering is incompatible with three-dimensional periodicity, creating a barrier to the formation of the crystalline phase. More complex models of liquids and glasses have been proposed later, favouring local 5-fold coordination [19]. Nowadays, these models based on ISRO are widely accepted as the origin of supercooling in metals and to be a basic structural element of liquid metals in general [20].

5.2.1 *Substrate-enhanced supercooling in AuSi eutectic droplets*

T. U. Schülli, R. Daudin, G. Renaud, A. Vaysset, O. Geaymond, A. Pasturel,
Nature 464, 1174 (2010).

In the years 2006-2010, a UHV gas source injection system was planned, developed and installed on the existing MBE chamber on BM32 in order to combine solid state- and gas-source growth. This project is aiming at the first *in situ* apparatus for VLS nanowire growth using x-rays. The first measurements however focused on the role of the catalyst and the supercooling behaviour reported in these. The study of their solid-liquid transition was performed, mapping out large regions in reciprocal space. This shed light on the influence of a particular surface reconstruction present on the Si(111) surface in the presence of gold. An analysis of the structure of this reconstruction yields that its atoms form pentagonal structures with shorter bond length than in a bulk Au fcc crystal. In the presence of this reconstruction a maximum supercooling of 360 K is observed. In its absence or on surfaces with similar chemistry but different atomic arrangement like on Si(001), the supercooling observed is significantly less pronounced. On the following pages our work on the supercooling behaviour of AuSi dropets on Si(111) and Si(001) surfaces is presented in the form of a journal article and supplementary information with data and graphs that are referred to in the article. As a result of the impact on the fundamental physics of liquids, an invited article was written presenting the topic of supercooling to a wider public, especially aiming pupils at high school level. This article is presented in appendix 7.

LETTERS

Substrate-enhanced supercooling in AuSi eutectic droplets

T. U. Schüllli^{1,2}, R. Daudin¹, G. Renaud¹, A. Vaysset¹, O. Geaymond³ & A. Pasturel⁴

The phenomenon of supercooling in metals—that is, the preservation of a disordered, fluid phase in a metastable state well below the melting point¹—has led to speculation that local atomic structure configurations of dense, symmetric, but non-periodic packing act as the main barrier for crystal nucleation^{2,3}. For liquids in contact with solids, crystalline surfaces induce layering of the adjacent atoms in the liquid^{4,5} and may prevent or lower supercooling⁶. This seed effect is supposed to depend on the local lateral order adopted in the last atomic layers of the liquid in contact with the crystal. Although it has been suggested that there might be a direct coupling between surface-induced lateral order and supercooling⁶, no experimental observation of such lateral ordering at interfaces is available⁶. Here we report supercooling in gold-silicon (AuSi) eutectic droplets, enhanced by a Au-induced (6×6) reconstruction of the Si(111) substrate. *In situ* X-ray scattering and *ab initio* molecular dynamics reveal that pentagonal atomic arrangements of Au atoms at this interface favour a lateral-ordering stabilization process of the liquid phase. This interface-enhanced stabilization of the liquid state shows the importance of the solid–liquid interaction for the structure of the adjacent liquid layers. Such processes are important for present and future technologies, as fluidity and crystallization play a key part in soldering and casting, as well as in processing and controlling chemical reactions for microfluidic devices or during the vapour–liquid–solid growth of semiconductor nanowires.

Clusters with icosahedral short-range order are now widely considered as basic structural elements of liquid metals and glasses^{3,7–9}. Their presence has been proven experimentally^{4,7,10} and by *ab initio* molecular dynamics simulations (MDS)¹¹. At solid–liquid interfaces, however, a description of the structure of liquids is difficult, as is the prediction of the influence of interfaces on ordering and more particularly supercooling. As highlighted in ref. 6, the degree to which a liquid can be supercooled strongly depends on the substrate in contact with it, as well as on thermal history. In recent experiments, enhanced layering in liquids at solid (crystalline)–liquid interfaces has been observed^{4,5}. However, tracking its influence on crystallization or supercooling requires an investigation of ordering in the liquid along the interface, which presents an experimental challenge. In the present work, we analyse the influence of different interfaces on the degree of supercooling and possible in-plane order in AuSi liquid droplets of near-eutectic composition. The effects of three substrates—Si(001), Si(111) with a Au-induced ($\sqrt{3} \times \sqrt{3}$)R30° reconstruction, and Si(111) with a Au-induced (6×6) reconstruction—are compared. Offering fluidity at low temperatures, such eutectic liquids are at the heart of the catalytic growth of semiconductor nanowires by the vapour–liquid–solid process¹². Recent *in situ* microscopy studies of the growth dynamics and nucleation of semiconductor nanowires^{13–15} suggest that Ge nanowires can grow below the AuGe eutectic temperature^{16,17}, with the catalysts' state depending

on thermal history. Furthermore, a possible modification of the eutectic temperature for nanostructures has been suggested¹⁸. These puzzling observations call for further investigations of the supercooling behaviour of metal–semiconductor alloys and their atomic structure at semiconductor interfaces.

We used *in situ* grazing incidence X-ray scattering in ultrahigh vacuum at beamline BM32 of the European Synchrotron Radiation Facility to study solid–liquid transitions on surfaces and nanostructures^{4,19}. The experimental results were compared to *ab initio* MDS¹¹. The experiment consisted in analysing, for different temperatures, the atomic structure of the silicon surface, that of the liquid/solid Au(Si) islands, and that of the AuSi/Si(111) (or AuSi/Si(001)) interface, special attention being paid to a potential correlation between them. The different steps of the experiment are schematically shown in Fig. 1. The complexity of this system required mapping extended regions in reciprocal space (Fig. 2a), to address all structural features at a given temperature. These extended reciprocal space maps were performed by variation of the momentum transfer $Q = 4\pi \sin(\theta)/\lambda$, where λ is the X-ray wavelength and θ half the scattering angle between the incident and scattered beams that are almost parallel to the sample surface (for details on experimental tools and sample preparation, see Methods Summary, Supplementary Information, and Supplementary Figs 2 and 4).

During annealing (Fig. 1, steps 2–3), the Au islands transform into liquid droplets exactly at the bulk eutectic temperature, $T_E = 636 \pm 5$ K, suggesting that the Si substrate provided atoms to reach the Au₈₁Si₁₉ eutectic composition. All diffraction peaks from Au disappear simultaneously at T_E and give way to a scattering signal that is characteristic of a liquid phase, as shown on the reciprocal space map of Fig. 2a. For annealing temperatures higher than $T_E + 40$ K ($=676$ K) and subsequent cooling (Fig. 1, step 4) more diffraction peaks appear, corresponding to a well defined Si(111)-(6×6) superstructure²⁰, as revealed in the reciprocal space map in Fig. 2a. When cooling down below T_E , no Bragg peaks from solid Au reappear, but the liquid-like scattering remains: the islands stay liquid. Cooling down further reveals that solidification happens only at $T_S = 513 \pm 5$ K (Fig. 1, step 5), that is, more than 120 K below T_E . After solidification, the (6×6) superstructure remains, together with powder diffraction rings from the face-centred-cubic (f.c.c.) Au structure. Reciprocal space maps for different sample preparations are shown in Supplementary Fig. 4.

Remarkably, this phase transition is found to be fully reproducible: when the temperature is cycled down and up, the above-described behaviour of the solid–liquid–solid transition remains: melting at T_E on heating, and solidification at $T_S = 513 \pm 5$ K on cooling. Moreover, the final T_S value is independent of the time spent (between a few tens of minutes to a few tens of hours) at T_S or between T_S and T_E . Several samples were investigated with the procedure described above, or with co-deposition of an Au₈₁Si₁₉ film with the eutectic composition, all

¹CEA, Institut Nanosciences et Cryogénie, SP2M, 17 rue des Martyrs, 38054 Grenoble, France. ²European Synchrotron Radiation Facility, BP 220, 38043 Grenoble, France. ³Institut Néel, CNRS, BP 166, 38042 Grenoble, France. ⁴SIMAP INPG, BP 75, 38402 Saint Martin d'Hères cedex, France.

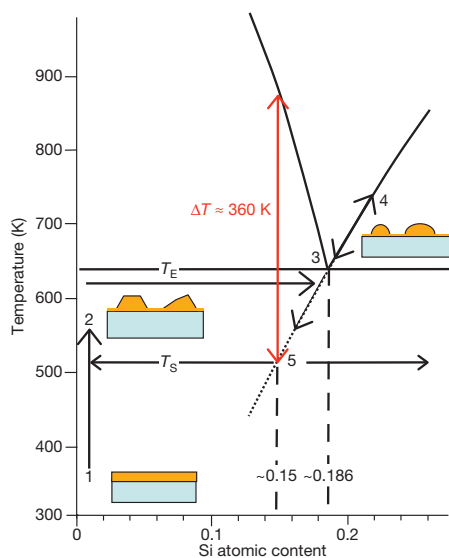


Figure 1 | Extract from the bulk AuSi phase diagram together with representations of the melting and solidification cycles of AuSi islands on an Si(111)-(6 × 6) reconstructed surface. The numbers 1 to 5 refer to successive experimental steps, and the large black arrows indicate the pathways followed by the islands during heating/cooling cycles. Seven monolayers of Au are deposited at room temperature (step 1; bottom inset). On annealing they transform into crystalline Au islands (step 2; middle inset). At $T_E = 636$ K, melting sets in and AuSi droplets with the eutectic composition ($\text{Au}_{81.4}\text{Si}_{18.6}$) are formed (step 3; top right inset). Heating up to 673 K before cooling (step 4) induces a (6 × 6) reconstruction, and leads to a preservation of the liquid phase down to 513 K (step 5), where phase separation and solidification occur (step 5). Above T_E , on heating or cooling, the liquid composition is expected to follow the Si liquidus. Below T_E , it follows the (extrapolated; dotted line) metastable Si liquidus. The degree of supercooling (red arrow) has to be measured between this latter and the Au liquidus above T_E for the corresponding composition of ~15 at.% Si. It amounts to ~360 K.

showing the same solidification temperature after cyclic melting and solidification.

The structure factor $S(Q)$ of the liquid in its supercooled state is shown in Fig. 3a. Very close to the origin (Fig. 3b), powder diffraction peaks are present, located exactly at the positions expected for the two-dimensional Au-Si crystalline structures reported to form on the surface of the liquid eutectic²¹. Figure 3e shows the intensity evolution around the first maximum of $S(Q)$ for decreasing temperatures through $T_S = 513$ K. The initially very broad intensity distribution narrows progressively approaching the solidification temperature, below which it collapses to give rise to the Au(111) Bragg peak. Hysteresis loops extracted from the integrated intensity of Au Bragg reflections (Supplementary Fig. 2) are shown in Fig. 3c for different Si surfaces and/or surface preparation. The lowest solidification temperature $T_S = 513 \pm 5$ K is observed for droplets on an Si(111)-(6 × 6) surface reconstruction, whereas it is significantly higher ($T_S = 563 \pm 5$ K) when heating the sample just above T_E , which only yields a precursory ($\sqrt{3} \times \sqrt{3}$)R30° reconstruction (Supplementary Fig. 4c). Proceeding similarly on an Si(001) surface (on which no reconstruction coexists with the liquid) only yields $T_S = 573 \pm 5$ K (Supplementary Fig. 3b). In all cases, peaks of the two-dimensional AuSi surface crystallites (Fig. 3b) were present and the deposited amount of Au was identical, leading to droplet sizes of 150–200 nm, too large to influence the solidification temperature. Remarkably, the size dependence is found to be weak for deposits between two and seven monolayers of Au ($T_S = (510\text{--}520) \pm 5$ K). One sample with a 30-monolayer Au deposit was investigated, yielding $T_S = 555 \pm 10$ K (Supplementary Fig. 7). This last value approaches that of $T_S = 573 \pm 5$ K, obtained when the Si

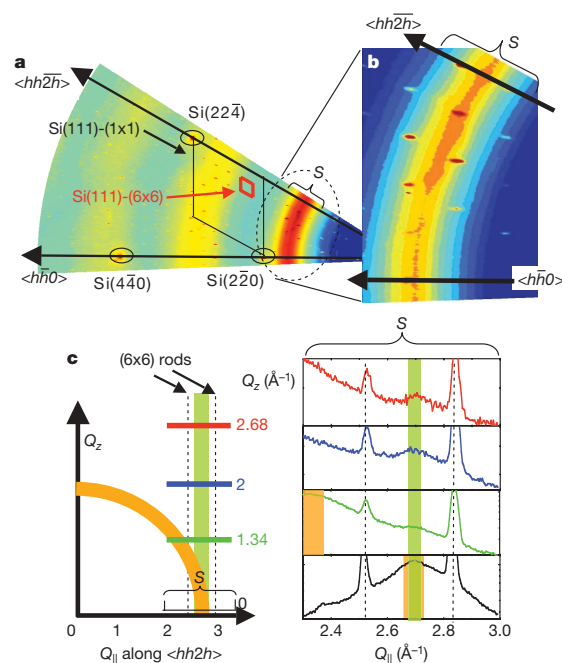


Figure 2 | Reciprocal space mapping of liquid AuSi islands on (6 × 6) reconstructed Si(111). **a**, Reciprocal space map of the liquid in its supercooled state on a (6 × 6) reconstructed Si(111) surface. Blue colour corresponds to low intensity, and red to high intensity, yellow being intermediate. Three bulk Bragg peaks are visible, together with a mesh of smaller peaks arising from the (6 × 6) surface/interface periodic superstructure. The three diffuse rings correspond to liquid-like scattering. **b**, Anisotropy of the first order maximum of the liquid structure factor: In the vicinity of strong (6 × 6) reconstruction peaks the signal from the liquid is enhanced, underlining morphological similarities between the crystalline surface and the adjacent liquid layers. **c**, Right: scans across the first order maximum of the liquid structure factor in the plane (along section S marked in **a** and **b**) and parallel to it for several values of out-of-plane momentum transfer, Q_z . Left: the sketch indicates in orange the position of the first maximum of the isotropic liquid. The green rod corresponds to the intensity distribution stemming from preferential in-plane order.

surfaces suffered from non-ideal preparation conditions (for example, carbon pollution), and is similar to values observed in a closed AuSi system without Si reservoir²².

The decrease of the solidification temperature T_S when the surface is reconstructed (that is, the Si(111)-(6 × 6)Au reconstruction) and with increasing interface/volume ratio shows the crucial role of this particular interface structure on the conservation of the liquid state. This suggests that the specific local atomic structure at the interface favours peculiar ordering effects in the adjacent liquid layers, eventually lowering the interface energy and rendering it a particularly inefficient nucleant for Au. Other crystallization mechanisms may be dominant, such as faceting of the free surface²³ or homogeneous nucleation of Au triggered by concentration fluctuations. The composition of the supercooled droplets may favour the latter process; Si regrowth through a (6 × 6) reconstruction is possible without perturbing this surface structure (Supplementary Fig. 8). This demonstrates that this reconstruction does not inhibit the redeposition of Si at the interface below the droplet while it adapts its composition to follow the Si liquidus line when cooling from above T_E , reaching the eutectic composition at T_E . Below T_E , the droplet's composition is expected to follow the metastable Si liquidus (Fig. 1, step 5). At 513 K, the liquid being Au enriched by ~3–4 at.% with respect to the eutectic composition (Fig. 1), the corresponding degree of supercooling has to be measured between the Au liquidus of the equilibrium phase diagram above T_E and the metastable (extrapolated) Si

LETTERS

NATURE | Vol 464 | 22 April 2010

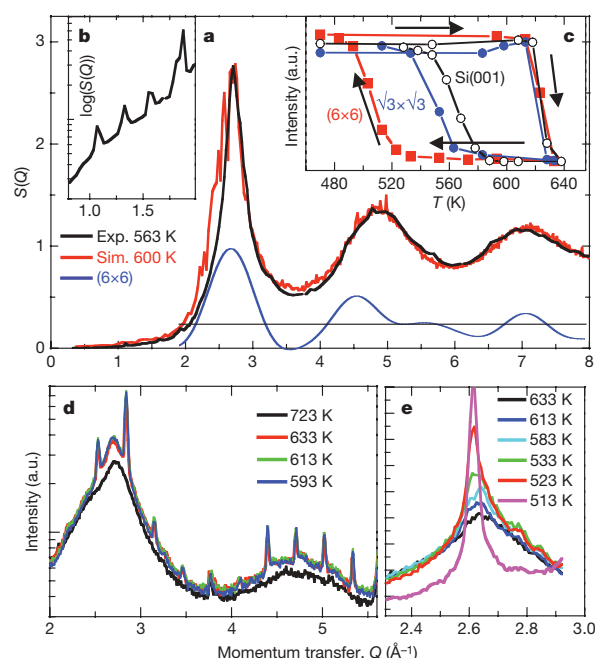


Figure 3 | Evolution of the liquid structure factor during cooling and solidification. **a**, Angular average of the experimental structure factor $S(Q)$ of liquid AuSi at 563 K (black line) together with the theoretical structure factor extracted from MDS at 600 K (red line). The blue line corresponds to the mean structure factor of the (6×6) reconstruction (Supplementary Fig. 5). **b**, Zoom (logarithmic scale) on the low- Q spectrum of the structure factor, showing the Bragg peaks from two-dimensional crystallites floating on the surface of liquid AuSi (ref. 21). **c**, Hysteresis loops of the integrated intensity of the Au(220) Bragg peak during the solid–liquid–solid transition of Au islands on Si(001) (black open circles), on a Si(111)- $(\sqrt{3} \times \sqrt{3})R30^\circ$ reconstruction (blue filled circles) and on a Si(111)- (6×6) reconstruction (red squares). **d**, Liquid structure factor (logarithmic scale) along the $\langle 1\bar{1}0 \rangle$ crystallographic direction of the Si(111) surface. The strong influence of the appearance of the (6×6) reconstruction on the structure of the liquid is visible. **e**, Evolution of the first maximum of the liquid structure factor in the supercooling regime. liquidus below T_E (red arrow in Fig. 1); this yields a remarkably large value of ~ 360 K.

Our experimental observation is further supported by *ab initio* MDS (see Supplementary Information for details) that allowed monitoring the structural evolution at three temperatures, above and below T_E . The $\text{Au}_{81}\text{Si}_{19}$ system was considered to be the prototype liquid for near-eutectic compositions; a change of 3–4 at.% Si does not modify the conclusions drawn from the structural analysis. The alloy was found to stay liquid even at 500 K, that is, well below T_E (Supplementary Fig. 9). The simulated liquid structure factor $S(Q)$ compares very well with the experimental one (Fig. 3a), confirming the accuracy of the simulations. To learn more about the detailed three-dimensional picture of the local structure of the liquid, we performed a common-neighbour analysis²⁴, which allows us to distinguish between various local structures, such as f.c.c., hexagonal close packed, body centred cubic, and icosahedral environments. The short-range order is found to display an appreciable proportion (46%) of pairs in local five-fold arrangement in the liquid state ($T = 700$ K); the supercooled regime is characterized by an increased fraction of five-fold atomic ordering (51% at $T = 600$ K and 54% at $T = 500$ K). The temperature dependent occurrence of five-fold clusters is shown in Supplementary Fig. 10.

Solid–liquid systems that present important interface-induced atomic layering (that is, short range order like stacking of adjacent liquid layers), such as Al droplets on Al_2O_3 , have shown significant supercooling^{5,6}, underlining the importance of investigating the

structure, both parallel and perpendicular to the interface, of these interfacial liquid layers. Indeed, the influence of a solid–liquid interface on the five-fold order inside the liquid has been discussed^{25,26}. In the present system, we have thus paid particular attention to the structure of the Au-induced (6×6) reconstruction of the Si(111) surface and its influence on the in-plane structure of the adjacent liquid, revealing a clear link between the structure of this reconstruction and that of the liquid.

Figure 3d shows high resolution measurements of the scattered intensity performed along a symmetry direction of the Si(111) surface, hence crossing its reconstruction peaks. The first and second orders of the liquid structure factor $S(Q)$ both reveal a marked correlation between the appearance of the (6×6) reconstruction peaks and an increase in intensity in the maxima of $S(Q)$. In addition, the radial intensity distribution obtained by integration of all diffraction peaks measured from the (6×6) reconstruction and their subsequent convolution by fast Fourier transform (detailed in Supplementary Fig. 6) compares well to the experimental and theoretical structure factors of the liquid (Fig. 3a), indicating close similarities of the main interatomic distances in the liquid and in the (6×6) structure. Note that our measurements average over a macroscopic surface composed of the free (6×6) Au reconstructed Si(111) surface between islands, and of the interface between the substrate and the islands; the latter covers only a few per cent of the total area. It is thus not strictly possible to conclude the existence of a long-range ordered (6×6) reconstruction at the substrate–droplet interface. However, the evidence of enhanced supercooling in the presence of this reconstruction on the one hand, and the high stability of it on the other hand (demonstrated, for example, by its fast recovery by gentle annealing after having been destroyed by ion bombardment) let us believe that the liquid–solid interface is at least locally reconstructed with the pentagonal order of the Au- (6×6) structure.

Zooming in on the first maximum of the liquids' $S(Q)$ (Fig. 2b) proves that under the influence of the (6×6) reconstruction, the liquid becomes anisotropic: the scattered intensity is more pronounced in the vicinity of the most intense peaks of the (6×6) reconstruction, indicating a structural similarity of the (6×6) structure and the adjacent liquid layers at the local scale. This is further evidenced in Fig. 2c, where scans across the first maximum of $S(Q)$ are presented for different out of plane momentum transfer, Q_z . For large Q_z , the isotropic liquid scattering is separated from a rod of scattering present for all Q_z at a constant in plane momentum transfer ($Q_{||}$) value. This rod is a signature of a lateral ordering in the liquid close to the solid surface. To interpret this correlation between the internal structure of the liquid and that of the (6×6) reconstruction, together with the enhanced supercooling, one needs to compare the theoretical and experimental structure of the liquid with the atomic arrangement of the (6×6) structure.

The detailed atomic structure of the Si(111)- (6×6) Au reconstruction was determined by measuring quantitatively 983 in-plane Bragg superstructure reflections, integrated and corrected for monitor, area, Lorentz and polarization corrections. The in-plane diffraction diagram (Supplementary Fig. 5) has $p6mm$ symmetry, resulting in 234 non-equivalent reflections with a 4.5% systematic uncertainty. The data were quantitatively analysed using ROD²⁷ software for surface structure analysis. Scans perpendicular to the surface on several reconstruction rods showed that this (6×6) superstructure is of monoatomic thickness. The final model ($\chi^2 = 2.8$ with only the Au atoms taken into account) is remarkably close to the model proposed in ref. 20 for the (6×6) surface reconstruction induced by a one-monolayer Au deposit. The atomic structure consists of a fairly disordered surface unit of low ($p31m$) symmetry, incoherently scattering with its twin with respect to the $[1\bar{1}0]$ mirror. It contains several deformed pentagons surrounding the three-fold axes (Fig. 4). The nearest-neighbour distance in these pentagons is 2.86 \AA at room temperature, denser than for gold in its bulk f.c.c. structure (2.90 \AA at 550 K), but close to the interatomic distance (2.84 \AA) in icosahedral Au clusters in the supercooled liquid,

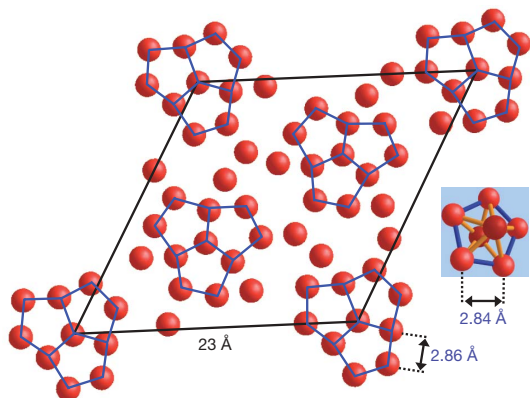


Figure 4 | Au-induced Si(111)-(6 × 6) surface leading to enhanced supercooling. Unit cell (black lozenge) of the complex (6 × 6) reconstruction (only the Au atoms are shown) formed at $T < 673$ K after annealing temperatures $T > 673$ K. A pentagonal cluster (see inset three-dimensional structure) present in the simulated liquid has similar topology and bond length (2.84 Å) as the surface structure (2.86 Å), smaller than in the Au f.c.c. lattice (2.90 Å). Out of 45 atoms in the unit cell, 30 are in a pentagonal environment (interconnected by blue lines).

as deduced from the MDS (Fig. 4 inset). Thus, the (6 × 6) surface structure offers perfect sites to stabilize the five-fold clusters, which in turn stabilize the supercooled metal.

This much enhanced degree of supercooling of liquid AuSi on the Si(111)-(6 × 6) surface compared to other Si surface structures shows the marked influence of a dense pentagonal atomic arrangement at the solid–liquid interface on the short range order and the metastability of a liquid. Although AuSi can be considered as a liquid with quite unusual properties, pentagonal arrangements have been shown to be favourable in a vast range of liquids^{2–11}. More generally, solid–liquid interfaces that favour pentagonal local ordering should lead to deep supercooling, because the origin of the barrier to nucleation of crystallographic phases is the formation of local icosahedral order in the liquid. Such interfaces can significantly affect the liquid in contact with them, thus controlling its stability. This may have important implications—for example, perhaps the containerless techniques required today to obtain supercooling could in the future be replaced by icosahedrally coated solid containers.

METHODS SUMMARY

Sample preparation. After oxide removal, the Si(111) surfaces formed a well-defined Si(111)-(7 × 7) reconstruction. Typically, seven atomic layers of Au were deposited at 300 K (room temperature), forming a 1.6-nm-thick film (Fig. 1, step 1). Owing to the low temperature, the Au film crystalline quality was found to be low, but showed a clear preferential epitaxy with identical directions of the two cubic lattices: $[1\bar{1}0]\text{Au}(111)||[1\bar{1}0]\text{Si}(111)$. On heating up to 623 K, which is 13 K below $T_E = 636$ K (Fig. 1, step 2), the Au film de-wets to form crystalline islands with a preferential in-plane epitaxy rotated by 19.2° with respect to the aligned epitaxy (that is, $[1\bar{1}0]\text{Au}(111)||[2\bar{3}1]\text{Si}(111)$). *In situ* X-ray peak width analysis, together with *ex situ* high resolution secondary electron microscopy and atomic force microscopy, showed islands of average width 150 nm and average height 25 nm (for the seven-monolayer deposit), which is typical for annealed gold layers of similar thickness²⁸. Smaller (larger) deposits are expected to lead to smaller (larger) islands. Both Si(111)-(6 × 6) and the $-(\sqrt{3} \times \sqrt{3})R30^\circ$ reconstructions have been reported on Si(111) for Au coverage around one monolayer. Here the $(\sqrt{3} \times \sqrt{3})R30^\circ$ is observed whatever the annealing temperature above T_E . However, it is replaced by the (6 × 6) after annealing above 673 K followed by cooling. More details are available as Supplementary Information.

Molecular dynamics simulations. In these simulations, 256 atoms at eutectic composition are arranged in a cubic box with periodic boundary conditions. Canonical NVT (constant number, volume, temperature) ensembles were assumed using the Vienna *ab initio* simulation package²⁹. The evolution of the system was followed at three temperatures (700, 600 and 500 K) as a function of

time (durations 30 ps, time step 3 fs), the last two runs being in the supercooled regime. More details are available as Supplementary Information.

Received 13 October 2009; accepted 23 February 2010.

- Turnbull, D. Kinetics of solidification of supercooled liquid mercury droplets. *J. Chem. Phys.* **20**, 411–424 (1952).
- Frank, F. C. Supercooling of liquids. *Proc. R. Soc. Lond. A* **215**, 43–46 (1952).
- Torquato, S. & Jiao, Y. Dense packings of the Platonic and Archimedean solids. *Nature* **460**, 876–879 (2009).
- Reichert, H. *et al.* Observation of five-fold local symmetry in liquid lead. *Nature* **408**, 839–841 (2000).
- Oh, S. H., Kauffmann, Y., Scheu, C., Kaplan, W. D. & Rühle, M. Ordered liquid aluminum at the interface with sapphire. *Science* **310**, 661–663 (2005).
- Greer, A. L. Liquid metals: supercool order. *Nature Mater.* **5**, 13–14 (2006).
- Wochner, P. *et al.* X-ray cross correlation analysis uncovers hidden local symmetries in disordered matter. *Proc. Natl Acad. Sci. USA* **106**, 11511–11514 (2009).
- Steinhardt, P. J., Nelson, D. R. & Ronchetti, M. Icosahedral bond orientational order in supercooled liquids. *Phys. Rev. Lett.* **47**, 1297–1300 (1981).
- Sheng, H. W., Luo, W. K., Alamgir, F. M., Bai, J. M. & Ma, E. Atomic packing and short-to-medium-range order in metallic glasses. *Nature* **439**, 419–425 (2006).
- Schenk, T., Holland-Moritz, D., Simonet, V., Bellissent, R. & Herlach, D. M. Icosahedral short-range order in deeply undercooled metallic melts. *Phys. Rev. Lett.* **89**, 075507 (2002).
- Jakse, N. & Pasturel, A. Local order of liquid and supercooled zirconium by *ab initio* molecular dynamics. *Phys. Rev. Lett.* **91**, 195501 (2003).
- Wagner, R. S. & Ellis, W. C. Vapor–liquid–solid mechanism of single crystal growth. *Appl. Phys. Lett.* **4**, 89–90 (1964).
- Hannon, J. B., Kodambaka, S., Ross, F. M. & Tromp, R. M. The influence of the surface migration of gold on the growth of silicon nanowires. *Nature* **440**, 69–71 (2006).
- Kim, B. J. *et al.* Kinetics of individual nucleation events observed in nanoscale vapor–liquid–solid growth. *Science* **322**, 1070–1073 (2008).
- Kodambaka, S., Tersoff, J., Reuter, M. C. & Ross, F. M. Germanium nanowire growth below the eutectic temperature. *Science* **316**, 729–732 (2007).
- Hofmann, S. *et al.* Ledge-flow-controlled catalyst interface dynamics during Si nanowire growth. *Nature Mater.* **7**, 372–375 (2008).
- Sutter, E. & Sutter, P. Phase diagram of nanoscale alloy particles used for vapor–liquid–solid growth of semiconductor nanowires. *Nano Lett.* **8**, 411–414 (2008).
- Adhikari, H., Marshall, A. F., Chidsey, C. E. D. & McIntyre, P. C. Germanium nanowire epitaxy: shape and orientation control. *Nano Lett.* **6**, 318–323 (2006).
- Pinardi, A. L., Leake, S. J., Felici, R. & Robinson, I. K. Formation of an Au–Si eutectic on a clean silicon surface. *Phys. Rev. B* **79**, 045416 (2009).
- Grozea, D. *et al.* Direct methods determination of the Si(111)-(6 × 6)Au surface structure. *Surf. Sci.* **418**, 32–45 (1998).
- Shpyrko, O. G. *et al.* Surface crystallization in a liquid AuSi alloy. *Science* **313**, 77–80 (2006).
- Chen, H. S. & Turnbull, D. Thermal properties of gold–silicon binary alloy near the eutectic composition. *J. Appl. Phys.* **38**, 3646–3650 (1967).
- Sutter, P. W. & Sutter, E. A. Dispensing and surface-induced crystallization of zeptolitre liquid metal–alloy drops. *Nature Mater.* **6**, 363–366 (2007).
- Honeycutt, J. D. & Andersen, H. C. Molecular-dynamics study of melting and freezing of small Lennard-Jones clusters. *J. Phys. Chem.* **91**, 4950–4963 (1987).
- Spaepen, F. Structural model for solid–liquid interface in monoatomic systems. *Acta Metall.* **23**, 729–743 (1975).
- Heni, M. & Lowen, H. Do liquids exhibit local fivefold symmetry at interfaces? *Phys. Rev. E* **65**, 021501 (2002).
- Vlieg, E. ROD: A program for surface X-ray crystallography. *J. Appl. Crystallogr.* **33**, 401–405 (2000).
- Schubert, L. *et al.* Silicon nanowhiskers grown on 111 > Si substrates by molecular-beam epitaxy. *Appl. Phys. Lett.* **84**, 4968–4970 (2004).
- Kresse, G. & Furthmüller, J. Efficiency of *ab-initio* total energy calculations for metals and semiconductors using a plane-wave basis set. *Comput. Mater. Sci.* **6**, 15–50 (1996).

Supplementary Information is linked to the online version of the paper at www.nature.com/nature.

Acknowledgements We thank J. Villain, G. Bauer, H. Reichert, Y. Bréchet and K. Oliver for their reading of the manuscript and T. Duffar, K. Zaidat, P. Guyot and P. Desrè for discussions.

Author Contributions T.U.S. initiated the work, and contributed to the experimental part; R.D. contributed to both the experimental and theoretical parts; G.R. contributed to the experimental work, A.P. to the theoretical simulations and O.G. to technical assistance. Together with G.R., A.V. analysed the structure of the Si(111)-(6 × 6) reconstruction. T.U.S., G.R., R.D. and A.P. wrote the paper.

Author Information Reprints and permissions information is available at www.nature.com/reprints. The authors declare no competing financial interests. Correspondence and requests for materials should be addressed to T.U.S. (schullli@esrf.fr).

SUPPLEMENTARY INFORMATION

1. Supplementary Methods:**Experimental set-up**

The sample preparation and the x-ray experiments have been carried out at the synchrotron beamline for *in situ* nanostructure growth (BM32) at the ESRF (European Synchrotron Radiation Facility, Grenoble, France) (A description of the ESRF and of the BM32 beamline can be found on <http://www.esrf.eu/UsersAndScience/Experiments/CRG/BM32/Beamline/SUV/index.html>), using an X-ray energy of 11 keV. Grazing incidence X-ray scattering (GIXS) and Surface X-Ray Diffraction (SXRD) were performed with the incident beam fixed at the critical angle (0.163°) for total external reflection, in order to be sensitive to the sample surface. The different Si-samples were outgassed at 500 K for 24 hours in a preparation chamber before being transferred under ultra high vacuum (UHV) into the growth chamber of the beamline. This UHV chamber [R. Baudoing-Savois, G. Renaud, et al., Nucl. Inst. and Meth. In Phys. Res. B. **159**, 120 (1999)], which is equipped with a large cylindrical beryllium window for x-ray transparency, was operated at a base pressure of $\sim 1 \times 10^{-10}$ mbar. In addition to x-ray scattering it is possible to perform reflection high energy electron diffraction (RHEED) measurements, especially useful for sample preparation. The Au deposition has been calibrated using a quartz microbalance, as well as *in situ* x-ray reflectivity.

Temperature control

The temperature of the sample surface was measured with two IRCON infrared pyrometers through a special sapphire window. Together they cover a temperature range from 470 to 2200 K. A calibration in the critical temperature regime for the present study has been done at the melting point of ultra pure lead at 600 K, confirming the accuracy based on earlier calibrations using bulk $\text{Al}_{89}\text{Si}_{11}$ eutectic with a melting point of 850 K. The calibration was further confirmed during each experiment since we always found the melting temperature of AuSi eutectic exactly at the expected temperature of 636 K. The temperature accuracy is evaluated to ± 5 K.

Sample preparation and island formation

The silicon surface was first deoxidized at 1300 K at a base pressure of 10^{-10} mbar. *In situ* RHEED and GIXS/SXRD both showed the formation of a well-defined $\text{Si}(111)-(7 \times 7)$ reconstruction, which is characteristic of a clean surface. After cooling down to room temperature, our standard procedure was to deposit 7 monolayers (ML) of Au (1.65 nm) (2, 10 and 30 ML were also done). A preferential (111) orientation, with low crystalline quality and a tendency to aligned epitaxy with the underlying substrate was observed.

After melting, supercooling and solidification, HR-SEM images of the islands reveal that some islands show marble-like structures similar to those shown in [N. Ferralis, R. Maboudian, C Carraro, J. Am. Chem. Soc. **130**, 2681 (2008)] with bulk Au crystals coexisting with Si crystals, whereas others seem to be of homogeneous nature.

Upon heating the sample from room temperature, a Au-induced $\text{Si}(111)-(\sqrt{3} \times \sqrt{3})R30^\circ$ reconstruction first appears around 400 K. It remains stable while improving in quality upon further heating. If the temperature of 673 K is not exceeded, only this reconstruction is observed. When heating above 673 K, and then cooling down, a Au-induced $\text{Si}(111)-(6 \times 6)$ reconstruction (which is closely linked to the $(\sqrt{3} \times \sqrt{3})R30^\circ$) takes over and then remains at all

temperatures below 673 K. The higher the annealing temperature, the better the quality of the final (6×6) structure below 673 K. The phase diagram for the determination of the eutectic point and the supercooling was taken from Okamoto, H. and Massalski, T.B. *Phase Diagrams of binary gold alloys*, ASM International Metals Park, USA (1987).

***Ab initio* molecular dynamics simulations:**

For the *ab initio* molecular dynamics simulations, canonical NVT (constant number, volume, temperature) ensembles were used using the Vienna *ab initio* simulation package. Projected augmented plane waves (PAWs) with the Perdew-Wang exchange-correlation potentials have been adopted. The valence state of each element has been previously defined in the provided PAW potentials. The temperature was controlled using a Nose thermostat [D.J Evans, B.L Holian, J. Chem. Phys. 83, 4069 (1985)]. A number of 256 atoms at the desired composition are arranged in a cubic box with periodic boundary composition. Only the Γ -point sampling was considered to sample the supercell Brillouin zone. Three temperatures were considered, namely T=700, 600 and 500K, the two latter being in the supercooled regime. For each temperature the typical durations of the runs are 30 ps with a time step of 3fs. The individual motion of the atoms can be followed by using the mean-square displacement: $\langle r^2(t) \rangle$.

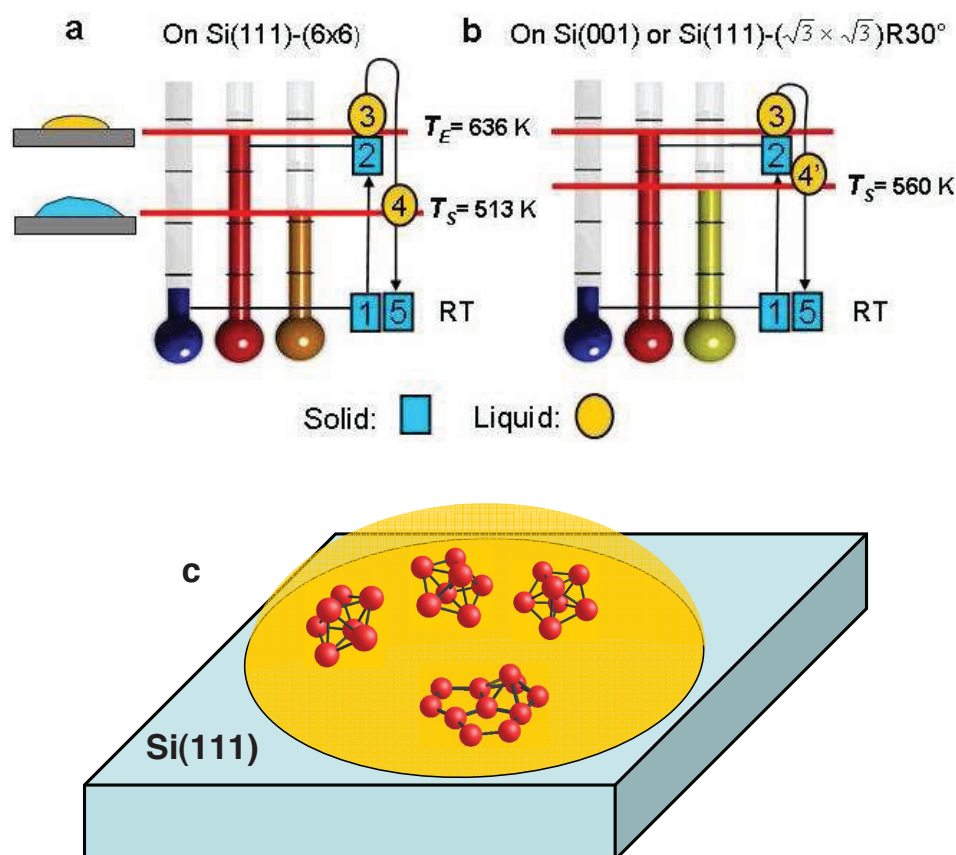
Neighbor analysis of the simulated liquid eutectic

The detailed three-dimensional picture of the local structure was extracted by common-neighbor analysis performed on inherent structures in which atoms are brought to local minima of the potential energy surface by applying a conjugated gradient technique. This method is able to distinguish between various local structures like fcc, hcp, bcc and icosahedral environments, describing them with the nomenclature composed of the four Honeycutt-Andersen indices: the first integer indicates whether or not atoms composing the pair studied are near-neighbors, the second one corresponds to the number of common nearest neighbors shared by the reference pair, the third one is the number of bonds between common nearest neighbors and the last one is used to distinguish structures with the same first three indices but differing from their topology. Considering this, the fcc structure is described by pairs with 1421 indices whereas 1661 and 1441 pairs are typical bcc configurations. Pairs with 1551, 1541, and 1431 indices are five fold symmetry indicators, the 1551 pair describing a perfect fivefold ring and the two last pairs being formed when the perfect fivefold structure is deformed.

doi: 10.1038/nature08986

SUPPLEMENTARY INFORMATION

Supplementary Figure 1:



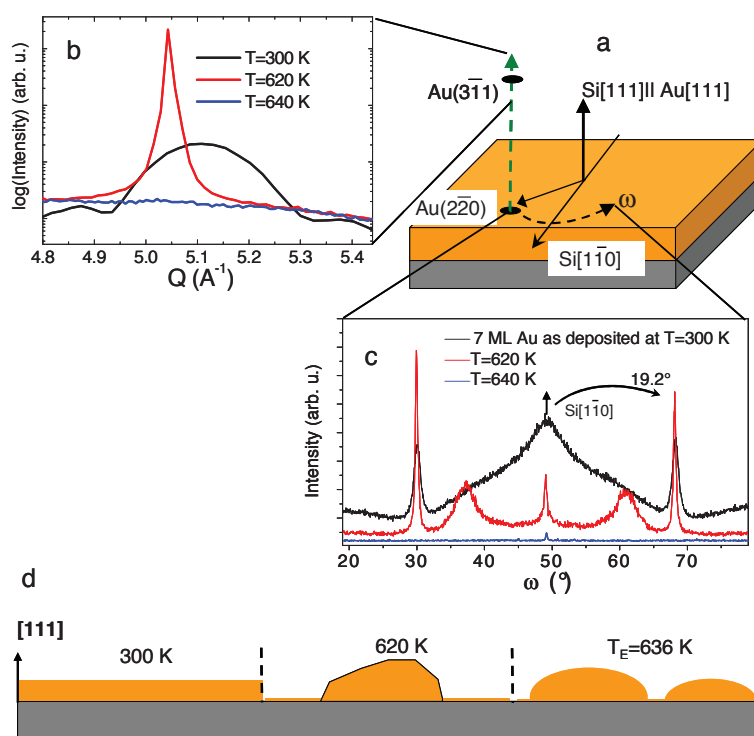
Melting and solidification cycles of AuSi islands on different Si surfaces – influence of the interface structure.

a, Solid-Liquid transition of the Au-Si islands on a Si(111)-(6x6) reconstructed surface. The numbers 1 to 5 refer to successive experimental steps. The blue (yellow) color indicates solid (liquid) islands. The islands are solid (steps 1,2) below the eutectic point at 636 K where melting sets in. Heating up to 673 K (step 3) prior to cooling leads to a preservation of the liquid phase down to 513 K (step 4), where phase separation and solidification occurs (step 5).

b, Solid-Liquid transition of the Au-Si islands on a Si(001) substrate (or a $(\sqrt{3} \times \sqrt{3})R30^\circ$ reconstructed Si(111) surface). The liquid phase is only preserved down to 560-570 K.

c, The pentagonal sites present on the Si(111)-(6x6) reconstructed surface may serve as seeds for icosahedral clusters and induce lateral order stabilisation of the liquid phase inside a AuSi droplet.

Supplementary Figure 2:



a, Sketch of different characterization scans that were performed to follow the evolution of the Au crystal structure during annealing.

b, Scan along the surface normal of the film, crossing the $(3\bar{1}1)_{\text{Au}}$ Bragg point. Its half width is inversely proportional to the thickness of the regarded crystallites. After deposition at room temperature size oscillations confirm the film thickness to be ~ 1.6 nm, as calibrated. Upon annealing at 620 K, 20 nm high crystalline Au islands form. At 640 K all crystalline signals disappear.

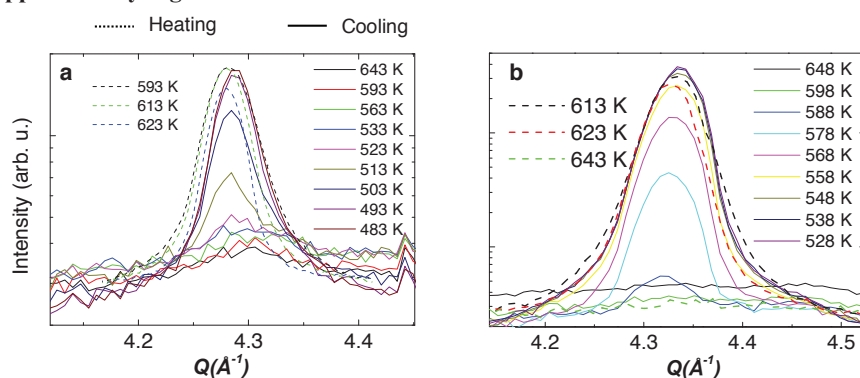
c, The crystallographic orientation in the plane was studied by rocking scans on the $\text{Au}(2\bar{2}0)$ peak, proving that the $[1\bar{1}0]$ axis of Au is oriented preferentially along the $\text{Si}[1\bar{1}0]$ direction. Upon annealing, an in-plane rotation of 19.2° is found, to the preferred epitaxy $[1\bar{1}0]_{\text{Au}} \parallel [2\bar{3}1]_{\text{Si}}$, as well as a growth of these crystallites in size. At the eutectic temperature of 636 K, the islands “melt” via the formation of the $\text{Au}_{81}\text{Si}_{19}$ eutectic.

d, Graphical representation of the different annealing steps followed in (b) and (c). The formation of islands happens prior to melting.

doi: 10.1038/nature08986

SUPPLEMENTARY INFORMATION

Supplementary Figure 3:

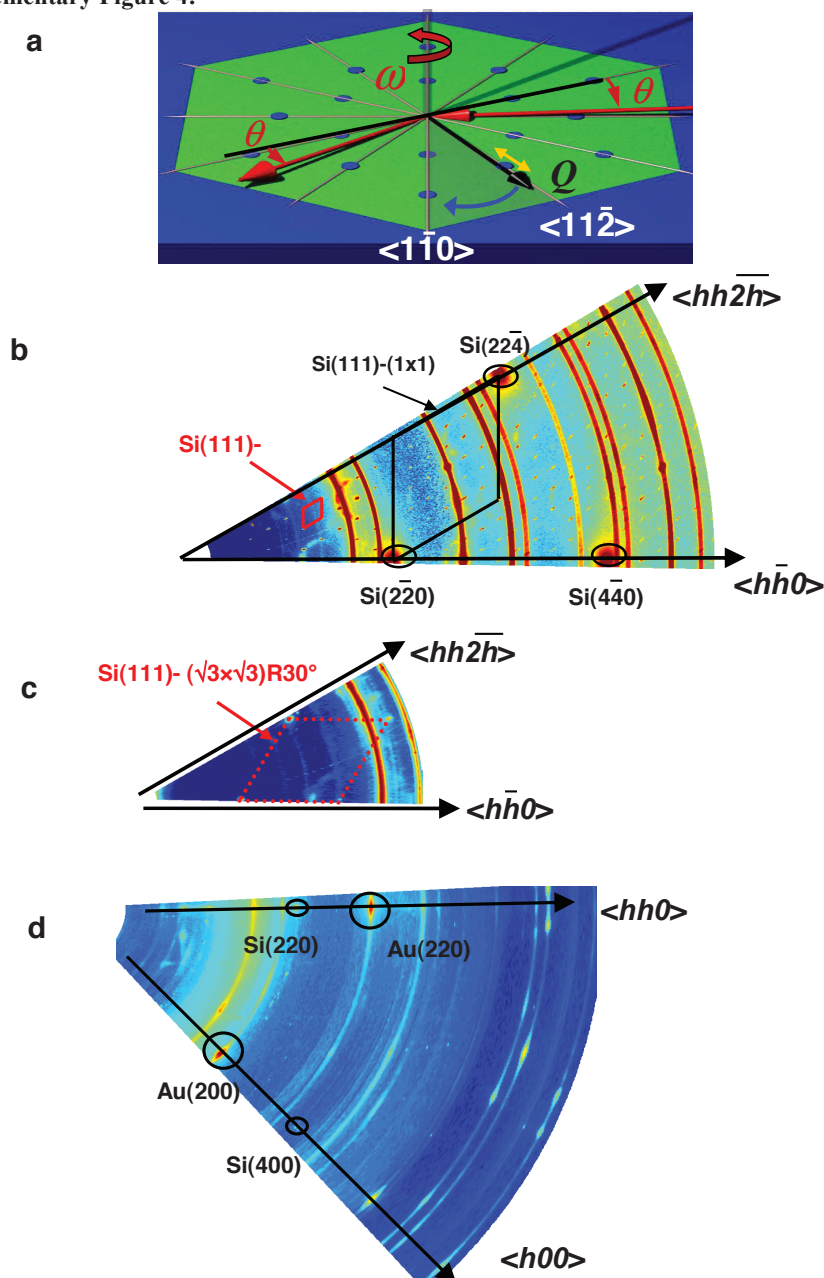


Melting, supercooling and solidification of the AuSi eutectic melt on the Si(111)-(6×6) (a) and Si(001) (b) surfaces.

a, Radial scans through the Au($2\bar{2}0$) Bragg peak for Au-islands on a Si(111)-(6×6) surface. The dashed lines describe the intensity during heating: the islands are still solid at 623 K. After melting at $T_E=636$ K and annealing at $T>673$ K, the islands stay liquid down to 513 K, where the crystalline signal reappears. The broad background that reduces significantly for $T<513$ K is the diffuse scattering by the liquid.

b, The same scenario as in (a) but on a Si(001) surface. Melting occurs for $T>636$ K, solidification sets in at 578 K.

Supplementary Figure 4:



In-plane extended reciprocal space maps at room-temperature on 7ML of Au on the Si(111)-(6 \times 6) (b), the Si(111)- $(\sqrt{3} \times \sqrt{3})R30^\circ$ (c) and Si(001) (d) surfaces.

a, Sketch of the measurement of an extended in plane reciprocal space map (RSM) of a symmetry equivalent section of the Si(111) surface. The incident and exit x-ray beams are

doi: 10.1038/nature08986

SUPPLEMENTARY INFORMATION

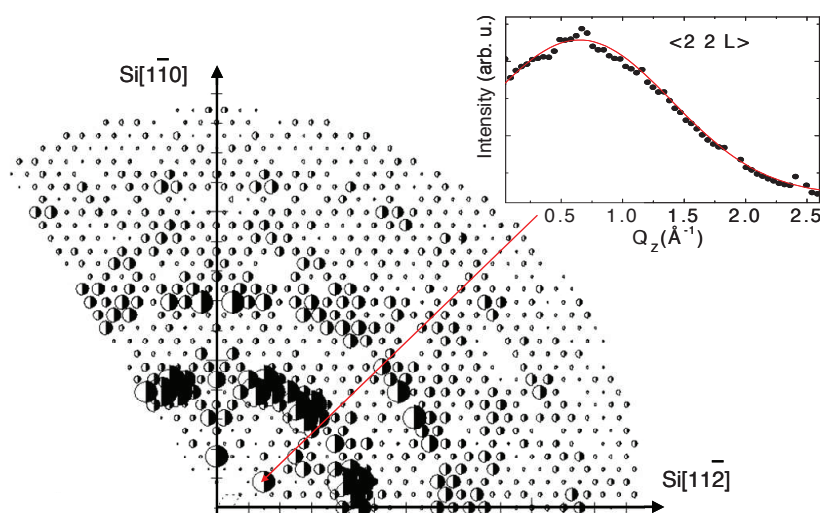
kept grazing with respect to the surface to ensure surface sensitivity. The in-plane momentum transfer Q is varied (yellow arrow) by changing the scattering angle 2θ . At each Q -value, a rocking scan (blue arrow) is performed through a rotation ω of the sample around its surface normal by more than 30° . Bulk Bragg peak positions are indicated by blue dots, together with two high-symmetry directions.

b, 35° angular section of in plane RSM after unmixing and solidification of the supercooled liquid on a (6×6) reconstructed Si(111) surface. Blue color corresponds to low intensity, and red to high intensities, the yellow one being intermediate. Three bulk Bragg peaks are visible, together with a mesh of smaller peaks arising from a surface/interface periodic superstructure. The reciprocal lattice units of the Si(111) surface and of its (6×6) reconstruction are indicated. Diffraction rings from polycrystalline Au are observed.

c, Cooling down the sample right after obtaining a eutectic melt at 636 K (not exceeding a sample temperature of 673 K) leaves a Si(111) surface with a $(\sqrt{3}\times\sqrt{3})R30^\circ$ reconstruction induced by the Au deposit, instead of the (6×6) that forms only after annealing at higher temperatures followed by cooling below 673K. Here a section of 32° of an in plane RSM is shown. The in-plane reciprocal unit cell of the Si(111)- $(\sqrt{3}\times\sqrt{3})R30^\circ$ reconstruction is indicated. The powder diffraction rings corresponding to the Au(111) and Au(200) lattice spacing are visible.

b, following similar procedures on Si(001) leaves an unreconstructed surface. The Au crystals are in a cube on cube epitaxy with the underlying Si substrate.

Supplementary Figure 5:



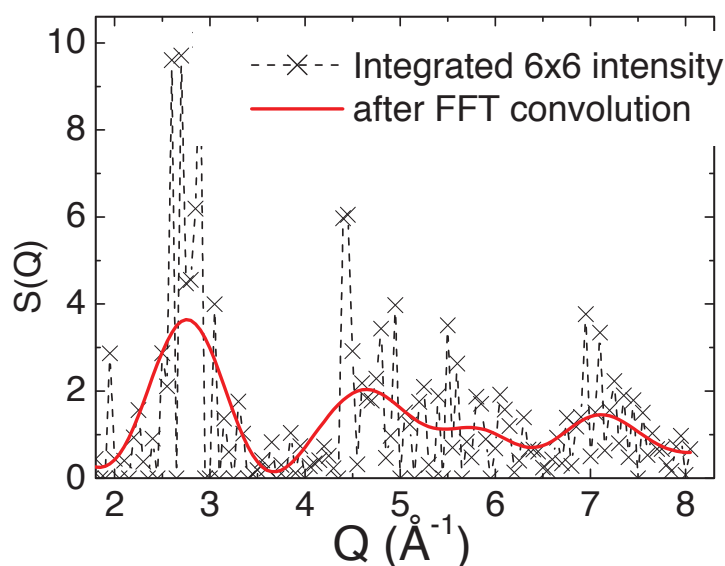
Surface diffraction analysis of the Si(111)- (6×6) reconstruction.

983

in-plane diffraction rods have been quantitatively measured to solve the atomic structure of the Si(111)- (6×6) reconstruction. The measurement covers 120° with $p6mm$ symmetry (systematic error $\sim 4.5\%$) and thus 4 symmetry relevant fractions. The black half disks area (resp. radii) are proportional to the experimental Bragg intensities (resp. structure factors), whereas the white half disks area are representative of the simulated intensities from the fitted structure model. Some reconstruction rods have also been quantitatively measured, along the

surface normal. One is presented to the right as a function of perpendicular momentum transfer. They reveal a thickness of the order of 2-3 Å showing that the structure is of mono-atomic thickness. The final model found is nearly identical to that published by Grozea et al²⁰. If only the top gold monolayer is included (model shown in Fig. 4), the final χ^2 is already 2.8. Including the underlying silicon bilayer improves the fit down to a χ^2 of 1.

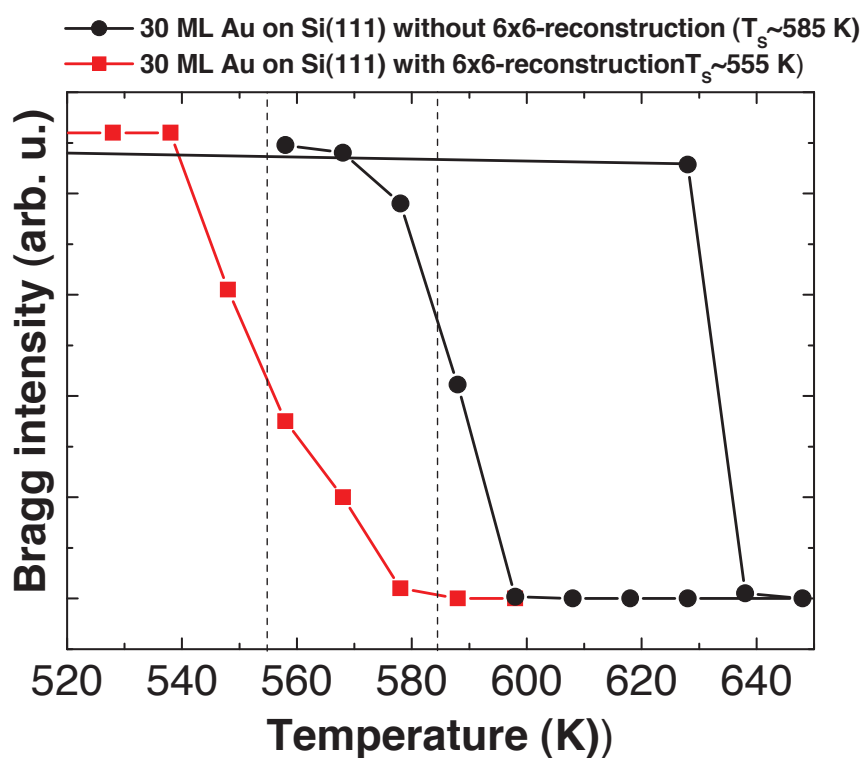
Supplementary Figure 6:



Mean structure factor extraction from the Si(111)-(6×6) reconstruction.

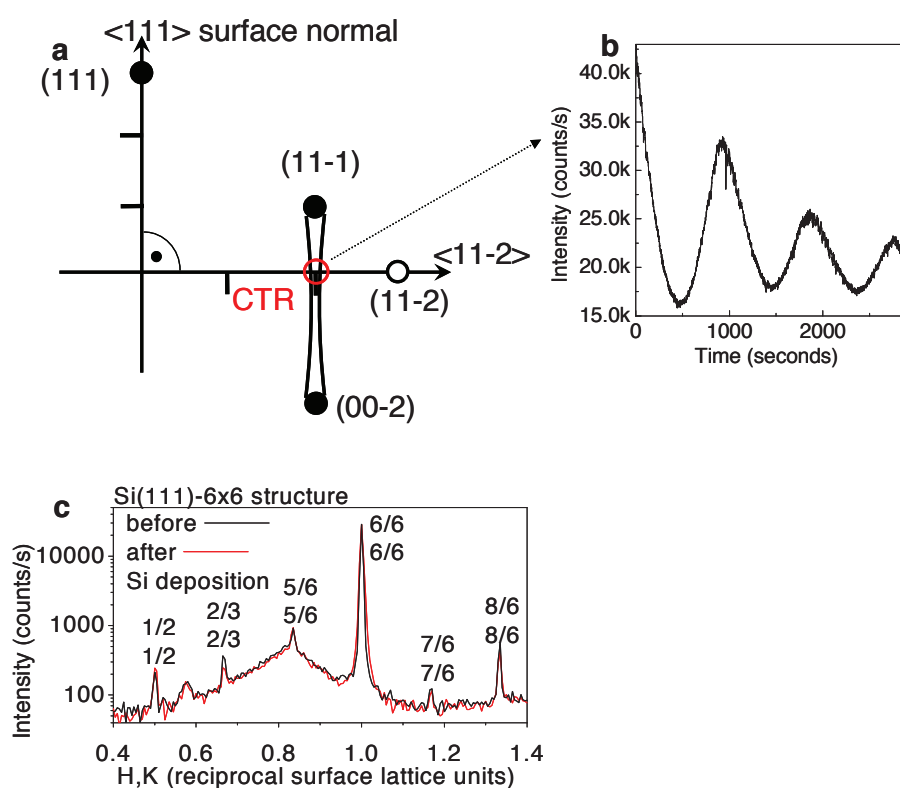
In order to be able to compare the intensity distribution of the liquid with the mean intensity distribution of the Si(111)-(6×6) reconstruction, and thus to show the similarity in local atomic structures, the intensity of all measured (6×6) diffraction peaks was sorted as a function of momentum transfer Q and summed up in intervals of 0.05 \AA^{-1} throughout the whole experimentally accessible range of 8.45 \AA^{-1} resulting in the black crosses. For every interval this sum was normalized taking into account the surface integration element in two-dimensional q -space. To smoothen the discrete characteristics of this curve and keep its representative nature of a one dimensional intensity distribution in reciprocal space, a fast Fourier transform convolution was used to filter out the higher frequency components. The function used consisted in a parabola having its maximum 1 at the origin and falling to zero at 0.5 \AA^{-1} . This treatment was performed using the ORIGIN software (<http://www.OriginLab.com>). The resulting smoothened curve is plotted in red and serves to see where the main maxima are located. It can serve as a guide to the eye for a comparison with a liquid structure factor.

Supplementary Figure 7:

**Solidification hysteresis for a deposit of 30 ML Au on Si(111).**

The influence of the Si(111)-6×6 surface structure is as well present for a 30 ML deposit but the solidification temperature is higher than for the 7 ML deposit. This can be attributed to bigger AuSi islands and thus to a decrease of the interface/volume ratio.

Supplementary figure 8:



Silicon regrowth on a Si(111) surface with a Si(111)-6×6 reconstructed Au-layer .

a, sketch of reciprocal space of a Si(111) surface. Along the $\langle 11\bar{2} \rangle$ in plane direction one crosses the crystal truncation rod (CTR) at the $(\frac{1}{3} \frac{1}{3} \frac{2}{3})$ position. The observed intensity at

this point oscillates during Si-deposition .

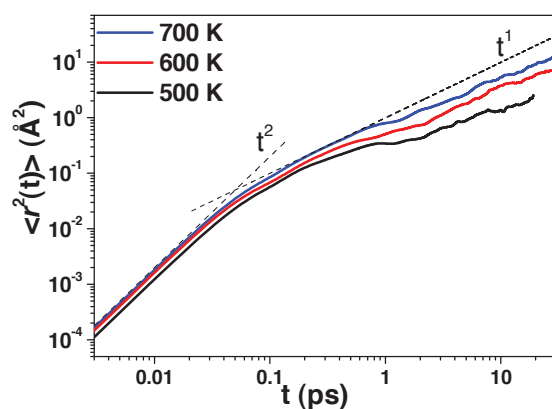
b, the intensity oscillates as a function of Si-deposition at $T=626$ K. These intensity oscillations are a proof for layer-by-layer growth on the Si(111) (see e.g. P. H. Fuoss et al., Phys. Rev. Lett. **63**,2389-2392, (1989).)

c, Reconstruction peaks of the 6x6 structure and first maximum of the liquid AuSi structure factor show no changes before and after the Si layer-by-layer growth.

doi: 10.1038/nature08986

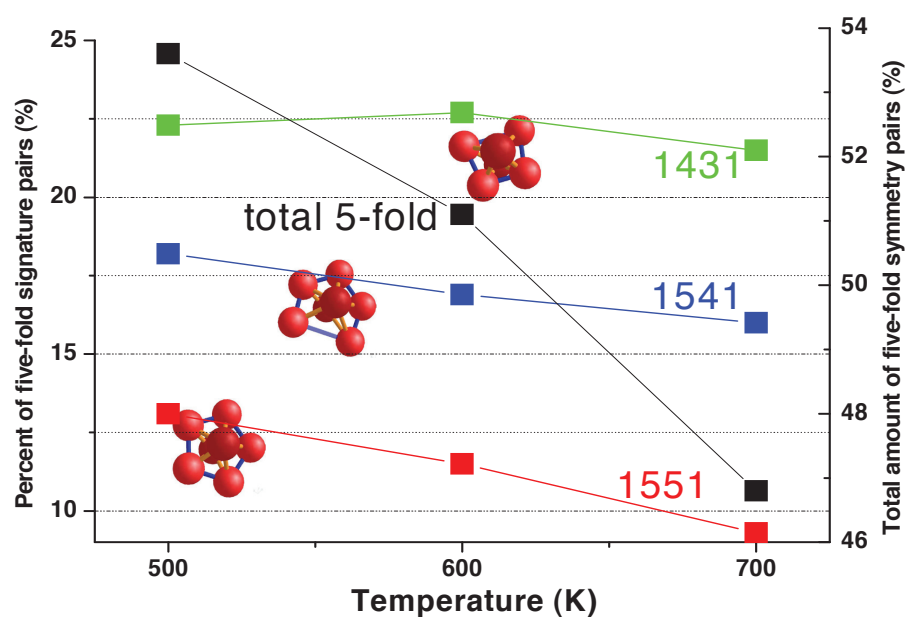
SUPPLEMENTARY INFORMATION

Supplementary Figure 9 :



The mean-square displacement $\langle r^2(t) \rangle$ as deduced from MDS is drawn for the three temperatures ($T=700\text{K}$, 600K , and 500K), revealing three distinctive regimes: a ballistic motion of the atom seen at very short times, in which the atoms motion amplitude evolves as t^2 , is followed by a crossover region, called the cage effect, where the slope of $\langle r^2(t) \rangle$ weakens. The latter is interpreted as a slowing down of the motion of the atoms as they encounter their first neighbors, forming coordination polyhedra whose characteristics are examined below. Finally, at longer times, the atoms enter a diffusive regime in which the mean-square displacement grows linearly with time.

Supplementary Figure 10:



Evolution of the quantity of the different icosahedral signature pairs with temperature. Red, green and blue lines correspond to 1551, 1541 and 1431 clusters respectively, referring to the left axis with typical topology for each one shown on insets. The black line represents the evolution of the total proportion of the five-fold symmetry clusters cited above (1551+1541+1431) referring to the right axis.

3. Supplementary Table

Self-diffusion coefficients estimated in the stable liquid (T=700K) as well as in the supercooled region (T=600K and 500K) from the corresponding velocity auto-correlation functions showing a diffusive regime during the time of the simulations as displayed in Fig. S4, and therefore prove a liquid behavior for the three temperatures.

Temperature (K)	Self-diffusion coefficients ($\text{\AA}^2 \cdot \text{ps}^{-1}$)
700	0.075
600	0.046
500	0.020

5.3 Gas environment and catalytic nanostructures

5.3.1 *Shape Changes of Supported Rh Nanoparticles During Oxidation and Reduction Cycles*

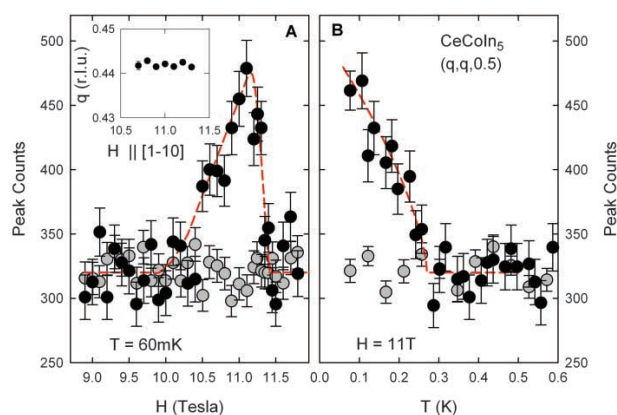
P. Nolte, A. Stierle, N. Y. Jin-Phillipp, N. Kasper, T. U. Schülli, H. Dosch,
Science 321, 1654 (2008).

The efficient oxidation of toxic gases by catalysts in car gas-pipe exhausts is eventually the most commonly known catalytic reaction in every days life. Although catalytic processes are the basis of many large scale industrial processes since one entire century, most of them have been found by trial and error and a fundamental understanding of the driving forces of catalytic reaction is still missing. This makes x-ray *in situ* experiments an extremely valuable tool in the study of catalysis. In the case of CO oxidation as one of the most important reactions in car exhaust devices, costly noble metals are used and thus an optimization of this application is highly desirable. Experience with metallic or oxide catalysts show that catalytic processes roughly scale with the exposed metallic surface. For the case of e.g. iron or copper this is usually obtained using wire wool or sponges. For more precious materials thin coatings are generally used.

as all these materials are used in a polycrystalline way, the catalytic activity of a particular crystal surface orientation cannot be easily deduced. This has inspired experimentalists to investigate catalytic processes on the surface of single crystals. As a catalytic process involves often different steps as adsorption of a molecule, change of oxidation state or morphology and reaction with another molecule, it may be possible that any of the processes favours a different crystal surface. In the following study, epitaxial nanostructures, a few nm in size, have been prepared out of Rhodium. Due to their small size and at elevated temperatures, these were able to slightly adapt their shape and thus the surface ratio between the predominant truncating facet orientations $\langle 100 \rangle$ and $\langle 111 \rangle$. The domination of the $\{111\}$ facets after growth vanishes and the $\{100\}$ facets become more important when oxygen is adsorbed. The exposure to CO, leads to an oxidation of these molecules which in exchange reestablishes the original shape of the islands.

REPORTS

Fig. 3. Neutron-scattering intensity at $(q, q, 0.5)$, (A) as a function of field at $T = 60$ mK and (B) as a function of temperature at $H = 11$ T. The gray circles represent the background scattering taken from the two nearest to the center channels of the psd. The dashed red line in (A) is a guide to the eye, whereas the dashed line in (B) describes the background and the onset of the magnetic order in a second-order phase transition with $\beta = 0.365$ fixed to the critical exponent of the three-dimensional Heisenberg universality class. The inset shows that the q is field-independent.



The intimate link between superconductivity and magnetic order in CeCoIn_5 suggests the presence of a specific coupling between these order parameters (23). The multicomponent magnetosuperconducting phase can be reached via two second-order phase transitions through a suitable path in the H - T phase diagram, which justifies the construction of a phenomenological Landau coupling theory. If one assumes that the superconducting gap at zero field Δ_d has $d_{x^2-y^2}$ symmetry, the possible coupling terms for magnetic fields in the basal plane that preserve time-reversal symmetry and conserves momentum can be written as $V_1 = \Delta_d^* M_q (H_x \Delta_{y-q}^{(5)} + H_y \Delta_{x-q}^{(5)}) + c.c.$, $V_2 = \Delta_d^* M_q (H_x D_x - H_y D_y) \Delta_{-q}^{(2)} + c.c.$, and $V_3 = \Delta_d^* M_q (H_x D_y - H_y D_x) \Delta_{-q}^{(3)} + c.c.$ Here, $(\Delta_{x-q}^{(5)}, \Delta_{y-q}^{(5)})$ belongs to the two-component even-parity Γ_5^+ state, $\Delta_{-q}^{(2)}$ and $\Delta_{-q}^{(3)}$ are the Γ_2^- and Γ_3^- odd-parity states (24), $c.c.$ stands for the complex conjugate of the preceding term, and M_q is the magnetic-order parameter. These additional superconducting order parameters include a finite momentum $-q$. (D_x, D_y) is the gauge invariant gradient. Introducing the magnetic field allows one to couple M_q in linear order to preserve time-reversal symmetry. These combinations allow for a second-order phase transition within the superconducting phase and a first-order transition to the nonmagnetic normal state. For the coupling term V_2 , no magnetic structure is induced for fields $H \parallel [100]$. Given the weak dependence of the Q phase on the magnetic field orientation in the basal plane, our measurements suggest the presence of a V_1 or V_3 coupling term, inducing the finite-momentum even-parity Γ_5^+ state or the odd-parity Γ_3^- state.

This Landau theory shows that incommensurate magnetic order induces a superconducting gap function that carries a finite momentum—the first experimental evidence of a superconducting condensate that carries a momentum. However, we show that this state may not arise purely from Pauli paramagnetic effects and the formation of a new pairing state between exchange-split parts of the Fermi surface, a state commonly known as the FFLO state (16, 17). In the FFLO state, the

pairing state carries a momentum of the Cooper pair that depends on the magnetic field via $|q| = 2\mu_B H / \hbar v_F$, where v_F is the Fermi velocity. However, the inset of Fig. 3A shows that $|q|$ is field-independent in CeCoIn_5 , at odds with this prediction, which indicates that an additional superconducting pairing channel with finite momentum is induced in conjunction with the cooperative appearance of magnetic order.

A superconducting order that carries momentum illustrates the wealth of quantum phases that can exist in solid matter. The important microscopic role of magnetic fluctuations in the formation of Cooper pairs in CeCoIn_5 is self-evident because superconductivity emerges at $H_{c2}(0)$ simultaneously with ordered magnetism.

References and Notes

1. C. Petrovic *et al.*, *J. Phys. Condens. Matter* **13**, L337 (2001).
2. A. D. Bianchi, R. Movshovich, I. Vekhter, P. G. Pagliuso, J. L. Sarrao, *Phys. Rev. Lett.* **91**, 257001 (2003).
3. J. Paglione *et al.*, *Phys. Rev. Lett.* **91**, 246405 (2003).

4. K. Izawa *et al.*, *Phys. Rev. Lett.* **87**, 057002 (2001).
5. N. J. Curro *et al.*, *Phys. Rev. B* **64**, 180514 (2001).
6. R. Movshovich *et al.*, *Phys. Rev. Lett.* **86**, 5152 (2001).
7. A. Vorontsov, I. Vekhter, *Phys. Rev. Lett.* **96**, 237001 (2006).
8. D. Hall *et al.*, *Phys. Rev. B* **64**, 212508 (2001).
9. R. Settai *et al.*, *J. Phys. Condens. Matter* **13**, L627 (2001).
10. A. D. Bianchi *et al.*, *Phys. Rev. Lett.* **89**, 137002 (2002).
11. A. D. Bianchi, R. Movshovich, C. Capan, P. G. Pagliuso, J. L. Sarrao, *Phys. Rev. Lett.* **91**, 187004 (2003).
12. A. D. Bianchi *et al.*, *Science* **319**, 177 (2008).
13. K. Kakuyanagi *et al.*, *Phys. Rev. B* **70**, 047602 (2005).
14. T. Watanabe *et al.*, *Phys. Rev. B* **70**, 020506 (2004).
15. H. A. Radovan *et al.*, *Nature* **425**, 51 (2003).
16. P. Fulde, R. A. Ferrell, *Phys. Rev.* **135**, A550 (1964).
17. A. I. Larkin, Y. N. Ovchinnikov, *Sov. Phys. JETP* **20**, 762 (1965).
18. P. Monthoux, D. Pines, G. G. Lonzarich, *Nature* **450**, 1177 (2007).
19. J. Flouquet *et al.*, *C. R. Phys.* **7**, 22 (2006).
20. B. L. Young *et al.*, *Phys. Rev. Lett.* **98**, 036402 (2007).
21. Materials and methods are available as supporting material on Science Online.
22. C. Stock, C. Broholm, J. Hudis, H. J. Kang, C. Petrovic, *Phys. Rev. Lett.* **100**, 087001 (2008).
23. A. Aperis, G. Varelogiannis, P. B. Littlewood, B. D. Simons, *J. Phys. Cond. Mat.*, in press; preprint available at http://arxiv.org/PS_cache/arxiv/pdf/0804/0804.2460v1.pdf.
24. M. Sigrist, K. Ueda, *Rev. Mod. Phys.* **63**, 239 (1991).
25. Work at ETH was supported by the Swiss National Science Foundation under contract PP002-102831. This work is based on experiments performed at the Swiss spallation neutron source SINQ, Paul Scherrer Institute, Villigen, Switzerland, and was supported by the Swiss National Center of Competence in Research program Materials with Novel Electronic Properties. Work at Los Alamos was performed under the auspices of the U.S. Department of Energy and supported in part by the Los Alamos Laboratory Directed Research and Development program. A.D.B. received support from the Natural Sciences and Engineering Research Council of Canada (Canada), Fonds Québécois de la Recherche sur la Nature et les Technologies (Québec), and the Canada Research Chair Foundation.

Supporting Online Material

www.sciencemag.org/cgi/content/full/1161818/DC1
Materials and Methods
References

16 June 2008; accepted 7 August 2008

Published online 21 August 2008;

10.1126/science.1161818

Include this information when citing this paper.

Shape Changes of Supported Rh Nanoparticles During Oxidation and Reduction Cycles

P. Nolte,¹ A. Stierle,^{1*} N. Y. Jin-Phillipp,¹ N. Kasper,¹ T. U. Schulli,² H. Dosch¹

The microscopic insight into how and why catalytically active nanoparticles change their shape during oxidation and reduction reactions is a pivotal challenge in the fundamental understanding of heterogeneous catalysis. We report an oxygen-induced shape transformation of rhodium nanoparticles on magnesium oxide (001) substrates that is lifted upon carbon monoxide exposure at 600 kelvin. A Wulff analysis of high-resolution in situ x-ray diffraction, combined with transmission electron microscopy, shows that this phenomenon is driven by the formation of an oxygen–rhodium–oxygen surface oxide at the rhodium nanofacets. This experimental access into the behavior of such nanoparticles during a catalytic cycle is useful for the development of improved heterogeneous catalysts.

Many industrial chemicals and fuels are synthesized with the use of heterogeneous, solid-phase catalysts that often

contain metals in the form of nanoparticles (NPs). The direct study of these catalysts is challenging, and model catalysts such as single crys-

tals and vicinal surfaces have been extensively investigated and have provided important insights (1–3). The emerging challenge for fundamental research is to provide a detailed microscopic understanding of the different physical and chemical processes that take place at NPs during catalytic reactions. Although there is a consensus that NPs should exhibit enhanced catalytic activity because (i) they possess an increased number of under-coordinated atoms and (ii) different low-index facets coexist [which should facilitate mass transport and thereby lift kinetic barriers known from single crystal surfaces (4)], it is still an open question as to whether the metallic or the oxidized state of the particle is the catalytically more active phase [Langmuir-Hinshelwood versus Mars-van Krevelen mechanism (5, 6)]. During catalytic cycling experiments, NPs undergo reversible size changes that are associated with cyclic shape changes, material redispersion, and sintering (7, 8).

Among the many catalytically active metals, the 4d transition metals [Ru, Rh, Pd, and Ag (1)] are finding increased use in organic reactions, the synthesis of biologically active compounds under sufficiently mild conditions, and the treatment of contaminated water. Rh is a well-known catalyst for hydrocarbon and CO oxidation, as well as for NO_x reduction in three-way car catalysts (9). Recent experimental and theoretical studies of 4d transition metal single-crystal surfaces carried out near atmospheric pressures suggest that their catalytic activities are related to an ultrathin metal oxide film on the surface (5, 10–12). In the case of Rh, a hexagonal O–Rh–O trilayer structure forms basically independently of the surface orientation whenever the oxygen chemical potential is near that of the bulk oxide (11, 13, 14). To date, it is not clear if such surface oxides do also form on the different facets of NPs and, if so, whether they are relevant in industrial catalysis.

In the past, transmission electron microscopy (TEM) has shown that metal NPs undergo shape changes as a function of the gas composition (15–17). Scanning tunneling microscopy experiments on the top facet of flat NPs have illustrated oxygen-induced superstructures at the edges of different facets (18), and recently, the shape of unsupported Pd and Rh NPs was investigated by density functional theory as a function of the oxygen chemical potential using the Wulff construction (19). The results of these experiments prove that surface oxides stabilize the low-index (100), (110), and (111) facets at chemical potentials near that for bulk oxide formation, which results in an overall rounding of the NPs.

To upgrade our microscopic understanding of the catalytic activity of NPs, the interplay between the shape and size change of the NPs and

the oxidation/reduction process must be established. Here, we report an in situ high-resolution x-ray diffraction (XRD) study of epitaxial Rh NPs on MgO(001) during oxidizing and reduction reactions, which uncovers a reversible facet rearrangement of the NP in direct relation to the formation of oxygen-induced superstructures. From a quantitative analysis of the extended reciprocal-space maps that have been recorded from the Rh nanofacets at elevated temperatures and under varying gas atmospheres, we can access the average NP shape and size with atomic resolution and obtain robust atomic insights into the structure of the surface oxide forming on the facets.

The XRD experiments were performed at beamline BM32 of the European Synchrotron Radiation Facility and at the Max Planck beamline of the Angström Quelle Karlsruhe. The photon energies were 11.04 and 10.5 keV, respectively. The in situ x-ray analysis was complemented by high-resolution TEM (HRTEM) performed on a JEOL 1250 atomic-resolution microscope that is operated at 1250 kV (20).

In the first experimental setup, we deposited the Rh NPs in situ at a substrate temperature of 670 K in the BM32 ultrahigh vacuum (UHV) surface XRD chamber, after cleaning the MgO substrates by sputtering and annealing under oxygen atmosphere (20). After the growth and an initial oxidation/reduction cycle, the sample was annealed at 970 K to achieve the equilibrium shape of the NPs. Wide-angle diffraction reciprocal-space mapping and grazing-incidence small-angle scattering (GISAXS) were performed simultaneously (20). In the second experimental setup, Rh was deposited on MgO in a laboratory UHV chamber, annealed at 870 K, and the sample was subsequently transferred into a portable UHV XRD chamber, which was shipped to the synchrotron radiation facility while maintaining UHV conditions. The epitaxial relation

between the Rh NPs and the MgO substrate was determined from reciprocal-space scans in high-symmetry directions. We find that the Rh NPs grow in a cube-on-cube epitaxy on MgO(001), with an in-plane angular distribution of 1.7° . After the annealing, the average lattice constant of the particles is equal to the bulk value for Rh ($a_{\text{fcc}} = 0.380$ nm, where fcc is face-centered cubic), resulting in a misfit of 9% to the MgO substrate. The particles exhibit a typical size distribution of $\sim 30\%$.

Figure 1A is a schematic view of the NP model together with the four shape parameters N_p , N_T , N_B , and N_E , which can be interrogated by XRD (21). N_p describes the particle diameter given by $a_{\text{fcc}}/\sqrt{2} \cdot N_p$; N_T and N_B describe the number of atomic layers involved in the top and bottom part of the particle, respectively. The parameter N_E gives the number of layers removed from the particle corners to form the side [100] type facets. The extended reciprocal-space maps contain detailed information about the shape and size of nanoscale objects (22). This is illustrated in Fig. 1B, which shows an experimental wide-range reciprocal-space map of the (110) plane taken at 600 K. The (111) Bragg reflection in the center of the map is interconnected with the neighboring Bragg reflections by broad intensity ridges along the [001], $[-1, 1, 1]$, and $[1, -1, 1]$ directions that emanate perpendicularly from the associated facets. The observation and quantitative analysis of these so called “crystal truncation rods” (23) in four symmetry-equivalent directions gives direct evidence for the truncated pyramidal shape of the nano-objects under investigation.

To obtain detailed information on the size and shape of the NPs, high-resolution reciprocal-space maps have been recorded from $(H, K) = (-0.5, 0.5)$ to $(0.5, -0.5)$ and from $L = 0.6$ to 0.84 , as indicated by the white box in Fig. 1B (here, H , K , and L represent the Miller indices of the bulk reciprocal lattice). In Fig. 2A (top) a high-resolution map of

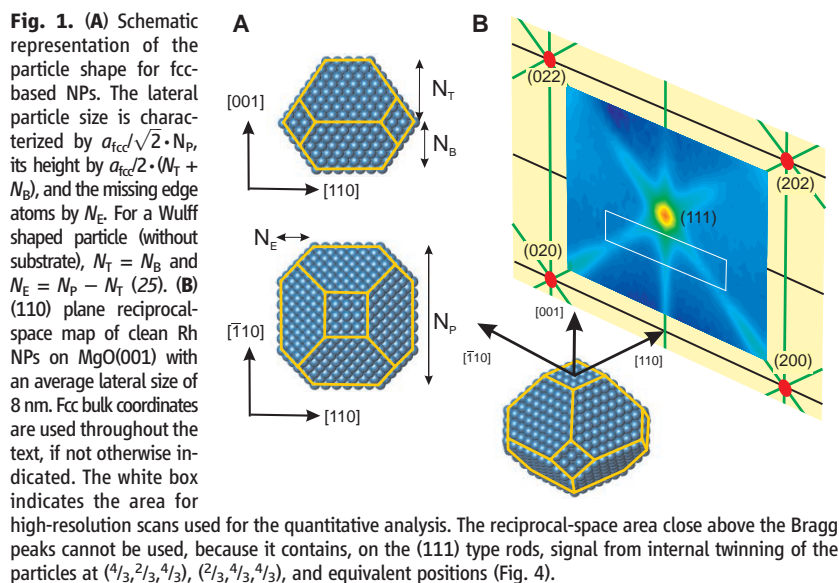


Fig. 1. (A) Schematic representation of the particle shape for fcc-based NPs. The lateral particle size is characterized by $a_{\text{fcc}}/\sqrt{2} \cdot N_p$, its height by $a_{\text{fcc}}/2 \cdot (N_T + N_B)$, and the missing edge atoms by N_E . For a Wulff shaped particle (without substrate), $N_T = N_B$ and $N_E = N_p - N_T$ (25). (B) (110) plane reciprocal-space map of clean Rh NPs on MgO(001) with an average lateral size of 8 nm. Fcc bulk coordinates are used throughout the text, if not otherwise indicated. The white box indicates the area for high-resolution scans used for the quantitative analysis. The reciprocal-space area close above the Bragg peaks cannot be used, because it contains, on the (111) type rods, signal from internal twinning of the particles at $(\frac{4}{3}, \frac{2}{3}, \frac{4}{3})$, $(\frac{2}{3}, \frac{4}{3}, \frac{4}{3})$, and equivalent positions (Fig. 4).

¹Max-Planck-Institut für Metallforschung, Heisenbergstrasse 3, D-70569 Stuttgart, Germany. ²Institut Nanosciences et Cyogénie/Service de Physique des Matériaux et des Microstructures, Commissariat à l’Energie Atomique, Grenoble, 38054 Grenoble Cedex 09, France.

*To whom correspondence should be addressed. E-mail: stierle@mf.mpg.de

REPORTS

the clean particles is plotted, as observed at 600 K under UHV conditions. The data can be understood in a straightforward way within a kinematical diffraction theory that discloses NPs with truncated octahedral shape (20). Figure 2A (middle) shows the best intensity fits associated with the average particle shape presented in Fig. 2A (bottom).

A straightforward understanding of the shape of a NP is provided by the Wulff construction, which is based on the rule $\frac{\gamma_i}{h_i} = \text{constant}$ (here, γ_i is the surface energy of facet plane i with distance h_i from the center of the unsupported particle) (24). From the fit to the data, we obtain the following parameter values: $N_P = 31 \pm 1$, $N_T = 20 \pm 1$, $N_B = 5 \pm 1$, and $N_E = 3 \pm 1$, corresponding to an average NP diameter of 8.3 nm and an average NP height of 4.8 nm. For the ratios of the surface energies, we deduce $\frac{\gamma_{100}}{\gamma_{111}} = \frac{h_{100}}{h_{111}} = \sqrt{3} \cdot \frac{N_T}{N_P} = 1.12 \pm 0.09$ for the top facets, which agrees well with the theoretical value of $(\gamma_{100}/\gamma_{111})^* = 1.16$ (19), but $\frac{\gamma_{100}}{\gamma_{111}} = \sqrt{3} \cdot \frac{N_P - N_E}{N_P} = 1.56 \pm 0.06$ for the side facets (the asterisk indicates theoretical values). This marked deviation from the expected value of $(\gamma_{100}/\gamma_{111})^*$ means that the side facets are noticeably smaller than predicted by the Wulff argument. We suggest that this observation is related to strain and/or NP edge effects (line tensions) neglected in the Wulff approach. The Rh NP adhesion energy $E_{ad} = \gamma_{100} \cdot \frac{N_T - N_E}{N_P} = 108 \pm 10 \text{ meV}/\text{\AA}^2$ (25) is less than the theoretical value $E_{ad}^* = 130 \text{ meV}/\text{\AA}^2$ associated with one extended monolayer of Rh on MgO(001), which is in-line with the trend that the adsorption energy decreases as a function of the Rh coverage (26).

In the next step, the Rh NPs were exposed to 3×10^{-5} mbar O_2 at 600 K [i.e., above the oxygen chemical potential for Rh_2O_3 bulk oxide formation (27)], and we simultaneously recorded the

XRD pattern (Fig. 2, B and C). We observed a distinct change in the XRD signal (see difference map in Fig. 2B) that essentially consists of an intensity enhancement along the (001) rod and an intensity loss along the (111) rods, which can also be observed in the large area difference map in fig. S2B (28). The best fit to this x-ray intensity change (Fig. 2B) results in an average NP shape as characterized by $N_P = 31 \pm 1$, $N_T = 16 \pm 1$, $N_B = 5 \pm 1$, and $N_E = 7 \pm 1$ (Fig. 2C), with an unchanged average NP diameter of 8.3 nm and a reduced average height of 4 nm. These reconfigured Rh NPs now have a nanosized oxide skin composed of an ultrathin hexagonal surface oxide layer, as we explain below.

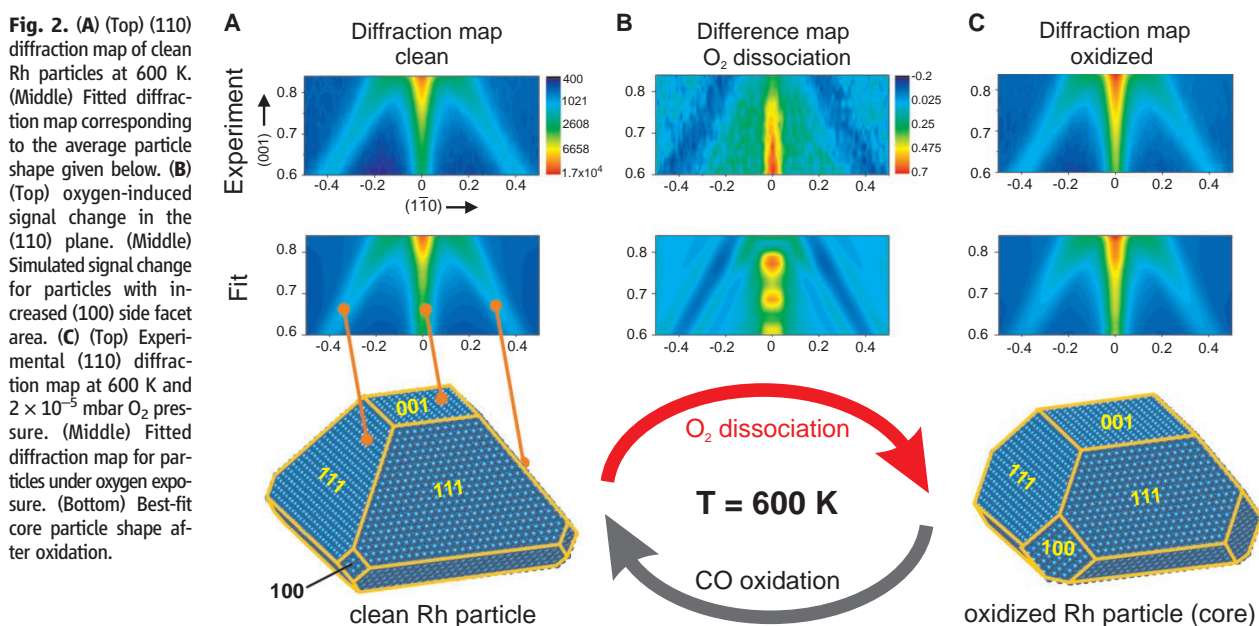
An unexpected result of this analysis is that the area of both the (100) side facets and the (001) top facet increases upon oxidation (29). This result implies that only intraparticle mass transport takes place during oxidation, which removes Rh atoms from the (100) side and top facets with an average amount that corresponds to the number of atoms incorporated into the surface oxide layers on all facets. However, the strong increase of the (110) facet area, which is predicted by theory (19) for the conditions applied, was not observed. Furthermore, no additional facets are formed in between the top (001) and (111) facets (they would readily be observable via additional diffraction intensities).

To get a microscopic insight into the forces that drive this NP shape transformation, we interrogated the atomistic structure of the oxidized (001) and (111) facets by quantitative surface XRD. Figure 3A shows a line scan along the (1, -1, 0) direction ($L = 0.3$) associated with clean NPs and NPs exposed to 2×10^{-5} mbar oxygen at 500 K, which witnesses the formation of an oxygen-induced (3x1) superstructure at the top

(001) nanofacet that progressively disappears upon further oxidation. The intensity of these superstructure reflections cannot be explained by a simple oxygen chemisorption structure; it is rather in line with a shifted-row structure that creates three-fold adsorption sites for oxygen (Fig. 3B). The two-dimensional character of this structure can be inferred from the rodlike diffraction pattern (fig. S4). A similar structure appears during the oxidation of $Pt_{25}Rh_{75}(100)$ single crystals (30) as a precursor for the surface oxide formation on Rh(100) (13).

When the sample temperature was only slightly increased to 550 K, a fast transformation takes place on the (001) top facets from the (3x1) adsorption structure to the hexagonal surface oxide that forms a $c(2 \times 8)$ coincidence structure with the underlying Rh lattice (Fig. 3, C and E) (13). At the same time, on the (111) side facets a hexagonal surface oxide is formed with a $p(9 \times 9)$ coincidence structure. The $c(2 \times 8)$ coincidence structure on the (001) facets and the $p(9 \times 9)$ structure on the (111) facets give rise to additional peaks that can be readily identified (Fig. 3C).

In the presence of the surface oxide on both the (111) and (100) facets, the theoretical value of the surface free energy ratio is lowered to $(\gamma_{100}/\gamma_{111})^* = 0.9$ (19). This value needs to be compared with our experimental data $(\gamma_{100}/\gamma_{111}) = \sqrt{3} \cdot \frac{N_T}{N_P} = 0.89 \pm 0.09$ and $(\gamma_{100}/\gamma_{111}) = \sqrt{3} \cdot \frac{N_P - N_E}{N_P} = 1.34 \pm 0.07$ for the top and side (100) facets, respectively. Thus, the observed increase of the total (100) type facet surface area is in good agreement with the Wulff prediction and can be directly related to the slightly higher stability of the surface oxide on the (100) facets, as compared with the (111) facets. Although bulk oxide formation is thermodynamically favored under the conditions applied (27), the surface oxide at



the Rh nanofacets is metastable and prevents bulk oxide growth.

A further key observation is that the oxygen-induced shape change of the Rh NPs is fully reversible when the surface oxide is removed by CO exposure (at 1×10^{-5} mbar). The observed x-ray intensity line scans (Fig. 3, C and E) obtained after reduction are identical to the clean particle scans, which is evidence for decomposition of the facet oxide layers. Simultaneously, the oxygen-induced intensity change of the scattering from the (111) and (001) facets (Fig. 2B) is reversible, as can be

inferred from the line scans in fig. S3, demonstrating the reformation of the clean particle facets.

Complementary information on the shape of the Rh NPs has been obtained by GISAXS (31), which has been carried out parallel to the above surface XRD experiment and by cross-section HRTEM (20). The observed marginal changes of the GISAXS patterns and associated line scans for two different azimuths confirm that the average particle size does not change during the oxidation and reduction process (fig. S5). The cross-section TEM image (Fig. 4) taken of a Rh

NP on MgO(001) along the (110) direction uncovers a NP shape that corresponds very well with the x-ray results (dashed line in Fig. 4A). We also observed structures with a different periodicity on the particle facets that can be identified as oxide over layers. In some cases (for instance, on the right facet of the particle in Fig. 4A), a one-monolayer-thick oxide layer can be observed with atomic resolution. The zoomed-in view of the white box in Fig. 4A reveals a surface layer on the (111) facet with a different periodicity, a finding that is strongly supported by the simulated TEM image contrast for the O–Rh–O surface oxide trilayer (box in Fig. 4B). The observation that the surface oxide is present, even after exposure of the sample to ambient conditions and the rather destructive TEM specimen preparation, gives us the first evidence for the presence of noticeable kinetic barriers toward bulk oxide formation once the surface oxide is formed.

Our high-resolution in situ oxidation experiments demonstrate that the surface oxide O–Rh–O trilayer stabilizes Rh NPs with low-index facets. We assume that this reversible shape transformation also occurs for smaller particles [as long as they have (111) and/or (100) facets] and that the observed surface oxide formation at the facets of the NPs also takes place in oxidation catalysis involving Rh NPs under technologically relevant conditions.

References and Notes

- G. Ertl, H. Knözinger, F. Schüth, J. Weitkamp, *Handbook of Heterogeneous Catalysis* (Wiley-VCH, Weinheim, Germany, 2008).
- M. D. Ackermann *et al.*, *Phys. Rev. Lett.* **95**, 255505 (2005).
- J. G. Wang *et al.*, *Phys. Rev. Lett.* **95**, 256102 (2005).
- E. Lundgren *et al.*, *Phys. Rev. Lett.* **92**, 046101 (2004).
- B. L. M. Hendriksen, S. C. Bobaru, J. W. M. Frenken, *Surf. Sci.* **552**, 229 (2004).
- C. H. F. Peden *et al.*, *J. Phys. Chem.* **92**, 1563 (1988).
- M. A. Newton, C. Belver-Coldeira, A. Martinez-Arias, M. Fernandez-Garcia, *Angew. Chem. Int. Ed.* **46**, 8629 (2007).
- M. Bäumer *et al.*, *Phys. Chem. Chem. Phys.* **9**, 3541 (2007).
- H. S. Gandhi, G. W. Graham, R. W. McCabe, *J. Catal.* **216**, 433 (2003).
- H. Over *et al.*, *Science* **287**, 1474 (2000).
- J. Gustafson *et al.*, *Phys. Rev. Lett.* **92**, 126102 (2004).
- J. Rogal, K. Reuter, M. Scheffler, *Phys. Rev. Lett.* **98**, 046101 (2007).
- J. Gustafson *et al.*, *Phys. Rev. B* **71**, 115442 (2005).
- C. Dri *et al.*, *J. Chem. Phys.* **125**, 094701 (2006).
- P. L. Hansen *et al.*, *Science* **295**, 2053 (2002).
- G. Rupprechter, K. Hayek, H. Hofmeister, *J. Catal.* **173**, 409 (1998).
- C. R. Henry, *Surf. Sci. Rep.* **31**, 231 (1998).
- K. Hojrup Hansen, Z. Slijvančanin, E. Lægsgaard, F. Besenbacher, I. Stensgaard, *Surf. Sci.* **505**, 25 (2002).
- F. Mittendorfer, N. Seriani, O. Dubay, G. Kresse, *Phys. Rev. B* **76**, 233413 (2007).
- See the supporting online material for details.
- N. Kasper *et al.*, *Surf. Sci.* **600**, 2860 (2006).
- U. Pietsch, V. Holy, T. Baumbach, *High-Resolution X-Ray Scattering* (Springer, New York, 2004).
- I. K. Robinson, D. J. Tweet, *Rep. Prog. Phys.* **55**, 599 (1992).
- G. Wulff, *Z. Kristallogr.* **34**, 445 (1901).
- W. L. Winterbottom, *Acta Metall.* **15**, 303 (1967).
- S. Nokbin, J. Limtrakul, K. Hermansson, *Surf. Sci.* **566–568**, 977 (2004).
- This corresponds to a chemical oxygen potential (19) $\mu = -1.04$ eV, $\mu(\text{Rh}_2\text{O}_3)$ is -1.23 eV.
- Noticeable oxygen-induced lattice distortions lead to intensity asymmetries between the low- Q and high- Q side of the associated Bragg point (where Q is the x-ray momentum transfer). Inspection of fig. S2B shows that this is not observed.

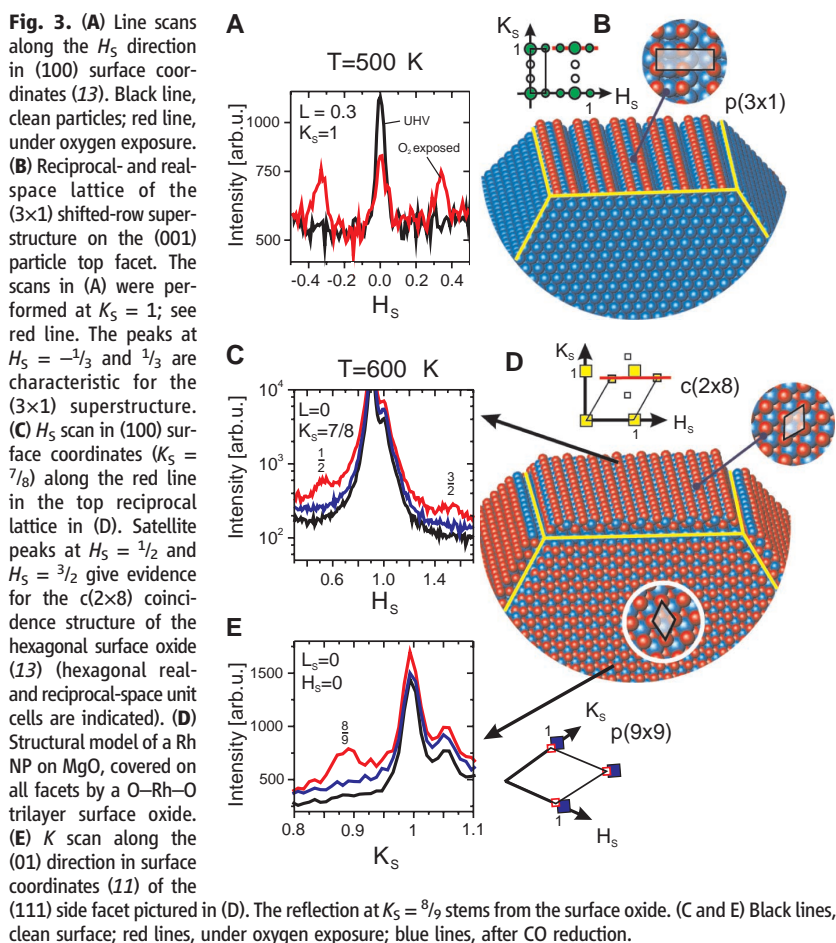


Fig. 4. (A) HRTEM micrograph of a Rh particle on MgO(001) in (110) view. On the left side, close to the substrate, a small twin is present with (111) twinning plane. From the XRD data, we can infer that $\sim 5\%$ of the particles are twinned. The dashed line represents the particle shape derived from the XRD data for the oxidized particles. The white box denotes the zoomed-in area of the surface oxide on (111) facets plotted in (B). (B) Atomically resolved structure of the O–Rh–O trilayer surface oxide on the (111) facets. In the box, a TEM image simulation is plotted as obtained from the structural model in the second inset. The dark spots correspond to Rh atom rows.

REPORTS

29. For slightly larger particles (diameter $D = 9$ nm), the formation of (100) side facet rods, in addition to (110) side facet rods, is observed upon oxidation. The latter is not observed for particles with $D = 8$ nm; for both see fig. S2.
30. M. Sporn *et al.*, *Surf. Sci.* **416**, 384 (1998).
31. G. Renaud *et al.*, *Science* **300**, 1416 (2003).

32. We thank G. Richter and M. Pudleiner for the preparation of Rh/MgO reference samples, N. Jeutter for help with the x-ray experiments, and the European Union for financial support under contract no. NMP3-CT-2003-505670 (NANO2).

Supporting Online Material

www.sciencemag.org/cgi/content/full/321/5896/1654/DC1
Materials and Methods

SOM Text
Figs. S1 to S5
References

22 May 2008; accepted 12 August 2008
10.1126/science.1160845

Polymer Pen Lithography

Fengwei Huo,^{1,2*} Zijian Zheng,^{1,2*} Gengfeng Zheng,^{1,2} Louise R. Giam,^{2,3}
Hua Zhang,^{1,2,†} Chad A. Mirkin^{1,2,3,‡}

We report a low-cost, high-throughput scanning probe lithography method that uses a soft elastomeric tip array, rather than tips mounted on individual cantilevers, to deliver inks to a surface in a “direct write” manner. Polymer pen lithography merges the feature size control of dip-pen nanolithography with the large-area capability of contact printing. Because ink delivery is time and force dependent, features on the nanometer, micrometer, and macroscopic length scales can be formed with the same tip array. Arrays with as many as about 11 million pyramid-shaped pens can be brought into contact with substrates and readily leveled optically to ensure uniform pattern development.

Lithography is used in many areas of modern science and technology, including the production of integrated circuits, information storage devices, video screens, microelectromechanical systems (MEMS), miniaturized sensors, microfluidic devices, biochips, photonic bandgap structures, and diffractive optical elements (1–6). Generally, lithography can be divided into two categories on the basis of patterning strategy: parallel replication and serial writing. Parallel replication methods such as photolithography (7), contact printing (8–11), and nanoimprint lithography (12) are useful for high-throughput, large-area patterning. However, most of these methods can only duplicate patterns, which are predefined by serial writing approaches and thus cannot be used to arbitrarily generate different patterns (i.e., one photomask leads to one set of feature sizes for a given wavelength). In contrast, serial writing methods—including electron-beam lithography (EBL), ion beam lithography, and many scanning probe microscopy (SPM)-based methods (13–16)—can create patterns with high resolution and registration but are limited in throughput (17, 18). Indeed, only recently have researchers determined ways to use two-dimensional cantilever arrays for dip-pen nanolithography (DPN) to produce patterned structures made of molecule-based materials over areas as large as square centimeters (19, 20).

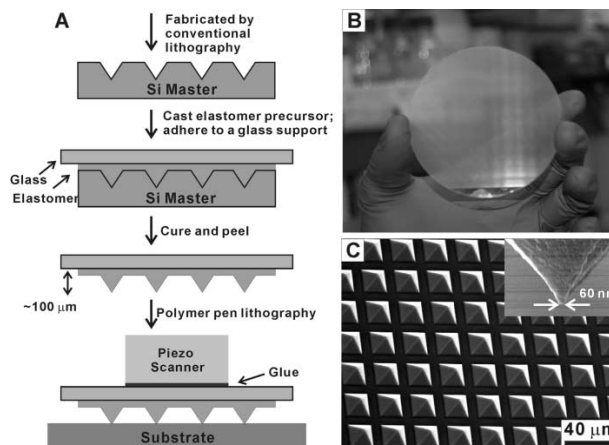
DPN uses an “ink”-coated atomic force microscope (AFM) tip to deliver soft or hard materials (e.g., molecular inks, nanoparticles, or sol gels) to a surface with high registration and sub-50-nm resolution in a “constructive” manner (3, 16, 21–23). When combined with high-density cantilever arrays, DPN is a versatile and powerful tool for constructing molecule-based patterns over relatively large areas with moderate throughput (1). The limitations of DPN are (i) the inability to easily and rapidly work across the micro- and nanometer-length scales in a single experiment (typically, either sharp tips are optimized to generate nanoscale features or blunt tips are used to generate microscale features) (24) and (ii) the need for fragile and costly two-dimensional cantilever arrays to achieve large-area patterning. Indeed, no simple strategy exists that allows one to rapidly pattern molecule-based features with sizes ranging from the nanometer to millimeter scale in a parallel, high-throughput, and direct-write manner. We report the development of polymer pen lithography (PPL), a low-cost, cantilever-free lithographic approach that, thus far, allows a digitized pattern

to be printed at spot sizes ranging from 90 nm to hundreds of μm simply by changing the force and time over which the ink is delivered.

In contrast with DPN and other SPM-based lithographies, which typically use hard silicon-based cantilevers, PPL uses elastomeric tips without cantilevers [typically polydimethylsiloxane (PDMS)] (25, 26) to deliver ink. A typical polymer pen array (Fig. 1) contains thousands of pyramid-shaped tips that are made with a master prepared by conventional photolithography and subsequent wet chemical etching (fig. S1) (27). The pyramids are connected by a thin PDMS backing layer (50 to 100 μm thick) that is adhered to a glass support before curing. The glass support and thin backing layer significantly improve the uniformity of the polymer pen array over large areas, to date up to an entire 3-inch (76.2-mm) wafer surface (Fig. 1B and fig. S2) (27). When the sharp tips of the polymer pens are brought into contact with a substrate, ink is delivered at the points of contact (Fig. 1A). An important feature for ensuring uniform ink delivery over large areas is that the amount of light reflected from the tips increases greatly when the tips make contact with the substrate (movie S1) (27). Thus, the transparent elastomer polymer pen array allows us to determine visually when all of the pens are in contact with an underlying substrate. The otherwise daunting task of leveling the array can be tackled in an experimentally straightforward manner.

We performed our PPL experiments with an Nscriptor system (NanoInk, Skokie, IL) equipped with a 90- μm closed loop scanner and commercial lithography software (DPNWrite, DPN System-2, NanoInk, Skokie, IL). Depending on intended use, the pitch of a pen array is deliberately set between 20 μm and 1 mm,

Fig. 1. (A) A schematic illustration of the polymer pen lithography setup. (B) A photograph of an 11-million-pen array. (C) Scanning electron microscope image of the polymer pen array. The average tip radius of curvature is 70 ± 10 nm (inset).



¹Department of Chemistry, Northwestern University, 2145 Sheridan Road, Evanston, IL 60208–3113, USA. ²International Institute for Nanotechnology, Northwestern University, 2145 Sheridan Road, Evanston, IL 60208–3113, USA. ³Department of Materials Science and Engineering, Northwestern University, 2145 Sheridan Road, Evanston, IL 60208–3113, USA.

*These authors contributed equally to this work.

†Current address: School of Materials Science and Engineering, Nanyang Technological University, 50 Nanyang Avenue, Singapore 639798, Singapore.

‡To whom correspondence should be addressed. E-mail: chadnano@northwestern.edu

Chapter 6

Outlook

Observing the growth of complex systems

With the intention of monitoring different processes, reactions and kinetics, x-rays found their place as an *in situ* tool, useful during the growth and synthesis of nanostructures. The examples presented in chapter 5 are furthermore underlining the strength of x-rays concerning the tolerance of sample environments and when probing phase transitions. The progressing availability of synchrotron radiation as well as the increase of the user community is bringing together more and more competences from different fields. This has definitely pushed the use of x-rays and the number of annual publications concerning the *ex situ* characterization of semiconductor nanostructures. Compared to widely available electron-based *in situ* methods as reflection of high energy electron diffraction (RHEED) or low energy electron diffraction (LEED), as well as microscopy methods, x-rays in the form of synchrotron radiation still will represent a more limited accessibility. The use of x-rays scattering during gas-source growth or while monitoring chemical reactions will certainly be a topic of central interest in the years to come. While a major installation for metal organic chemical vapour deposition (MOCVD) of III-V semiconductors operates at the advanced photon source (APS) in Argonne/USA since several years, similar installations eventually offering higher material and process flexibility seem to be an interesting option for current developments or refurbishment on existing synchrotrons in Europe. A major motivation may lie in the growing interest on semiconductor nanowires which require, several growth and preparation steps involving solid, liquid and gaseous phases. These growth procedures may require solid state MBE deposition of small metal catalysts followed by a CVD process to bring in the semiconductor elements. Compared to MBE deposition of thin films or SK-grown islands, these procedures are more difficult to describe by theoretical models and thus conclusive simulations of the atomistic growth process seem almost unreachable. *In situ* studies thus seem to be of importance and may even be the only method to understand and utilize the driving forces for nanowire formation. To trace an atomistic picture of the growth, *in-situ* TEM [21] may be used at very low gas pressures, otherwise, under standard CVD conditions, x-rays seem to be best suited as a probe of the structure of liquid catalysts, solid nanowires and the growth front at the same time. On beamline BM32 at the ESRF in Grenoble, a project aiming at the *in situ* observation of nanowire growth funded in the framework of the *fondation*

nanosciences [22] is currently being realized. The *in situ* CVD system is in the commissioning phase and consists of four gas lines.

As a central point in this project a UHV-compatible CVD gas injection system for a variety of process gases has been installed, allowing a quick change from UHV growth (e.g. during surface preparation and metal catalyst deposition) to CVD growth (wire/heterostructures growth). This extension to the previous instrument allowing for MBE and CVD growth whilst applying x-ray scattering methods on a powerful synchrotron source is the only of its kind in Europe and, in terms of flexibility, worldwide. Figure 6.1 schematically shows the different steps of the wire fabrication and the various parameters accessible by *in situ* x-ray scattering during the growth for the example of SiGe-wires based on MBE-grown Au-catalysts and silane/germane as process gases.

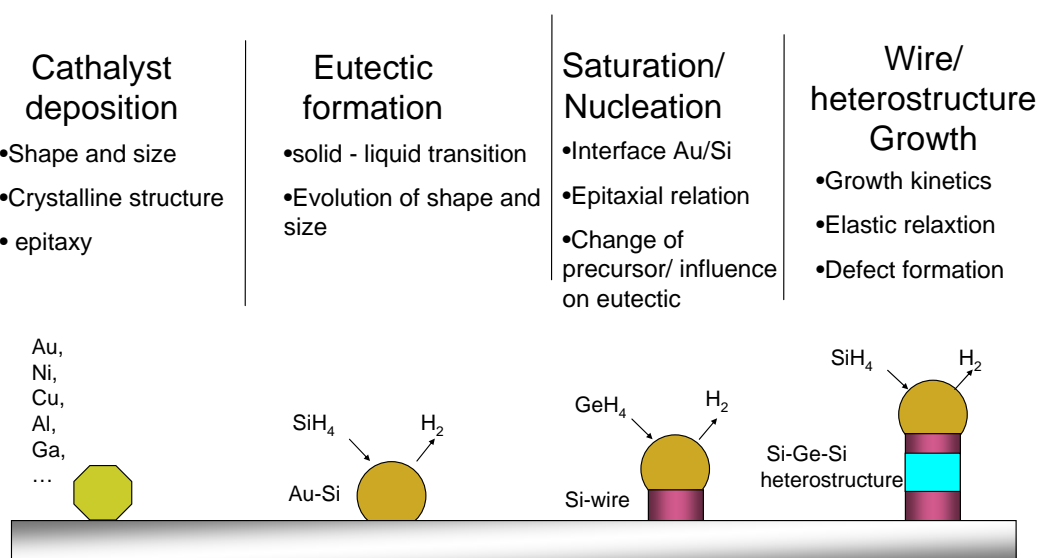


Figure 6.1: Overview of the accessible parameters *via in situ* x-ray scattering during different stages of the catalytic growth of SiGe nanowires on Si(111). (a): deposition of the metallic catalyst. (b) Exposure to silane (SiH₄), causes to the catalyst to crack the molecules, release the hydrogen and form a liquid phase eutectic. (c): After saturation of the eutectic, Si nucleates on the Si-surface and forms a Si-wire. (d) Alternative exposure to SiH₄ and GeH₄ causes the growth of a heterostructure inside the wire.

The establishment of this method will certainly also lead to an extension of the complexity of

the investigated wire systems. Heterostructures of group IV semiconductors and, in a later stage of the project, semiconductors of III-V nitride type will certainly be in the focus of interest.

With the installation of the UHV-CVD equipment, the CBE-Vapour liquid solid (VLS) transition will be investigated in detail. Here, x-ray diffraction definitely offers a tool yielding unequaled information about details and kinetics of this process. These range from extreme sensitivity to the solid-liquid transition up to stages of solidification and epitaxial relationship. Diffraction yields the possibility to follow in detail the formation of eutectics. As shown in section 5.2 this point may be of major interest, especially as the use of compatible metal catalysts is a key problem for applications of nanowires. Because Au is detrimental to Si semiconducting properties, efforts to search for alternative metals as catalysts, such as Al, Ga, Cr or Ni will certainly occupy the field of structural research on nanowires. In parallel projects studying other CVD growth processes are starting up. Among such projects are the CVD deposition of graphene layers (work in progress), while observing their commensurate or coherent adhesion to the surface potential of metals or insulators. In the mid-term future, other carbon based systems may be of interest as the CVD growth of SiC or Diamond. Both materials are troubled by the formation of dislocations during growth, a problem that can be analyzed by *in situ* diffraction as demonstrated in section 2.4.

In conclusion apart from studying growth of nanowires, a combined instrument allowing for *in situ* studies of MBE and CVD growth will also allow for experiments that attack fundamental questions of surface chemistry and the growth dynamics from gas atmospheres. The request for new investigation tools in this field is already at present of major impact. It will further increase with the boiling activity concerning CVD growth of nanowires.

Chapter 7

Appendix: Supercooling and science in school

The phenomenon of supercooling has been subject to numerous investigations using x-rays or neutron diffraction in order to try to create a link to the existence of icosahedral short range order. As such five fold symmetry clusters are predicted by theory, the resulting diffraction patterns were frequently simulated and compared to the scattered intensity distribution of liquids. The first direct link traced between pentagonal order and supercooling was supplied by the study presented in 5.2. It triggered a wide interest in international newspapers and initiated discussions about the presences of the phenomenon in daily life. This was at the origin of popular scientific animation and discussion about supercooling in television and journals. The most complete work in this context is presented in this appendix that includes an invited article for the magazine *Science in School* [23]. It has free online access and its print version is available to all European high schools as a science teaching support.

The stability of different states of matter and the metastability of liquids
Science in School 17, 17 (2010).

Science is cool... supercool

Tobias Schüllli

Science in School **17,17** (2010).

The following pages resume on the different states of matter and the phase transitions in between them. The phenomenon of metastability is explained at the example of supercooling. Supercooling can have its origin in the nucleation barrier present for homogeneous nucleation. This can be easily demonstrated in the classroom by using supercooled water prepared in a freezer. Deep supercooling in metals is better explained by the presence of an internal structure of the liquid presenting 5-fold order and hindering solidification in the form of a crystal.

Cutting-edge science

Science is cool... supercool

When we cool something below its freezing point, it solidifies – at least, that’s what we expect. **Tobias Schüllli** investigates why this is not always the case.

How is it possible that clouds at high altitude, at a temperature lower than 0 °C, consist of tiny droplets of water instead of ice? Actually, under certain conditions, liquids can remain liquid well below their melting point. Although this phenomenon, known as supercooling, was discovered in 1724 by Daniel Gabriel Fahrenheit (Fahrenheit, 1724), it is still the subject of much research.



- ✓ Physics
- ✓ Ages 13-18

One of nature’s strange phenomena is that, for some substances, the melting point is not always the same as the freezing point. In this article, Tobias Schüllli leads us into the world of condensed matter; he introduces the differences between the states of matter, and provides an explanation of this apparent anomaly: supercooling.

The article can be used in various ways as a teaching aid. Teachers could get their students to read the article and then initiate a classroom discussion, not only about changes in states of matter but also about modern research methods in the field of condensed matter physics. To ensure that the students had understood the text, the teacher could question them, for example about conditions of crystal growth.

The article could also inspire some readers to develop their own educational material on the topic of supercooling.

Furthermore, the simple classroom activity in the article may demonstrate to students that it is not only temperature that determines the state of matter.

Vangelis Koltsakis, Greece

REVIEW

The different states of matter

For scientists, the liquid phase is a curious state of matter between order and disorder. The disordered state of matter is well illustrated by the perfect gas: the thermal movement of the individual atoms (or molecules) is so important that the attractive forces between them play no role and they move freely through space. At the other extreme, in the solid state, every atom remains at a fixed site, tightly bound to its neighbours. Driven by

the optimisation of chemical bonds and binding energies, this generally leads to the densest packing of the atoms, in a repeated three-dimensional arrangement, which is called a crystal. Therefore, what we call a solid is in fact, most of the time, a crystalline solid.

In the liquid – intermediate – state, the neighbouring atoms touch each other as in the solid state (both states are thus referred to as *condensed matter*), but the individual atoms can

migrate around, inhibiting the formation of the perfect regular pattern of a crystal. The density of a liquid (compared to a gas) thus differs very little from that of the solid state (see Figure 1).

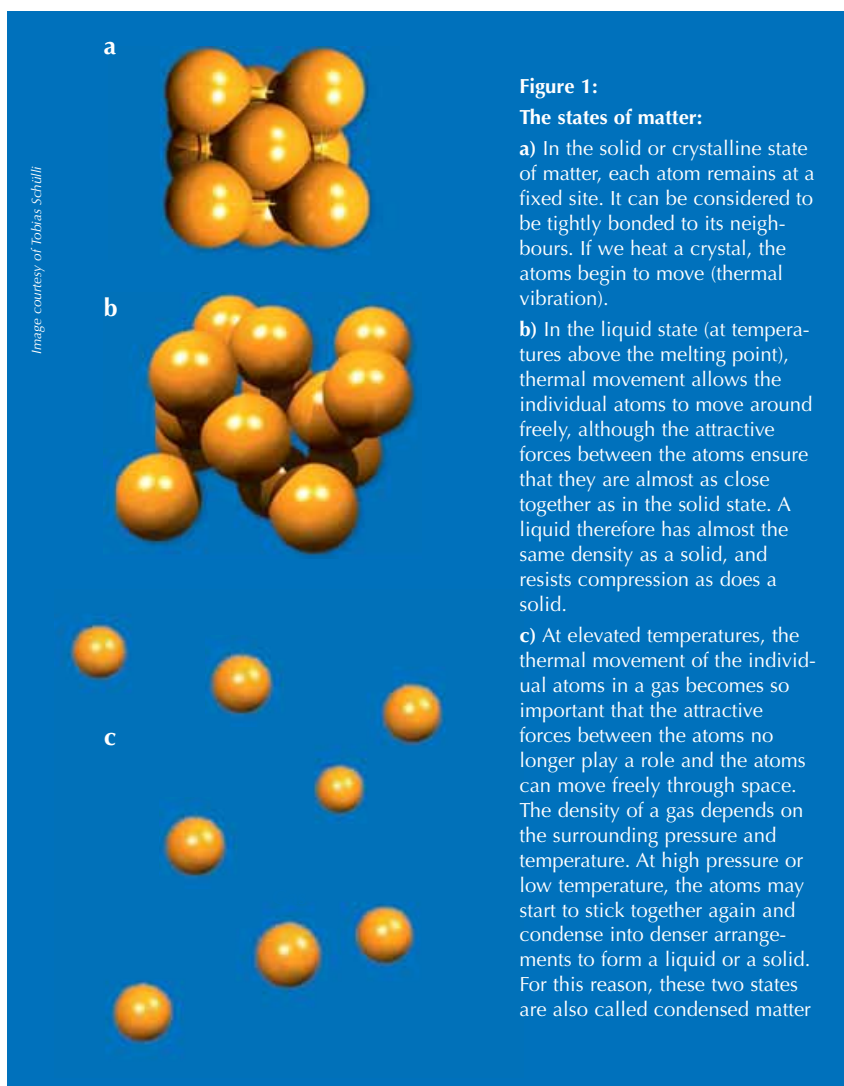
Although a liquid is considered to be mainly disordered, atoms may arrange themselves locally in small clusters, giving rise to the notion of *local order*. The exact nature of these states of local order is very difficult to observe experimentally, but is believed to play a crucial role in the transition of a substance from a disordered phase to an ordered one.

Whether a particular substance is in the gaseous, solid or liquid phase depends on the temperature and pressure. Ice at atmospheric pressure will melt at 0 °C, mercury at -39 °C and gold at 1064 °C. As they get warmer, solids (crystals) melt at exactly these temperatures. However, the opposite is not true: when a liquid is cooled to its melting point, the formation of a crystal is possible but does not necessarily happen at exactly the melting point (Figure 2). In the striped area of the figure, a pure liquid (with no crystalline impurities) will remain liquid. We say that the liquid is supercooled. This state of matter is said to be *metastable* (Figure 3).

How can we explain supercooling?

The first explanation of supercooling lies in the physics of crystallisation. The formation of a crystal requires a nucleus of regularly arranged atoms, around which the crystal can grow. Crystallisation most commonly occurs when the liquid is in contact with a solid surface or when the liquid contains crystalline impurities; it is as if the liquid mimics the ordered structure of the neighbouring surface. This is called *heterogeneous nucleation*, starting from a *seed*.

In the absence of a crystalline solid, the spontaneous formation of a large and regular structure from the disor-



Cutting-edge science

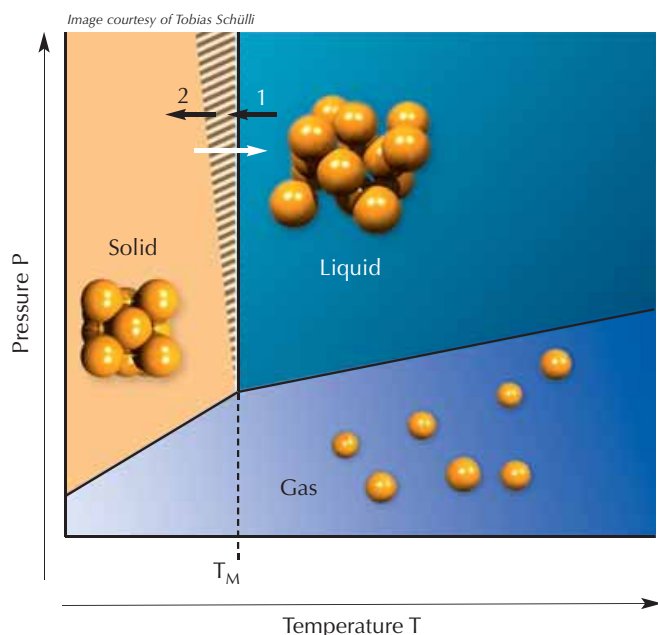


Figure 2: Phase transitions. When the temperature is raised, the solid (crystal) melts, transforming into a liquid (white arrow) at exactly the melting point, T_M . When the liquid is cooled below T_M (black arrow 1), solidification is possible but does not necessarily occur. In the striped area, a pure liquid (with no crystalline impurities) will not solidify. If the liquid is cooled further, it will solidify (black arrow 2)

dered liquid is unlikely. Although small numbers of atoms may spontaneously form a regular arrangement, these clusters are usually too small to serve as crystallisation nuclei, and quickly re-dissolve in the liquid. A pure liquid, therefore, needs to be significantly supercooled before *homogeneous nucleation* occurs: a few atoms in the liquid spontaneously order in the right manner to form a crystal that is large and stable enough to serve as the nucleus for further crystal growth (Figure 4).

Most of the tiny droplets of water which constitute stratiform and cumulus clouds do not contain any seed crystals; these droplets can remain liquid well below 0°C .

Deep supercooling in metals

Even more spectacular than water, which can be supercooled only about

40 degrees below its melting point of 0°C , are metals, which can exist as liquids at several hundred degrees below their melting point. This is known as *deep supercooling* and has challenged scientists to go beyond the crystal nucleation theory to explain the metastability of liquids (Turnbull, 1952).

Scientists have speculated that the internal structure of some liquids could be incompatible with crystallisation. In the 1950s, Frederick Charles Frank suggested that the densest arrangement of a small number of atoms may be different to the local arrangement of atoms in a crystal, and that these clusters in a liquid are therefore ordered in the wrong way to serve as a crystallisation nucleus (Frank, 1952).

As a model, Frank used the icosahedron: a central atom with twelve sur-

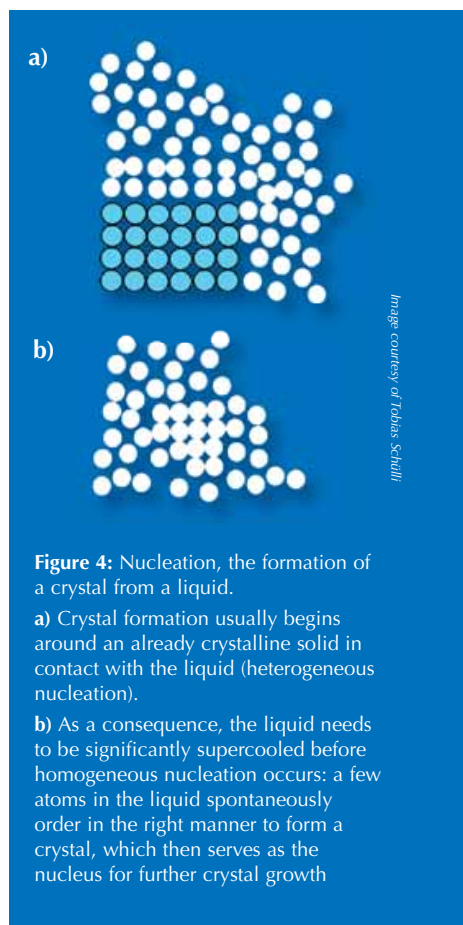
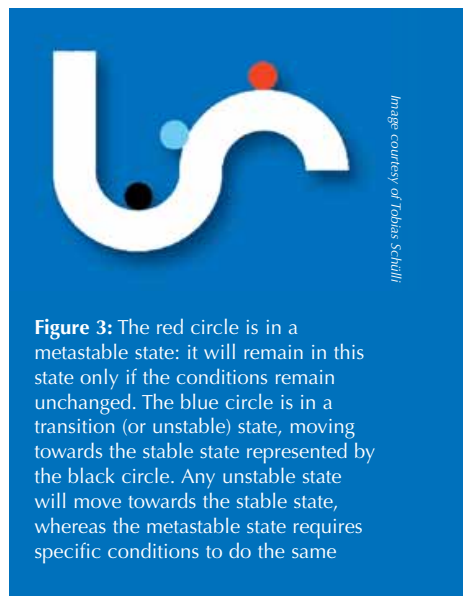


Image courtesy of Nicola Graf

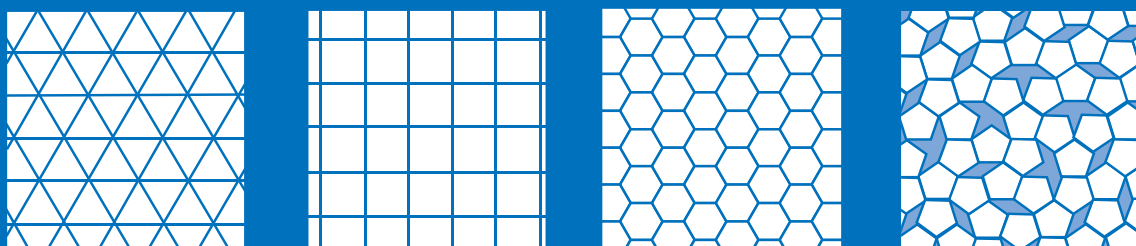


Figure 5: Triangles (three-fold symmetry), squares (four-fold symmetry) and hexagons (six-fold symmetry) can fill a plane perfectly, whereas pentagons (five-fold symmetry) cannot

rounding atoms. Such a structure, which has a pentagonal symmetry, cannot form the basis of a crystal. Generally, a crystalline structure has to repeat in three dimensions, like bricks in a wall. A cubic arrangement, for example, is an excellent structure for a crystal, as it is both dense and perfectly regular.

Using a two-dimensional comparison, triangles, rectangles or hexagons

can fill a plane perfectly, whereas pentagons cannot (Figure 5). In three dimensions, pentagonal structures are incompatible with the formation of a crystal (Figure 6).

Recent simulations and theoretical models support Frank's idea, suggesting that a significant fraction of the atoms in liquids arrange themselves in clusters with five-fold symmetry, thus presenting an obstacle to crys-

tallisation. So far, however, very few experiments have allowed the visualisation of pentagonal symmetry in liquids (Reichert et al., 2000).

Supercooling in semiconductor nanostructures

My own encounter with the phenomenon of supercooling was not really intentional. Actually, the focus of my research, within a team at the



CLASSROOM ACTIVITY

Experiment with supercooling

Place an unopened bottle of still mineral water in the freezer for 1–2 hours. After this time, the water should be around -10 to -5 °C. Because the water should have no solid impurities in it, it should still be liquid even at this temperature – it is supercooled.

Carefully remove the bottle from the freezer, then hit it on the table or with your hand. You should be able to see that the water crystallises (freezes), with the ice formation progressing very quickly through the whole bottle. The crystallisation is triggered by the shock wave travelling through the liquid. (The shock wave is another possible explanation of why aeroplanes leave a visible trail of water crystals behind them.)

This can only be achieved in liquids that do not contain seeds that may provoke crystallisation. It is

unlikely to work with tap water, which may contain crystalline impurities that trigger crystallisation closer to the melting (freezing) point of water.

Note: do not leave the bottle in the freezer for too long, because once the water gets below -10 to -5 °C, it will freeze, even if there are no crystalline impurities.



Images courtesy of Tobias Schüll

Cutting-edge science

Images courtesy of Tobias Schülli

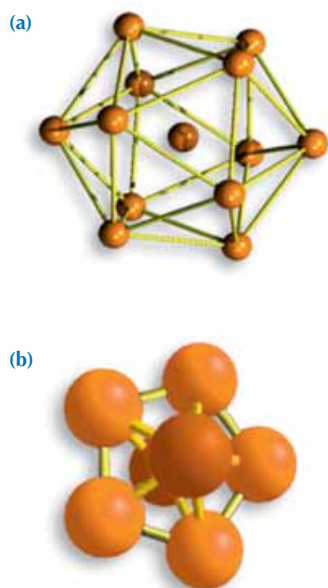


Figure 6: Two examples of structures that are not compatible with the formation of a crystal:

- (a) An icosahedron, the densest arrangement possible for 13 atoms.
 (b) A cluster of 7 atoms with pentagonal symmetry

CEA^{w1} in Grenoble, France, was to understand and improve novel growth methods for semiconductor nanostructures. In these methods, the processes of solidification and nucleation are crucial. The attention of our team was attracted by a report on supercooling in droplets of metal–semiconductor alloys: these droplets offered us a good system to study the influence of a crystalline seed (a silicon surface) on the solidification of the alloy.

We deposited tiny droplets (0.1–0.2 μm) of a liquid gold–silicon alloy on a silicon surface, prepared under ultra-high vacuum conditions, a standard technique used in semiconductor processing. We observed that, while in contact with this crystalline surface, the droplets remained liquid at 240 $^{\circ}\text{C}$, well below their melting point (which is 363 $^{\circ}\text{C}$). To understand this extraordinary supercooling behaviour (usually only observed in the absence of crystalline seeds), we carried out

an experiment at the European Synchrotron Radiation Facility (ESRF)^{w2}, also in Grenoble. The scattering of very intense X-rays produced in a synchrotron is a unique way to obtain information about the arrangement of atoms in a liquid and on solid surfaces.

We fired X-rays almost parallel to the surface of the silicon crystal on which the droplets of gold–silicon alloy had been deposited. At an angle of only 0.1 $^{\circ}$ (a technique called *grazing*

Figure 7: Droplets of liquid gold–silicon alloy all melted at the same temperature. As they cooled, however, the differences in the crystalline silicon surfaces on which the droplets sat affected the temperature at which the droplets crystallised.

(a) When the silicon crystal was cut along the cubic facets, the silicon atoms at the surface that was in contact with the droplet were arranged in a square lattice. On this surface, the droplets crystallised at about 60 K below their melting point. X-ray results showed that the droplet had crystallised in a structure and orientation similar to the silicon crystal on which it sat.

(b) When the silicon crystal was cut in the spatial diagonal of the cube, the silicon atoms at the surface that was in contact with the droplet were arranged in a triangular lattice. The droplet on this surface crystallised at about 70 K below its melting point. X-ray results showed that the droplet too had crystallised in a structure and orientation similar to the silicon crystal on which it sat.

(c) The silicon crystal was cut as in (b) but underwent a special treatment at high temperature that provoked the formation of a pentagonal atomic arrangement of gold atoms bonded to the silicon surface. On this surface, the droplets remained in their metastable liquid phase down to 120 K below the melting point – deeply supercooled

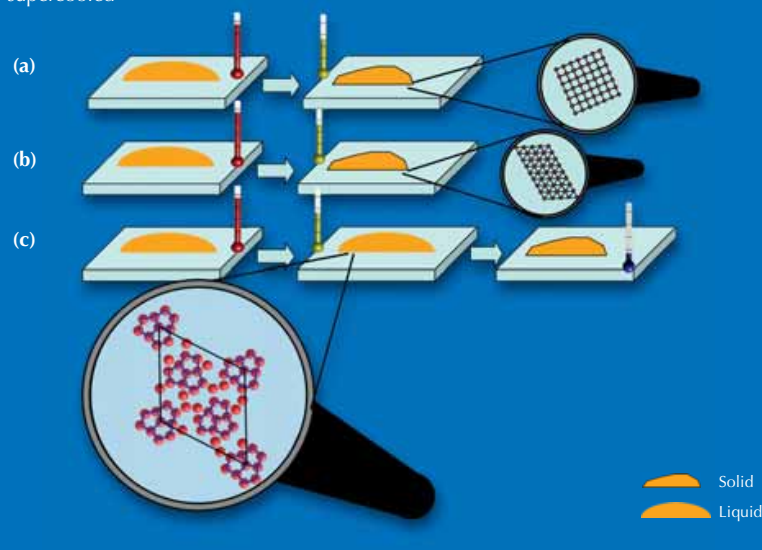


Image courtesy of Tobias Schülli

incidence), the X-rays are reflected by the flat silicon surface and penetrate the droplets deposited on it. The scattered X-rays carry information about the atomic arrangement of the last atomic layer of the silicon surface, as well as about the structure of the droplets.

These experiments allowed us to determine the state (liquid or crystalline) of the droplets as they were cooled, and to determine the exact atomic arrangement of the upper atomic layer of the silicon surface. The X-ray results showed that in the uppermost atomic layer of the silicon surface, the atoms were arranged with five-fold symmetry. On these surfaces, even when cooled to more than 100 degrees below their melting point, the droplets remained liquid.

A more detailed analysis of the solid / liquid interface revealed that these pentagonal surface structures were formed from a single layer of gold atoms bonded tightly to the silicon crystal. As explained before, we generally expect liquids to mimic the solid structure with which they are in contact, provoking heterogeneous nucleation. Our measurements showed that such mimicry of the surface structure takes place, but that it can have the opposite effect: a structure that is incompatible with the formation of a 3D crystal can force the liquid to locally adopt the 'wrong' type of order. Instead of triggering heterogeneous nucleation, this increases the stability of the supercooled phase of the liquid (see Figure 7).

After 60 years of research into supercooling of metals, this is finally the experimental demonstration that five-fold symmetry affects the metastability of a liquid (Schüllli et al., 2010; Greer, 2010).

References

- Fahrenheit DG (1724) Experimenta & observationes de congelatione aquæ in vacuo factæ. *Philosophical Transactions* **33**: 78-84. doi: 10.1098/rstl.1724.0016
- Frank FC (1952) Supercooling of liquids. *Proceedings of the Royal Society* **215**: 43-46. doi: 10.1098/rspa.1952.0194
- Greer AL (2010) Materials science: a cloak of liquidity. *Nature* **464**: 1137-1138. doi: 10.1038/4641137a
Download the article free of charge on the *Science in School* website (www.scienceinschool.org/supercooling#resources), or subscribe to *Nature* today: www.nature.com/subscribe.
- Reichert H et al. (2000) Observation of five-fold local symmetry in liquid lead. *Nature* **408**: 839-841. doi: 10.1038/35048537
Download the article free of charge on the *Science in School* website (www.scienceinschool.org/supercooling#resources), or subscribe to *Nature* today: www.nature.com/subscribe.
- Schüllli TU et al. (2010) Substrate enhanced supercooling in AuSi eutectic droplets. *Nature* **464**: 1174-1177. doi: 10.1038/nature08986
Download the article free of charge on the *Science in School* website (www.scienceinschool.org/supercooling#resources), or subscribe to *Nature* today: www.nature.com/subscribe.
- Turnbull D (1952) Kinetics of solidification of supercooled liquid mercury droplets. *Journal of Chemical Physics* **20**: 411-424. doi: 10.1063/1.1700435

Web references

w1 – The CEA is the French Atomic Energy and Alternative Energies Commission (*Commissariat à l'énergie atomique et aux énergies alternatives*). To learn more, see: www.cea.fr

w2 – The European Synchrotron Radiation Facility (ESRF) is an international research institute for cutting-edge science with photons. ESRF is a member of EIROforum, the publisher of *Science in School*. To learn more, visit: www.esrf.eu

Resources

For a further consideration of clouds, see:

Ranero Celius K (2010) Clouds: puzzling pieces of climate. *Science in School* **17**: x-y.
www.scienceinschool.org/2010/issue17/clouds

To see all other *Science in School* articles about ESRF, see www.scienceinschool.org/esrf

Tobias Schüllli studied physics and mathematics at the University of Stuttgart, Germany. He obtained his PhD at the Johannes Kepler University Linz, Austria, for the development of X-ray scattering methods in the study of semiconductor nanostructures. In 2003 he joined the *Commissariat à l'énergie atomique et aux énergies alternatives* (CEA) Grenoble, where he studied crystal surfaces and nanostructure growth in situ using synchrotron radiation at the ESRF. In 2009, he moved to ESRF and is in charge of the upgrade of one of its instruments, dedicated to the study of nanostructures and interfaces using highly focused X-ray beams.



Bibliography

- [1] H. Kiessig, *Ann. d. Physik* **10**, 769 (1931).
- [2] M. A. Krivoglaz, *X-ray and neutron diffraction in non-ideal crystals* (Springer, Berlin, Heidelberg, 1996).
- [3] I. Kegel *et al.*, *Phys. Rev. Lett.* **85**, 1694 (2000).
- [4] J. Stangl, V. Holý, and G. Bauer, *Rev. Mod. Phys.* **76**, 725 (2004).
- [5] B. E. W. D. T. Keating, *J. Appl. Phys.* **22**, 286 (1951).
- [6] A. Di Cicco, *Phys. Rev. Lett.* **81**, 2942 (1998).
- [7] L. Zhang *et al.*, *Phys. Rev. Lett.* **85**, 1484 (2000).
- [8] H. Dosch, *Critical phenomena at surfaces and interfaces* (Springer, Berlin, 1992).
- [9] R. Feidenhansl, *Surf. Sci. Rep.* **10**, 105 (1989).
- [10] I. Robinson, *Rep. Prog. Phys.* **55**, 599 (1992).
- [11] G. Renaud, B. Villette, I. Vilfan, and A. Bourret, *Phys. Rev. Lett.* **73**, 1825 (1994).
- [12] R. Baudoing-Savois *et al.*, *Nucl. Instr. Meth. Phys. Res. B.* **149**, 213 (1999).
- [13] J. B. Hannon, S. Kodambaka, F. M. Ross, and R. M. Tromp, *Nature* **440**, 66 (2006).
- [14] S. Kodambaka, J. Tersoff, M. C. Reuter, and F. M. Ross, *Science* **316**, 729 (2007).
- [15] D. G. Fahrenheit, *Philosophical Transactions* **33**, 78 (1724).
- [16] D. Turnbull, *J. Journ. Appl. Phys.* **20**, 817 (1949).
- [17] D. Turnbull, *J. Journ. Appl. Phys.* **21**, 1022 (1950).
- [18] F. C. Frank, *Proc. R. Soc. London A* **215**, 43 (1952).
- [19] H. W. Sheng *et al.*, *Nature* **439**, 419 (2006).
- [20] P. J. Steinhardt, D. R. Nelson, and M. Ronchetti, *Phys. Rev. Lett.* **47**, 1297 (1981).
- [21] B. J. Kim *et al.*, *Science* **322**, 1070 (2008).

[22] www.fondation-nanosciences.fr .

[23] www.scienceinschool.org .

Zusammenfassung

In der vorliegenden Arbeit werden Studien der Beobachtung des Wachstums von Nanostrukturen mittels Röntgenstreuung vorgestellt. Sie dienen dem tieferen Verständnis von kinetischen Prozessen welche für das Zustandekommen bestimmter Strukturen verantwortlich sind. Insbesondere beim Inselwachstum wie es z.B. beim selbstorganisierten Wachstum von Halbleiter Quantenpunkten angestrebt wird, sind viele Eigenschaften der endgültigen Struktur nur erklärbar wenn man alle Phasen des Wachstums, möglichst auf atomarer Ebene verfolgen kann. Zur Auswertung von Röntgenstreudaten bedarf es zwar in den meisten Fällen gewisser Modellannahmen, diese sind jedoch weitgehend überprüft, nicht zuletzt aus der genauen Kenntnis vieler Modellparameter welche mittels anderer Methoden wie z.B. der Transmissionselektronenmikroskopie bestimmt wurden. Im Falle der Röntgenstreu-Untersuchung von Nanostrukturen während ihres Wachstums erlaubt dies dann eine erfahrungsgestützte Interpretation der Daten welche nicht gleichzeitig mit anderen Methoden überprüfbar sind. Für eine Verfolgung bestimmter Parameter wie Kristallstruktur, Gitterverzerrungen sowie chemische Zusammensetzung *während* des Wachstums von Halbleiter Nanostrukturen eignen sich Röntgenstremethoden auf einzigartige Weise. Sie sind kompatibel mit hohen Temperaturen, sowie tolerant gegenüber verschiedener Probenumgebungen welche zum Wachstum benötigt werden.

Die ersten Experimente, welche in dieser Arbeit vorgestellt werden untersuchen die Anordnung der Oberflächenatome eines Siliziumkristalles im Falle der Bedampfung mit wenigen Atomlagen (typischerweise ein bis drei) Germanium. Die Bestimmung der Strukturveränderung in drei Dimensionen welche die obersten fünf bis zehn Atomlagen betrifft gibt Aufschluss über die darin enthaltene elastische Energie, sowie die chemische Zusammensetzung jeder Atomlage. Sie erlaubt somit Rückschlüsse über Austauschprozesse von Silizium- und Germanium Atomen, welche zu einer Durchmischung des abgeschiedenen Germaniums führen. Diese Parameter beeinflussen die Stabilität dieses dünnen Films während späterer Wachstumsphasen.

Weitere Untersuchungen beschäftigen sich den darauffolgenden Wachstumsphasen des Systems Germanium/Silizium. Besondere Aufmerksamkeit gilt den frühen Stadien des Inselwachstums, welches nach etwa vier bis fünf Atomlagen aufgedampften Germaniums einsetzt. In dieser Phase bilden sich kleine Kristallite an der Oberfläche, welche mit ihrem Kristallgitter kohärent an das Siliziumsubstrat angebunden sind. Anders als im geschlossenen Film können die Kristallgitter sich in solchen Inseln lateral ausdehnen und somit den 4.2 % Längenunterschied zwischen den Silizium und Germanium Atombindungen teilweise ausgleichen. Es liegt daher auf der Hand, die elastische Energie nicht nur als treibende Kraft des Inselwachstums an sich, sondern auch der genauen Inselmorphologie anzusehen. Zur experimentellen Bestimmung der elastischen

Energie bedarf es jedoch genauer Kenntnis der chemischen Zusammensetzung sowie des Gitterparameters, also des Atomabstandes in den Inseln. Diese beiden Parameter können durch Röntgendiffraktion während des Inselwachstums bestimmt werden. Desweiteren kann die äussere Form der Inseln mittels Röntgenkleinwinkelstreuung praktisch ohne Annahme von Modellen ermittelt werden wenn, wie im vorliegenden Falle, die Inseln durch wohldefinierte Facetten begrenzt sind. Insofern kann diese als *in situ* Messmethode bezeichnete Verfolgung des Wachstums von Nanostrukturen einen Zusammenhang zwischen Morphologie und innerer Struktur herstellen. Für Anwendungen dieser Halbleiter Nanostrukturen ist die Kenntnis und wenn möglich die Einflussnahme auf die Parameter Zusammensetzung und elastische Energie des Gitters wichtig, da beide die Bandstruktur beeinflussen.

Eine weitere wichtige Eigenschaft solcher Inseln ist die Versetzungsfreiheit. Das eventuelle Auftreten von Versetzungen ist mittels Röntgenstreuung leicht zu beobachten und somit ein weiteres Argument für *in situ* Messungen. Allgemein lässt sich sagen daß Durchmischungspänomene sowie das Ausbilden von Versetzungen zur Gitterrelaxation als Konkurrenz zur elastischen Deformation thermodynamisch verstanden sind. Jedoch befinden sich die Inseln während des Wachstumsprozesses in der Regel weit weg vom thermodynamischen Gleichgewicht. Es ist daher auf theoretischem Wege nur schwer möglich diese Prozesse und damit die Inselentstehung und Gestalt zu verstehen oder vorherzusagen. Insbesondere die Diffusionswege und damit die Herkunft des Siliziums in den Inseln stellt sich dabei als Schwierigkeit heraus and bleibt aufwändigen numerischen Simulationen vorbehalten. Die hier vorgestellten Arbeiten eröffnen in diesem Sinne Einsichten auf einem Gebiet welches so bisher mit anderen Methoden nur schwer zugänglich war.

Der zweite Teil der Arbeit widmet sich komplexeren Wachstumsmethoden sowie metallischen Nanostrukturen wie sie bei z.B. bei der Gaskatalyse oder der Herstellung von Halbleiter Nanodrähten eine Rolle spielen. Hierbei wird das Potential der *in situ* Röntgenanalyse im Falle des Wachstums aus der Gasphase deutlich. Das Wachstum von Halbleiter Nanodrähten bedingt eine Metall-Halbleiterphase welche auch bei relativ niedrigen Temperaturen flüssig ist und als Katalysator dient. Der Übergang von der flüssigen in die feste Phase ist durch Röntgenbeugung besonders einfach zu beobachten, wobei zusätzlich eine gewisse Strukturinformation über die mittleren Atomabstände in der Flüssigkeit zugänglich ist. In diesen Prozessen stellen Röntgenmethoden die einzige Möglichkeit dar während des Wachstums die atomare Struktur der Nanodrähte, des flüssigen Katalysators, sowie der Grenzfläche zwischen beiden zu ermitteln. Letztere erweist als Wachstumsfront des kristallinen Drahtes von besonderem Interesse. Dieses Potential rechtfertigt derzeit den Ausbau bestehender Ultra-Hoch-Vakuum Kamern zu Anlagen, welche molekularstrahlepitaktisches Wachstum mit Abscheidungsmethoden aus der Gasphase kombinieren können.

Im Anhang der Arbeit wird eine populärwissenschaftliche Behandlung der Struktur von Flüssigkeiten vorgestellt, welche in Anlehnung an die Ergebnisse des letzten Kapitels verfasst wurde.